


专业技术职务申报简表（理工类-2016 版）

所在单位： 生物与医学工程学院

填表时间： 2016 年 05 月 16 日

姓 名	汪待发	性别	男	出生年月	1984.04	
最后学历	博士	学位	博士	拟申请专业技术职务	副教授	
现任专业技术职务	讲师	现任专业技术职务批准时间			2010.10	
申报学科（一级/二级学科名称）		生物医学工程		研究方向	散射生物光子学	
申报类别	<input checked="" type="checkbox"/> 教师 <input type="checkbox"/> 科学研究 <input type="checkbox"/> 工程 <input type="checkbox"/> 实验 <input type="checkbox"/> 其他					

主要学习工作经历及海外经历（从高中起，应连续）

起止年月		学习与工作单位	学历、学位、专业、职务
起	止		
1998.09	2001.07	潜山野寨高中	高中生
2001.09	2005.07	清华大学生物与医学工程系	本科生
2005.09	2010.07	清华大学生物与医学工程系	博士生
2010.07	今	北京航空航天大学生物与医学工程学院	讲师
2014.04	2015.09	加州理工学院电子系	访问学者（500 天）

研究水平和特点概述（限填 200 字）

长期从事散射生物光子学研究，发表 SCI 论文十余篇，总引用数超过 300 次，主持包括国家自然科学基金和博士点基金在内的课题 6 项，经费到款 159 万。利用光子散射探索小动物或人体深部的功能和分子成像，所主持研发的大型近红外光谱脑功能成像仪已产业化；压制光子散射攻克组织光学聚焦的深度极限这一领域重要难题，2015 年提出超快深部光学聚焦方法，世界上首次透过含血流的 2mm 厚强散射活体组织获得了高能量、高对比度光学聚焦，9 个月内他引 10 次（google scholar）。

请填写任现职以来取得的代表性学术成果情况（限填 5 项，其中论文不少于 3 篇，奖励、专著或教材等各不多于 1 项）

学术论文题目	发表刊物或会议	发表（出版）时间	收录、他引情况	影响因子	期刊分区及排名/总数	作者排名
Focusing through dynamic tissue with millisecond digital optical phase conjugation	Optica	2015.08	SCI、7 次	美国光学学会 OSA	2014 年旗舰新刊	第 1 作者
Noncontact full-angle fluorescence molecular tomography system based on rotary mirrors	Applied Optics	2015.08	SCI、0 次	1.784	Q2 36/87	第 1 作者
High-Performance fluorescence molecular tomography through shape-based reconstruction using spherical harmonics parameterization	Plos One	2014.04	SCI、3 次	3.234	Q1 9/57	第 1 作者
Fluorescence molecular tomography using a two-step three-dimensional shape-based reconstruction with graphics processing unit acceleration	Applied Optics	2012.12	SCI、5 次	1.784	Q2 36/87	第 1 作者
Full-angle fluorescence diffuse optical tomography with spatially coded parallel excitation	IEEE Transactions on Information Technology in Biomedicine	2010.11	SCI、2 次	2.493	Q1 5/24	第 1 作者

任现职以来发表论文及收录情况：收录类别、作者贡献（第一、通讯等）仅计算 1 次；论文收录以图书馆检索证明为准，未检索到的来源刊论文仅计算 1 篇

类别	合计	SCI	SSCI	CSSCI	EI	ISTP	中文核心期刊	其他
一、符合职称申报条件论文	10	5			3		2	
其中：1.第一作者	8	5			3			
2.学生第一本人第二作者								

3.通讯作者	2					2	
二、其他	5	5					
任现职以来获得国家级教学/科研成果奖 <u>0</u> 项；省部级教学/科研成果一等奖前五名、二等奖前三名或三等奖第一名 <u>0</u> 项。请填写任现职以来获得教学、科研、管理奖励情况（限填3项，代表作成果除外）							
获奖项目	奖励名称		颁奖部门	奖励级别	获奖时间	人数	排名
人才项目	北京航空航天大学蓝天新秀		北京航空航天大学	校级	2010年	1	1
任现职以来共获得排名第一（含学生第一本人第二）授权专利 <u>4</u> 项，其中发明专利 <u>4</u> 项，实用新型 <u>0</u> 项，外观设计 <u>0</u> 项。请填写任现职以来共获得已授权专利情况（限填3项）							
专利名称	专利类型	授权日期	批准机构	专利号	权利单位	人数	排名
一种多光学信息同步检测的双参数荧光分子断层成像装置及方法	中国发明专利	2012.07.04	中华人民共和国国家知识产权局	CN201110090186.0	北京航空航天大学	3	1
一种基于旋转镜的全角度荧光分子断层成像装置	中国发明专利	2014.04.16	中华人民共和国国家知识产权局	CN201210394893.3	北京航空航天大学	6	1
任现职以来共主持纵向项目 <u>5</u> 项（不含参与，以任务书为准）：其中国家级 <u>1</u> 项，经费到款 <u>32</u> 万；省部级 <u>4</u> 项，经费到款 <u>17</u> 万；千万元以上 <u>0</u> 项，经费到款 <u>0</u> 万；请填写任现职以来主持的纵向项目（限填5项）							
项目名称		项目来源	起止时间	到款/经费总额			
融合多光学信息的双参数荧光分子断层成像方法的研究		国家自然科学基金	2012.01~2014.12	32万/32万			
融合多光学信息的双参数荧光分子断层成像的理论和算法研究		博士点基金	2012.01~2014.12	4万/4万			
任现职以来其他项目情况（限填3项）							
项目名称	项目来源	起止时间	负责人	承担份额/总额	主持/参与		
多通道近红外光脑功能成像仪NIR-BRAIN研制	企业	2013.05~2016.04	汪待发	102万/102万	主持		
任现职以来的教育教学情况：主讲课程共计 <u>305</u> 学时；指导本科生毕设 <u>4</u> 人次；指导硕士研究生 <u>5</u> 人次；指导博士研究生 <u>0</u> 人次。请填写任现职以来主讲的3门课程							
课程名称	起止时间	课程学时	本人授课学时	授课次数	授课对象	课程性质	
数值计算方法	2011.09~2014.01	32	30	3	本科生	选修	
生理信号检测与处理实验	2013.04~2013.06	18	9	1	研究生	学位课	
临检测试技术及装备	2016.03~2016.06	32	32	1	本科生	必修	
主要学术兼职（限填3项）							
学术兼职名称		受聘日期		颁授机构			
无							
任现职以来其他业绩成果（限100字）	指导本科生获得冯如杯竞赛一等奖和二等奖各一次。建设生物光学实验室；协助指导研究生2名、博士生1名。依托学院，服务产业，为北京谊安集团研发核心涡轮控制器；为北京纳通医疗集团研发了椎弓根内固定手术智能辅助装置。						
本人确认表内所填内容属实，如与事实不符，本人愿承担一切责任。 本人签字：汪待发 日期：2016.05.28							
申请人所填内容真实性核实无误。			单位负责人签字： 日期：				
单位审核人签字： 日期：			（加盖单位公章） 日期：				

注：本表限1页，需正反面打印或用黑色钢笔、签字笔填写，本人签名，不得任意添加其他内容。如有空项，请填写“无”。

Focusing through dynamic tissue with millisecond digital optical phase conjugation

DAIFA WANG,^{1,2,†} EDWARD HAOJIANG ZHOU,^{1,†} JOSHUA BRAKE,¹ HAOWEN RUAN,¹ MOOSEOK JANG,¹ AND CHANGHUEI YANG^{1,*}

¹Departments of Electrical Engineering and Bioengineering, California Institute of Technology, Pasadena, California 91125, USA

²Key Laboratory for Biomechanics and Mechanobiology of Ministry of Education, School of Biological Science and Medical Engineering, Beihang University, Beijing, China

*Corresponding author: chyang@caltech.edu

Received 18 May 2015; revised 16 July 2015; accepted 21 July 2015 (Doc. ID 240996); published 7 August 2015

Digital optical phase conjugation (DOPC) is a new technique employed in wavefront shaping and phase conjugation for focusing light through or within scattering media such as biological tissues. DOPC is particularly attractive as it intrinsically achieves a high fluence reflectivity in comparison to nonlinear optical approaches. However, the slow refresh rate of liquid crystal spatial light modulators and limitations imposed by computer data transfer speeds have thus far made it difficult for DOPC to achieve a playback latency of shorter than ~ 200 ms and, therefore, prevented DOPC from being practically applied to thick living samples. In this paper, we report a novel DOPC system that is capable of 5.3 ms playback latency. This speed improvement of almost 2 orders of magnitude is achieved by using a digital micromirror device, field programmable gate array (FPGA) processing, and a single-shot binary phase retrieval technique. With this system, we are able to focus through 2.3 mm living mouse skin with blood flowing through it (decorrelation time ~ 30 ms) and demonstrate that the focus can be maintained indefinitely—an important technological milestone that has not been previously reported, to the best of our knowledge. © 2015 Optical Society of America

OCIS codes: (110.0113) Imaging through turbid media; (070.5040) Phase conjugation; (110.0180) Microscopy.

<http://dx.doi.org/10.1364/OPTICA.2.000728>

1. INTRODUCTION

Focusing light through tissues has long been a challenge for biomedical optics. The turbid nature of tissues strongly scatters light and hinders the formation of a sharp focus. Recently, research in the field of wavefront shaping has shown that by correcting the wavefront incident on scattering media, focus can be constructed at an arbitrary location behind the sample [1,2]. Different strategies have been developed to realize this process including iterative wavefront optimization [1,3–5], transmission matrix measurement [6–8], and optical phase conjugation (OPC) [9–11]. Among these, OPC implements the corrected wavefront by recording the scattered light field globally and then playing back the conjugate light field by a phase conjugate mirror (PCM) without time-consuming iterations. Since the process of elastic light scattering is time symmetric, by playing a conjugate version of the scattered wavefront back through the scattering medium, the conjugate input wavefront can be recovered.

By employing OPC, a number of novel techniques for focusing light through or within a scattering medium have recently been developed. These include time-reversed ultrasonically encoded light (TRUE) [12,13], time reversal of variance-encoded light (TROVE) [14], time reversal by analysis of changing wavefronts from kinetic targets (TRACK) [15], and time-reversed adapted-perturbation (TRAP) focusing [16]. These methods have

the potential to improve or enable biomedical applications such as deep tissue imaging, photodynamic therapy, and noninvasive cytometry.

There are two major advantages of OPC compared to other wavefront shaping techniques. First, it is able to arrive at the correct wavefront solution without iteration. Second, the number of controllable optical modes in the playback wavefront can be very high, $\sim 5 \times 10^5$ modes or more. Optical phase conjugation methods can be categorized into two primary groups. Nonlinear OPC methods [12,17,18] employ nonlinear crystals to store the scattered field and propagate the phase conjugate field. In contrast, the digital optical phase conjugation (DOPC) method [13–16] uses an electronic camera in an interferometric setup to capture the optical wavefront information and subsequently produce a suitable OPC field by using that information to pattern a spatial light modulator (SLM).

The DOPC method has several intrinsic advantages over nonlinear OPC methods. First, whereas nonlinear crystals are strongly dependent on wavelength, DOPC can freely work with a broad range of wavelengths. Second, DOPC provides the flexibility to render wavefront playback beyond a single OPC field. In fact, TROVE, TRACK, and TRAP all exploit this unique capability of DOPC to render complex and nuanced wavefronts. In the case of TRACK and TRAP, for example, the rendered wavefront is

actually a differential DOPC wavefront. Third, and perhaps most important, the DOPC method has the intrinsic ability to achieve a fluence reflectivity greater than unity. Here, we define fluence reflectivity as the ratio between the total amount of light that one can play back on the conjugate wavefront to the total amount of scattered light required to determine the conjugate wavefront in the first place. While nonlinear OPC methods can in principle provide gain enhancement by temporally squeezing the playback photon packet [19], a practical and useful approach to deliver large amounts of energy over an extended period of time has not been demonstrated.

Currently, the DOPC method does have a significant disadvantage versus nonlinear OPC methods' response speeds. Recently, nonlinear methods with system response latencies of the order of milliseconds have been reported [20,21]. In contrast, DOPC systems reported thus far have response times of the order of hundreds of milliseconds or more [22]. This slow response is due to the use of slow liquid crystal SLMs and conventional personal computer (PC)-based data transfer. Fast response speed is a key criterion if we are to apply OPC methods usefully for *in vivo* applications in thick samples. This is mainly due to the dynamic nature of biological tissue caused by the constant motion of the scatterers within. This rate of change is dependent both on sample thickness and the degree of immobilization. As a reference point, the scattered field of 532 nm light through an unclamped living mouse skin flap has a speckle decorrelation time of ~ 30 ms. When the same tissue is clamped, this decorrelation time increases to ~ 300 ms [22].

The primary goal of this paper is to show that the use of a high-speed digital mirror device (DMD) and field programmable gate array (FPGA) data processing allows DOPC to achieve high response speeds, as well. While using the binary modulation of the DMD to accomplish wavefront shaping may seem

counterintuitive, and the oblique reflection angle significantly complicates DOPC system alignment, overcoming these challenges enables us to incorporate the strengths of the DOPC while minimizing the response time of the system. In this paper, we report a novel DMD-based DOPC system with a demonstrated playback latency of 5.3 ms. We demonstrate that our system is capable of focusing light through 2.3 mm thick unclamped mouse dorsal skin with a decorrelation time of less than 30 ms. By repeating the DOPC procedure 50 or even more times per second, we are able to maintain indefinitely the focus through the living sample. This demonstration of sustainable focusing through a thick living sample with blood flowing through it is the first of its kind and opens the door for new applications of OPC in the deep tissue regime of live biological samples.

2. METHODS

A simplified schematic of the DMD-based DOPC system is shown in Fig. 1(a). A complete optical scheme can be found in Supplement 1. The light paths of the setup for recording and playback are shown in Figs. 1(b) and 1(c), respectively. As shown in Fig. 1(b), in the recording step, all the pixels on the DMD are turned off. This causes the playback beam to diffract away from Camera 1 and onto a beam dump. The sample beam and reference beams are combined at BS3, reflected by BS4 and Mirror 2, and travel back through BS4 to Camera 1, where their interference pattern is measured. In the playback step shown in Fig. 1(c), the FPGA processes the camera data to generate a suitable wavefront solution and sends it to the DMD, which displays the corresponding phase map. The playback beam then propagates through BS4, BS3, and L3 to the sample. Meanwhile, the sample beam is blocked by a fast shutter to prevent backscattering off the sample. This playback process results in a focus

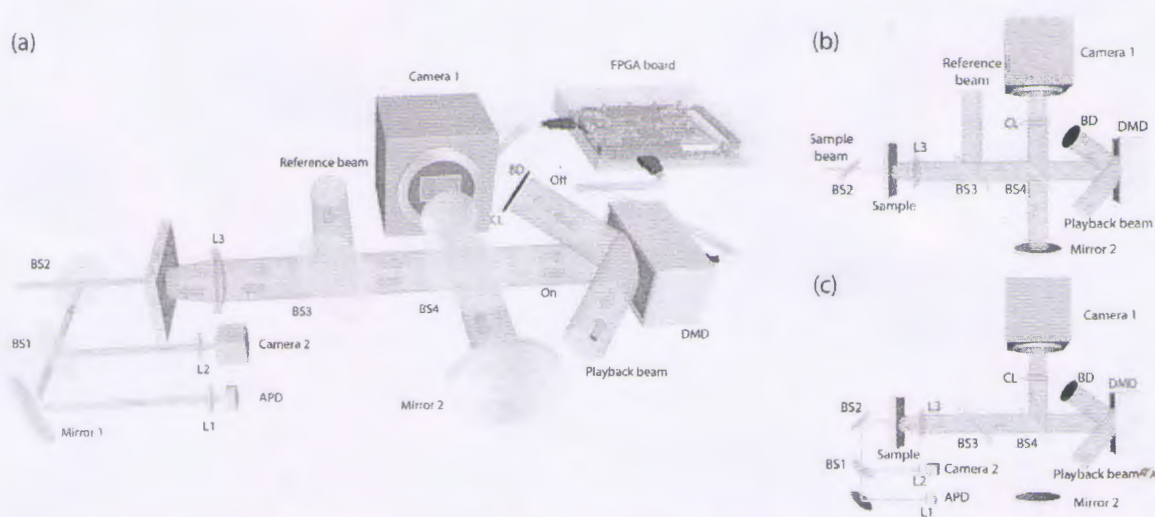


Fig. 1. (a) Simplified schematic of the DMD-based DOPC. A 2.5 mm diameter collimated beam from the laser source (Excelsior 532 nm single mode, 200 mW, Spectra-Physics) is incident onto the sample through BS2. Scattered light from the sample is collected by L3 and is combined with the reference beam by BS3. The combined reference and sample beam is reflected by BS4 and Mirror 2, passes through BS4, and is captured by Camera 1 (pco.edge 5.5, PCO-TECH). The DMD (W4100, Wintech) and Mirror 2 are aligned symmetrically with reference to BS4, and the DMD surface is imaged onto the camera sensor chip by CL (AF-S VR Micro-NIKKOR 105 mm f/2.8G IF-ED, Nikon) with pixel-to-pixel alignment. Camera 1 and the DMD are connected through a host FPGA (ViClaro IV GX Camera Link Development Kit, Microtronix). The conjugate result is observed on Camera 2 (Prosilica GX 1920, Allied Vision) and the APD (SPCM-AQRH-14, Excelitas). (b) Optical path schematic of the recording step. (c) Optical path schematic of the playback step (L, lens; BS, beam splitter; BD, beam dump; CL, camera lens; APD, avalanche photodiode).

observed through the sample on Camera 2 and a corresponding peak recorded by the avalanche photodiode (APD). As the reference beam and playback beam are two separate beams, the fluence reflectivity is limited only by the damage threshold of the DMD and the laser power. In our system, the fluence reflectivity was set at 2000. As response speed is a design priority, each major component of this system is chosen and adapted for this purpose. We will discuss each component in the following subsections.

A. Single-Shot Binary Phase Retrieval

To compute the correct phase map to display on the DMD, Camera 1 captures the interference pattern between the reference field $E_{\text{ref}}(x, y)$ and the sample field $E_{\text{sam}}(x, y)$. This interference pattern can be described as: $I_i(x, y) = I_{\text{ref}}(x, y) + I_{\text{sam}}(x, y) + 2\sqrt{I_{\text{ref}}(x, y)I_{\text{sam}}(x, y)}\cos|\Delta\theta|$, where $I_{\text{ref}}(x, y)$ and $I_{\text{sam}}(x, y)$ are the intensity of the reference and sample fields, respectively, and $\Delta\theta$ is their phase difference. By setting $\langle I_{\text{sam}}(x, y) \rangle \ll I_{\text{ref}}(x, y)$, $I_i(x, y)$ can be approximated as

$$I_i(x, y) \approx I_{\text{ref}}(x, y) + 2\sqrt{I_{\text{ref}}(x, y)I_{\text{sam}}(x, y)}\cos|\Delta\theta|. \quad (1)$$

Then, $I_{\text{ref}}(x, y)$ can be measured independently by blocking the sample beam and, by comparing it to $I_i(x, y)$, we can determine the range in which the absolute phase difference $|\Delta\theta|$ lies

$$\begin{aligned} I_i(x, y) < I_{\text{ref}} &\rightarrow \frac{\pi}{2} < |\Delta\theta| \leq \pi, \\ I_i(x, y) > I_{\text{ref}} &\rightarrow 0 \leq |\Delta\theta| \leq \frac{\pi}{2}. \end{aligned} \quad (2)$$

In this way, the intensity of the interference pattern at a point (x, y) can be used to recover the binary phase of $E_{\text{sam}}(x, y)$ in a single shot. In comparison, two methods commonly applied in DOPC systems, phase stepping holography [23] and off-axis holography [24], are capable of fully recovering the sample field but sacrifice either speed or spatial resolution. While DOPC playback with binary phase information is less efficient than with perfect phase information, this small sacrifice in efficiency yields a large enhancement in response speed.

B. FPGA-Based Data Processing and Transfer

An FPGA board [as shown in Fig. (2)] is implemented in the DOPC system for data processing and transfer. It has a camera link connection directly to the recording camera and a high definition multimedia interface (HDMI) connection to the DMD. This allows full frame (1920×1080) interference pattern transfer in 5.0 ms (6.8 Gb/s) and full frame size phase map transfer in 1.56 ms (1.8 Gb/s). Here, the phase map transfer time is the time from starting the binary phase data transfer to completing the stable display on the DMD. Although the DMD chip (DLP9500, TI) has a fast refreshing speed of up to 23 K fps, the standard 60 Hz HDMI display interface of the W4100 board limits the performance. To fully utilize the fast response speed of the DMD, we designed custom firmware for the FPGA controller (Virtex 5, Xilinx) on the W4100 board. With a custom HDMI protocol, we encode 24 binary pixels into one 24 bit RGB pixel of standard HDMI, allowing us to achieve fast binary image transfer. In the recording step, the FPGA board reads out the interference image from the recording camera and retrieves the phase in parallel. Once the phase map is ready and has been adjusted to compensate for the curvature of the DMD (see Supplement 1), it is transferred to the DMD board and displayed. Compared to a computer, the FPGA allows for greatly accelerated data processing

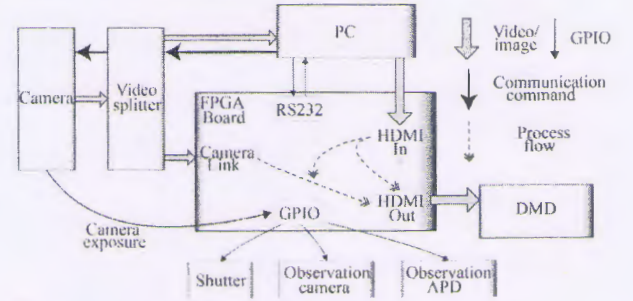


Fig. 2. Functional schematic of the FPGA-based DOPC.

and transfer speeds. When using a PC as the host processor in DOPC, the multitask scheduling and hardware access wrapping in modern operating systems limits the latency between recording and playback steps to a minimum of around 200 ms [22]. In contrast, as an FPGA inherently has a highly parallel computing capacity, the processing latency for binary phase retrieval is eliminated by overlapping the phase processing with the camera image transfer. In addition to the speed of the FPGA system, our setup allows for data collection and processing to be seamlessly switched to the PC for time-insensitive optical system debugging and pixel-pixel alignment between the recording camera and the DMD. To achieve this, a video splitter (CLV-402, Vivid Engineering) is implemented to switch the output of the recording camera between the PC and the FPGA. An HDMI interface is also set up between the PC and FPGA to allow the PC to transfer phase maps to the DMD.

C. DMD-based Phase Conjugation

When a conjugate phase map is displayed on the DMD, the DMD implements a binary amplitude modulation scheme [25] to construct a conjugate focus through the tissue. Here we will analyze the binary phase modulation scheme, which, although essentially identical to binary amplitude modulation, is formulated here to easily integrate into the framework of phase conjugation [26].

When using the DMD for light modulation, every individual micromirror acts as a diffractive element and together the whole DMD acts as a 2D blazed grating. As shown in Fig. 3(a), when a pixel is turned on, it will tilt 12° clockwise in the diagonal direction. This oblique angle complicates the DOPC system design, as it is a challenge that does not exist for SLM-based DOPC systems. To address this, we choose to illuminate the DMD with an appropriately tilted light field such that the diffracted light propagates perpendicularly with respect to the surface of the DMD. This propagation direction is subject to the blazed grating equation, which is a function of the center-to-center distance between the individual micromirrors in the array (d), the angle of incidence (ϕ) with respect to the DMD surface normal, the wavelength (λ), and the diffraction order (n). Setting the diffraction angle to fix the diffraction direction normal to the DMD surface yields a simplified form of the blazed grating equation

$$d \sin \phi = n\lambda. \quad (3)$$

However, in order to achieve the maximum possible intensity of the diffraction beam, the incident angle should be chosen so that the central peak of the sinc^2 envelope determined by the

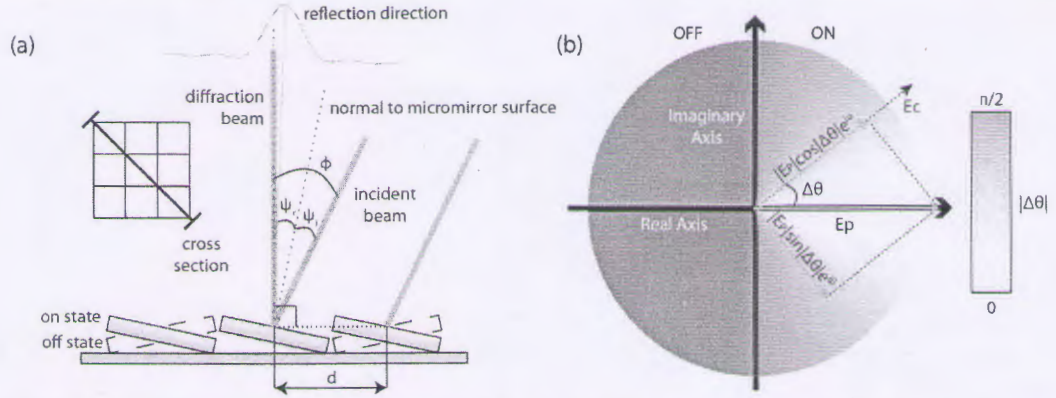


Fig. 3. (a) DMD diffraction demonstration. (b) Binary phase modulation of a DMD. E_p is the field played back by the DMD, E_c is the desired phase conjugate field, and $\Delta\theta$ is the phase difference between E_c and E_p . When a pixel of the DMD is turned on, it plays back the phasor E_p , which can be decomposed into two orthogonal components. One is in the direction of the desired phase conjugate field E_c with an amplitude modulated by $\cos|\Delta\theta|$ and contributes to the focus. The other component orthogonal to E_c is modulated by $\sin|\Delta\theta|$ and contributes to the background.

direction of the specular reflection from each individual micro-mirror matches as closely with the direction normal to the DMD surface as possible. Combining the simplified blazed grating equation above with the law of reflection ($\psi_i = \psi_r$), which determines the location of the sinc^2 envelope, we can solve for the incident angle to maximize the intensity of the diffracted beam. Given a light source with a wavelength of 532 nm and $d = 10.8\sqrt{2} \mu\text{m}$ from the dimensions of the DMD, we solve to find the optimum incident angle and diffraction order to be $\phi = 24.7^\circ$ and $n = 12$, respectively.

After optimizing the alignment of the DMD in the DOPC system, we fit the binary amplitude modulation of the DMD into a phase conjugation framework. Since the diffracted light from the DMD has a uniform phase, we can spatially choose whether it is played back or not by manipulating each pixel's state. As shown in Fig. 3(b), without loss of generality, we suppose playback beam E_p has uniform amplitude A and phase zero. For an electric field $E_c = |E_c|e^{i\alpha}$, which is the optimal phase conjugate solution to be played back, there is a phase difference $\Delta\theta$ between E_c and E_p . Using the binary phase retrieval algorithm described earlier, we determine whether an individual pixel should be played back. If $|\Delta\theta|$ is less than $\pi/2$, the corresponding pixel is turned on. Otherwise, it is turned off. When we turn on the pixel, E_p can be decomposed into orthogonal phase vectors, as shown in Fig. 3(b). This allows us to derive the phase modulation function of the DMD in DOPC as

$$f(|\Delta\theta|) = \begin{cases} 0, & \frac{\pi}{2} < |\Delta\theta| \leq \pi \\ \cos|\Delta\theta|e^{i\alpha} + \sin|\Delta\theta|e^{i\beta}, & 0 \leq |\Delta\theta| \leq \frac{\pi}{2} \end{cases} \quad (4)$$

This means that when $0 \leq |\Delta\theta| \leq \frac{\pi}{2}$ and a pixel of the DMD is turned on to represent a certain E_c , we will play back the electric field $|E_p| \cos|\Delta\theta|e^{i\alpha}$, which has the phase of E_c and amplitude modulated by $\cos|\Delta\theta|$, along with an orthogonal electric field $|E_p| \sin|\Delta\theta|e^{i\beta}$ with amplitude modulated by $\sin|\Delta\theta|$. The cosine term will be played back as a correct component of the phase conjugate field, and construct a peak. The sine term, which has an orthogonal phase, will make no contribution to the peak recovery and will form a background in the playback field. Following a similar derivation in Refs. [13,25] (see details in Supplement 1),

we find the theoretical peak-to-background ratio (PBR) for DMD-based DOPC to be

$$\text{PBR} = \frac{1/2 + (N-1)/2\pi}{M} \approx \frac{N}{2\pi M}, \quad (5)$$

where M is the number of modes in the focus, and N is the number of controllable modes on the DMD. Implementing the DMD in the DOPC setup allows our system to save more than 10 ms for conjugate phase display compared to the time reported in liquid-crystal (LC)-SLM-based DOPC systems [13,15,22]. When a voltage is applied to an LC-SLM based on nematic liquid crystal technology, it usually takes over 10 ms to turn to the specified direction. This limits the refresh rate to tens of hertz. In contrast, a DMD, which is based on microelectromechanical system (MEMS) technology, has a response time of around 18 μs with a 23 kHz refresh rate [27], over 2 orders of magnitude faster than typical LC-SLMs.

D. Workflow of Fast DOPC

The workflow of our system is shown in Fig. 4. Prior to operation, the reference beam intensity distribution is recorded. Then the DOPC loop starts. At the beginning of every loop, all of the DMD pixels are turned off and the interference pattern is captured. Once the intensity of a pixel is transferred from the camera and stored by the FPGA, its binary phase is processed and recovered. After all the pixels are processed, the binary phase map is transferred to the DMD and displayed for a designated time. During the process, the fast shutter, exposure of the observation camera, and the recording of the APD signal are synchronized by the FPGA general purpose input/outputs (GPIOs). Each loop is synchronized by the exposure and transfer signals of the recording camera.

As shown in Fig. 4, the playback latency is the sum of the time required by the recording exposure, data transfer from the recording camera to the FPGA (recording transfer), and binary phase transfer from the FPGA to the DMD (phase transfer). For a full frame size of 1920×1080 (up to 2.1×10^6 controllable modes) and 0.5 ms exposure, the time from the start of the exposure to playback is 7.06 ms. A rolling shutter is used for the recording exposure, so neighbor rows start to expose successively with a 9.17 μs delay. The time latency is calculated from the average

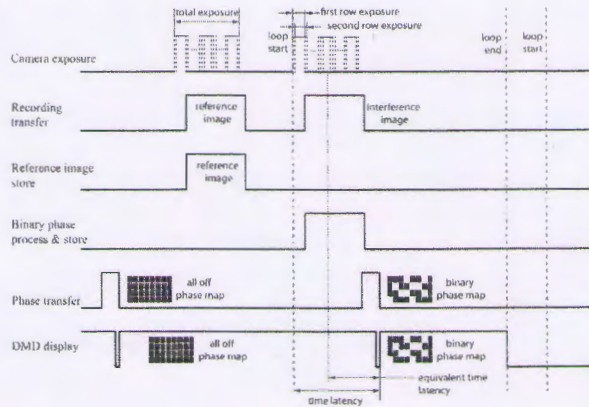


Fig. 4. Workflow of the FPGA-based DOPC.

exposure start time to the time playback starts. The latency is quantified by the following experiments.

3. RESULTS

A. Playback Latency Quantification

To evaluate the actual playback latency of our system, DOPC experiments were conducted on tissue samples with a controllable decorrelation time using a moving tissue strategy [20]. A piece of 3 mm thick chicken breast ($\mu_s = 30/\text{mm}$, $g = 0.965$) was sandwiched between two 1 mm thick glass slides. In the middle layer, a 3 mm thick U-shaped spacer was placed surrounding the chicken

breast to guarantee its thickness and mobility [as shown in Fig. 5 (a)]. During the experiment, samples were changed before they dried out to ensure their scattering properties. The whole sample was held by a translation stage with a motorized actuator (LTA-HS, Newport) to generate different decorrelation times by varying the lateral velocity.

The decorrelation time of the tissue itself was several seconds [13], which meant that the amount of decorrelation in a period of several milliseconds was negligible. To avoid the effects of slow decorrelation when the stage was accelerating, experiments were done when the stage had reached full speed. Tissue decorrelation curves when lateral velocity was set to 0.2 mm/s and 0.25 mm/s are shown in Figs. 5(b) and 5(c), respectively. Here we define the decorrelation time τ as the time t when the speckle correlation coefficient r_c decreases to $1/e$. Fitting with a Gaussian function $r_c = e^{-t^2/\tau^2}$ [28], we can find the decorrelation time τ is 6.2 and 5.0 ms for each case. The conjugate focus results for the two cases are shown in Fig. 5(d). Given that the motion-induced degradation ratio of PBR is identical to the drop in the speckle correlation coefficient [22], it is straightforward to conclude that the system playback latency is identical to the decorrelation time of the sample when the PBR achieved on a moving sample is $1/e$ of the static PBR. From the results, the PBR is 88 for 0.2 mm/s and 56 for 0.25 mm/s. Comparing these to the value of the static PBR divided by e (~ 65), we can tell the time latency is slightly more than 5.0 ms, which can be accurately calculated as 5.3 ms.

B. OPC Efficiency Quantification

As shown in Eq. (5), PBR is related to both number of input modes (N , number of speckle grains on the DMD) and number

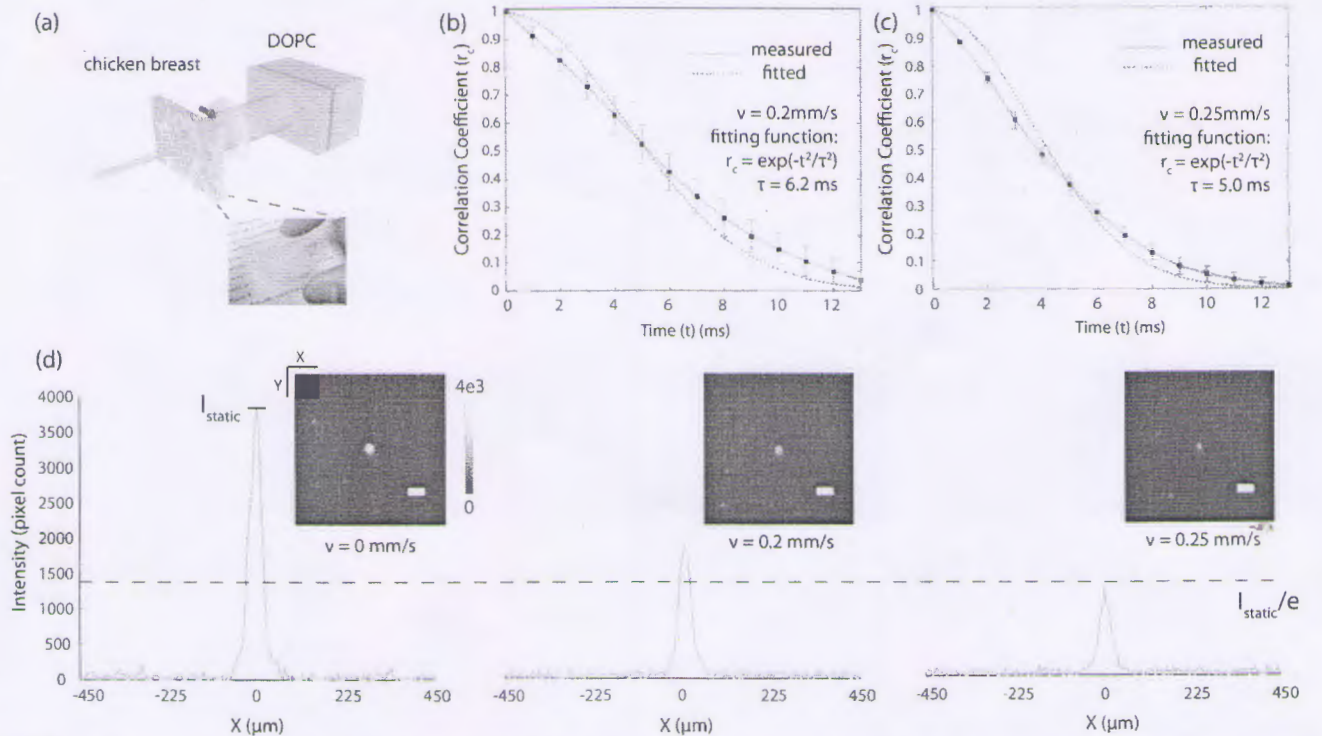


Fig. 5. (a) Moving sample setup. (b), (c) Moving sample speckle decorrelation curves at lateral velocity 0.2 and 0.25 mm/s. Error bars indicate standard deviation over 10 datasets. (d) Conjugate focus images and cross-section peak plots when the sample was static, moving at 0.2 and 0.25 mm/s.

of output modes (M , number of speckle grains in the focus). Therefore, it is not a fair comparison to quantify DOPC performance merely by the PBR for different numbers of output modes. However, OPC efficiency, which is the ratio of PBR achieved on a system to theoretical PBR, sets a suitable standard for different systems. To evaluate the OPC efficiency of our system, we used our DOPC system to focus light through an opal diffuser (10DIFF-VIS, Newport). Based on the derivation of DMD-based conjugation and the measured interference pattern on the recording camera, we determined the speckle size to be 4 pixels wide on the DMD. Since the DMD has 1920×1080 pixels, the number of optical modes we can access with the DMD equals 1.3×10^5 . To determine the number of modes in the focus, we examined the conjugate focus through the sample. When the conjugate beam was played back, we observed a focus on the observation camera with a PBR of 630 and full width at half-maximum (FWHM) of $45 \mu\text{m}$, as shown in Fig. 6. When we displayed a random pattern on the DMD, the speckle FWHM was $13 \mu\text{m}$, computed from the autocorrelation of the speckle pattern. From these two measurements, we can find that the number of modes in the focus is ~ 12 . From the PBR equation, we calculated the optimal PBR as $1.3 \times 10^5 / (12 \cdot 2\pi) \approx 1700$, which means our system performance has an efficiency of 37%.

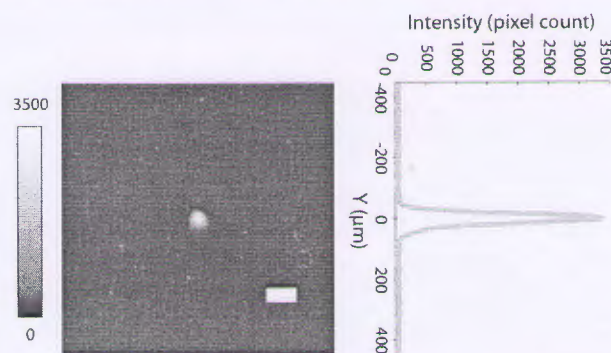


Fig. 6. PBR quantification. Scale bar is $100 \mu\text{m}$.

C. In Vivo Experiments

In vivo experiments were demonstrated by focusing through the dorsal skin of a living mouse. For the *in vivo* sample, a regular white laboratory mouse was shaved on the dorsal skin flap. Then its dorsal skin was mounted to a clip device. Isoflurane was implemented as the inhalational anesthesia both in preparation and during the experiment. All of these procedures and the dosage of chemicals followed protocols of the Institutional Animal

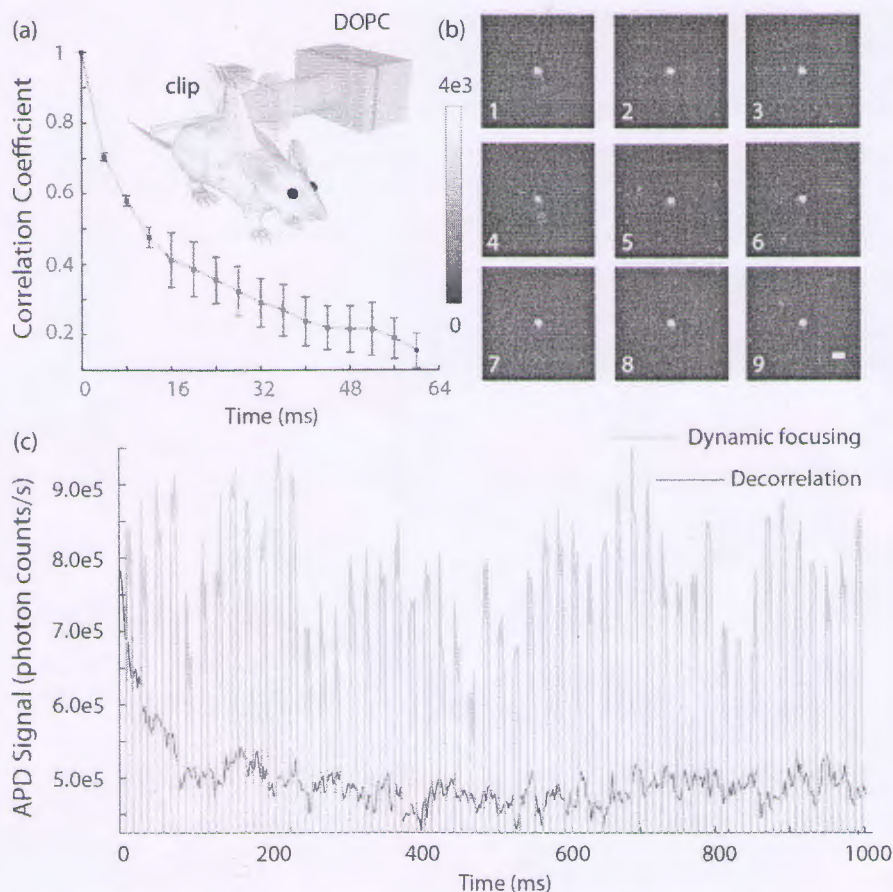


Fig. 7. (a) Clipped mouse dorsal skin setup and speckle decorrelation curve of *in vivo* tissue. Error bars indicate standard deviation over 10 datasets. (b) Continuous conjugate foci through clipped sample (see also Visualization 1). (c) APD plot for sustainable foci and decorrelation focus. Scale bar is $100 \mu\text{m}$. In the experiment, to accurately distinguish the focus intensity from background in the APD signal, a background (I_b) was measured first when the focus totally vanished, which is 5×10^5 in the APD plot.

Care and Use Committee at the California Institute of Technology.

As shown in Fig. 7(a), a clip fixed the upper edge of the skin on a transparent plastic plate, which was placed at the sample position. In this way, the bottom of the dorsal skin was in a natural free status. The sample beam was incident onto the bottom part of the skin, which had a thickness of around 2.3 mm. Before DOPC was applied, a series of scattering speckle patterns from the tissue were captured by the recording camera to analyze the tissue decorrelation time and form the decorrelation curve plotted in Fig. 7(a). From this curve we can tell its decorrelation time is 28 ms, where the decorrelation time is defined as the time when the speckle correlation coefficient decreases to $1/e$. After that, DOPC was conducted with an exposure time of 0.5 ms on the recording camera, at a refresh rate of 50 Hz and a playback holding time of 10 ms. A series of images from the observation camera triggered by the playback signal with an exposure time of 3 ms are included in Fig. 7(b) and Visualization 1 (5 s video) along with a corresponding APD plot in Fig. 7(c). From the focus images and APD plot, we can tell a clear focus was constructed and maintained through unrestricted tissue on a living animal. From the average of 10 images, we calculate that the PBR is 180. For our system, a refresh rate up to 100 Hz with flexible holding time is achievable. It should also be noted that in the middle of the movie we can observe a short failing of conjugation due to severe body movement from respiration, not due to the decorrelation of the tissue itself.

4. DISCUSSION AND CONCLUSION

In this work, we demonstrated what we believe to be the first DMD-based DOPC system. This system is capable of playback with latency of the order of milliseconds, a speed improvement of approximately 2 orders of magnitude over prior DOPC systems. Using the fast DOPC system, we demonstrated the ability to create an indefinitely sustainable focus through unrestricted tissue on a living animal, a capability that has not been previously reported for any OPC experiments. While nonlinear approaches can, in principle, provide this capability as well, this DOPC approach is direct and can provide a greater than unity fluence reflectivity. Our system can achieve greater than 2000 fluence reflectivity, which is crucial for thick *in vivo* tissue application. In our case, the playback beam is set to ~ 10 mW and the total fluence of the scattered light from the sample is ~ 5 μ W. We further quantified our playback latency as 5.3 ms. While the background due to unmodulated light will need to be addressed in the binary phase retrieval method, it will be straightforward to extend this technology to existing OPC-based technology, such as TRUE, TROVE, and TRACK, and apply it in living tissue for biological applications. Compared to phase-only OPC, DMD-based DOPC encounters a PBR reduction of 80% (from $\pi/4$ to $1/2\pi$). However, for the DMD-based DOPC system, the PBR can be further improved by tuning $I_{\text{ref}}/\langle I_{\text{sam}} \rangle$ in the single-shot binary phase retrieval. For example, suppose I_{ref} and I_{sam} have intensities of the same order of magnitude; then the binary phase retrieval equation will be

$$\text{DMD}(x, y) = \begin{cases} 1, & I_i(x, y) < I_{\text{ref}}(x, y) \rightarrow |\alpha - \pi| < \phi \\ & \phi = \arccos\left(1/2\sqrt{I_{\text{ref}}/I_{\text{sam}}}\right) < \frac{\pi}{2}. \\ 0, & \text{else} \end{cases} \quad (6)$$

As I_{sam} follows a Rayleigh distribution [29], by comparing the intensity difference we can statistically select a smaller phase range 2ϕ than π . The theoretical PBR in this condition (detailed derivation in Supplement 1) is a unimodal function of $I_{\text{ref}}/\langle I_{\text{sam}} \rangle$, which achieves up to 12.6% higher PBR at $I_{\text{ref}}/\langle I_{\text{sam}} \rangle = 1.61$ than when $I_{\text{ref}} \gg \langle I_{\text{sam}} \rangle$. In our experiments, we selected this condition as closely as possible. However, due to the dynamic and heterogeneous nature of biological tissue, it is likely that the PBR could have been further improved by fine-tuning this ratio to more accurately select this optimal condition.

Recently, focusing through thin *ex vivo* tissue samples (200 μ m chicken breast) was demonstrated at submicrosecond timescales by using the self-organization of an optical field inside a multi-mode laser cavity [30]. Despite its speed, the approach demonstrated only around 1000 controllable modes, and the number of controllable modes will significantly diminish for thicker samples. This hinders its applications to thick *in vivo* tissue. In addition, the technique relies on optical feedback from the target position, preventing it from being extended to noninvasive techniques with a guide star to focus inside biological tissue.

The flexibility of the DOPC system also provides the additional ability to trade-off controllable modes for reduced playback latency. Since the time for recording and phase transfer is proportional to frame size, shrinking the frame size can further decrease the playback latency. For example, if the frame size is reduced to 1920×70 , the playback latency is below 1 ms. Although the PBR will also decrease for smaller frame sizes, up to 1.3×10^5 controllable pixels are still available at a frame size of 1920×70 . In practice, we could balance the number of controllable modes (PBR) and time latency based on the decorrelation properties of different samples.

The architecture of our DOPC system also has the potential to be applied in microsecond scale wavefront shaping. Currently, the playback latency is determined by the sum of the time required by the recording exposure, data transfer from the camera to the FPGA, and binary phase transfer from the FPGA to the DMD. As the development of fast and sensitive scientific cameras continues, the exposure time and recording transfer time can be reduced by orders of magnitude. Here we have used an exposure time of 0.5 ms, the minimum exposure time available for the camera, which may be reduced to tens of microseconds or even several microseconds in the future. Meanwhile, the sample beam intensity has to match the shorter exposure. This will be hindered by tissue absorption, which can be addressed by switching from the 532 nm laser source to near-infrared wavelengths, which have orders of magnitude lower tissue absorption. The minimal wavelength dependency of the DOPC system compared to nonlinear OPC systems allows this conversion to a different wavelength regime to be direct. We anticipate that with near-infrared light, *in vivo* DOPC applications on tissue centimeters thick can be realized. Finally, a phase transfer time of around 50 μ s can be realized by using a better FPGA (e.g., Altera Stratix V) and a custom-designed data transfer interface to match the maximum refresh rate of the DMD (23 kHz). With the development of faster DMD devices, this time may be further reduced to several microseconds. As the decorrelation rate of tissue drastically increases with thickness, such improvements would ultimately enable wavefront shaping to be applied for optogenetics in the whole brain, *in vivo* deep tissue imaging, and photodynamic therapy for internal organs.

Funding. China Scholarship Council (CSC); GIST-Caltech (CG2012); National Institute of Neurological Disorders and Stroke (NINDS) (1U01NS090577-01); National Institutes of Health (NIH) (1DP2OD007307-01).

Acknowledgment. The authors would like to thank Benjamin Judkewitz and Roarke Horstmeyer for their suggestions and discussion.

[†]These authors contributed equally to this work.

See Supplement 1 for supporting content.

REFERENCES

1. I. M. Vellekoop and A. P. Mosk, "Focusing coherent light through opaque strongly scattering media," *Opt. Lett.* **32**, 2309–2311 (2007).
2. A. P. Mosk, A. Lagendijk, G. Leroosey, and M. Fink, "Controlling waves in space and time for imaging and focusing in complex media," *Nat. Photonics* **6**, 283–292 (2012).
3. I. M. Vellekoop, A. Lagendijk, and A. P. Mosk, "Exploiting disorder for perfect focusing," *Nat. Photonics* **4**, 320–322 (2010).
4. D. B. Conkey, A. M. Caravaca-Aguirre, and R. Piestun, "High-speed scattering medium characterization with application to focusing light through turbid media," *Opt. Express* **20**, 1733–1740 (2012).
5. H. Yilmaz, W. L. Vos, and A. P. Mosk, "Optimal control of light propagation through multiple-scattering media in the presence of noise," *Biomed. Opt. Express* **4**, 1759–1768 (2013).
6. S. Popoff, G. Leroosey, M. Fink, A. C. Boccara, and S. Gigan, "Image transmission through an opaque material," *Nat. Commun.* **1**, 81 (2010).
7. T. Chaigne, O. Katz, A. C. Boccara, M. Fink, E. Bossy, and S. Gigan, "Controlling light in scattering media noninvasively using the photo-acoustic transmission matrix," *Nat. Photonics* **8**, 58–64 (2014).
8. J. Yoon, K. Lee, J. Park, and Y. Park, "Measuring optical transmission matrices by wavefront shaping," *Opt. Express* **23**, 10158–10167 (2015).
9. Z. Yaqoob, D. Psaltis, M. S. Feld, and C. Yang, "Optical phase conjugation for turbidity suppression in biological samples," *Nat. Photonics* **2**, 110–115 (2008).
10. C.-L. Hsieh, Y. Pu, R. Grange, and D. Psaltis, "Digital phase conjugation of second harmonic radiation emitted by nanoparticles in turbid media," *Opt. Express* **18**, 12283–12290 (2010).
11. H. Ruan, M. Jang, B. Judkewitz, and C. Yang, "Iterative time-reversed ultrasonically encoded light focusing in backscattering mode," *Sci. Rep.* **4**, 7156 (2014).
12. X. Xu, H. Liu, and L. V. Wang, "Time-reversed ultrasonically encoded optical focusing into scattering media," *Nat. Photonics* **5**, 154–157 (2011).
13. Y. M. Wang, B. Judkewitz, C. A. DiMarzio, and C. Yang, "Deep-tissue focal fluorescence imaging with digitally time-reversed ultrasound-encoded light," *Nat. Commun.* **3**, 928 (2012).
14. B. Judkewitz, Y. M. Wang, R. Horstmeyer, A. Mathy, and C. Yang, "Speckle-scale focusing in the diffusive regime with time reversal of variance-encoded light (TROVE)," *Nat. Photonics* **7**, 300–305 (2013).
15. E. H. Zhou, H. Ruan, C. Yang, and B. Judkewitz, "Focusing on moving targets through scattering samples," *Optica* **1**, 227–232 (2014).
16. C. Ma, X. Xu, Y. Liu, and L. V. Wang, "Time-reversed adapted-perturbation (TRAP) optical focusing onto dynamic objects inside scattering media," *Nat. Photonics* **8**, 931–936 (2014).
17. P. Lai, X. Xu, H. Liu, and L. V. Wang, "Time-reversed ultrasonically encoded optical focusing in biological tissue," *J. Biomed. Opt.* **17**, 0305061 (2012).
18. P. Lai, Y. Suzuki, X. Xu, and L. V. Wang, "Focused fluorescence excitation with time-reversed ultrasonically encoded light and imaging in thick scattering media," *Laser Phys. Lett.* **10**, 075604 (2013).
19. C. Ma, X. Xu, and L. V. Wang, "Analog time-reversed ultrasonically encoded light focusing inside scattering media with a 33,000 × optical power gain," *Sci. Rep.* **5**, 8896 (2015).
20. Y. Liu, P. Lai, C. Ma, X. Xu, A. A. Grabar, and L. V. Wang, "Optical focusing deep inside dynamic scattering media with near-infrared time-reversed ultrasonically encoded (TRUE) light," *Nat. Commun.* **6**, 5904 (2015).
21. B. Jayet, J.-P. Huignard, and F. Ramaz, "Optical phase conjugation in Nd: YVO₄ for acousto-optic detection in scattering media," *Opt. Lett.* **38**, 1256–1258 (2013).
22. M. Jang, H. Ruan, I. M. Vellekoop, B. Judkewitz, E. Chung, and C. Yang, "Relation between speckle decorrelation and optical phase conjugation (OPC)-based turbidity suppression through dynamic scattering media: a study on *in vivo* mouse skin," *Biomed. Opt. Express* **6**, 72–85 (2015).
23. I. Yamaguchi and T. Zhang, "Phase-shifting digital holography," *Opt. Lett.* **22**, 1268–1270 (1997).
24. M. Liebling, T. Blu, and M. Unser, "Complex-wave retrieval from a single off-axis hologram," *J. Opt. Soc. Am. A* **21**, 367–377 (2004).
25. D. Akbulut, T. J. Huisman, E. G. van Putten, W. L. Vos, and A. P. Mosk, "Focusing light through random photonic media by binary amplitude modulation," *Opt. Express* **19**, 4017–4029 (2011).
26. I. M. Vellekoop, "Controlling the propagation of light in disordered scattering media," *arXiv:0807.1087* (2008).
27. D. Dudley, W. M. Duncan, and J. Slaughter, "Emerging digital micromirror device (DMD) applications," *Proc. SPIE* **4985**, 14–25 (2003).
28. G. Volpe, G. Volpe, and S. Gigan, "Brownian motion in a speckle light field: tunable anomalous diffusion and selective optical manipulation," *Sci. Rep.* **4**, 3936 (2014).
29. J. W. Goodman, *Statistical Optics* (Wiley-Interscience, 2000).
30. M. Nixon, O. Katz, E. Small, Y. Bromberg, A. A. Friesem, Y. Silberberg, and N. Davidson, "Real-time wavefront shaping through scattering media by all-optical feedback," *Nat. Photonics* **7**, 919–924 (2013).

Noncontact full-angle fluorescence molecular tomography system based on rotary mirrors

DAIFA WANG, JIN HE, HUITING QIAO, PING LI, YUBO FAN, AND DEYU LI*

Key Laboratory for Biomechanics and Mechanobiology of Ministry of Education, School of Biological Science and Medical Engineering, Beihang University, Beijing, China

*Corresponding author: deyuli@buaa.edu.cn

Received 5 May 2015; revised 19 July 2015; accepted 19 July 2015; posted 20 July 2015 (Doc. ID 240342); published 6 August 2015

We propose a novel noncontact fluorescence molecular tomography system that achieves full-angle capacity with the use of a new rotary-mirrors-based imaging head. In the imaging head, four plane mirrors are mounted on a rotating gantry to enable illumination and detection over 360° . In comparison with existing full-angle systems, our system does not require rotation of the specimen animal, a large and heavy light source (with scanning head), or a bulky camera (with filters and lens). The system design and implementation are described in detail. Both physical phantom and *in vivo* experiments are performed to verify the performance of the proposed system. © 2015 Optical Society of America

OCIS codes: (110.0113) Imaging through turbid media; (110.1758) Computational imaging; (110.3010) Image reconstruction techniques; (110.6960) Tomography.

<http://dx.doi.org/10.1364/AO.54.007062>

1. INTRODUCTION

Fluorescence molecular tomography (FMT) is an emerging technology that provides noninvasive, quantitative, three-dimensional imaging of fluorescence markers *in vivo*. Benefitting from mathematical modeling of light transport inside highly scattering tissue, this technique overcomes the limitations of depth information loss in the simple and widely used planar reflectance imaging [1]. At present, FMT has been successfully applied in observing fluorescence-tagged biological processes occurring deep inside tissues, such as enzyme activity [2], expressions of cancer markers [3,4], and targeted agent delivery [5].

The inherent scattering nature of biological tissue limits the spatial resolution of FMT in deep tissue. Many efforts have been made in the past decade to enhance the spatial and temporal performance of FMTs, including developing novel reconstruction algorithms and image acquisition designs [6,7]. In early FMT schemes, the imaging systems were generally fiber based [2], wherein optical fibers were used to transfer the input excitation light to the object surface and the output emission light to detectors. However, such systems are disadvantageous in several ways. The limited number of source-detector pairs in such systems restricts the achievable spatial resolution. Moreover, matching fluid is generally used to enhance the attachment of the fibers to irregular small-animal surfaces and photon transportation modeling; however, the presence of an additional scattering medium between fibers and the animal surface further degrades the spatial performance. The subsequently

developed camera-based noncontact imaging systems have overcome these limitations by allowing the implementation of over 1 million source-detector pairs [1,8].

As in the case of x-ray computed tomography (CT), it has been proven that multiple projection directions over full angles (360°) are crucial for accurate FMT reconstruction [9]. In this regard, several approaches have been proposed to increase the number of projection view directions for camera-based noncontact imaging systems. The most straightforward and easy way is to rotate the small animal [10–12]. However, the imaged small animal has to be carefully suspended by a holder, which unnaturally restricts the animal while also making the imaging preparation process rather complex. While the animal's rotation speed is generally set to very low values to reduce the risk of internal organ movement, this limits the system's temporal performance in observing fast dynamic processes. On the other hand, several groups have developed systems that involve the rotation of the camera/light source [13–15]. In these systems, the rotary gantry needs to be carefully designed to mount the bulky camera (with filters and lens) and light source (with a scanning head), and further, the problem of twisting of the large number of power and signal cables during rotation needs to be addressed. Currently, most systems of this type utilize the rotary gantry used in commercial small-animal CT systems, and the gantry rotation speed is generally low in consideration of the bulky mounted components.

In the context of the limitations of these approaches, researchers have noted that a conical mirror can be used to

map the full-angle view to a single image plane, and, hence, it has been widely used in nonrotary full-angle-view applications such as endoscopy [16,17]. A conical-mirror-based imaging system for small-animal optical molecular tomography was first proposed for bioluminescence tomography applications [18], wherein there is no requirement for scanning by an excitation light. Li *et al.* were the first to propose a conical-mirror-based FMT system [19]. In their system, to project the full-angle data to a single camera chip, the small animal is generally placed far away from the camera. Only the small ring portion of the camera is utilized to image the full-angle view, which limits the sampling density. In addition, the close placement of mirror surfaces to the animal also causes multiple backreflections of the excitation and emission beams to some extent, which leads to degradation of reconstructed image quality. To overcome the backreflection issue, Lee *et al.* subsequently proposed a system with dual conical mirrors [20]. The use of conical mirror pairs has also led to better utilization efficiency of the camera sensor chip. However, in contrast to Li *et al.*'s system, which has no rotary parts [19], in newer conical-mirror-pair systems, a large and heavy light source with a scanning head is mounted on a rotating gantry for light illumination at different projection directions. Apart from area-detector (camera)-based systems, in recent years, FMT systems with point detectors [photomultiplier tubes (PMTs)] have also been used to obtain a noncontact full-angle view [21,22]. In a previous study [21], seven dual-wavelength time-resolved detection channels were used, and small-animal rotation was performed to achieve the full-angle view. In [22], lightweight lens-coupled optical fibers (five detection fibers and one excitation fiber) were arranged in a fan-beam geometry and mounted on a rotating gantry. With the use of digital photon counting PMTs, these systems are advantageous for time-resolved measurements [21,23] and ultra-weak signal applications such as imaging large animals (rats) [23] or endogenous contrast [24]. However, as the detector number is limited in such systems, obtaining a large number of source-detector pairs generally takes long acquisition time.

In this work, we propose a novel camera-based FMT system wherein full-angle view is achieved by the use of four plane mirrors (called rotary mirrors in this article) mounted on a rotary gantry. In comparison with previous camera-based FMT systems, our system offers the following advantages. First, there is no need to rotate the small animal, the large and heavy light source (with scanning heads), or the bulky camera (with filters and lens). Second, compared to conical-mirror-based systems [19], our system's camera utilization efficiency is greater and does not suffer from the backreflection effect.

This paper is organized as follows. In section 2, the system and its parameter considerations are described. In section 3, the evaluation of the system with physical phantom and *in vivo* experiments is described. Section 4 discusses and concludes the paper.

2. METHODS

A. Experimental Setup

Figure 1(a) shows the schematic of the proposed system, whose main components are a laser, a full-angle scanning and projection unit, and a detection camera. The full-angle scanning and

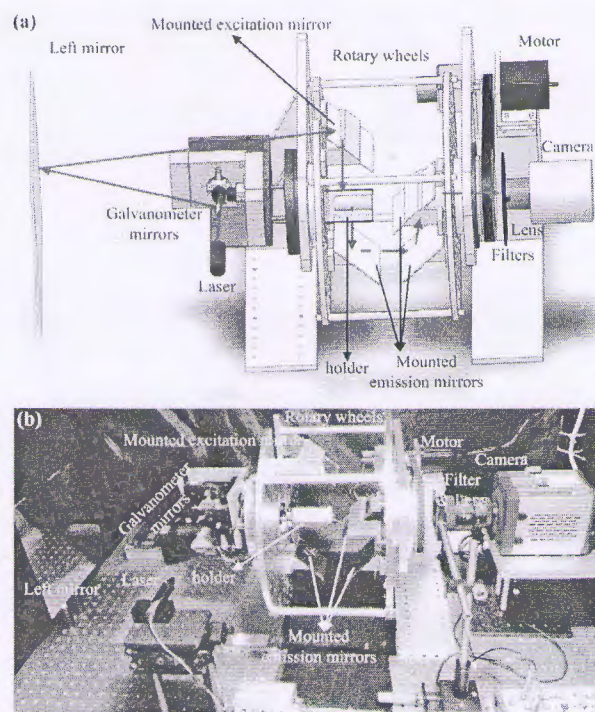


Fig. 1. Setup of a full-angle fluorescence molecular tomography system based on rotary mirrors. (a) Schematic of the system. (b) Photograph of actual system.

projection unit enables the system to acquire multiple projection images over the full angle. In this unit, raster excitation point light scanning for a specific view direction is performed by a pair of galvanometer mirrors (Viasho), a plane mirror (the "left mirror") positioned at the left end of the device, and a reflectance mirror mounted on the rotary wheels. The rotation of the wheels enables the mounted excitation mirror and three emission mirrors to project excitation light onto the imaged object surface and deliver the emission light to the detector at different angles over 360 deg. All the mirrors including the left mirror, galvanometer mirrors, and the rotary mirrors (mounted excitation and emission mirrors) are silver coated to provide high reflection efficiency (>97%) for visible to near-infrared light wavelengths.

The details of the paths traversed by the light beams in the system are as follows. The laser beam from the diode laser source (780 nm, 14 mW) is guided through a pair of galvanometer mirrors (scanning). After being reflected successively by the left plane mirror and the mounted excitation mirror on the rotary gantry, the laser beam is directed to the imaged object (fixed on the holder) surface. The two galvanometer mirrors allow raster scanning of the laser beam over one side of the object surface. The transmitted excitation light and emission light beams exiting from the opposite side of the imaged surface are reflected successively by the three mounted emission mirrors. These beams finally pass through the inner core of the right rotary wheel and are directed to the detector. The detector is a highly sensitive sCMOS camera (Neo 5.5, Andor) coupled to a 60 mm f/2.8D lens (Nikkor, Nikon). The camera has a

large-sized chip with 2560×2160 pixels (chip area of $16.6 \text{ mm} \times 14 \text{ mm}$) with 16 bit dynamic range, and it is cooled to -30°C to ensure ultralow imaging noise (read noise of 1 e- and dark current of 0.015 e-/pixel/s). The image field of view is $11.2 \text{ cm} \times 9.4 \text{ cm}$, which is sufficiently large for whole-body mouse imaging. When collecting fluorescence images, a $832 \pm 18.5 \text{ nm}$ bandpass (FF01-832/37-25, Semrock) filter is positioned in front of the lens, which provides high light-filtering ability [optical density (OD) >10 at excitation light wavelength]. For excitation light images, a neutral density filter of 1% transmittance (GCC-301061, Daheng) is used instead to prevent possible damage to the camera due to high-energy photons. The three emission mirrors are mounted on the rotary wheels and inclined at 45° to the horizontal axis. Consequently, the object plane near the small-animal surface can be accurately imaged by the camera without there being any differences in the optical path lengths. The homemade rotary gantry (diameter of 40 cm) containing two connected rotary wheels allows guiding of the laser direction and data detection over multiple projection angles. The wheels are supported by two U-shaped mechanical arms fixed on the optical table. For some projection angles (over 30° and below 150°), the excitation light is blocked by the left mechanical supporting arm. Consequently, a large window is opened in the left arm to ensure excitation light illumination at a projection angle of 90° . As shown in Fig. 1, both rotary wheels have 10-cm-diameter holes in the center. For the left wheel, the inner core is used to aid in fixing the object holder. With this design, the object holder can be fixed on the left supporting arm and remain static when the wheels are rotating. For the right wheel, the inner core allows excitation and emission light to travel through it. A stepper dc motor (57BYG350DL, Syntron) rotates the gantry through a toothed belt and a pair of gears. The ratio between the two gears is 4:1. A motor controller (SH30806, Syntron) drives the motor rotation with a resolution of 0.015° . In comparison to a conventional gantry that is mounted with bulky components, our gantry is relatively simple in terms of design since only four lightweight mirrors are mounted on it. Consequently, the load torque to the motor is small, and no power or signal cables are moved (there is no cable twisting) during the rotation. The system is controlled by means of a graphical user interface that was developed using Labwindows.

For the alignment of the rotary wheels and camera, the key is to ensure that the rotation axis of the wheels is perpendicular to the camera chip, with the axis lying along the chip center. In the proposed imaging device, the object white-light images at different projection angles can be acquired if we provide highly diffused ambient light illumination. In other words, white-light illumination is required to be near-uniform over 360° , which is easily achieved by reflecting the light multiple times from a table lamp with the surrounding shielding fabric and the optical table. Consequently, with the utilization of the acquired white-light images, the system alignment is considerably easier than that for conical-mirror-based systems [19,20] or point-detector-based systems [21,22]. The alignment can be achieved in two steps. First, we place a graph paper in the object plane and fix it on the rotary wheel. When the wheels rotate through an angle, the acquired graph paper image will rotate by the

same angle, since three mirrors are used in the emission path. Subsequently, by rotating the wheels, we can determine the image rotation center and make it overlap with the camera chip center. Second, similar to the method used in small-animal rotation-based systems [25], we can use a cylindrical object and its silhouettes at different angles to iteratively determine and fix the tilt between the camera and the rotation axis.

Accurate laser scanning over the desired field of view needs careful consideration in terms of the component setup that involves excitation light scanning; the considered parameters include the relative distances between the rotary wheel and light source and the angle of the mounted reflection mirror. To achieve the desired illumination scanning for each projection direction, the laser beam should be able to reach the mounted excitation mirror for all possible mirror positions. To ensure that there is sufficient space to position the imaged object, the bottom part of the mounted excitation mirror is set at a height of at least 10 cm from the horizontal axis, and the upper part of the mirror (11 cm length) is subsequently $\sim 19 \text{ cm}$ from this axis. Hence, the path length of the light from the galvanometer mirror to the rotary wheel should be at least $19/\tan(2\theta_{\max}) = 76 \text{ cm}$, where $\theta_{\max} = 7^\circ$ is the maximum deflection angle of the galvanometer mirrors. It is to be noted that the smaller is the distance d_{gm} between the galvanometer mirror and the rotary wheel, the more compact is the total size of the light scanning section. Here, d_{gm} is 17 cm, and it is limited by the space needed for supporting the rotary wheel and for fixing the galvanometer mirrors. Consequently, the distance from the left rotatory wheel to the left mirror, d_{bm} , is set as $d_{\text{bm}} = 47 > (76 + 17)/2 \text{ cm}$. Since it is easier and better for modeling if the illumination angles are all nearly parallel to the view direction at different scanning positions, optimization of the angle α_{mm} of the mounted mirror was performed by minimizing the mean angle deviation to the view. Based on the results shown in Fig. 2(b), α_{mm} was chosen to be 40° . This configuration corresponds to a mirror of size $8 \text{ cm} \times 11 \text{ cm}$ and scanning field of view of $8 \text{ cm} \times 7 \text{ cm}$, values that are sufficient for whole-body mouse imaging.

The use of multiple projection directions has been proved to be critical to obtaining a better spatial resolution along with reduced artifacts. In the proposed system, because of "shielding" by the mechanical support arm, some projection directions (lying in the range of 30° – 150° , except 90°) are not fully accessible for illumination scanning. As projections from the opposite sides of these "unavailable" viewing directions can be performed, by optimizing the illumination point sources' distribution, the information loss corresponding to these unavailable directions can be mostly compensated. Herein, we focus mainly on demonstrating and verifying the proof-of-concept of our system. In the future, illumination at these "shielded" angles can be achieved by using transparent material (e.g., glass) to replace the opaque parts on the mechanical support arm.

B. Image Reconstruction

For a source–detector pair (\vec{r}_s, \vec{r}_d) , with the assumption that light travels from \vec{r}_s to position \vec{r} and from \vec{r} to detector \vec{r}_d and integrating over the whole imaged domain Ω , the detected fluorescence signal $\Phi_{\text{em}}(\vec{r}_s, \vec{r}_d)$ can be expressed as

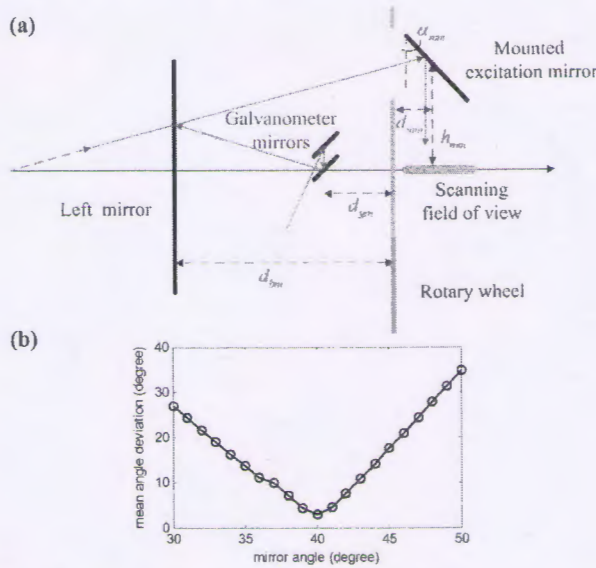


Fig. 2. Laser beam scanning process in the proposed system. (a) Path traversed by light in the laser beam scanning process. (b) Optimization of the angle α_{mm} of the mounted excitation mirror.

$$\Phi_{em}(\vec{r}_s, \vec{r}_d) = \Theta_{em} \int_{\Omega} \Phi_{ex}(\vec{r}_s, \vec{r}) G_{em}(\vec{r}, \vec{r}_d) f(\vec{r}), \quad (1)$$

where $f(\vec{r})$ denotes the fluorescence distribution, and Θ represents the total system amplification factor corresponding to the quantum efficiency, detection efficiency, etc. The subscripts ex and em indicate the excitation light and emitted fluorescence wavelengths, respectively, and G denotes Green's function. For source-detector separations of more than several millimeters, light propagation in turbid tissue media can be modeled by a partial differential equation called the diffusion equation. Green's function $G(\vec{r}_s, \vec{r})$ can subsequently be solved via numerical techniques, such as the finite element method [26,27], by setting the spatially localized impulse function $\delta(\vec{r} - \vec{r}_s)$ as the source term.

The uneven system amplification factor Θ and unknown heterogeneity of the imaged medium severely affect the accuracy of light propagation modeling and deteriorate the inverse reconstruction quality. The normalized Born method [28] has been proven an effective approach to reduce these negative influences. In the Born method, instead of emission data alone, the normalized ratio $\Phi_{born} = \Phi_{em}/\Phi_{ex}$ of the corresponding measurements at the emission and excitation wavelengths is used for reconstruction:

$$\Phi_{born}(\vec{r}_s, \vec{r}_d) = \frac{\Theta_{em}}{\Theta_{ex}} \int_{\Omega} \frac{G_{ex}(\vec{r}_s, \vec{r}) G_{em}(\vec{r}, \vec{r}_d)}{G_{ex}(\vec{r}_s, \vec{r}_d) f(\vec{r})}. \quad (2)$$

By discretizing the imaged domain to n_v uniform voxels with volume ΔV , the above integral equation can be transformed to the following linear equation:

$$\Phi_{born}(\vec{r}_s, \vec{r}_d) = \sum_{i=1}^{n_v} G(\vec{r}_s, \vec{r}_i) G(\vec{r}_i, \vec{r}_d) / G(\vec{r}_s, \vec{r}_d) \Delta V f(\vec{r}_i). \quad (3)$$

For data from all M source-detector pairs, a matrix-vector product form can be generated as

$$\Phi_{born} = W \begin{bmatrix} f(\vec{r}_1) \\ \vdots \\ f(\vec{r}_{n_v}) \end{bmatrix}, \quad (4)$$

where W denotes the weight matrix with size $M \times n_v$. The above linear system is highly ill-posed, which makes direct inversion impossible. In this study, the random access algebraic reconstruction technique (R-ART) [29] with non-negative constraints, which has been widely applied for FMT [11,28], is used for solving the linear system.

C. Correction of Glass Plate Holder Refraction

Acquiring the object 3D surface is important for diffusive light propagation modeling. For rotation-based full-angle FMT [10–12], the object 3D surface can be easily recovered using Radon-transform-based methods [30,31] from the object silhouettes over the full angle. In earlier applications of these methods, the imaged small animal was generally suspended or held by a “mouse fixer” and the imaged region had no shielding. In the proposed system, a 0.2-cm-thick transparent glass plate is used as the small-animal holder. At different projection angles, the holder covers different parts of the imaged object when viewing from the camera. As shown in Fig. 3(a), due to the refraction effect, the acquired silhouette tends to become larger than the actual one when a part of the object is imaged

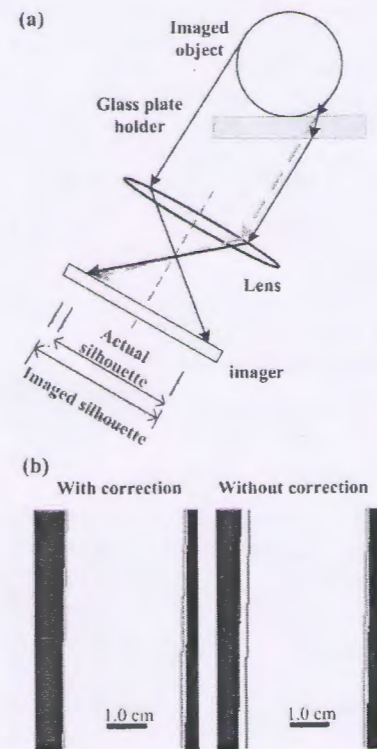


Fig. 3. Silhouette correction. (a) Refraction occurring at plate glass holder. (b) The overlay of the projected boundary (red lines) of the recovered 3D surface and acquired silhouette. For the surface recovery, 72 silhouettes were acquired over 5 deg steps.

through the holder, which globally translates to a small error distance when the object is totally behind the plate. The refraction effect is non-negligible and therefore needs to be pre-corrected for accurate surface recovery. As shown in Fig. 3(b), for a cylindrical object (diameter of 3.0 cm), without correction, the recovered surface does not correctly align with the acquired silhouettes for some projection directions, with deviations of up to 0.2 cm. In contrast, the mismatch is greatly reduced with correction. Similarly, such a correction also needs to be performed for the acquired excitation and fluorescence images.

3. EXPERIMENTS AND RESULTS

The performance and effectiveness of the proposed system was evaluated via experiments with physical phantom and *in vivo* mouse imaging experiments.

A. Physical Phantom Experiments

A single fluorescence target experiment was performed at first to evaluate the tomography capability of the proposed system. A solid phantom with an embedded fluorescence target was used for this purpose, and the phantom's structural image was obtained using a small-animal CT (Skyscan, Bruker). The solid phantom was prepared as follows [19]. Buffered saline and 2% agar were heated to 95°C. The agar was dissolved in saline and the mixture was cooled by decreasing the temperature. At 60°C, intralipid was added. At 40°C, the liquid mixture was poured into a glass cylinder (inner diameter of 2.4 cm and outer diameter of 2.8 cm), and a fluorescence tube was also inserted into the cylinder. The fluorescence tube was prepared by filling a transparent glass tube (0.3 cm inner diameter and 0.5 cm outer diameter) with 40 μ L 4 μ mol/L Indocyanine Green (ICG) dissolved in dimethylsulfoxide (DMSO). The prepared phantom was refrigerated for 2 h prior to the experiment. The optical properties of the solid phantom are similar to those of 1% intralipid ($\mu'_s = 10 \text{ cm}^{-1}$, $\mu_a = 0.02 \text{ cm}^{-1}$). In the experiment, both excitation and emission data were collected over 15 deg steps. At each projection direction, 15 illumination positions were scanned over an area of 1.2 cm \times 2.0 cm in steps of 0.4 cm \times 0.5 cm, as indicated in Fig. 4(a). The illumination settings were chosen empirically, and it is noteworthy that these settings can further be optimized theoretically to increase the number of acquired data sets or reduce the total number of light sources [9,11,32]. The acquired fluorescence projections (exposure time of 1.0 s and pixel binning of 4 \times 4) at different angles are shown in Fig. 4(a). These projections indicate large scattering of light in turbid media. In the tomography reconstruction, the imaged region was discretized to 3.2e3 uniform voxels (0.15 cm \times 0.15 cm \times 0.15 cm). From the projection images, totally 4.4e4 source-detector pairs were obtained in the reconstruction. Further, 50 R-ART iterations were performed with a relaxation parameter of 0.05. Figure 4(b) shows the results of this experiment. From the overlaid fluorescence and structural images, we observe that the reconstructed target closely matches the actual target in terms of both localization and size.

Next, the sensitivity of the proposed system was evaluated by quantifying the smallest ICG quantities that could be

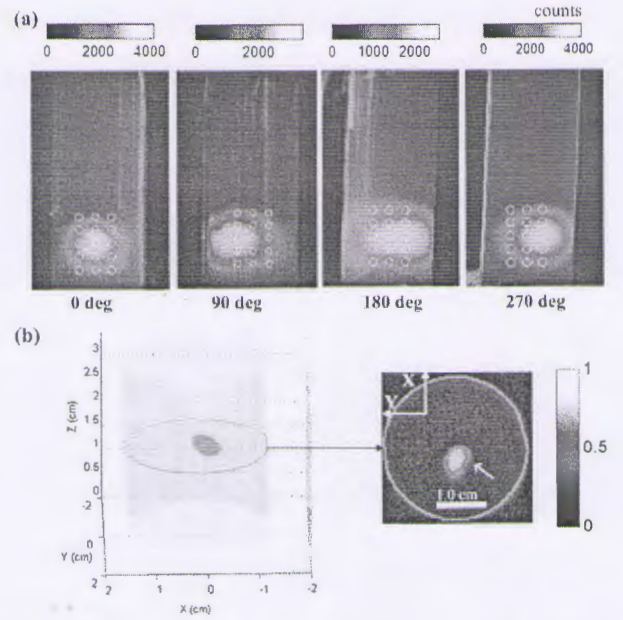


Fig. 4. Physical phantom imaging experiment. (a) Overlaid fluorescence images along four different projection directions. The white markers represent the illumination positions, with the diamond marker representing the position corresponding to the fluorescence image. (b) Reconstructed fluorescence image. The tomography fluorescence slice image shown is normalized to its maximum value.

detected in a near-slab-shaped tank filled with 1% intralipid. The geometrical size of the phantom was 5 cm \times 5 cm \times Z cm, where Z is the thickness of the filled intralipid. Three thicknesses were adopted (2.5, 3.0, and 3.5 cm), covering the range of the mouse size over different view directions. The fluorophore was prepared by filling 40 μ L ICG (dissolved in DMSO) in the glass tube (0.3 cm inner diameter and 0.5 cm outer diameter). Two different concentrations were selected (0.004 μ mol/L and 0.0004 μ mol/L, corresponding to ICG quantities of 160 fmol and 16 fmol, respectively). As shown in Fig. 5(a), for each thickness, the tube was placed 1.2 cm away from the bottom side. Similar to a previous study [23], the signal-to-background ratio (SBR) was chosen for evaluating the sensitivity:

$$\text{SBR} = \frac{\text{mean}(|I_F - I_{bg}|)}{\text{mean}(|I_{bg} - I'_{bg}|)}, \quad (5)$$

where I_F represents the acquired fluorescence intensity image; I_{bg} and I'_{bg} are two independently acquired background intensity images in the absence of the fluorophore. Herein, in calculating the SBR, a 1.0 cm \times 1.0 cm region of interest was selected around the maximum fluorescence signal position. Parameter I_{bg} consists of the components of excitation light leakage, autofluorescence, ambient light, and camera dark noise. The ambient light can be significantly reduced with sufficient shielding and digitally subtracted, while the autofluorescence can be reduced or removed with autofluorescence removal methods [33]. The excitation light leakage can be estimated from the excitation light image and subtracted or

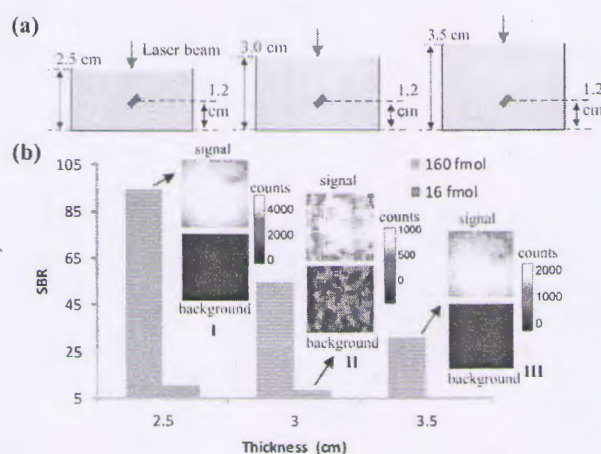


Fig. 5. Sensitivity evaluation experiment. (a) Phantom setup. (b) Fluorescence SBR of different thicknesses and ICG quantities. For conditions I, II, and III, the exposure time was 60, 360, and 180 s, respectively. The size of the signal and background images shown is 1.0 cm \times 1.0 cm.

reduced using improved fluorescence filters. Hence, without loss of generality, only the camera dark noise and the shot-noise term of other background contributions (excitation light leakage, autofluorescence, and ambient light) are considered as the sensitivity restriction factor, as depicted by the denominator of the right-hand side of Eq. (5). In image acquisitions, the pixel binning was 8×8 , and the exposure time varied with ICG quantities from 60 to 480 s. From the SBR data of ICG quantity of 160 fmol in Fig. 5(b), we found that a 1 cm increase in thickness led to around 3 times decrease in SBR. However, for the same thickness increase, the detected fluorescence signal intensity decreased nearly 1 order (7 times). The reason is that, along with the thickness increase, the background signal contribution from excitation light leakage and autofluorescence also decreased. For ICG quantity of 16 fmol, the fluorescence signal could be clearly observed for 3.0 cm thickness, with SBR of 8. However, for this ICG quantity, the fluorescence signal became hard to differentiate for 3.5 cm thickness. Hence, the detection limit of the system was less than 16 fmol for thickness no more than 3.0 cm. For 3.5 cm thickness and 160 fmol ICG, the SBR was 31. Then, the sensitivity limit for 3.5 cm thickness was within the range of 16 to 160 fmol and can be estimated close to 16 fmol side (e.g., around 40 fmol) from the SBR data in Fig. 5(b).

B. In Vivo Experiments

We performed FMT imaging of a small animal to examine the efficacy of our system. This experiment was approved by the Science and Ethics Committee of the School of Biological Science and Medical Engineering in Beihang University, China. One nude mouse (5 weeks, 22 g) was anesthetized with pentobarbital and placed on the glass plate holder, as shown in Fig. 5(a). A small fluorescence tube (40 μ L 4 μ mol/L ICG (dissolved in DMSO) filled into a glass tube of 0.3 cm inner diameter and 0.5 cm outer diameter) was embedded inside the nude mouse.

In the full-angle tomography experiment, the fluorescence (exposure time of 1.0 s and pixel binning of 8×8) and excitation projections were acquired along multiple directions in 15 deg steps. Subsequently, the mouse was scanned along 18 directions in the permissible direction range. For each direction, three illumination positions were scanned in steps of 0.4 cm, as shown in Fig. 6(a). After optical imaging, the mouse was scanned using the small-animal CT. For reconstruction, the imaged region was discretized to 1.1×10^3 uniform voxels ($0.15 \text{ cm} \times 0.15 \text{ cm} \times 0.15 \text{ cm}$). From the projection images, a total of 1.1×10^4 source-detector pairs were obtained in the reconstruction. The optical properties of the mouse were assumed to be homogeneous ($\mu'_s = 10 \text{ cm}^{-1}$, $\mu_a = 0.1 \text{ cm}^{-1}$) for simplicity. One hundred R-ART iterations were performed with a relaxation parameter of 0.01. As shown in Fig. 6(b), the reconstructed target matched well with the actual one, with the center position showing a small deviation of 0.06 cm. We speculate that the deviation may be caused by unknown heterogeneities relating to the optical properties and inherent resolution limitations arising due to light diffusion. This result demonstrates the feasibility of the proposed system for *in vivo* applications.

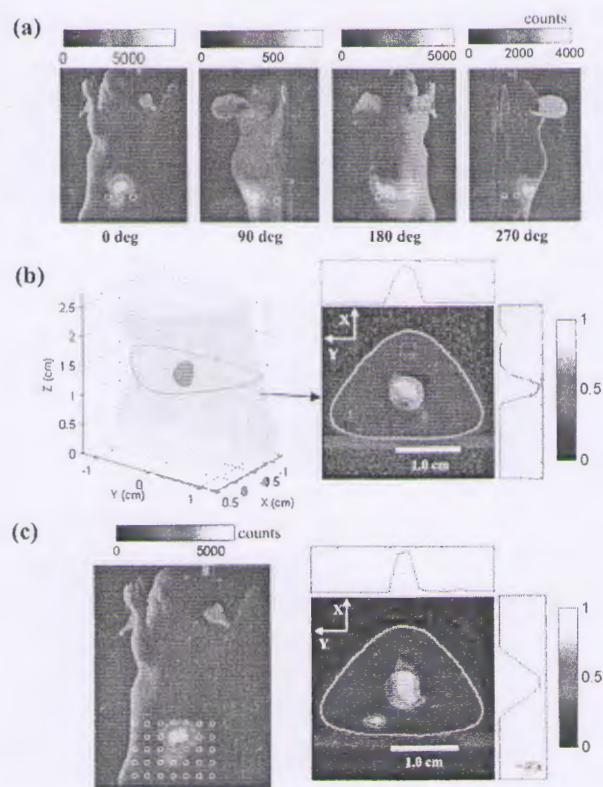


Fig. 6. Mouse imaging experiment. A fluorescence target was embedded inside the abdominal region of the mouse. (a) Overlaid fluorescence images for four different projection directions. (b) Reconstructed image for full-angle projection. (c) Image for single-direction projection. Left: fluorescence projection. Right: overlaid reconstructed image. In (a) and (c), the white markers represent the illumination positions, with the diamond marker representing the position corresponding to the fluorescence image. The tomography slice images shown are normalized to their maximum values.

Tomography with a single projection direction was also performed for the purpose of comparison. We performed sequential scanning of 35 illumination positions (0.30 cm × 0.30 cm), as shown in Fig. 6(c). In total, 1.0e4 source-detector pairs were acquired from the 35 projection images, which was close to the corresponding number of pairs in the full-angle case.

As shown in Fig. 6(c), stronger artifacts appeared near the boundary. The boundary artifacts were caused by the higher noise sensitivity of the boundary voxels [34–37]. Close to the boundaries, the diffusion approximation is less accurate or not valid, and the small 3D surface mismatch also significantly influences the forward modeling of the boundary voxels. The artifacts can be reduced to some extent using more suitable algorithms [36–38]. Acquiring more useful imaging information also aids in reducing the artifacts. As shown in Fig. 6(b), with the advantage of the full-angle view, the observed boundary artifacts were considerably reduced. The full width at half-maximum (FWHM) values in the full-angle case were 0.30 and 0.38 cm along the X and Y axes, respectively. In contrast, in the single-projection-direction case, the FWHM values of the reconstructed target were 0.58 and 0.30 cm along the X and Y-axes, respectively. The considerably lower resolution was obtained along the X axis because no projection operation was performed along the Y direction [9]. The contrast-to-noise ratio (CNR) parameter was also used to evaluate and compare the image quality of the reconstructed slice images in Figs. 6(b) and 6(c). CNR is a measure that indicates whether a localized image feature is well discernible against the image noise, and has been widely used to characterize the performance of a FMT reconstruction system [39] and algorithm [34]. CNR is defined as

$$\text{CNR} = \frac{\text{mean}(I_{\text{ROI}}) - \text{mean}(I_{\text{bg}})}{\sqrt{\omega_{\text{ROI}}\text{var}(I_{\text{ROI}}) + \omega_{\text{bg}}\text{var}(I_{\text{bg}})}}, \quad (6)$$

where I_{ROI} is the reconstructed fluorescence signal within the actual fluorophore inclusion (ROI, region of interest), and I_{bg} is the fluorescence signal in the complement of the ROI. ω_{ROI} and ω_{bg} are the weight factors, which were set to the fraction of area occupied by the ROI and background, respectively. Herein, the ROI was determined from the CT image. The CNR for the full-angle and single-projection-direction cases were 6.4 and 4.3, respectively, indicating that the targets were well discernible in both cases (CNR > 3) [39]. The CNR evaluation further quantitatively confirmed that the full-angle case obtained much better image quality. In summary, the comparison of the above results again evidences that full-angle projection is essential and important for improved FMT results.

4. DISCUSSION AND CONCLUSION

In this study, we proposed and demonstrated a novel noncontact small-animal FMT imaging system with full-angle capacity. Since our system utilizes rotary planar mirrors for illumination and signal acquisition, the small animal need not be rotated, and this makes the experimental procedure easier and faster. The bulky components including scanning light source and the camera also do not require rotation, thereby considerably simplifying system design. In addition, in comparison with the

conical-mirror-based system, the proposed system offers the advantages of overcoming backreflections and more efficient utilization of the camera's dynamic range. Both physical phantom and *in vivo* experiments were performed to evaluate the performance of the proposed system.

When compared with system architecture that requires mounting of the light sources and camera on a gantry [13–15], the architecture of lightweight plane mirrors simplifies the gantry design and enables fast rotation speeds. These advantages become more significant when incorporating more FMT functions, such as multiple-wavelength capacity, frequency-domain, and time-domain detection. Multiple-wavelength capacity is important for FMT, as it provides the benefits of tissue autofluorescence reduction or removal [33], simultaneous observation of multiple biological activities by multiple probes [40], and wider applicability for a series of fluorescence probes operating in the range from visible to near-infrared light. This is why existing commercial small-animal optical tomography systems (single-projection-view FMT including IVIS spectrum imaging and the FMT 2500 LX from Perkin Elmer) support multiple wavelengths. In this case, more light sources and coupling optical components (such as beam splitters) and larger filter wheels and more filters have to be integrated. In comparison with continuous-wave imaging in the demonstrated proof-of-concept system, frequency-domain and time-domain detection can be used to obtain more information, such as the fluorescence lifetime, and provide higher spatial resolution, such as utilizing early-arrival photons [41]. However, for both these imaging domains, the light source and detection parts make the system considerably more bulky. A light modulator must be added for operation in the frequency domain, and the pulse laser that is used for time-domain detection is always very large. Further, a large time-gated image intensifier needs to be coupled to the detection camera. For example, in [15], wherein a noncontact full-angle frequency domain FMT is demonstrated, the primary challenge is the selection of the minimally sized components and the mounting of all these still-bulky components on the rotation gantry. However, with the proposed imager, all these additional components can be fixed on the optical table, making system extension to related applications considerably easier.

As regards the proposed imager, the three emission plane mirrors also contribute to loss in detection efficiency. To address this issue, high-reflection (>97% efficient for visible to near-infrared light) silver-coated mirrors were chosen. The energy loss caused by the mirrors was consequently less than 9%. In the demonstrated system, the optical path from the small animal to the image sensor was around 53 cm. Apart from the field-of-view considerations, this length was chosen to reduce the depth effect (amplification variations) caused by the 3D mouse shape. In future systems, this length can be further reduced by optimizing the placement of emission mirrors, gantry design, and the imaging lens. However, when compared with systems that do not use mirrors, our triple mirrors indeed lengthen the optical path, which also leads to loss in detection efficiency. It should be noted that when compared to the imaging performance of the conical-mirror-based system, which maps the full-angle view to a single image sensor, the optical

path problem of our imager is less severe. Although the detection efficiency in our case is slightly reduced, the signal-to-noise ratio (SNR) reduction depends on practical conditions. In fluorescence image detection, the noise consists of four components: excitation light leakage, autofluorescence, ambient light, and camera dark noise. The two former components are the dominant noise sources; however, these noise signals travel the same path as the fluorescence signal of interest and are reduced at the same level. As regards ambient light, the noise level is similar in all kinds of systems, and it can be reduced by sufficient shielding and digital subtraction. As a deep-cooling scientific camera is used, the camera dark noise is ultralow. When the fluorescence signal is high, the camera dark noise is negligible, and the SNR can be maintained by increasing the exposure time. For low fluorescence quantification conditions, we can analyze the SNR issue from two aspects. If the dominating noise term including excitation light leakage and autofluorescence is post-removed, the system sensitivity can be greatly enhanced. For our imager, very low ICG quantities from 16 to 160 fmol could be detected in 1% intralipid with a thickness ranging from 2.5 to 3.5 cm. One example is that, if a background image is acquired before injection of fluorescence targets, post-removal can be performed by subtracting the background image from fluorescence image. In this condition, for ultralow fluorescence light detection, the camera dark noise becomes a significant part. Hence, the SNR decreases to near the same level as that of the signal energy loss. In contrast, if post-noise-removal is not performed, the system sensitivity decreases by 1 order of magnitude or more, and the camera dark noise can be considered negligible. Consequently, for a detectable fluorescence signal, the SNR does not decrease since we can increase the exposure time to compensate for the limited energy loss.

In summary, in this study, we proposed a novel noncontact full angle imager for camera-based FMT. In future studies, we plan to focus on integrating this full-angle FMT system with x-ray CT and applying it to biological research areas such as cancer treatment evaluation.

Funding. 111 Project (B13003); National Natural Science Foundation of China (NSFC) (61108084, 81101123); Research Fund for the Doctoral Program of Higher Education of China (20111102120039).

Acknowledgment. We thank Miss Qiaohong Tang for assisting us in testing the system in the initial stage, and Dr. Wenying Liu and Yu Wang for their suggestions regarding the system's mechanical design. We would also like to thank Editage (<https://www.editage.com>) for English language editing.

REFERENCES

1. E. E. Graves, J. Ripoll, R. Weissleder, and V. Ntziachristos, "A sub-millimeter resolution fluorescence molecular imaging system for small animal imaging," *Med. Phys.* **30**, 901–911 (2003).
2. V. Ntziachristos, C. H. Tung, C. Bremer, and R. Weissleder, "Fluorescence molecular tomography resolves protease activity in vivo," *Nat. Med.* **8**, 757–761 (2002).
3. X. Montet, V. Ntziachristos, J. Grimm, and R. Weissleder, "Tomographic fluorescence mapping of tumor targets," *Cancer Res.* **65**, 6330–6336 (2005).
4. Y. Lu, C. D. Darné, I. Tan, G. Wu, N. Wilganowski, H. Robinson, A. Azhdarinia, B. Zhu, J. C. Rasmussen, and E. M. Sevick-Muraca, "In vivo imaging of orthotopic prostate cancer with far-red gene reporter fluorescence tomography and in vivo and ex vivo validation," *J. Biomed. Opt.* **18**, 101305 (2013).
5. K. O. Vasquez, C. Casavant, and J. D. Peterson, "Quantitative whole body biodistribution of fluorescently-labeled agents by non-invasive tomographic imaging," *PLoS ONE* **6**, e20594 (2011).
6. F. Leblond, S. C. Davis, P. A. Valdés, and B. W. Pogue, "Pre-clinical whole-body fluorescence imaging: Review of instruments, methods, and applications," *J. Photochem. Photobiol. B* **98**, 77–94 (2010).
7. C. Darné, Y. Lu, and E. M. Sevick-Muraca, "Small animal fluorescence and bioluminescence tomography: a review of approaches, algorithms and technology update," *Phys. Med. Biol.* **59**, R1–R64 (2014).
8. S. V. Patwardhan, S. R. Bloch, S. Achilefu, and J. P. Culver, "Time-dependent whole-body fluorescence tomography of probe bio-distributions in mice," *Opt. Express* **13**, 2564–2577 (2005).
9. T. Lasser and V. Ntziachristos, "Optimization of 360 projection fluorescence molecular tomography," *Med. Image Anal.* **11**, 389–399 (2007).
10. N. Deliolanis, T. Lasser, D. Hyde, A. Soubret, J. Ripoll, and V. Ntziachristos, "Free-space fluorescence molecular tomography utilizing 360° geometry projections," *Opt. Lett.* **32**, 382–384 (2007).
11. D. Wang, X. Liu, F. Liu, and J. Bai, "Full-angle fluorescence diffuse optical tomography with spatially coded parallel excitation," *IEEE Trans. Inf. Technol. Biomed.* **14**, 1346–1354 (2010).
12. N. Ducros, A. Bassi, G. Valentini, G. Canti, S. Arridge, and C. D'Andrea, "Fluorescence molecular tomography of an animal model using structured light rotating view acquisition," *J. Biomed. Opt.* **18**, 020503 (2013).
13. Y. Lin, W. C. Barber, J. S. Iwanczyk, W. Roeck, O. Nalcioğlu, and G. Gulsen, "Quantitative fluorescence tomography using a combined tri-modality FT/DOT/XCT system," *Opt. Express* **18**, 7835–7850 (2010).
14. R. B. Schulz, A. Ale, A. Sarantopoulos, E. Soehngen, M. Zientkowska, and V. Ntziachristos, "Hybrid system for simultaneous fluorescence and x-ray computed tomography," *IEEE Trans. Med. Imaging* **29**, 465–473 (2010).
15. C. D. Darné, Y. Lu, I. Tan, B. Zhu, J. C. Rasmussen, A. M. Smith, S. Yan, and E. M. Sevick-Muraca, "A compact frequency-domain photon migration system for integration into commercial hybrid small animal imaging scanners for fluorescence tomography," *Phys. Med. Biol.* **57**, 8135–8152 (2012).
16. M. Sheu, C. Chiang, W. Sun, J. Wang, and J. Pan, "Dual view capsule endoscopic lens design," *Opt. Express* **23**, 8565–8575 (2015).
17. M. Kfoury, O. Marinov, P. Quevedo, N. Faramarzpour, S. Shirani, L. W.-C. Liu, Q. Fang, and M. J. Deen, "Toward a miniaturized wireless fluorescence-based diagnostic imaging system," *IEEE J. Sel. Top. Quantum Electron.* **14**, 226–234 (2008).
18. G. Wang, H. Shen, K. Durai, X. Qian, and W. X. Cong, "The first bioluminescence tomography system for simultaneous acquisition of multiview and multispectral data," *Int. J. Biomed. Imag.* **2006**, 58601 (2006).
19. C. Li, G. S. Mitchell, J. Dutta, S. Ahn, R. M. Leahy, and S. R. Cherry, "A three-dimensional multispectral fluorescence optical tomography imaging system for small animals based on a conical mirror design," *Opt. Express* **17**, 7571–7585 (2009).
20. J. H. Lee, H. K. Kim, C. Chandhanayyong, F. Y. Lee, and A. H. Hielscher, "Non-contact small animal fluorescence imaging system for simultaneous multi-directional angular-dependent data acquisition," *Biomed. Opt. Express* **5**, 2301–2316 (2014).
21. E. Lapointe, J. Pichette, and Y. Bérubé-Lauzière, "A multi-view time-domain non-contact diffuse optical tomography scanner with dual wavelength detection for intrinsic and fluorescence small animal imaging," *Rev. Sci. Instrum.* **83**, 063703 (2012).
22. D. Kepshire, N. Mincu, M. Hutchins, J. Gruber, H. Dehghani, J. Hynarowski, F. Leblond, M. Khayat, and B. W. Pogue, "A microcomputed tomography guided fluorescence tomography system for small animal molecular imaging," *Rev. Sci. Instrum.* **80**, 043701 (2009).

23. F. Leblond, K. M. Tichauer, R. W. Holt, F. El-Ghoussein, and B. W. Pogue, "Toward whole-body optical imaging of rats using single-photon counting fluorescence tomography," *Opt. Lett.* **36**, 3723–3725 (2011).
24. D. S. Kepshire, S. L. Gibbs-Strauss, J. A. O'Hara, M. Hutchins, N. Mincu, F. Leblond, M. Khayat, H. Dehghani, S. Srinivasan, and B. W. Pogue, "Imaging of glioma tumor with endogenous fluorescence tomography," *J. Biomed. Opt.* **14**, 030501 (2009).
25. A. D. Silva, M. Leabad, C. Driol, T. Bordy, M. Debourdeau, J. Dinten, P. Peltié, and P. Rizo, "Optical calibration protocol for an x-ray and optical multimodality tomography system dedicated to small-animal examination," *Appl. Opt.* **48**, D151–D162 (2009).
26. X. Song, D. Wang, N. Chen, J. Bai, and H. Wang, "Reconstruction for free-space fluorescence tomography using a novel hybrid adaptive finite element algorithm," *Opt. Express* **15**, 18300–18317 (2007).
27. M. Schweiger, S. R. Arridge, M. Hiraoka, and D. T. Delpy, "The finite element method for the propagation of light in scattering media: boundary and source conditions," *Med. Phys.* **22**, 1779–1792 (1995).
28. A. Soubret, J. Ripoll, and V. Ntziachristos, "Accuracy of fluorescent tomography in the presence of heterogeneities: study of the normalized Born ratio," *IEEE Trans. Med. Imag.* **24**, 1377–1386 (2005).
29. A. Kak and M. Slaney, *Computerized Tomographic Imaging* (IEEE, 1987).
30. D. Wang, X. Liu, Y. Chen, and J. Bai, "In-vivo fluorescence molecular tomography based on optimal small animal surface reconstruction," *Chin. Opt. Lett.* **8**, 82–85 (2010).
31. H. Meyer, A. Garofalakis, G. Zacharakis, S. Psycharakis, C. Mamalaki, D. Kioussis, E. N. Economou, V. Ntziachristos, and J. Ripoll, "Noncontact optical imaging in mice with full angular coverage and automatic surface extraction," *Appl. Opt.* **46**, 3617–3627 (2007).
32. R. W. Holt, F. Leblond, and B. W. Pogue, "Toward ideal imaging geometry for recovery independence fluorescence molecular tomography," *Proc. SPIE* **8574**, 857403 (2013).
33. H. Xu and B. W. Rice, "In-vivo fluorescence imaging with a multivariate curve resolution spectral unmixing technique," *J. Biomed. Opt.* **14**, 064011 (2009).
34. J. Baritau, K. Hassler, and M. Unser, "An efficient numerical method for general L_p regularization in fluorescence molecular tomography," *IEEE Trans. Med. Imaging* **29**, 1075–1087 (2010).
35. S. Lam, F. Lesage, and X. Intes, "Time domain fluorescent diffuse optical tomography: analytical expressions," *Opt. Express* **13**, 2263–2275 (2005).
36. S. C. Davis, H. Dehghani, J. Wang, S. Jiang, B. W. Pogue, and K. D. Paulsen, "Image-guided diffuse optical fluorescence tomography implemented with Laplacian-type regularization," *Opt. Express* **15**, 4066–4082 (2007).
37. W. Xie, Y. Deng, K. Wang, X. Yang, and Q. Luo, "Reweighted L_1 regularization for restraining artifacts in FMT reconstruction images with limited measurements," *Opt. Lett.* **39**, 4148–4151 (2014).
38. D. Wang, J. He, H. Qiao, X. Song, Y. Fan, and D. Li, "High-performance fluorescence molecular tomography through shape-based reconstruction using spherical harmonics parameterization," *PLoS ONE* **9**, e94317 (2014).
39. S. C. Davis, B. W. Pogue, H. Dehghani, and K. D. Paulsen, "Contrast-detail analysis characterizing diffuse optical fluorescence tomography image reconstruction," *J. Biomed. Opt.* **10**, 050501 (2005).
40. G. Zacharakis, R. Favicchio, M. Simantiraki, and J. Ripoll, "Spectroscopic detection improves multi-color quantification in fluorescence tomography," *Biomed. Opt. Express* **2**, 431–439 (2011).
41. M. J. Niedre, R. H. D. Kleinea, E. Aikawa, D. G. Kirsch, R. Weissledera, and V. Ntziachristos, "Early photon tomography allows fluorescence detection of lung carcinomas and disease progression in mice in vivo," *Proc. Natl. Acad. Sci. USA* **105**, 19126–19131 (2008).



High-Performance Fluorescence Molecular Tomography through Shape-Based Reconstruction Using Spherical Harmonics Parameterization

Daifa Wang^{1,2}, Jin He², Huiting Qiao², Xiaolei Song³, Yubo Fan², Deyu Li^{2*}

1 State Key Laboratory of Software Development Environment, Beihang University, Beijing, China, **2** Key Laboratory for Biomechanics and Mechanobiology of Ministry of Education, School of Biological Science and Medical Engineering, Beihang University, Beijing, China, **3** The Russell H. Morgan Department of Radiology and Radiological Sciences, Division of MR Research, Johns Hopkins University School of Medicine, Baltimore, Maryland, United States of America

Abstract

Fluorescence molecular tomography in the near-infrared region is becoming a powerful modality for mapping the three-dimensional quantitative distributions of fluorochromes in live small animals. However, wider application of fluorescence molecular tomography still requires more accurate and stable reconstruction tools. We propose a shape-based reconstruction method that uses spherical harmonics parameterization, where fluorophores are assumed to be distributed as piecewise constants inside disjointed subdomains and the remaining background. The inverse problem is then formulated as a constrained nonlinear least-squares problem with respect to shape parameters, which decreases ill-posedness because of the significantly reduced number of unknowns. Since different shape parameters contribute differently to the boundary measurements, a two-step and modified block coordinate descent optimization algorithm is introduced to stabilize the reconstruction. We first evaluated our method using numerical simulations under various conditions for the noise level and fluorescent background; it showed significant superiority over conventional voxel-based methods in terms of the spatial resolution, reconstruction accuracy with regard to the morphology and intensity, and robustness against the initial estimated distribution. In our phantom experiment, our method again showed better spatial resolution and more accurate intensity reconstruction. Finally, the results of an *in vivo* experiment demonstrated its applicability to the imaging of mice.

Citation: Wang D, He J, Qiao H, Song X, Fan Y, et al. (2014) High-Performance Fluorescence Molecular Tomography through Shape-Based Reconstruction Using Spherical Harmonics Parameterization. PLoS ONE 9(4): e94317. doi:10.1371/journal.pone.0094317

Editor: Jonathan A. Coles, Glasgow University, United Kingdom

Received: November 11, 2013; **Accepted:** March 14, 2014; **Published:** April 14, 2014

Copyright: © 2014 Wang et al. This is an open-access article distributed under the terms of the Creative Commons Attribution License, which permits unrestricted use, distribution, and reproduction in any medium, provided the original author and source are credited.

Funding: This study was funded by the State Key Laboratory of Software Development Environment (No. SKLSDE-2011ZX-12), the National Natural Science Foundation of China (Nos. 61108084, 81101123), Research Fund for the Doctoral Program of Higher Education of China (No. 20111102120039), Key Laboratory for Biomechanics and Mechanobiology of Ministry of Education. The funders had no role in study design, data collection and analysis, decision to publish, or preparation of the manuscript.

Competing Interests: The authors have declared that no competing interests exist.

* E-mail: deyuli@buaa.edu.cn

Introduction

Near-infrared fluorescence molecular tomography (FMT) is used for the three-dimensional (3D) localization and quantification of fluorescent targets deep inside turbid tissue. As a convenient and cost-effective small animal imaging modality, it can provide accurate visualization and quantification of the distribution of fluorescent tracers. Various applications have been proposed or carried out using this tool to monitor diseases at the molecular level, such as enzyme activity [1], mapping expressions of cancer markers [2], [3], and monitoring targeted drug delivery [4]. Davis *et al.* recently presented multicolor imaging to monitor two cancer markers simultaneously [5]. Although some devices for FMT are commercially available, the need for higher spatial resolution and more quantitative and reliable reconstruction hinders the wider application of this technique.

The recovery of 3D fluorescence distribution from boundary measurements is a nonlinear inverse problem. Because of the scattered light propagation inside turbid tissue media, the problem is highly ill posed and thus susceptible to data noise and model errors. The ill-posedness makes FMT reconstruction a significant

challenge. As a solution, additional prior information is generally applied through different regularization techniques. Smooth distribution constraints are typically imposed through methods such as Tikhonov regularization [6]. Information on the sparse distribution is utilized through different compressed sensing techniques [7], [8]. Edge enhancement priors are utilized by penalizing the fluorescence intensity gradient as a regularized term, such as in the total variation method [9], [10], [11], [12]. The development of multimodality FMT systems [13], [14] has boosted the fusion of information derived from anatomical structures [15], [16]. High-density sampling [17], which increases the amount of boundary measurements, has also proven effective, and several studies have focused on investigating the optimal source-detector configurations for different kinds of FMT imaging systems [18], [19]. Although these advances have been critical to moving FMT from the laboratory to commercial applications, great challenges remain in order to obtain 3D fluorescence distributions stably and accurately.

In many specific applications, the distribution of fluorescent targets can be well described as the sum of a small number of subdomains (shapes) with constant piecewise intensities. This

approximation is very suitable for tumor applications, where the fluorescence agent binds specifically to tumor tissue. With shape parameterization, the number of unknowns is greatly reduced, which in turn decreases the ill-posedness of the reconstruction. Shape parameterization has been applied to diffuse optical tomography [20], [21], bioluminescence tomography [22], and electrical impedance tomography [23]. For FMT reconstruction, several studies have used a piecewise constant assumption. Álvarez *et al.* [24] applied a level set to time-resolved FMT to implicitly impose shape constraints, where the distributions are recovered with the piecewise constant assumption and the lifetime is estimated using a gradient method. They performed a series of numerical simulations to verify its effectiveness. Despite the reduced ill-posedness, shape-based reconstruction is still a nonlinear and ill-posed problem, and the initial conditions critically affect its solution. To overcome this limitation, Laurain *et al.* [25] extended topological sensitivity analysis to generate good initial estimates for shape-based FMT and evaluated the effectiveness through numerical simulations. In our previous work, we performed shape based reconstruction by assuming the fluorescent targets to be regular ellipsoids [26]. A two-step solver was developed to enhance the robustness against the initial values and noise, and graphics processing unit (GPU) acceleration was adopted to accelerate the computation of the Jacobian matrix and gradient.

In this work, we developed a novel shape-based reconstruction method by introducing spherical harmonics [27] for shape modeling. Compared to our previous ellipsoid approximation, spherical harmonics can better model irregular targets [20], [23], [28], which leads to more accurate recovered images. In the proposed method, the inverse problem is parameterized with respect to the spherical harmonics coefficients of the shape boundaries. To stabilize the solution, the two-step strategy is expanded, and a modified block coordinate descent approach is introduced to recover shape parameters. Since the computation of the Jacobian matrix and gradient with respect to the spherical harmonics coefficients is rather complex and time-consuming, we accelerate their calculations by using GPU based on our previous work [26] on ellipsoid shape parameters. We evaluated the proposed method using numerical simulation, a physical phantom, and *in vivo* data, and it demonstrated much better performance than conventional voxel-based reconstruction.

Methods

Forward problem

In turbid tissue media, the light propagation for source-detector separations of more than several millimeters can be modeled by a partial differential equation called the diffusion equation. By setting the spatially localized impulse function $\delta(\vec{r}-\vec{r}_s)$ as the source term, the Green's function $G(\vec{r}_s, \vec{r})$ can then be solved via numerical techniques such as the finite element method (FEM) [29], [30]. By considering that light travels from \vec{r}_s to position \vec{r} and from \vec{r} to detector \vec{r}_d and integrating over the whole imaged domain Ω , the forward mapping from the fluorescence distribution $f(\vec{r})$ to the received fluorescence signal $\Phi_{em}(\vec{r}_s, \vec{r}_d)$ for the source-detector pair (\vec{r}_s, \vec{r}_d) can be expressed as

$$\Phi_{em}(\vec{r}_s, \vec{r}_d) = \Theta_{em} \int_{\Omega} \Phi_{ex}(\vec{r}_s, \vec{r}) G_{em}(\vec{r}, \vec{r}_d) f(\vec{r}) dV(\vec{r}) \quad (1)$$

where Θ represents the total system amplification factor from the quantum efficiency, detection efficiency, etc. The subscripts *ex* and *em* indicate the excitation light and emitted fluorescence

wavelengths, respectively. In FMT reconstruction, using the normalized Born ratio $\Phi_{born} = \Phi_{em}/\Phi_{ex}$ of the corresponding measurements at the emission and excitation wavelengths has been proven to provide much more robust performance with respect to the uneven system amplification factor Θ and unknown heterogeneity of the imaged medium compared to using the fluorescence signals alone [31]. Given Green's functions, the normalized Born ratio can be written as follows:

$$\Phi_{born}(\vec{r}_s, \vec{r}_d) = \Theta_{em}/\Theta_{ex} \int_{\Omega} G_{ex}(\vec{r}_s, \vec{r}) G_{em}(\vec{r}, \vec{r}_d) / G_{ex}(\vec{r}_s, \vec{r}_d) f(\vec{r}) dV(\vec{r}) \quad (2)$$

For numerical computation, the above integral equation is generally discretized using the piecewise constant voxel basis as follows:

$$\Phi_{born}(\vec{r}_s, \vec{r}_d) = \sum_{i=1}^{n_V} G(\vec{r}_s, \vec{r}_i) G(\vec{r}_i, \vec{r}_d) / G(\vec{r}_s, \vec{r}_d) \Delta V f(\vec{r}_i) \quad (3)$$

where the imaged domain is divided into n_V uniform voxels with volume ΔV . For data from all M source-detector pairs, a matrix-vector product form can be generated from Eq. (3):

$$\Phi_{born} = W \begin{bmatrix} f(\vec{r}_1) \\ \vdots \\ f(\vec{r}_{n_V}) \end{bmatrix} \quad (4)$$

where W is the weight matrix with size $M \times n_V$. The above linear system is highly ill posed, which makes direct inversion impossible. A priori information is typically required for stabilization, such as smooth constraints imposed via Tikhonov regularization.

We assumed that the fluorescent targets have sharp interfaces and are distributed as piecewise constants. That is, the imaged domain Ω can be split into n disjointed subdomains $\Omega_i, i=1, \dots, n$ and the remaining background $\Omega_0 = \Omega \setminus \bigcup_{i=1}^n \Omega_i$ with constant concentrations $\rho_i + \rho_0$ and ρ_0 , respectively. Then, the fluorescence distribution is expressed as follows:

$$f(\vec{r}) = f(x, y, z) = \rho_0 + \sum_{i=1}^n \rho_i U(\vec{r} \in \Omega_i) \quad (5)$$

where U is the unit step function. In our previous work [23], we used ellipsoids to approximate the subdomains for simplicity; however, this approach is limited with regard to modeling irregular geometries. Spherical harmonics can represent fairly intricate 3D polar shapes well (a polar shape can be described as a single-value function in spherical coordinates with respect to a center position). Since more accurate shape modeling yields better shape reconstruction performance, we adopted real-value spherical harmonics to parameterize the arbitrary 3D subdomain boundaries $\partial\Omega_i$, as introduced in [28]. Then, the surface locations $\vec{r} \in \partial\Omega_i$ of boundary $\partial\Omega_i$ are represented in spherical coordinates with respect to a given center (x_c, y_c, z_c, i) :

$$\vec{r} \in \partial\Omega_i = \sum_{l=0}^N \sum_{m=-l}^l C_l^m \bar{Y}_l^m(\vartheta, \varphi) \quad (6)$$

where $\{C_l^m\}$ are the expansion coefficients and N is the maximum degree of spherical harmonics used. The real value basis function

$\tilde{Y}_l^m(\vartheta, \varphi)$ is defined as follows:

$$\tilde{Y}_l^m(\vartheta, \varphi) = \begin{cases} \operatorname{Re}[Y_l^m](\vartheta, \varphi), m \leq 0 \\ \operatorname{Im}[Y_l^m](\vartheta, \varphi), m > 0 \end{cases} \quad (7)$$

where Y_l^m are the spherical harmonics functions of complex values [24]. Then, a single fluorescence inclusion can be parameterized using $(N+1)^2$ expansion coefficients for up to N -order spherical harmonics, the center position, and the fluorescence concentration. In addition to the background concentration ρ_0 , a total of $n((N+1)^2 + 4) + 1$ shape parameters model the piecewise constant fluorescence distribution with n disjointed subdomains, which can be depicted by the new notation ζ . In this study, we used second-order spherical harmonic coefficients.

Inverse problem

To recover the shape parameters ζ , a least-squares minimization function is established to minimize the difference between theoretical predictions and practical measurements:

$$\begin{aligned} \arg \min_{\zeta} \Psi(\zeta) &= \frac{1}{2} \|\Phi_{\text{born}} - F(\zeta)\|_2^2 \\ &= \frac{1}{2} \|\Phi_{\text{born}} - Wf_{\zeta}\|_2^2 \\ \text{s.t. } 1) \rho_i, \rho_0 &\geq 0, i = 1, \dots, n \\ 2) x_c^{\min} &\leq x_c \leq x_c^{\max}, y_c^{\min} \leq y_c \leq y_c^{\max}, z_c^{\min} \leq z_c \leq z_c^{\max} \\ 3) r^{\min} &\leq r_i \leq r^{\max}, r_i \in \partial\Omega_i, i = 1, \dots, n \\ 4) r_i &\geq \min(r_i) \geq 1/c \max(r_i), r_i \leq \max(r_i) \leq c \min(r_i), c \geq 1, \\ & r_i \in \partial\Omega_i, i = 1, \dots, n \\ 5) V_i \cap V_j &= \emptyset, \forall i, j, i \neq j \end{aligned} \quad (8)$$

Herein, given a previously defined uniform voxel discretization with sufficient small size such as $0.7 \times 0.7 \times 0.7 \text{ mm}^3$, the theoretical predictions $F(\zeta)$ are computed via a matrix-vector product based on Eq. (4). The fluorescence distribution vector f_{ζ} is generated by transforming the shape parameters to the voxel grids through Eqs. (5)–(7). For stable reconstruction, reasonable constraints are imposed to the shape parameters. The first constraint is the nonnegativity of the fluorescence intensity. The second is to restrict the shape centers inside box bound of the image object. The following two constraints prevent the radius from being too small or large and geometric shapes from being too narrow. The final constraint (non-overlap) guarantees the disjointedness of the subdomains.

Although the unknowns are greatly reduced because of the spherical harmonics, Eq. (8) is still a complex nonlinear problem. An appropriate iterative solver is needed for its numerical solution, which relies on the shape gradient and Hessian matrix. However, gradient-based solvers are extremely sensitive to the initial conditions, and getting a good initial estimate inside the imaged object is generally a difficult and challenging task. In our previous work [26], since different types of shape parameters contribute differently to the measurement data, we handled the ellipsoid shape parameters using a two-step strategy and proved its capability of improving the robustness against initial conditions. Based on the previous work, we introduced a two-step and

modified block coordinate descent strategy for spherical harmonics-based shape reconstruction, as shown in Fig. 1. In the first step, by setting the initial shapes as spheres, Eq. (8) is solved with the spherical harmonics expansion coefficients as invariants; this yields relatively good initial conditions for the next step, especially for the center positions. A modified block coordinate descent strategy is then employed in the second step. That is, the parameters of blocks 1 (center positions and intensities) and 2 (spherical harmonics expansion coefficients and intensities) are separately estimated at even and odd iterations. Herein, the center positions and spherical harmonics expansion coefficients are placed into different blocks, as they have weak logical connections and can be separated. However, the fluorescence intensities are put into both blocks since they have strong logical connections with the other shape parameters. This is different from the standard block coordinate descent method, where each variable appears in only one block. As shown in Fig. 1, the maximum iteration number of each step (N_{first} and N_{max} minus N_{first}) obviously influences the final reconstruction result. Empirically, N_{first} was set to 20. This number is sufficient to get a good estimation of the center positions; a larger value does not produce an obvious improvement but requires more computation time. For the second step, more iterations generally yield a better shape but may produce over-optimization. This is because of the high ill-posedness of the recovered block 2; details are discussed later in the discussions and conclusion section. In our experience, N_{max} can be set to a relatively low value such as 40 in the presence of a high level of noise and model error. N_{max} can be set to a relatively large value such as 80 in the presence of a moderate level of noise and model error.

In each step, a Newton-type method is used as an iterative solver for the nonlinear minimization problem, where the update $\zeta^k + 1$ for ζ is given by

$$\begin{aligned} \zeta^{k+1} &= \\ \zeta^k + \arg \min_{\delta\zeta} \frac{1}{2} \|J\delta\zeta - (\Phi_{\text{born}} - F(\zeta^k))\|_2^2 + C(\zeta^k + \delta\zeta) \end{aligned} \quad (9)$$

Herein, $J = \partial F / \partial \zeta$ is the Jacobian matrix. $C(\zeta)$ is the penalty term because of the shape constraints $c(\zeta) \leq 0$ and is imposed through the popular exterior penalty function method. Then, a minimization program with an increasing sequence of penalty parameters t as $t \rightarrow \infty$ is generated:

$$\begin{aligned} \zeta^* &= \arg \min_{\zeta} L(\zeta, t) = \\ \frac{1}{2} \|J\zeta - (\Phi_{\text{born}}^{\text{meas}} - F(\zeta^k))\|_2^2 + t \sum_j \{\min[0, c_j(\zeta^k + \zeta)]\}^2 \end{aligned} \quad (10)$$

where ζ is a new notation to denote $\delta\zeta$. In each t -sub problem, ζ is updated via Newton's method, and t is doubled:

$$\begin{aligned} (\zeta)^{n+1} &= \\ (\zeta)^n + (\nabla_{\zeta}^2 L + \lambda I)^{-1} \{-J^T [J\zeta - (\Phi_{\text{born}} - F(\zeta^k))] - \nabla_{\zeta} C\} \\ t^{n+1} &= 2t^n \end{aligned} \quad (11)$$

where the Hessian matrix $\nabla_{\zeta}^2 L$ is $J^T J + \nabla_{\zeta}^2 C$. Since $\nabla_{\zeta}^2 L$ is poorly conditioned, regularization is added with parameter λ for stable inversion, and an iterative solver is used with the symmetric LQ method (MATLAB function `symmlq`). The parameter λ was

empirically selected to be 10^{-3} and worked well in the simulation and physical experiments.

Generally, the background volume is much larger than the targets. To improve the conditioning of the inverse problem, the background fluorescence intensity is scaled during reconstruction:

$$\rho'_0 = \rho_0 / \text{scal} \quad (12)$$

In this study, the scale factor *scal* was set to 100.

Computation of objective function value, gradient, and Jacobian matrix

For Eq. (8), the Jacobian matrix computation can be expressed as

$$J = \partial F(\zeta) / \partial \zeta = W \partial f_i / \partial \zeta \quad (13)$$

Since f_i is a nonlinear function of ζ , the perturbation method is used to compute $\partial f_i / \partial \zeta_j$ using a sufficient small perturbation $\Delta \zeta_j$:

$$\partial f_i / \partial \zeta_j \approx \frac{\Delta f_i}{\Delta \zeta_j} = \frac{\Delta f_i(\zeta + \Delta \zeta_j) - \Delta f_i(\zeta)}{\Delta \zeta_j} \quad (14)$$

Eqs. (8), (13), and (14) show that the shape-voxel mapping $f(\tilde{r}_i)$ is the basic component for evaluating J and $F(\zeta)$ and that it is critical to evaluating the non-overlap constraint. As no analytical expression is available for this nonlinear mapping, we can directly calculate $f(\tilde{r}_i)$ by uniformly dividing the corresponding voxel into $16 \times 16 \times 16$ fine sub-voxels with centers \tilde{r}_{ij} :

$$f(\tilde{r}_i) = \sum_{j=0}^{4095} \rho_{ij} U(\tilde{r}_{ij} \in \Omega_t) / 4096 \quad (15)$$

Herein, the point-in-shape test $\tilde{r}_{ij} \in \Omega_t$ is performed according to Eqs. (6) and (7).

Similar to our previous work [26], the frequently performed basic operations (i.e., weight matrix multiplication and shape-voxel mapping) take more than 90% of the computation time. Hence, we accelerated them using the advanced CUDA GPU platform [32], [33], where the former is performed using the standard CUDA CUBLAS library and the latter is performed as shown in Fig. 2(a). Generally, a shape target is small compared to the whole imaging domain, and processing the many non-overlapped voxel-shape pairs using GPU is inefficient [32], [33]. Hence, a voxel-shape pairing procedure is first performed with CPU by judging the overlap between a voxel and the bounding box of a shape. GPU is then used to determine the concrete overlapped volume for each voxel-shape pair through concurrently executed threads.

As shown in Fig. 2(a), the point in shape test $U(\tilde{r}_{ij} \in \Omega_t)$ is the most important component of the shape-voxel mapping. For the polar shape, this test is performed by comparing the radius \tilde{r}_{ij} from the shape center to the point and the radius r_s of the corresponding shape surface point, as illustrated in Fig. 2(b). Theoretically, r_s can be directly calculated using Eq. (6); however, this is time-consuming. For faster computation, we adopted an interpolation technique. A triangular-mesh unit sphere surface is introduced where each mesh node has a pair of spherical coordinates (θ, ϕ) , as shown in Fig. 2(c). These mesh nodes can then determine the parametric surface by finding their new

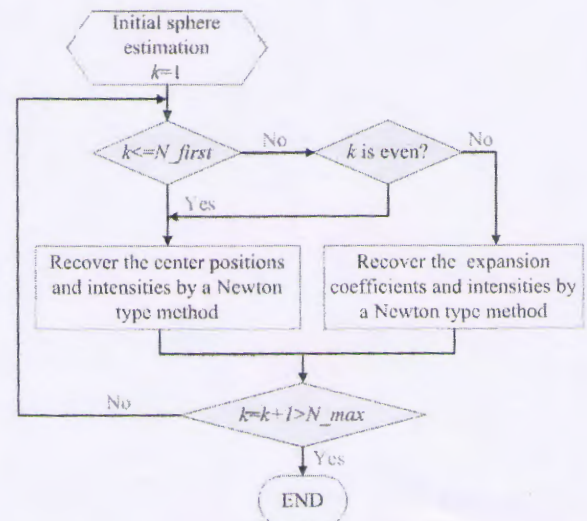


Figure 1. Optimization of spherical harmonics shape parameters. In the first step (the initial N_{first} iteration), the unknown targets are assumed to be spheres. In the second step (the following iterations until the maximum iteration number N_{max}), a modified block coordinate descent strategy is adopted to alternately recover the grouped shape parameters.
doi:10.1371/journal.pone.0094317.g001

distances from the center through Eq. (6). The unit sphere transformation is inspired by [28], where the mapped mesh was mainly used for boundary element method discretization and solution. The (θ, ϕ) space is then uniformly refined to 100×100 grids, and the corresponding radii are calculated by interpolation from those mesh nodes. Then, given a point \tilde{r}_{ij} with spherical coordinates (θ_{ij}, ϕ_{ij}) , the radius of the corresponding surface point $\tilde{r}_s(\theta_{ij}, \phi_{ij})$ can be easily determined through two-dimensional interpolation among the four neighbor points in the 100×100 regular grids. As this lookup table operation is rather simple, it can be easily implemented through GPU.

Voxel-based reconstruction

In the experiments, the proposed method was compared with traditional voxel-based reconstruction. In general, voxel-based reconstruction is formulated as a linear system:

$$\Phi_{\text{born}} = Wp \quad (16)$$

where p is the fluorescence distribution in 3D voxels and W is the weight matrix as described in Eq. (4). The linear system is ill posed, which means that direct inversion is impossible. In this study, two techniques were used for its solution: the random access algebraic reconstruction technique (R-ART) with nonnegative constraints, which has been widely applied for FMT [34,35]; and Tikhonov regularization, where Eq. (16) is transformed into an L_2 regularized solution:

$$\arg \min_{p \geq 0} \Psi(p) = \frac{1}{2} (\|\Phi_{\text{born}} - Wp\|_2^2 + \gamma \|p\|_2^2) \quad (17)$$

where γ is the regularization parameter. The regularized least-squares problem is solved by using the conjugation gradient

method, and the nonnegative constraints are imposed through the exterior penalty function method.

Experiments and Results

The performance and effectiveness of the proposed method was evaluated through numerical simulations and experiments with a physical phantom and a mouse *in vivo*. All reconstructions were performed on our desktop computer, which has an Intel 2.8-GHz quad-core CPU, 16 GB RAM, and an NVIDIA GTX 480 graphics card.

Numerical simulations

A series of simulations was performed to compare the proposed method with the traditional voxel-based method and evaluate its performance in the presence of noise and background contrasts.

To mimic the heterogeneous optical properties of a real mouse, a cylinder model (6.0 cm height and 2.0 cm diameter) with two cylindrical heterogeneities (6.0 cm height and 0.35 cm diameter) was used, as shown in Fig. 3. Reasonable optical properties were chosen with a background of $\mu_a = 0.3 \text{ cm}^{-1}$, $\mu_s' = 10.0 \text{ cm}^{-1}$ and heterogeneity of $\mu_a = 0.5 \text{ cm}^{-1}$, $\mu_s' = 10.0 \text{ cm}^{-1}$. Full angle data-acquisition was adopted [34], where data were simulated for 24 evenly distributed projection angles around the model. For each projection angle, the light source was sequentially scanned over five positions in steps of 0.3 cm to generate five projections. For each projection, the detector sampling on the charge coupled device (CCD) detection field of view was over a $1.8 \text{ cm} \times 2.2 \text{ cm}$

region with 0.2 cm spacing. The data simulations were performed using FEM.

In the reconstructions, we simply assumed the imaged object to be homogenous with optical properties of $\mu_a = 0.3 \text{ cm}^{-1}$, $\mu_s' = 10.0 \text{ cm}^{-1}$ to mimic the unknown heterogeneity in practical cases. During all of the numerical experiments, the same geometry constraints were applied with $0.04 \text{ cm} \leq r \leq 0.5 \text{ cm}$, $c = 10$, $-1.0 \text{ cm} \leq x, y \leq 1.0 \text{ cm}$, and $2.0 \text{ cm} \leq z \leq 4.0 \text{ cm}$. Eighty iterations (one update in Eq. 9 corresponds to one iteration) were performed in the shape-based reconstructions, where the first step took 20 iterations. The 3D voxels for the Jacobian matrix calculation were inside the cylinder model and over $(-1.01, 0) \text{ cm} \times (-1.01, 0) \text{ cm} \times (2.04, 0) \text{ cm}$ with a voxel size of $0.07 \text{ cm} \times 0.07 \text{ cm} \times 0.07 \text{ cm}$. In the comparison experiments, 3D voxels were also used in voxel-based reconstruction. In the voxel-based reconstruction, both R-ART and Tikhonov regularization were adopted. R-ART was iterated 200 times with a relaxation parameter of 0.1. The Tikhonov regularization parameter was empirically set to 1×10^{-3} , which gave a good balance between stability and smoothing. The conjugate gradient method was performed until the relative difference between neighboring iterations was less than 1×10^{-6} .

Reconstruction of dual inclusions of different shapes. We evaluated the proposed method with closely placed dual inclusions of various shapes; these included ellipsoids, cuboids, and triangular prisms. The parameters are specified in Table 1. There was no fluorescence in the background. Then, 5% Gaussian noise was added to the synthetic measurements.

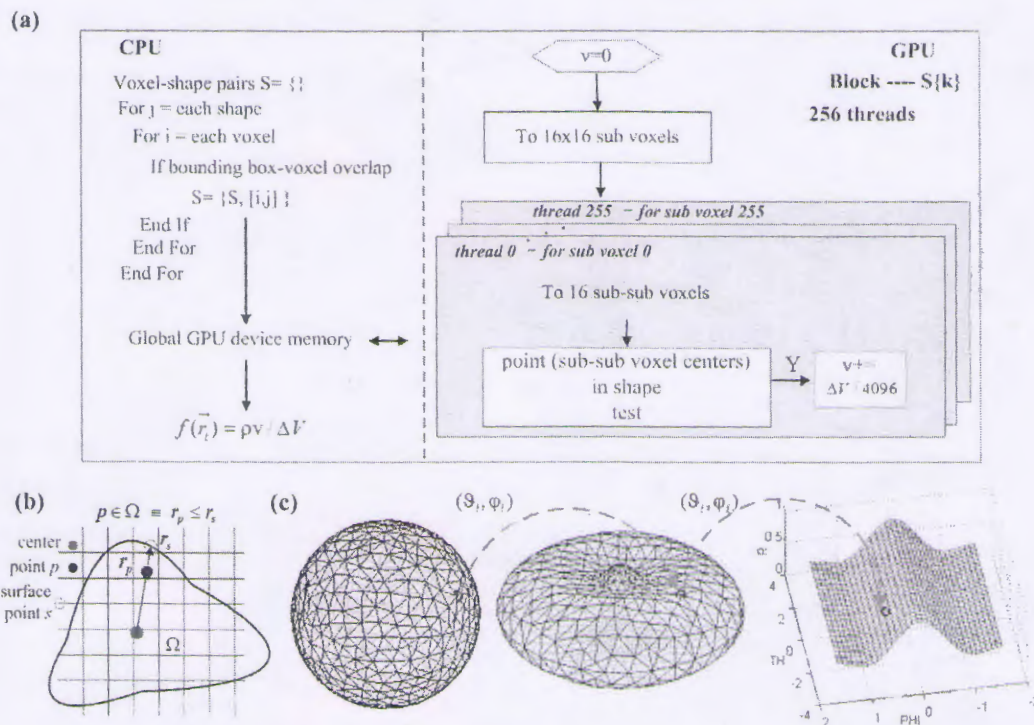


Figure 2. Shape-voxel mapping. (a) Flowchart of the GPU-accelerated computation of shape-voxel mapping. (b) Illustration of how to determine whether a point is inside a polar shape. (c) Digitalization of spherical harmonics parameterized shape with triangular mesh surface. The parameterized-shape surface mesh (middle) is generated by mapping a predefined triangular meshed unit sphere surface (left). For each mesh node (e.g., blue circle), its new radius on the parameterized-shape surface is found by keeping its (θ_i, ϕ_i) unchanged. Further, a regular table is generated in the spherical coordinates (θ, ϕ) space from these mesh nodes for faster point-in-shape determination.

As shown in Fig. 4, neither R-ART nor Tikhonov regularization could resolve the dual targets for all of the different shapes. In contrast, because of the shape parameterization, the proposed method demonstrated much better resolution capability. It clearly separated the adjacent dual inclusions and matched intensities and morphology well. The free background was also accurately estimated. Of course, because of the high photon scattering in tissues and the presence of noise and heterogeneity, fully accurate recovery of the true shapes was still impossible. The better resolution capability of the proposed method is because of the successful utilization of shape priors, which greatly reduces the space of possible solutions. In other words, the shape-based method can find a better solution without getting stuck in the many cut solution branches.

As a benefit of the parallel acceleration by GPU, the shape reconstruction time was typically within several minutes. For example, the shape optimization for the dual ellipsoids took about 159 s. Without GPU, the computation time was about 83 min, which was 31 times longer.

To evaluate the performance with respect to different initial values, we selected dual spheres with different center distances away from the true inclusions, which represented initial shapes with different extents of goodness. As shown in Fig. 5, the proposed method worked well and demonstrated robust performance since it considered and handled the difference among shape parameters through the two-step and modified block coordinate descent strategy. In contrast, although not shown here, the straightforward method of simply recovering all parameters simultaneously generally corrupted the reconstruction process. The objective function value could not be decreased effectively, and the true inclusions were not found.

In some cases, it may be impossible to reliably determine the targets number *a priori*. By assuming more targets than actually needed, the proposed method can handle this problem to some extent. As demonstrated in Fig. 5, with three initial targets, the proposed method still recovered the true targets well, whereas the false target was reconstructed with ultra-low intensity.

Different noise level. To evaluate the sensitivity of the proposed method to noise, different levels of Gaussian noise (2.5%–40%) were added to the synthetic measurements. The dual ellipsoids case was used as the configuration of the fluorescent targets, and the background was fluorescence-free. As shown in Fig. 6, neither voxel-based method could resolve the targets even

at the lowest noise level. In contrast, the proposed method clearly separated and estimated the adjacent dual inclusions for various noise levels up to 40%; thus, it showed strong robustness against noise jamming.

Different background contrast level. Even state-of-the-art fluorescent probes still find it difficult to completely bind to targets without residuals in the background. Thus, we evaluated the performance of the proposed method using different contrast levels from 100:1 to 10:20. The dual ellipsoids case was used as the configuration of the fluorescent targets. In addition, 1% Gaussian noise was added to the synthetic measurements.

As shown in Fig. 7, the background fluorescence could not be properly estimated by both voxel-based methods; both showed an obvious nonuniform distribution in the background region. In addition, the boundary artifacts gradually increased with the background fluorescence. For Tikhonov regularization, its spreading and smoothing effects became more evident in the presence of background fluorescence, especially at a low contrast level. Similar to the previous background-free case, the dual targets could not be resolved. In contrast, the proposed method demonstrated much better resolution capability and quantification. For all contrast levels, the dual targets were clearly separated. The background value was accurately reconstructed with a small absolute error that was within 0.001. These results verified the effectiveness of the proposed method under low fluorescence contrast conditions.

Physical experiments

Physical phantom and *in vivo* experiments were performed to evaluate the feasibility of the proposed method for practical applications. Our fluorescence imaging system, which was developed in-house, was used for data acquisition, as shown in Fig. 8(a). The imaged object was placed on a rotational stage for multiple angle image acquisition. The laser and detector were placed on opposite sides of the stage. The semiconductor laser (785 nm wavelength) output a small laser spot around 1 mm in diameter with a power of 14 mW. The detector was a highly sensitive sCMOS camera (Neo, Andor, Belfast, Northern Ireland, U.K.) coupled with a Nikkor 60 mm f/2.8D lens (Nikon, Melville, NY). The camera had a large chip area of 2560×2160 pixels with a 16-bit dynamic range. During the data acquisition, the sCMOS chip was cooled to -30°C to reduce dark current noise. A neutral density filter of 1% transmittance (Daheng, Beijing, China) and $840 \pm 18.5\text{ nm}$ band-pass fluorescence filter (Semrock, Rochester, NY) were used for excitation and fluorescence image collection, respectively. In addition, 72 white light images were collected to reconstruct the object's 3D surface [36].

In the phantom experiment, a glass cylinder (inner diameter of 2.43 cm and outer diameter of 2.83 cm) was filled with intralipid (1% concentration $\mu_s' = 10\text{ cm}^{-1}$, $\mu_a = 0.02\text{ cm}^{-1}$). Two fluorescence inclusions were embedded closely together with a 0.10 cm edge-to-edge distance. Each inclusion was produced by pouring 40 μL of indocyanine green (concentration of 4 $\mu\text{mol/L}$) into a transparent glass tube (0.3 cm inner diameter and 0.5 cm outer diameter). Excitation and fluorescence data were collected at 36 projection angles evenly distributed over 360° . For each projection angle, three excitation positions along the horizontal direction were scanned sequentially at a distance of 0.3 cm. For voxel-based reconstruction, 50 R-ART iterations were performed with a relaxation parameter of 0.05. For shape-based reconstruction, 40 iterations were performed, and geometry constraints were applied with $0.04\text{ cm} \leq r \leq 0.5\text{ cm}$, $c=3$, and targets centers inside the bounding box of the image object.

The fluorescence projection images in Fig. 8(b) show the high level of light scattering in turbid media. With the voxel-based

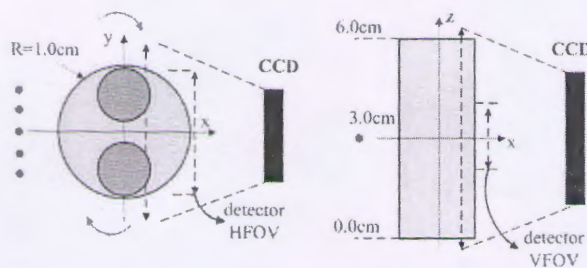


Figure 3. Simulation experiment sketch. A full-angle CCD camera-based imaging system configuration was used for the data simulation. The imaged object was a cylinder phantom with two embedded cylinder heterogeneities (different absorption coefficients). For each projection, five different excitation sources were scanned (red dots), and the detectors, which corresponded to selected detection points on the image plane, were within 1.8 cm of the detector horizontal FOV (HFOV) and 2.2 cm of the detector vertical FOV (VFOV) with a detector spacing of 0.2 cm.

doi:10.1371/journal.pone.0094317.g003

Table 1. Parameters for inclusions with various shapes.

ellipsoid	(r_x, r_y, r_z)	(x_c, y_c, z_c)	ρ
target 1	(0.22 0.11 0.15)	(0.00 0.25 3.00)	1.00
target 2	(0.22 0.11 0.15)	(0.00 -0.25 3.00)	1.00
cuboid	(L, W, H)	(x_c, y_c, z_c)	ρ
target 1	(0.40 0.20 0.20)	(0.00 0.25 3.00)	1.00
target 2	(0.40 0.20 0.20)	(0.00 -0.25 3.00)	1.00
prism	(E, H)	(x_c, y_c, z_c)	ρ
target 1	(0.50 0.30)	(0.00 0.30 3.00)	1.00
target 2	(0.50 0.30)	(0.00 -0.30 3.00)	1.00

The second column lists the geometric dimensions: radii for the ellipsoid, edge length for the cuboid, and edge and height for the triangular prism.
doi:10.1371/journal.pone.0094317.t001

method (R-ART), the dual inclusions were merged, and artifacts were present near the object boundary. In contrast, the two close targets were clearly separated by the proposed method with acceptable center deviations of 0.06 and 0.15 cm. The relative difference between the accumulated fluorescence intensities of the two targets was 8.4%, which may be partly caused by inevitable model error and the cross-talk between the two close inclusions. The actual free background was also accurately estimated. Overall, the results demonstrated that the proposed method has better resolution capability than traditional voxel-based reconstruction for practical applications.

A small animal experiment was performed to verify the feasibility of the proposed method for *in vivo* applications. This experiment was approved by the Science and Ethics Committee of the School of Biological Science and Medical Engineering in Beihang University, China. One nude mouse (5 weeks, 21 g) was

anesthetized with pentobarbital and fixed on a glass plate holder, as shown in Fig. 8(a). A small fluorescence glass tube (0.3 cm diameter and 0.5 cm length, concentration of 4 $\mu\text{mol/L}$) was embedded inside the nude mouse. The fluorescence and excitation projections were collected at a single projection angle. As shown in the first column of Fig. 8(c), the point light sources were scanned at 5×7 positions with steps of 0.3 cm. In the reconstruction, the mouse optical properties were assumed to be homogeneous ($\mu'_s = 10\text{cm}^{-1}$, $\mu_a = 0.3\text{cm}^{-1}$) for simplicity. For voxel-based reconstruction, 30 R-ART iterations were performed with a relaxation parameter of 0.01. For shape-based reconstruction, 40 iterations were performed, and geometry constraints were applied with $0.04\text{cm} \leq r \leq 0.5\text{cm}$, $c = 3$, and target centers inside the bounding box of the image object. As shown in Fig. 8(c), the reconstructed fluorescence had a high value around the boundary and a widespread distribution inside the object. Compared to the actual single fluorescence inclusion, the reconstructed fluorescence was not acceptable. This was partly because of the limited projection angle, complex heterogeneous optical properties of the mouse, and the presence of an auto-fluorescent background. The proposed method, which benefited from the reduced number of unknowns, gave a better result. It recovered a single fluorescence inclusion and the background. This preliminary experiment demonstrated the feasibility of the proposed method for *in vivo* applications.

Discussions and Conclusion

We proposed a shape-based reconstruction method for fluorescence molecular tomography that uses spherical harmonics parameterization. The inverse problem is formulated as a constrained nonlinear least-squares problem. To guarantee successful reconstruction and enhance robustness against initial conditions and noise, a two-step and modified block coordinate descent strategy was introduced to handle different shape parameters. Reasonable geometrical constraints are also enforced via the exterior penalty function method for further stability and

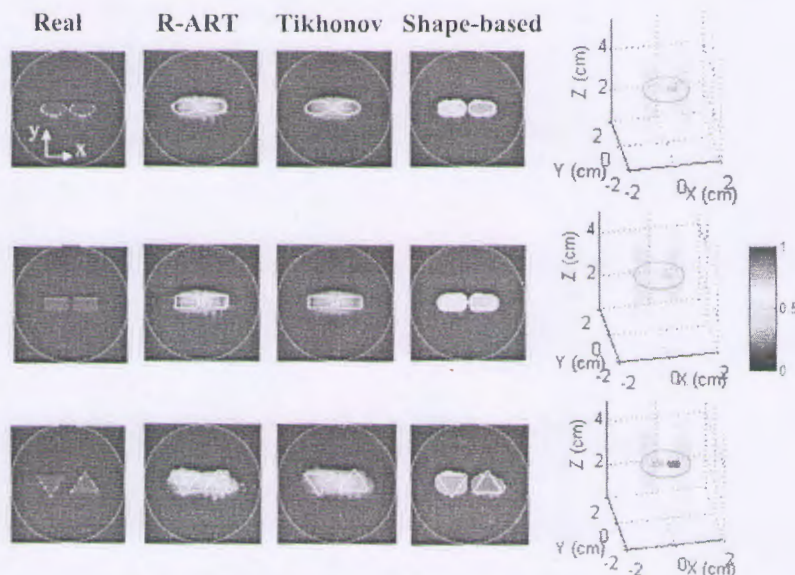


Figure 4. Comparison of the results from the proposed method and voxel-based reconstructions. In the slice images, the red circles denote the outer boundary of the imaged object, and the white lines denote the boundaries of the real inclusions. The slice images are of 3.0 cm height.

doi:10.1371/journal.pone.0094317.g004

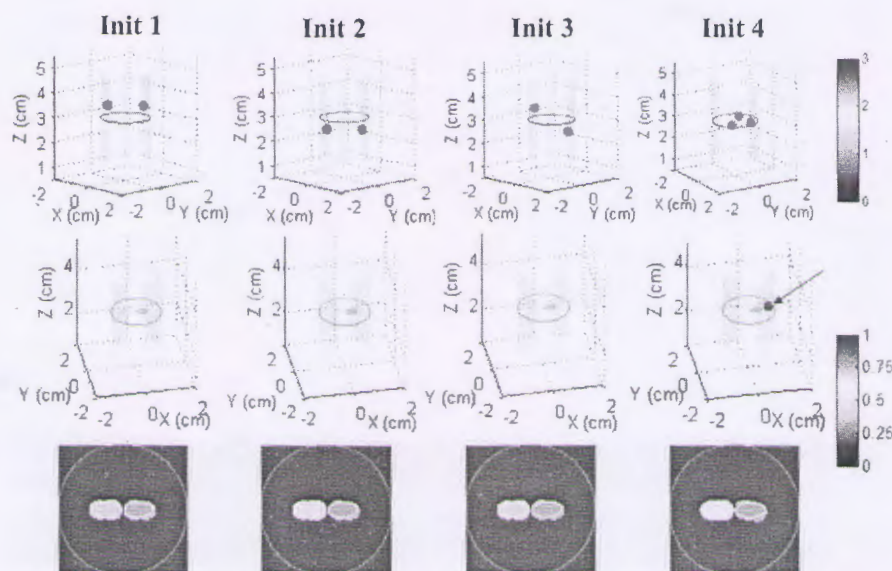


Figure 5. Reconstruction results with different initial estimates. In the slice images, the red circle denotes the boundary of the imaged object, and the white lines denote the boundaries of the real inclusions. The slice images are of 3.0 cm height.
doi:10.1371/journal.pone.0094317.g005

accuracy. During the optimization, the objective function value and Jacobian matrix are calculated using the perturbation method, which is also greatly accelerated using GPU. The results of the numerical simulation and physical phantom and *in vivo* experiments all demonstrated the effectiveness of the proposed method.

Because of the incorporated shape priors and the resulting reduction in the dimensions of the inverse problem, the proposed method demonstrated better resolution capability than the conventional voxel-based method in the numerical and physical experiments. However, compared to voxel-based methods, the proposed method has the weakness of a relatively small application range. In application scenarios, the fluorescence distribution should be approximated as the sum of a small number of subdomains with piecewise constant intensities.

Although the number of unknowns is greatly reduced, attention should be paid to optimization techniques, as the shape-based reconstruction is still nonlinear and ill posed. If the difference in contributions to boundary measurements by the shape parameters

is not considered and these parameters are simply recovered simultaneously, the reconstruction generally fails. In the proposed method, a two-step and modified block coordinate descent strategy is introduced. The optimization strategy stabilized the shape-based reconstruction against up to a 40% noise level. It also ensured the robustness of the proposed method against different initial values for noise and heterogeneity, even when the target number is not known *a priori*. In many cases, a fluorescent background is inevitable. As demonstrated in the numerical simulations, the proposed method worked well for low fluorescence contrasts down to 100:20. This capacity was further verified in the *in vivo* experiment.

An intuitive explanation for the proposed optimization strategy is as follows. For a target, small deviations in its center position and expansion coefficients vary the boundary measurements for different methods. The center position deviation alters the distance from the target to different boundary sides; thus, it mainly changes the profiles of fluorescence projections. In contrast, the deviation

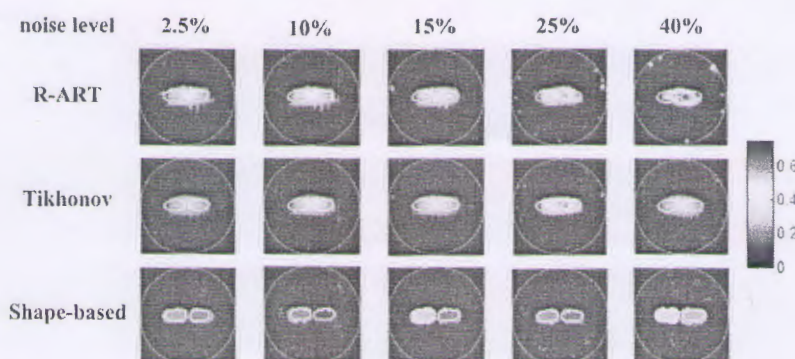


Figure 6. Reconstruction results of different noise levels. The red circle denotes the boundary of the imaged object, and the white lines denote the boundaries of the real inclusions. The slice images are of 3.0 cm height.
doi:10.1371/journal.pone.0094317.g006

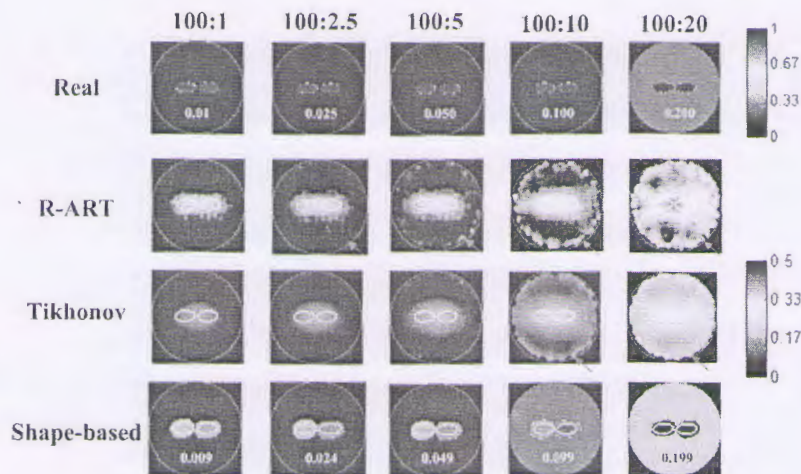


Figure 7. Reconstruction results of different fluorescence contrasts. The red circle denotes the boundary of the imaged object, and the white lines denote the boundaries of the real inclusions. The slice images are of 3.0 cm height.
doi:10.1371/journal.pone.0094317.g007

of each expansion coefficient changes the target geometry and mainly changes the projection details. The difference in contributions requires the center position and expansion coefficients to be handled differently. In particular, the center position needs to be

estimated first to approximate the coarse components of the fluorescence projections.

The proposed optimization strategy also has a mathematical explanation. For the Hessian matrixes of blocks 1 and 2, and all

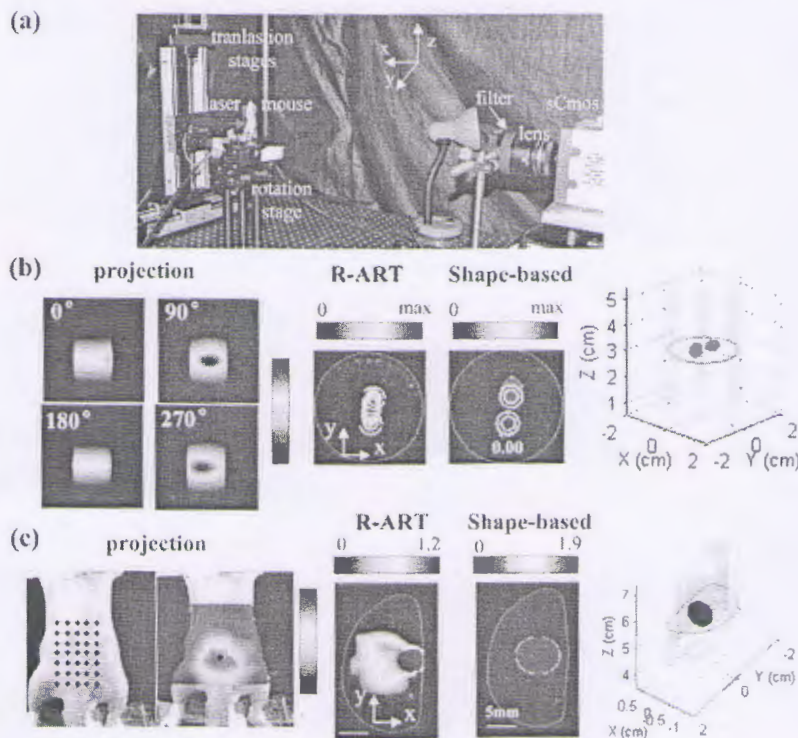


Figure 8. Physical experiments. (a) The full angle fluorescence molecular tomography system developed in-house. (b) Physical phantom experiment. Two fluorescence inclusions were placed closely together inside a cylinder phantom with a 0.10 cm edge-to-edge distance. The white circles denote the inner (solid line) and outer (dash line) boundaries of the real inclusions. (c) *In vivo* experiment. A fluorescence inclusion was embedded inside a nude mouse. The grid of black dots overlaid on the mouse represents the excitation light sources. For the slice images in (b) and (c), the red circle denotes the boundary of the imaged object, and every two slice images are at the same height, as depicted by the red circle in the corresponding 3D image.
doi:10.1371/journal.pone.0094317.g008

shape parameters, their condition numbers are different in orders of magnitude. For example, in the initial dual spheres case (Init 1 in Fig. 5), the condition numbers of the corresponding regularized Hessian matrixes (empirically selected regularization parameter of 1×10^{-3}) were 1.1×10^3 , 9.6×10^4 , and 1.3×10^6 , respectively. The high Hessian matrix condition number of block 2 means that the recovery of expansion coefficients is highly sensitive to noise and model error. Compared to block 2, the Hessian matrix condition number of block 1 was almost two orders of magnitude smaller, which means that the estimation of its variable elements is much less sensitive to error. This is why we use a two-step reconstruction scheme since the first step has the inherent advantage of much better stability. Compared to the two blocks, the Hessian matrix condition number for all shape parameters becomes even higher. Thus, when the shape parameters are recovered simultaneously in the second step, the estimation of the center positions is negatively affected by the expansion coefficients and becomes much more ill posed. Hence, the modified block coordinate descent strategy was adopted to alternately update blocks 1 and 2, which makes the second step more stable.

The convergence of the modified block coordinate descent optimization should be clarified since the standard coordinate descent method generally finds a local minimum. Although it is difficult to determine the convergence of the standard coordinate descent method [37] when the variables cannot be separated, modified block coordinate descent optimization can find a global minimum or near-global minimum in the presence of noise. The reasons are as follows. In the second step, the reconstruction has a relatively good initial estimate provided by the first step, especially for the center positions. Moreover, parameters with strong logical connections are put into the same block. In other words, the two blocks can be considered separable to some extent.

In the numerical simulation, the GPU accelerated the shape-based reconstruction about 30 times faster. The increased acceleration is important for the proposed method, as it guarantees the shape reconstruction time is only several (typically less than 3) minutes. By transforming the complex and frequently performed point-in-shape operation to a lookup table procedure, the GPU

implementation becomes easier, and the computation speed becomes faster.

Apart from shape-based methods, total variation (TV) has attracted a great deal of attention in recent years since it can also strengthen the boundary edges between targets and background. Instead of directly incorporating shape priors, TV penalizes the intensity gradient information as the regularized term. Hence, it has the advantage of requiring fewer assumptions on the shape geometry and the weakness of not reducing the unknown dimensions. In recent years, TV has seen advances for FMT and demonstrated its superiority over traditional L_2 regularization in background-free cases [10], [11], [12]; future progress may demonstrate its effectiveness for low fluorescence contrast conditions. Since TV problem is highly nonlinear, its performance depends on the developed solution algorithm and selected regularization parameters. Hence, focus is presently on finding the optimal parameters or developing an automated parameter selection method. In comparison, the proposed method does not have the problem of determining regularization parameters, and selecting the geometry constraints for application is intuitive and simple. In general, the two techniques of shape-based reconstruction and TV are developing towards preserving the boundary edges for piece-constant fluorescence distributions. Each has its own strengths and weaknesses and thus needs further attention.

In this study, the normalized Born method [31] was used to reduce the negative effects of unknown heterogeneous optical properties. Shape parameterization can also be used to estimate the optical properties of different inner organs and helps better model the photon propagation inside small animals. Thus, the shape-based reconstruction quality can be further improved. In future work, we will focus on developing a full shape-based method to recover optical properties and successfully guide fluorescence distributions.

Author Contributions

Conceived and designed the experiments: DW DL YF XS. Performed the experiments: DW JH HQ. Analyzed the data: DW JH HQ. Contributed reagents/materials/analysis tools: DW. Wrote the paper: DW HQ XS DL.

References

1. Ntziachristos V, Tung CH, Bremer C, Weissleder R (2002) Fluorescence molecular tomography resolves protease activity in vivo. *Nature Medicine* 8: 757–761.
2. Montet X, Ntziachristos V, Grimm J, Weissleder R (2005) Tomographic fluorescence mapping of tumor targets. *Cancer Research* 65: 6330–6336.
3. Ntziachristos V, Schellenberger EA, Ripoll J, Yessayan D, Graves E, et al. (2004) Visualization of antitumor treatment by means of fluorescence molecular tomography with an annexin V-Cy5.5 conjugate. *Proceedings of the National Academy of Sciences of the United States of America* 101: 12294–12299.
4. Vasquez KO, Casavant C, Peterson JD (2011) Quantitative Whole body biodistribution of fluorescent-labeled agents by non-invasive tomographic imaging. *Plos One* 6: e20594. doi:10.1371/journal.pone.0020594.
5. Davis SC, Samkoe KS, Tichauer KM, Sexton KJ, Gunn JR, et al. (2013) Dynamic dual-tracer MRI-guided fluorescence tomography to quantify receptor density in vivo. *Proceedings of the National Academy of Sciences of the United States of America* 110: 9025–9030.
6. Li M, Cao X, Liu F, Zhang B, Luo J, et al. (2012) Reconstruction of fluorescence molecular tomography using a neighborhood regularization. *IEEE Transactions on Biomedical Engineering* 59: 1799–1803.
7. Mohajerani P, Eftekhari AA, Huang J, Adibi A (2007) Optimal sparse solution for fluorescent diffuse optical tomography: theory and phantom experimental results. *Applied Optics* 46: 1679–1685.
8. Han D, Tian J, Zhu S, Feng J, Qin C, et al. (2010) A fast reconstruction algorithm for fluorescence molecular tomography with sparsity regularization. *Optics Express* 18: 8630–8646.
9. Dutta J, Ahn S, Li C, Cherry SR, Leahy RM (2012) Joint L1 and total variation regularization for fluorescence molecular tomography. *Physics in Medicine and Biology* 57: 1459–1476.
10. Chamorro-Servent J, Abascal JFP, Aguirre J, Arridge S, Correia T, et al. (2013) Use of Split Bregman denoising for iterative reconstruction in fluorescence diffuse optical tomography. *Journal of Biomedical Optics* 18: 076016.
11. Freiburger M, Clason C, Scharfetter H (2012) Total variation regularization for 3D reconstruction in fluorescence tomography: experimental phantom studies. *Applied Optics* 51: 8216–8227.
12. Freiburger M, Clason C, Scharfetter H (2010) Total variation regularization for nonlinear fluorescence tomography with an augmented Lagrangian splitting approach. *Applied Optics* 49: 3741–3747.
13. Schulz RB, Alc A, Sarantopoulos A, Freyer M, Soehngen E, et al. (2010) Hybrid System for Simultaneous Fluorescence and X-ray Computed Tomography. *IEEE Transactions on Medical Imaging* 29: 465–473.
14. Guo X, Liu X, Wang X, Tian F, Liu F, et al. (2010) A combined fluorescence and microcomputed tomography system for small animal imaging. *IEEE Transactions on Biomedical Engineering* 57: 2876–2883.
15. Lin Y, Yan H, Nalcioglu O, Gulsen G (2009) Quantitative fluorescence tomography with functional and structural a priori information. *Applied Optics* 48: 1328–1336.
16. Hyde D, Miller EL, Brooks DH, Ntziachristos V (2010) Data Specific Spatially Varying Regularization for Multi-Modal Fluorescence Molecular Tomography. *IEEE Transactions on Medical Imaging* 29: 365–374.
17. Graves EE, Ripoll J, Weissleder R, Ntziachristos V (2003) A sub-millimeter resolution fluorescence molecular imaging system for small animal imaging. *Medical Physics* 30: 901–911.
18. Wang D, Liu X, Liu F, Bai J (2010) Full-angle fluorescence diffuse optical tomography with spatially coded parallel excitation. *IEEE Transactions on Information Technology and Biomedicine* 14: 1346–1354.
19. Lasser T, Ntziachristos V (2007) Optimization of 360° projection fluorescence molecular tomography. *Medical Image Analysis* 11: 389–399.

27

20. Zacharopoulos A, Schweiger M, Kolehmainen V, Arridge S (2009) 3D shape based reconstruction of experimental data in diffuse optical tomography. *Optics Express* 17: 18940–18956.
21. Schweiger M, Dorn O, Zacharopoulos A, Nissila I, Arridge SR (2010) 3D level set reconstruction of model and experimental data in diffuse optical tomography. *Optics Express* 18: 150–164.
22. Liu K, Yang X, Liu D, Qin C, Liu J, et al. (2010) Spectrally resolved three-dimensional bioluminescence tomography with a level-set strategy. *Journal of the Optical Society of America A* 27: 1413–1423.
23. Babaeizadeh S, Brooks DH (2007) Electrical impedance tomography for piecewise constant domains using boundary element shape-based inverse solutions. *IEEE Transactions Medical Imaging* 26: 637–647.
24. Alvarez D, Medina P, Moscoso M (2009) Fluorescence lifetime imaging from time resolved measurements using a shape-based approach. *Optics Express* 17: 8843–8855.
25. Laurain A, Hintermuller M, Freiburger M, Scharfetter H (2013) Topological sensitivity analysis in fluorescence optical tomography. *Inverse Problems* 29: 025003.
26. Wang D, Qiao H, Song X, Fan Y, Li D (2012) Fluorescence molecular tomography using a two-step three-dimensional shape-based reconstruction with graphics processing unit acceleration. *Applied Optics* 51: 8731–8744.
27. \Wikipedia website. Available: http://en.wikipedia.org/wiki/Spherical_harmonics. Accessed 2014 Mar 26.
28. Zacharopoulos AD (2004) Three-Dimensional Shape-Based Reconstructions in Medical Imaging. University of London. Ph.D. Thesis.
29. Song X, Wang D, Chen N, Bai J, Wang H (2007) Reconstruction for free-space fluorescence tomography using a novel hybrid adaptive finite element algorithm. *Optics Express* 15: 18300–18317.
30. Schweiger M, Arridge SR, Hiraoka M, Delpy DT (1995) The finite element method for the propagation of light in scattering media: Boundary and source conditions. *Medical Physics* 22: 1779–1792.
31. Soubret A, Ripoll J, Ntziachristos V (2005) Accuracy of fluorescent tomography in the presence of heterogeneities: Study of the normalized Born ratio. *IEEE Transactions on Medical Imaging* 24: 1377–1386.
32. NVIDIA Corporation (2011) NVIDIA CUDA C Programming Guide 4.0.
33. NVIDIA Corporation (2010) NVIDIA's Next Generation CUDA Compute Architecture: Fermi.
34. Deliolanis N, Lasser T, Hyde D, Soubret A, Ripoll J, et al. (2007) Free-space fluorescence molecular tomography utilizing 360° geometry projections. *Optics Letters* 32: 382–384.
35. Koenig A, Hervé L, Jossierand V, Berger M, Boutet J, et al. (2008) In vivo mice lung tumor follow-up with fluorescence diffuse optical tomography. *Journal of Biomedical Optics* 13: 011008.
36. Wang D, Liu X, Chen Y, Bai J (2010) In-vivo fluorescence molecular tomography based on optimal small animal surface reconstruction. *Chinese Optics Letters* 8: 82–85.
37. Beck A, Tetruashvili L (2013) On the Convergence of Block Coordinate Descent Type Methods. *SIAM Journal of Optimization* 23: 2037–2060.

第1作者论文

Fluorescence molecular tomography using a two-step three-dimensional shape-based reconstruction with graphics processing unit acceleration

Daifa Wang,^{1,2} Huiting Qiao,² Xiaolei Song,³ Yubo Fan,² and Deyu Li^{2,*}

¹State Key Laboratory of Software Development Environment, Beihang University, Beijing 100191, China

²Key Laboratory for Biomechanics and Mechanobiology of Ministry of Education, School of Biological Science and Medical Engineering, Beihang University, Beijing 100191, China

³The Russell H. Morgan Department of Radiology and Radiological Sciences, Division of MR Research, Johns Hopkins University School of Medicine, Baltimore, Maryland 21287, USA

*Corresponding author: deyuli@buaa.edu.cn

Received 27 August 2012; revised 10 November 2012; accepted 26 November 2012;
posted 27 November 2012 (Doc. ID 175036); published 19 December 2012

In fluorescence molecular tomography, the accurate and stable reconstruction of fluorescence-labeled targets remains a challenge for wide application of this imaging modality. Here we propose a two-step three-dimensional shape-based reconstruction method using graphics processing unit (GPU) acceleration. In this method, the fluorophore distribution is assumed as the sum of ellipsoids with piecewise-constant fluorescence intensities. The inverse problem is formulated as a constrained nonlinear least-squares problem with respect to shape parameters, leading to much less ill-posedness as the number of unknowns is greatly reduced. Considering that various shape parameters contribute differently to the boundary measurements, we use a two-step optimization algorithm to handle them in a distinctive way and also stabilize the reconstruction. Additionally, the GPU acceleration is employed for finite-element-method-based calculation of the objective function value and the Jacobian matrix, which reduces the total optimization time from around 10 min to less than 1 min. The numerical simulations show that our method can accurately reconstruct multiple targets of various shapes while the conventional voxel-based reconstruction cannot separate the nearby targets. Moreover, the two-step optimization can tolerate different initial values in the existence of noises, even when the number of targets is not known *a priori*. A physical phantom experiment further demonstrates the method's potential in practical applications. © 2012 Optical Society of America

OCIS codes: 170.6960, 170.3010, 170.6280, 170.3880.

1. Introduction

Using the advanced fluorescence-labeling and optical-imaging technique, fluorescence imaging makes it possible to better understand the mechanism of human disease at cell or molecular level in small animal models *in vivo*. However, conventional fluorescence imaging using reflected illumination can

only get two-dimensional projection images, which inherently results in poor localization and photon quantification due to the strong scattering of photons [1]. Recently, fluorescence molecular tomography (FMT), aiming at three-dimensional (3D) localization and quantification of fluorescence targets, has drawn great attention and become a research hot spot [2].

In FMT, one attempts to recover the 3D distribution of fluorescence targets embedded deeply (up to several centimeters) inside a small animal such as

a nude mouse from noninvasive measurements of emitted light. In the reconstruction the 3D volume is usually digitalized to a number of voxels. However, the reconstruction of FMT is usually a highly ill-posed problem as a large number of unknown parameters need to be resolved from the limited number of boundary measurements. Therefore, there is always a tradeoff between image resolution and stabilization of the inverse problem. In other words, better spatial resolution requires smaller voxels, but the increase of voxel numbers will cause susceptibility to data noise and model errors. For improvement, many trails have already been made by applying additional prior information, such as anatomical structure [3–5], local smoothness [6], or sparsity [7–9].

Shape-based reconstruction has emerged in recent years for tomography imaging, where the targets are assumed as the sum of a small number of subdomains with piecewise-constant contrasts. With shape parameterization, the number of unknowns will be largely reduced, greatly decreasing the ill-posedness of reconstruction. The shape-based techniques are either of implicit parameterization methods or explicit parameterization methods. In implicit parameterization methods, the shape boundaries are implicitly defined by the zero level of level-set functions. For example, it has already been applied in bioluminescence tomography fields such as diffuse optical tomography [10,11], bioluminescence tomography [12], and time-resolved FMT [13]. The level-set method is suitable for arbitrary target shape, yet the computation for the evolution of level sets is relatively complex. In explicit parameterization methods, different approaches [14–19] including ellipsoid, spherical harmonics, B-Spline, etc. have been used in different tomography modalities. In this paper, we assume that the fluorescence targets are ellipsoids. The assumption is reasonable for many practical applications such as *in situ* tumors or functional groups that can be effectively approximated by ellipsoid shapes. The parametric model can provide important medical benefit information including location, size, orientation, and contrast. In addition, this level of information may be used as the prior knowledge for other more complex shape-based reconstruction (e.g., spherical harmonics approximation) methods, thereby simplifying the algorithm development and improving its performance, which will be investigated in our future work.

Herein, the FMT reconstruction is formulated as a nonlinear optimization problem with respect to ellipsoid parameters. Reasonable geometrical constraints are applied for better robustness and accuracy. The exterior penalty function method [20] is used to enforce the constraints. Since various shape parameters contribute differently to the boundary measurements, a distinctive optimization algorithm is required for successful recovery, even though the number of unknowns has been greatly reduced. One straightforward way is to recover all shape parameters simultaneously, which is called one-step

optimization in this article. However, in a condition featuring no good initial estimation and a high level of noises, the simple approach may fail in finding a successful solution. Although only results of a single inclusion case were provided, previous reports for diffuse optical tomography [14] and electrical impedance tomography [18] have suggested that better shape-based reconstruction performance would be expected if assuming the unknown shapes as spheres at the initial stage of the inverse algorithm. For FMT, this strategy (one-step optimization with sphere preparation) does do a better job, but is still far from expected, as demonstrated in Section 3.B. Here, we still use spheres to get relatively good initials, but we only recover the center positions and fluorescence intensities in the initial step, while the radii are fixed. After that, in the second step, all the shape parameters are successively recovered. With the proposed two-step algorithm, much better robustness to initial values in the existence of noises is achieved.

During the reconstruction, the calculations of the objective function value and the Jacobian matrix are frequently performed. Since the forward mapping from shape parameters to boundary measurements is highly nonlinear, establishing a fast operator to calculate these components is challenging. For example, the ellipsoid shape-based diffuse optical tomography [14] took reconstruction time from 5 to 24 h, most of which was spent on these basic computation components. To establish the operator, one needs to solve the diffusion equation for calculating light propagation at first. Since the analytical solution of the diffusion equation is limited for simple regular geometries, in general we need a numerical method, such as the boundary element method (BEM) or the finite element method (FEM). When using BEM, different operators were proposed for diffuse optical tomography [19] and electrical impedance tomography [18] by generating the boundary element mesh dependent on the target shapes. In our method, we adopt FEM for its advantages in handling irregular geometries and heterogeneous optical properties. A 3D mesh subdivision-based technique [15] was proposed to map the target shapes to the finite element mesh in the operator for diffuse optical tomography. In [21], a 3D voxel was used as the link between the shape parameters and the boundary measurements for bioluminescence tomography. In this study, similarly, we deduce an operator for FMT based on the 3D voxel link. Compared to operators [14,18,19] that solve the forward model every time, the deduced operator only solves the forward model its first time; thus its speed improves. However, the up to 10 min of optimization time still requires further acceleration. In the last couple of years, the fast development of multicore and many-core processors, especially the graphics processing unit (GPU), makes it possible for great speed enhancement in personal computers. In this study, we further accelerate the deduced operator to several tens of times faster by using the GPU technology.

Then, the optimization time is reduced to less than 1 min when using an NVIDIA GTX-480 graphics card.

The remainder of this article is organized as follows. In Section 2, the forward diffusion model and the inverse problem are introduced. The two-step optimization algorithm is presented, and the GPU-accelerated operator for FEM-based computation of the objective function value and the Jacobian matrix is described. In Section 3, numerical simulation experiments are used to verify the proposed method. In Section 4, a physical phantom experiment is used to evaluate its reliability in practical applications. Finally, discussions and conclusions are presented in Section 5.

2. Methods

A. Forward and Inverse Problems

In FMT, instead of the fluorescence signals alone, the normalized born ratio $\Phi_{\text{born}}^{\text{meas}}$ of measured fluorescence Φ_m^{meas} and excitation Φ_x^{meas} signals is usually used for reconstruction. The benefit is that the negative effects of uneven system amplification factor and the heterogeneous optical properties can be reduced [22]. For a source-detector pair (\vec{r}_s, \vec{r}_d) with a point-light source $\delta(\vec{r} - \vec{r}_s)$ at position \vec{r}_s and a detector at location \vec{r}_d , by considering that light travels from \vec{r}_s to position \vec{r} and from \vec{r} to detector \vec{r}_d and integrating over the whole domain Ω , the forward mapping from fluorescence distribution $f(\vec{r})$ to the normalized born ratio is expressed as follows:

$$\begin{aligned} \Phi_{\text{born}}^{\text{meas}}(\vec{r}_s, \vec{r}_d) &= \Phi_m^{\text{meas}}(\vec{r}_s, \vec{r}_d) / \Phi_x^{\text{meas}}(\vec{r}_s, \vec{r}_d) \\ &= \int_{\Omega} G(\vec{r}_s, \vec{r}) G(\vec{r}, \vec{r}_d) / G(\vec{r}_s, \vec{r}_d) f(\vec{r}) d\vec{r}, \quad (1) \end{aligned}$$

where $G(\vec{r}_1, \vec{r}_2)$ is the Green's function that describes photon propagation from a point \vec{r}_1 to another position \vec{r}_2 . In a highly diffusive tissue medium, the Green's function can be computed using the diffusion equation coupled with Robin-type boundary condition [23,24]:

$$\begin{cases} -\nabla \cdot [D(\vec{r}) \nabla G(\vec{r}_s, \vec{r})] + \mu_a(\vec{r}) G(\vec{r}_s, \vec{r}) = \delta(\vec{r} - \vec{r}_s) & \vec{r} \in \Omega \\ 2AD(\vec{r}) \partial G(\vec{r}_s, \vec{r}) / \partial \vec{n} + G(\vec{r}_s, \vec{r}) = 0 & \vec{r} \in \partial \Omega \end{cases} \quad (2)$$

where $\mu_a(\vec{r})$ is the absorption coefficient and $D(\vec{r}) = 1/(3(\mu_a(\vec{r}) + \mu'_s(\vec{r})))$ is the diffusion coefficient with $\mu'_s(\vec{r})$ as the reduced scattering coefficient. Ω is the domain of the imaged object with $\partial \Omega$ as its boundary. A is a constant depending on the optical refractive-index mismatch on the boundary and \vec{n} denotes the outward normal of the boundary.

By discretizing the domain Ω to a tetrahedron finite element mesh, the FEM is used to solve the partial derivative equation. Then, Eq. (2) is transformed to a linear equation as follows:

$$KG = Q, \quad (3)$$

where K is the called stiff matrix in FEM, which is sparse positive definite and contains the contribution of tissue optical properties. Q is a vector corresponding to the source term. By solving Eq. (3), the vector G of light distribution values at finite-element nodes is obtained, which can be then used to interpolate the value at an arbitrary point inside Ω . Further details can be referred to in [23,24].

Generally, the imaged object is discretized to voxels for reconstruction. However, voxel representation suffers from the over-smooth effect, resulting in deteriorated image resolution. Instead of voxel representation, in this article, we represent the fluorescence targets by a summation of n ellipsoids with constant fluorescence intensity ρ , center positions (x_c, y_c, z_c) , anisotropic radius (r_x, r_y, r_z) , and Euler rotation angles (α, β, γ) ,

$$f(\vec{r}) = f(x, y, z) = \sum_{i=1}^n \rho_i U(1 - X_i^T R_i^T \Sigma_i R_i X_i), \quad (4)$$

where

$$X_i = \begin{bmatrix} x - x_{c,i} \\ y - y_{c,i} \\ z - z_{c,i} \end{bmatrix}, \quad \Sigma_i = \begin{bmatrix} 1/r_{x,i} & & \\ & 1/r_{y,i} & \\ & & 1/r_{z,i} \end{bmatrix},$$

$$R_i = R_{\alpha_i} R_{\beta_i} R_{\gamma_i},$$

with

$$R_{\alpha_i} = \begin{bmatrix} \cos \alpha_i & \sin \alpha_i & \\ -\sin \alpha_i & \cos \alpha_i & \\ & & 1 \end{bmatrix},$$

$$R_{\beta_i} = \begin{bmatrix} 1 & & \\ & \cos \beta_i & \sin \beta_i \\ & -\sin \beta_i & \cos \beta_i \end{bmatrix},$$

$$R_{\gamma_i} = \begin{bmatrix} \cos \gamma_i & \sin \gamma_i & \\ -\sin \gamma_i & \cos \gamma_i & \\ & & 1 \end{bmatrix}.$$

U is the unit step function. As many fluorescence targets including tumors are localized and small, the ellipsoid shape approximation is reasonable and a good choice.

In FMT reconstruction, the unknown fluorescence distribution is recovered by iteratively minimizing the difference between theoretical predictions and practical measurements. Then, for the unknown shape parameters ζ , the inverse reconstruction can be formulated as a least-squares minimization function as follows:

$$\arg \min_{\zeta} \Psi(\zeta) = \frac{1}{2} \|\Phi_{\text{born}}^{\text{meas}} - F(\zeta)\|_2^2,$$

s.t. 1) $\rho \geq 0$,

$$2) r^{\min} \leq r \leq r^{\max},$$

$$3) c_{xy}r_x \leq r_y \leq 1/c_{xy}r_x, c_{yz}r_y \leq r_z \leq 1/c_{yz}r_y,$$

$$c_{zx}r_z \leq r_x \leq 1/c_{zx}r_z,$$

$$4) x_c^{\min} \leq x_c \leq x_c^{\max}, y_c^{\min} \leq y_c \leq y_c^{\max}, z_c^{\min} \leq z_c \leq z_c^{\max},$$

$$5) -\pi/2 < \beta \leq \pi/2,$$

$$6) S_i \cap S_j = \emptyset, \quad \forall i, j, i \neq j, \quad (5)$$

where $\Phi_{\text{born}}^{\text{meas}}$ is the vector of the normalized born ratio. $F(\zeta)$ represents the predicted values $\Phi_{\text{born}}^{\text{cal}}$ at corresponding measurement points. To stabilize the reconstruction, six naturally chosen constraints are imposed in the above equation. Constraint (1) is the nonnegativity of the fluorescence intensity. Constraints (2) and (3) are for the anisotropic radius, with constraint (2) to reasonably restrict the radius range, and constraint (3) to avoid too-narrow shape. Constraint (4) represents the box restrictions for center positions, which is typically set as the geometrical size bound of the imaged object. For Euler angles, α and r are modulus to 2π , but β covers only π range. Hence, we apply angle constraints only on β as in constraint (5). The different targets are assumed to not overlap with each other, as described in constraint (6). This means the overlap volume of any two targets should be zero,

$$V_{\text{overlap}, i, j} = \int_{\Omega} [(f(\vec{r})_i / \rho_i + f(\vec{r})_j / \rho_j) > 1] = 0, \quad \forall i, j, i \neq j. \quad (6)$$

As most of the above constraints are applied directly on geometry sizes such as radius or width, we transform Eq. (6) into a similar form as follows:

$$r_{\text{overlap}, i, j} = \sqrt[1/3]{3V_{\text{overlap}, i, j} / (4\pi)} = 0, \quad \forall i, j, i \neq j, \quad (7)$$

where the geometry size of the overlap volume is obtained by simply assuming it as a sphere.

B. Two-Step Optimization

In this subsection, the proposed two-step optimization algorithm is described.

As described in Section 1, different types of shape parameters contribute differently to the measurement data, requiring distinct considerations in solving Eq. (5). As illustrated in Fig. 1, we sequentially estimate the different shape parameters in two steps. At first, fixing the given radius and setting the rotation angles to zero, we solve Eq. (5) to update target centers and fluorescence intensities. In this step, the initial targets are usually set as small spheres. After that, based on the obtained relatively

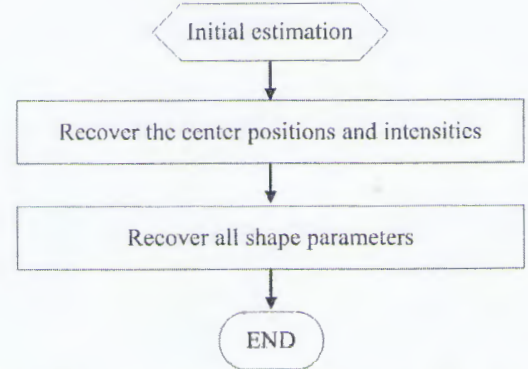


Fig. 1. Two-step optimization of ellipsoid-shape parameters.

good estimation, we recover all the shape parameters simultaneously in the second step.

In each step, we use the same optimization method described as follows. A typical way to minimize the nonlinear least-squares function Eq. (5) is a Newton-type method. The optimal is then found by iterations of local linearization and Taylor expansion around the current estimate,

$$\zeta^{k+1} = \zeta^k + \arg \min_{\delta\zeta} \frac{1}{2} \|J\delta\zeta - (\Phi_{\text{born}}^{\text{meas}} - F(\zeta^k))\|_2^2 + C(\zeta^k + \delta\zeta). \quad (8)$$

Here, $J = \partial F / \partial \zeta$ is the Jacobian matrix due to linearization, whose computation details are described in Section 2.C. $C(\zeta)$ is the penalty term due to the constraints $c(\zeta) \leq 0$ in Eq. (5). Different ways can be used to enforce the constraint term. Here, the popular exterior penalty-function method is chosen [20]. Then, Eq. (8) is transformed to minimization programs with an increasing sequence of penalty parameters t as $t \rightarrow \infty$,

$$\begin{aligned} \delta\zeta &= \arg \min_{\delta\zeta} L(\delta\zeta, t) \\ &= \frac{1}{2} \|J\delta\zeta - (\Phi_{\text{born}}^{\text{meas}} - F(\zeta^k))\|_2^2 \\ &\quad + t \sum_j \{\min[0, c_j(\zeta^k + \delta\zeta)]\}^2. \end{aligned} \quad (9)$$

In each t -sub problem, t is doubled and $\delta\zeta$ is updated via Newton's method as

$$\begin{aligned} (\delta\zeta)^{n+1} &= (\delta\zeta)^n + (J^T J + \nabla_{\delta\zeta}^2 C + \lambda \Lambda)^{-1} \\ &\quad \{-J^T [J\delta\zeta - (\Phi_{\text{born}}^{\text{meas}} - F(\zeta^k))] - \nabla_{\delta\zeta} C\} \\ t^{n+1} &= 2t^n, \end{aligned} \quad (10)$$

where $J^T J + \nabla_{\delta\zeta}^2 C$ is the Hessian matrix $\nabla_{\delta\zeta}^2 L$. The applied identity regularization matrix Λ with regularization parameter λ is for reducing the singularity of the Hessian matrix. Moreover, the conjugate-gradient method and golden line-search method

are used in Newton's method for effective update. In Eq. (10), contributions to $\nabla_{\delta\zeta}C$ and $\nabla_{\delta\zeta}^2C$ of constraints (1) through (5) can be analytically computed. For constraint (6), its contribution $\nabla_{\delta\zeta}C_6$ to $\nabla_{\delta\zeta}C$ can be computed using the perturbation method. Then, the contribution $\nabla_{\delta\zeta}^2C_6$ to Hessian matrix $\nabla_{\delta\zeta}^2C$ is approximated using a straightforward formula as

$$\nabla_{\delta\zeta}^2C_6 = (\nabla_{\delta\zeta}C_6)^T(\nabla_{\delta\zeta}C_6)/t. \quad (11)$$

C. GPU-Accelerated Operator

Now, we start to describe the details of the proposed GPU-accelerated operator for fast computing the Jacobian matrix J and the objective value $\Psi(\zeta)$. In addition, the operator also calculates the contributions to the gradient and the Hessian matrix due to the nonoverlap constraint.

As described in Eqs. (1) and (4), the predicted measurements are a complex integration over the whole domain. For computation, the integration should be mapped to a discretized domain. In this study, a uniform 3D voxel discretization with voxel volume ΔV is used. Then, $F(\zeta)$ is transformed as the summation over all n_V voxels,

$$F(\zeta)(\vec{r}_s, \vec{r}_d) = \sum_{i=1}^{n_V} G(\vec{r}_s, \vec{r}_i)G(\vec{r}_d, \vec{r}_i)/G(\vec{r}_s, \vec{r}_d)\Delta Vf(\vec{r}_i), \quad (12)$$

where $f(\vec{r}_i)$ is the mean fluorescence distribution inside the voxel i . In Eq. (12), $G(\vec{r}_d, \vec{r}_i)$ is used instead of $G(\vec{r}_i, \vec{r}_d)$, since the two terms are equal based on adjoint theory, but the former usually takes less computation time. For all M source-detector pairs, a matrix-vector product form can be generated from Eq. (12),

$$F(\zeta) = W \begin{bmatrix} f(\vec{r}_1) \\ \vdots \\ f(\vec{r}_{n_V}) \end{bmatrix}, \quad (13)$$

where W is the weight matrix with size $M \times n_V$. Then, the Jacobian matrix J can be expressed as follows:

$$J = \partial F(\zeta)/\partial \zeta = W \partial \begin{bmatrix} f(\vec{r}_1) \\ \vdots \\ f(\vec{r}_{n_V}) \end{bmatrix} / \partial \zeta. \quad (14)$$

Using perturbation method, $\partial f(\vec{r}_i)/\partial \zeta_j$ can be defined using a sufficiently small perturbation $\Delta \zeta_j$ as follows:

$$\partial f(\vec{r}_i)/\partial \zeta_j = \frac{\Delta f(\vec{r}_i)}{\Delta \zeta_j} = \frac{\Delta f(\vec{r}_i)(\zeta + \Delta \zeta_j) - \Delta f(\vec{r}_i)(\zeta)}{\Delta \zeta_j}. \quad (15)$$

From Eqs. (13)–(15), we can see that the computation of J and $F(\zeta)$ is composed of two basic operations, where one is shape-voxel mapping ($f(\vec{r}_i)$) and the other is a matrix multiplication. As the computation burden of the objective function value $\Psi(\zeta)$ mostly lies in $F(\zeta)$, the two basic operations of $F(\zeta)$ are also the key computation components for $\Psi(\zeta)$. We calculate $f(\vec{r}_i)$ by dividing the corresponding voxel to $16 \times 16 \times 16$ uniform subvoxels. Specific procedures including bounding box testing and two-stage discretization are added to speed the calculation. Although Fig. 2 is for GPU-accelerated computation, it can be used to illustrate the CPU implementation, except that all executions are performed sequentially on CPU.

However, further acceleration is urgently needed. Since shape-voxel mapping is frequently performed during the reconstruction, much time is spent on it. Meanwhile, much time is also spent on the matrix multiplication operation. On the whole, during the shape-parameters optimization, the two basic operations take more than 90% of the computation time, where the details can be referred to in Section 3.C.

In recent years, GPU-accelerated scientific computing has attracted more and more attention since the release of computer unified device architecture (CUDA) by NVIDIA in 2007 [25]. CUDA allows GPU programming with C languagelike interface for NVIDIA GPUs, thus easing the development of general-purpose applications compared to traditional GPU programming languages. Despite becoming easier in programming, note that good performance of the CUDA program still requires careful consideration of the GPU architecture. In the optical tomography field, CUDA GPU has already been successfully applied in Monte Carlo simulation [26–28], numerical forward model computation [29], etc.

In our desktop computer, an NVIDIA GTX480 graphics card was used to provide CUDA GPU computation capacity. The GTX 480 is one representative of the latest Fermi GPU architecture of NVIDIA. GTX 480 has 15 streaming multiprocessors (SMs), each with 32 scalar processors. In addition, each SM has up to 32 k register memory and 48 k shared memory for fast on-chip memory access. More details about the Fermi architecture can be referred to in [30].

Following is the acceleration of the two basic operations using the CUDA GPU computing technology. First, the matrix multiplication is easily accelerated using the CUDA CUBLAS library [31]. Second, analogous to the CPU implementation, a CUDA-based implementation of shape-voxel mapping is developed, as illustrated in Fig. 2. As an ellipsoid target is usually small compared to the whole domain, it does not overlap with many voxels. Moreover, since the data transfer between GPU SMs and the global GPU-device memory is relatively low [25,30], processing the many unoverlapped voxel-ellipsoid pairs using GPU will let the SMs wait for the low data transfer and work at low efficiency,

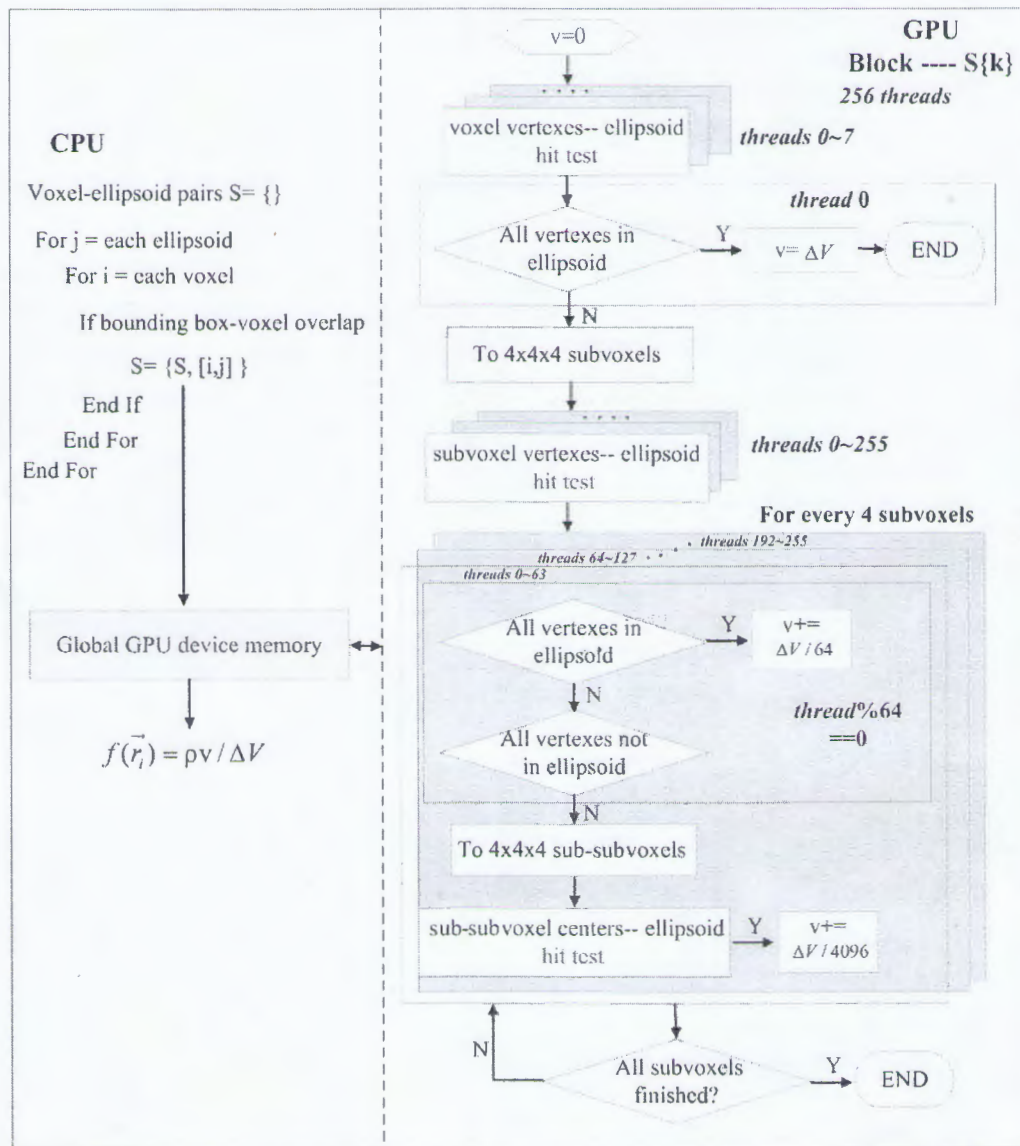


Fig. 2. (Color online) Flowchart of the GPU-accelerated computation of shape-voxel mapping. One GPU block deals with only one voxel-ellipsoid pair with 256 threads. Two levels of discretization are used for faster speed. For each subvoxel, 64 threads are formed in one group to process it.

limiting the speedup performance. Hence, a voxel-ellipsoid pairing procedure is performed using CPU at the beginning by judging whether the bounding box of an ellipsoid overlaps with a voxel, as shown in the left part of Fig. 2. Then, GPU is used to determine the concrete overlapped volume for each voxel-ellipsoid pair. Similarly to the CPU implementation, for speedup enhancement, this determination is implemented by iteratively discretizing the corresponding voxel to $16 \times 16 \times 16$ small volumes in two stages. That is, the corresponding voxel is divided to $4 \times 4 \times 4$ subvoxels in the first stage, and a subvoxel will be further discretized to $4 \times 4 \times 4$ sub-subvoxels in the second stage if it is partly overlapped with the corresponding ellipsoid. In the GPU parallel implementation, one GPU block (a set of threads executed on the

same SM) is used to process one voxel-ellipsoid pair, where the 256 threads inside the block execute the frequently performed point-in-ellipsoid tests parallelly. To avoid interference among threads, note that the overlapped volume obtained in each thread is added to different element of a shared memory array of size 256, rather than directly to the same variable.

D. Voxel-Based Reconstruction

In this article, we need to compare the performance of the proposed shape-based reconstruction and the traditional voxel-based reconstruction. Hence, we briefly describe the used voxel-based reconstruction method here. Voxel-based reconstruction is typically formulated as a least-squares problem as follows:

$$\xi = \arg \min_{\xi} \frac{1}{2} \|\Phi_{\text{born}}^{\text{meas}} - W\xi\|_2^2$$

s.t. $\xi \geq 0$, (16)

where ξ is the vector of the fluorescence intensities in 3D voxels, and W is the weight matrix as described in Eq. (13). Equation (16) is solved using the random-access algebraic reconstruction technique (R-ART) [32] with nonnegative constraints, which has been widely applied in FMT.

3. Numerical Simulation Experiments

In this section, we evaluate the performance and effectiveness of the proposed method through numerical simulation experiments.

As shown in Fig. 3, a cylinder model (6.0 cm height and 2.0 cm diameter) with optical properties $\mu_a = 0.3 \text{ cm}^{-1}$, $\mu_s = 10.0 \text{ cm}^{-1}$ was used. The optical properties adopted were close to the optical properties of the midtorso of mice, while the geometry sizes were close to the mean one during our previous *in vivo* experiments. A full-angle optical data-acquisition setup was adopted [33,34] for its better image resolution. Data were simulated for 18 projection angles evenly distributed over the full angle. In each projection angle, four projections were acquired sequentially, where the four excitation point sources were at 3 cm height slice and with 0.4 cm distance from each other. For each projection, the detectors were over a $1.8 \text{ cm} \times 2.2 \text{ cm}$ field of view with 0.15 cm spacing, as depicted in Fig. 3. The total number of source-detector pairs was 12,960. The measurements were simulated using the FEM, where the cylinder model was discretized into 8283 nodes and 42,903 tetrahedron elements. 5% of Gaussian noises were added to all the synthetic measurements. The adopted noise level was close to that in physical experiments.

During all the reconstructions, the same geometry constraints were applied with $r^{\min} = 0.04 \text{ cm}$, $r^{\max} = 0.50 \text{ cm}$, $c_{xy} = c_{yz} = c_{zx} = 1/3$, $x_c^{\min} = y_c^{\min} = -1.0 \text{ cm}$, $x_c^{\max} = y_c^{\max} = 1.0 \text{ cm}$, $z_c^{\min} = 2.0 \text{ cm}$, and $z_c^{\max} = 4.0 \text{ cm}$. The 3D voxels for Jacobian

matrix calculation were inside the cylinder model and over $(-1.0 \sim 1.0) \text{ cm} \times (-1.0 \sim 1.0) \text{ cm} \times (2.0 \sim 4.0) \text{ cm}$ with voxel size $0.07 \text{ cm} \times 0.07 \text{ cm} \times 0.07 \text{ cm}$. The total voxels number was 16,907. In the following subsection, the 3D voxels were also used in voxel-based reconstruction. 100 iterations [one update in Eq. (6) corresponding to one iteration] were performed in shape-based reconstructions. For two-step optimization, the two steps took 50 iterations, respectively. Similarly, for one-step optimization with sphere preparation, the initial sphere reconstruction took 50 iterations. All the reconstructions were performed on our desktop computer with Intel 2.8 GHz quad-core CPU, 16 GB RAM, and an NVIDIA GTX 480 graphics card.

A. Comparisons with Voxel-Based Reconstruction

We compared the proposed method and the traditional voxel-based reconstruction using two close inclusions with various shapes. The detailed parameters are summarized in Table 1. In voxel-based reconstruction, R-ART was performed with an iteration number of 200 and a relaxation parameter of 0.1.

As shown in Fig. 4, when using voxel-based reconstruction, the two inclusions couldn't be resolved in all test cases. In contrast, the proposed method demonstrated much better resolution ability, where the two inclusions were clearly separated. Moreover, from the shown slice images at 3.0 cm height, it is seen that the reconstructed shapes matched the original ones very well in orientation, size, location, and fluorescence intensity. Of course, recovering the geometry exactly the same is impossible in the existence of noises, even when the targets are ellipsoids. As summarized in Table 2, for all test cases, the center deviations were within 0.018 cm, and the relative errors of accumulated fluorescence intensity were within 5.78%. The small reconstruction errors can be further reduced as the noise level decreases. These results suggest that the proposed method can work well for various shapes, even though it is based on the ellipsoid-shape hypothesis.

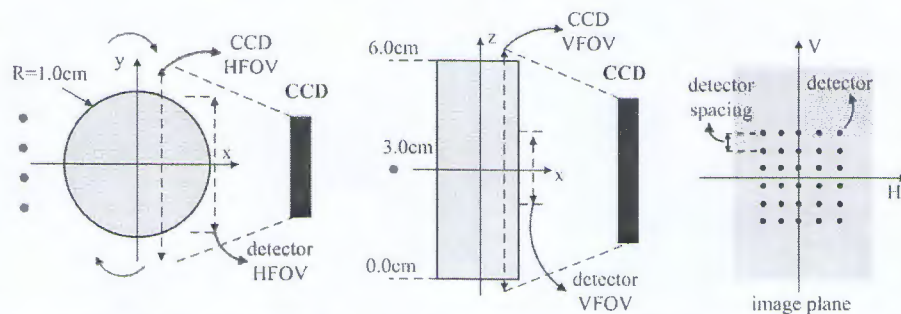


Fig. 3. (Color online) Simulation experiment sketch. A full-angle CCD camera-based imaging system is used for simulated data acquisition. The cylinder phantom object can be rotated to a different projection angle. A CCD camera with horizontal \times vertical field of view (CCD HFOV \times CCD VFOV) is used to capture excitation and fluorescence projection images at each projection angle. In the simulation, full-angle acquisitions were performed at 18 evenly distributed projection angles. For each projection angle, four projections were simulated with excitation source at different positions, as depicted by the red dots (in the left and middle parts). For each projection, the detectors, corresponding to selected detection points on the image plane, are within 1.8 cm detector horizontal FOV and 2.2 cm detector vertical FOV with 0.15 cm detector spacing.

Table 1. Parameters for Inclusions with Various Shapes for Cube or Cuboid Shapes, the Anisotropic Radii are Half its Edge Lengths, Respectively

Shape	(r_x, r_y, r_z)	(x_c, y_c, z_c)	(α, β, γ)	ρ	Accumulated Fluorescence Intensity
Ellipsoid	(0.25 0.15 0.15)	(0.00 0.225 3.00)	($\pi/4$, 0.00, 0.00)	1.00	0.0236
	(0.25 0.15 0.15)	(0.00 -0.225 3.00)	($\pi/4$, 0.00, 0.00)	1.00	0.0236
Cube	(0.15 0.15 0.15)	(0.00 0.25 3.00)	(0.00, 0.00, 0.00)	1.00	0.0270
	(0.15 0.15 0.15)	(0.00 -0.25 3.00)	(0.00, 0.00, 0.00)	1.00	0.0270
Cuboid	(0.25 0.15 0.15)	(0.00 0.20 3.00)	(0.00, 0.00, 0.00)	1.00	0.0450
	(0.25 0.15 0.15)	(0.00 -0.20 3.00)	(0.00, 0.00, 0.00)	1.00	0.0450

B. Robustness to Different Initial Values

We evaluated the robustness of the proposed method to different initial values. The test case of dual ellipsoid inclusions in the previous subsection was used.

At first, we compared the two-step optimization strategy with one-step optimization with or without sphere initialization. The target number was assumed the same as the actual one. Note that the second step of the two-step optimization is in fact a one-step optimization, except that a good initial has already been provided by the first step. In other words, both the one-step and two-step methods will get similar solutions given a good initial value. Therefore, in the comparisons, we are more interested in the performance of these methods given different degrees of bad initial values. Considering this, four representative initial estimates were chosen, where they were set as dual spheres at different positions, as summarized in Table 3. The initial estimates 1 were seen as a good initial, since their locations and intensities were both close to the real

ones. In contrast, the other three initial estimates were worse. In particular, the initial estimates 3 and 4 were far away from the real ones, with their centers at a different height slice. It is seen that the bad degree of initial estimates 1–3 increased by increasing the center distances between initial estimates and true targets. Initial estimates 4 were chosen by only greatly increasing the radii of initial estimates 3. Then, we could observe the sensitivity of the two-step method to the different initial sphere radii used. As shown in Fig. 5, for initial estimates 1, both the one-step and the two-step optimizations achieved successful reconstructions, with the two targets clearly resolved. However, for other initials not that good, the one-step optimization cannot separate the targets. In contrast, using the two-step optimization, nearly the same reconstruction results were obtained for the different degrees of bad initial values. When the one-step optimization algorithm with sphere preparation was run, it did a relatively better job than that without sphere preparation for

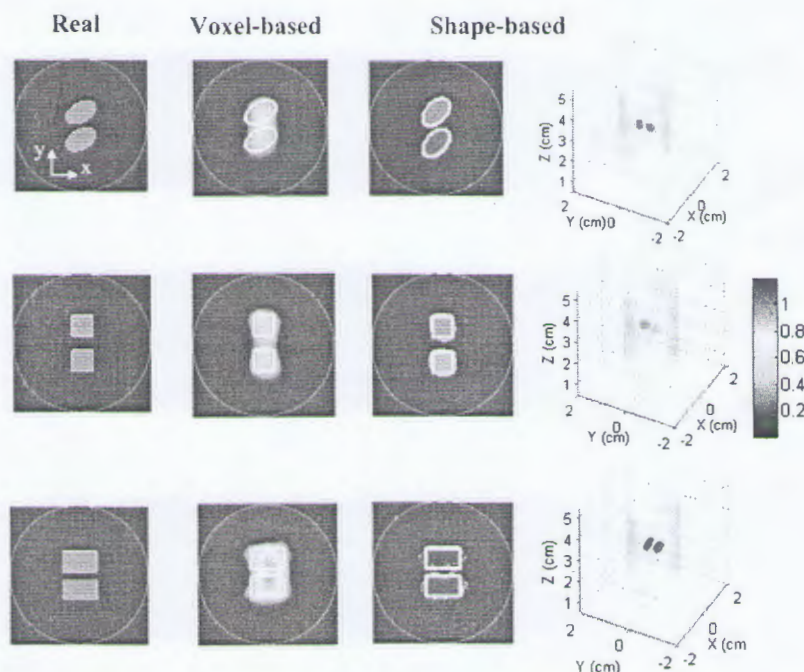


Fig. 4. (Color online) Comparison results between the proposed method and voxel-based reconstruction. In slice images, the red circles denote the outer boundary of the imaged object, and the white lines denote the boundaries of the real inclusions. The slice images are of 3.0 cm height.

Table 2. Reconstructed Parameters for Inclusions with Various Shapes

Shape	(r_x, r_y, r_z)	(x_c, y_c, z_c)	(α, β, γ)	ρ	Accumulated Fluorescence Intensity
Ellipsoid	(0.247 0.138 0.150)	(-0.002 0.240 3.00)	(0.367 0.200 0.253)	1.033	0.0221
	(0.254 0.150 0.140)	(0.001 -0.210 3.00)	(0.450 -0.210 0.139)	1.127	0.0250
Cube	(0.176 0.186 0.206)	(0.00 0.246 3.00)	(0.228 -1.26 0.415)	0.986	0.0278
	(0.205 0.183 0.192)	(-0.003 -0.252 3.00)	(-0.612 0.529 -0.118)	0.902	0.0272
Cuboid	(0.336 0.121 0.213)	(-0.007 0.216 3.00)	(-0.643 -0.077 0.690)	1.201	0.0434
	(0.325 0.171 0.175)	(0.007 0.193 3.00)	(0.241 -0.263 -0.093)	1.167	0.0476

initial values 2, but the obtained fluorescence contrasts were still slightly worse than those of two-step optimization. Moreover, it got stuck in a local minimum for other worse initial values, with the two targets merged. Overall, the results demonstrate that the proposed two-step optimization is robust to initial values, and its performance are much better than the one-step optimization with or without sphere preparation. The results also verify that the distinct consideration in different shape parameters is essential for shape-based reconstruction.

Since the actual target number is usually uncertain in some practical applications, we evaluated the performance of the proposed method in these circumstances. The initial estimates were set as some small separated spheres with 0.15 cm radii, as shown in the first column of Fig. 6. As shown in the third column of Fig. 6, when the assumed targets were more, the proposed method could also distinguish the real targets successfully, yet some quality degradation was also observed in the images. Since the false targets were usually reconstructed with ultra-low intensity and small volume, the determination of the actual target number would be possible through the following approach. First, reconstructions with more assumed targets are performed. Then, we can determine the actual number by excluding the false targets that contribute little to boundary measurements.

As shown in the middle column of Fig. 6, the reconstructed targets may overlap if no constraints were applied. It is interesting that the combination of the overlapped targets was close to the actual targets. This means that if we do not mind the overlap, this solution also seems acceptable. Note that the role of geometrical constraints is not limited to the demonstrated. In fact, it also plays an important role in stabilizing the shape reconstruction for more complex conditions, such as a higher level of modeling

error and data noises, or more complex fluorescence target distribution.

C. GPU Acceleration

The ability of the GPU-accelerated operator was evaluated on our personal desktop computer with one NVIDIA GTX 480 card. Spherical targets were used in most of this investigation for simplicity. GPU acceleration was implemented in different parts of the proposed method, including calculation of the Jacobian matrix, the predicated measurements, and part of the constraints. Herein, we selected the Jacobian matrix as an example.

As described in Section 2.C, the GPU acceleration of Jacobian matrix calculation is composed of two operations, including shape-voxel mapping and matrix multiplication. As shown in Fig. 7(a), the CPU computation time for shape-voxel mapping depended on target number and target size. Corresponding to Fig. 7(a), the effect of GPU acceleration of shape-voxel mapping was shown in Fig. 7(b). The speedup times varied from about 10 to 40, where the CPU computation times of 0.059–1.55 s were reduced from 0.0062 to 0.0412 s, respectively. The trend was that larger size and more targets corresponded to more acceleration. The reason is that a more efficient pipeline of GPU SMs can be generated, since larger size and more targets corresponded to more voxel-ellipsoid pairs. As shown in Fig. 7(c), the CPU computation time of matrix multiplication varied for target number. It is interesting that for even target number, the computation time was smaller than that for the previous odd target number. The phenomenon was caused by the concrete implementation of the matrix multiplication in MATLAB. Overall, GPU speedup range from 31× to 60× was achieved for this operation, as shown in Fig. 7(d). Figure 7(e) plotted the total acceleration of Jacobian matrix calculation for different cases, demonstrating speedup from 26.8× to 51×.

In Fig. 7(f), the total speedup of the optimization process was also provided to show the overall GPU acceleration capacity. The test case of dual ellipsoid inclusions in Section 3.A was used, and two targets were assumed in the reconstruction. With GPU acceleration, a speedup of 13.6× was achieved, reducing the total computation time from around 612 to 45 s. Since only some parts of the optimization codes were accelerated, the total effect of speedup wasn't as large as that in Fig. 7(e).

Table 3. Initial Estimates of Dual Small Spheres

Estimates	r	(x_c, y_c, z_c)	ρ
1	0.15	(0.00 0.40 3.00)	3.00
	0.15	(0.00 -0.40 3.00)	3.00
2	0.15	(0.40 0.00 3.00)	3.00
	0.15	(-0.40 0.00 3.00)	3.00
3	0.15	(0.40 0.00 3.50)	3.00
	0.15	(-0.40 0.00 3.50)	3.00
4	0.35	(0.40 0.00 3.50)	3.00
	0.35	(-0.40 0.00 3.50)	3.00

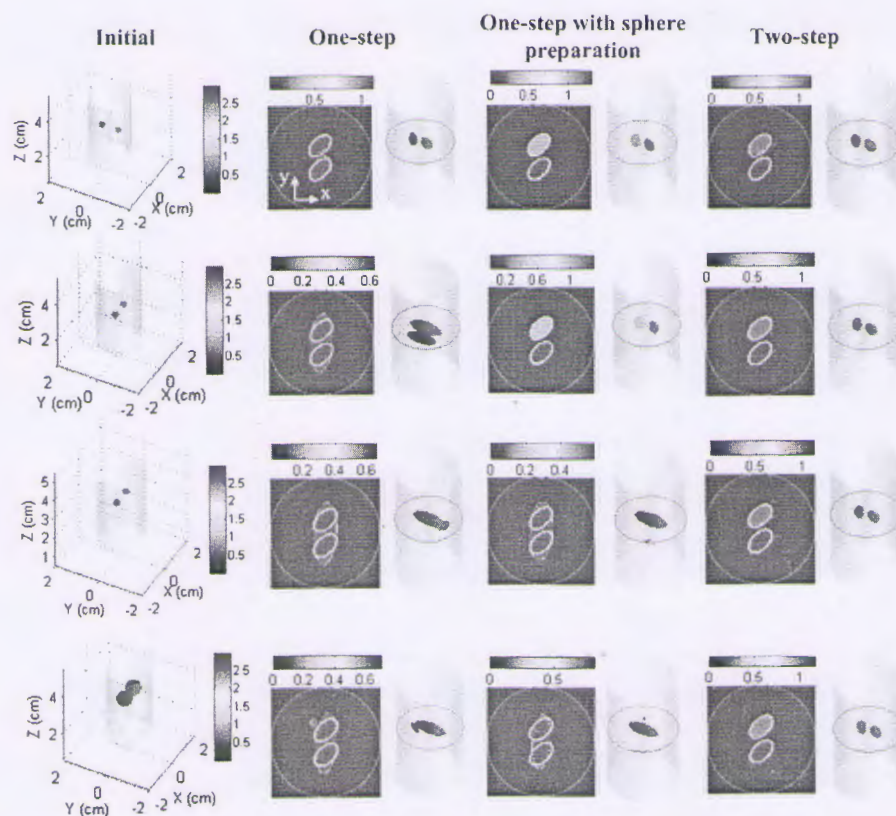


Fig. 5. (Color online) Reconstruction results with different initial estimates of dual small spheres. In slice images, the red circle denotes the boundary of the imaged object, and the white lines denote the boundaries of the real inclusions. The slice images are of 3.0 cm height.

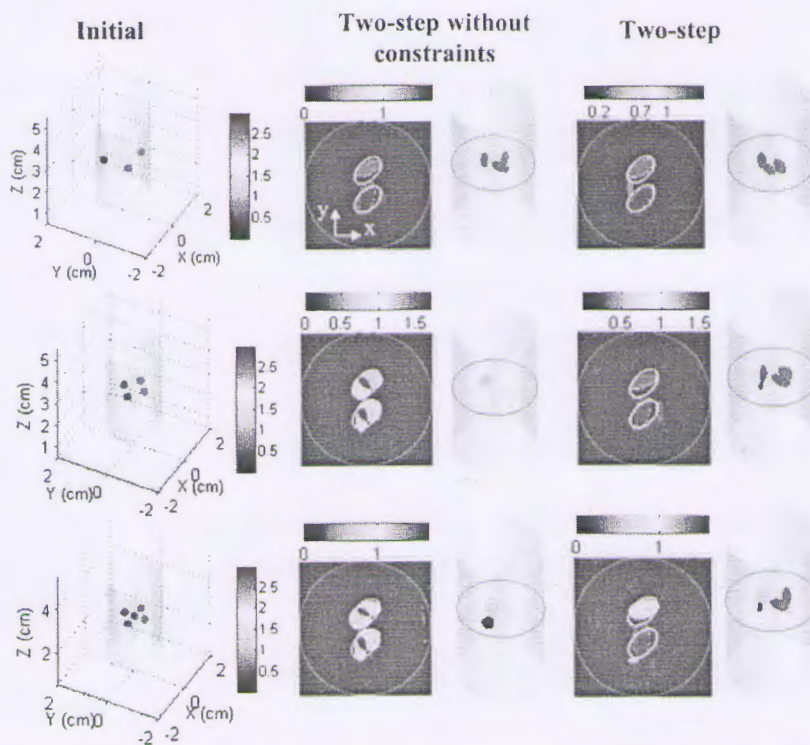


Fig. 6. (Color online) Reconstruction results with the assumed target number larger than two. In slice images, the red circle denotes the boundary of the imaged object, and the white lines denote the boundaries of the real inclusions. The slice images are of 3.0 cm height.

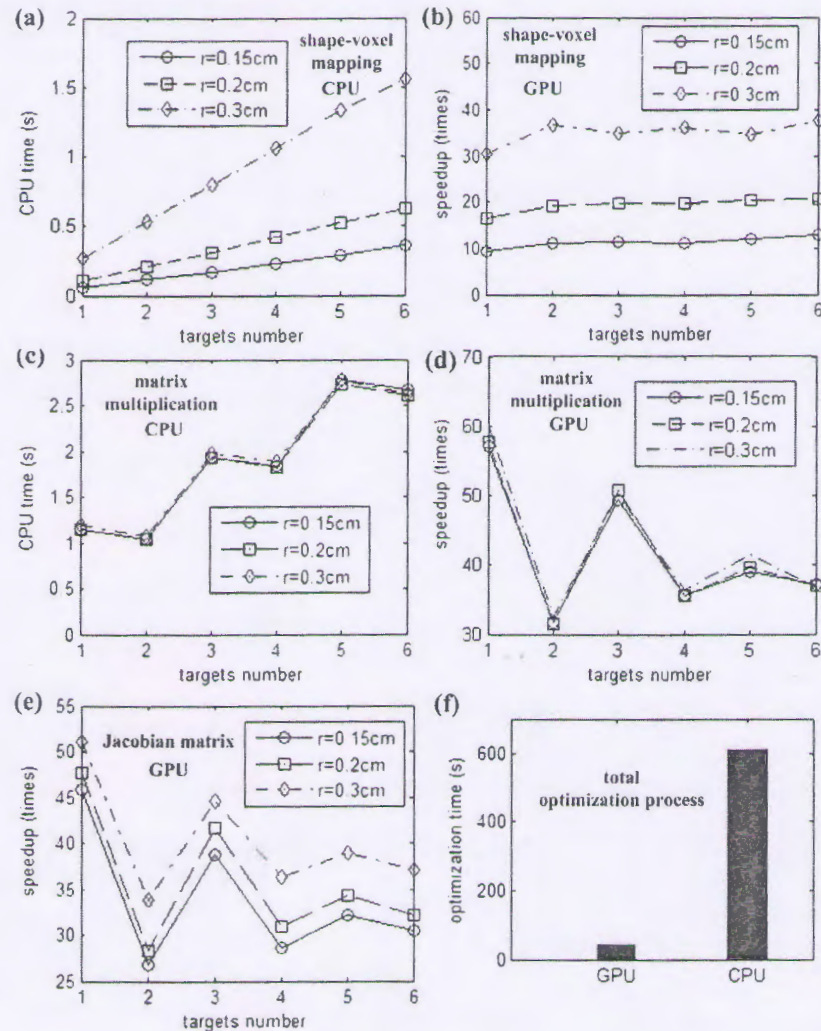


Fig. 7. (Color online) Evaluation of GPU acceleration. The investigated targets were spheres for simplicity. (a)–(e) CPU and GPU computation of Jacobian matrix for different cases. The Jacobian matrix calculation is composed of two basic operations including shape-voxel mapping and matrix multiplication. (a) CPU execution time of shape-voxel mapping operation. (b) GPU speedup of shape-voxel mapping operation. (c) CPU execution time of matrix multiplication operation. (d) GPU speedup of matrix multiplication operation. (e) GPU speedup of whole Jacobian matrix computation. (f) GPU speedup of the total optimization process.

4. Physical Phantom Experiment

A physical phantom experiment was performed to evaluate the reliability of the proposed method in practical applications. The phantom was made of a glass cylinder (inner diameter 2.43 cm and outer diameter 2.83 cm) filled with 1% intralipid ($\mu'_s = 10\text{ cm}^{-1}$, $\mu_a = 0.02\text{ cm}^{-1}$). Two transparent glass tubes (0.3 cm inner diameter and 0.5 cm outer diameter) were filled with 40 μL Indocyanine green (ICG) with a concentration of 4 $\mu\text{mol/L}$, producing two small fluorescence inclusions of 0.5 cm length. The two inclusions were immersed inside the phantom close to each other with 0.16 cm edge-to-edge distance.

As shown in Fig. 8(a), the phantom was placed on a rotation stage for full angle imaging. On one side, a small laser spot at 785 nm wavelength and 16 mW power was focused on the back surface of the imaged object as the excitation light source. On the opposite

side, a 2560×2160 pixels, 16 bit, -30°C cooled Andor Neo sCMOS camera (Andor, Belfast, Northern Ireland, UK) was placed with a Nikkor 60 mm $f/2.8D$ lens (Nikon, Melville, New York). The CCD field of view was $8.28\text{ cm} \times 9.82\text{ cm}$. For excitation and fluorescence image collection, a neutral density filter of 1% transmittance (Daheng, Beijing, China) and a $840 \pm 18.5\text{ nm}$ band-pass fluorescence filter (Semrock, Rochester, New York) were placed in front of the lens, respectively. These images were collected at 36 projection angles evenly distributed over 360° . In each projection angle, five excitation positions along horizontal direction with 0.2 cm distance were scanned, corresponding to five projection images. Before FMT reconstruction, the phantom 3D surface must be obtained at first, which could be recovered from silhouettes at different projection angles [35]. To extract the silhouettes, 72 white-light images

were captured evenly over full angle. When collecting white-light images, the excitation light was switched off, a table lamp was set on to generate white ambient lighting, and the neutral density filter was still used to protect the CCD camera.

With dense CCD pixels, we have high-density sampling of the image plane, resulting in a huge number of detected signals. In FMT reconstruction, oversampling does not improve the reconstruction quality but results in more computation burden [36], and weak signals with low signal-to-noise ratio usually contribute little or even negative to the solution. Based on these considerations, for each projection image, we selected detection points over a $2.0\text{ cm} \times 2.2\text{ cm}$ field of view with 0.2 cm spacing (detailed illustration is similar to that in Fig. 3) for reconstruction. The 3D voxel used was over $1.5\text{ cm} \times 1.5\text{ cm} \times 2.2\text{ cm}$ 3D regions with 0.1 cm mesh spacing, and only the mesh inside the object was considered. For voxel-based reconstruction, 50 R-ART iterations and relaxation parameter of 0.05 were used. For shape-based reconstruction, geometry constraints were applied with $r^{\min} = 0.04\text{ cm}$, $r^{\max} = 0.50\text{ cm}$, $c_{xy} = c_{yz} = c_{zx} = 1/2$, $x_c^{\min} = y_c^{\min} = -1.5\text{ cm}$, $x_c^{\max} = y_c^{\max} = 1.5\text{ cm}$, $z_c^{\min} = 2.0\text{ cm}$, and $z_c^{\max} = 4.6\text{ cm}$, and 100 iterations were performed to update the shape parameters.

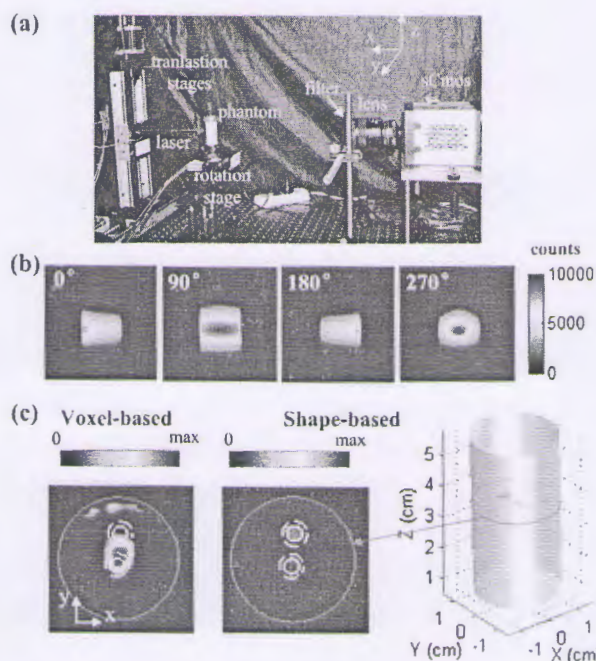


Fig. 8. (Color online) Physical phantom experiment. Two fluorescence inclusions were closed placed inside a cylinder phantom with 0.16 cm edge-to-edge distance. (a) Full-angle fluorescence molecular system. (b) Fluorescence projection images. (c) Reconstructed images. In slice images, the red circle denotes the boundary of the imaged object, and the white circles denote the inner (solid line) and outer (dashed line) boundaries of the real inclusions. The two slice images are at the same height slice, as depicted by the red circle in the 3D image. The images are shown with intensity range from 0 to their maximum, respectively.

From the shown fluorescence projection images at different angles of one excitation position in Fig. 8(b), we can see the high level of light diffusion. As shown in Fig. 8(c), the reconstructed targets of the two inclusions were merged in voxel-based reconstruction. In addition, artifacts also existed near the object boundary. In contrast, the two close inclusions were clearly separated with the proposed method. The targets locations were close to the real ones, with small center deviations of $0.045\text{--}0.075\text{ cm}$, respectively. The relative difference between the accumulated fluorescence intensities of the two targets was 22.5%. This difference was partly caused by measurement noises, the model error of the void and transparent regions of the glass tubes [37], and some extent of cross-talk between the two close inclusions. Overall, results demonstrate that the proposed method has better resolve ability than the traditional voxel-based reconstruction.

5. Discussions and Conclusions

In this article, we have proposed a GPU-accelerated two-step algorithm with ellipsoid shape parameterization for FMT. The inverse problem is formulated as a nonlinear least-squares problem. For robust reconstruction, a two-step optimization algorithm is proposed, where only the centers and intensities are first recovered to find a relatively good estimation for the successive reconstruction of all shape parameters. Reasonable geometrical constraints are also enforced via the exterior penalty-function method for further stability and accuracy. For computation speedup, a fast GPU-accelerated operator is proposed as finite-element-method-based calculation of the objective function value and the Jacobian matrix. Both numerical and physical phantom experiments demonstrate the effectiveness of the proposed method.

The proposed method demonstrates better resolve ability for dual inclusions of various shapes than the conventional voxel-based reconstruction in both numerical simulations and the physical phantom experiment. The advantage is due to the reduction in the dimension of the inverse problem. Although the unknowns are greatly reduced, particular care should also be taken in the shape-based reconstruction. As demonstrated in the simulation experiments, the targets may not be separated without good initial estimates, if a simple one-step optimization is used. In contrast, with the proposed two-step optimization algorithm, more reliable and robust reconstructions are achieved.

In some applications, the actual targets number may not be known *a priori*. The proposed method still works when assuming relatively more targets, although some extent of image-quality deterioration may be caused. Moreover, at this time, the actual targets number may be determined by excluding the false targets that contribute little to boundary measurements.

The GPU-accelerated operator greatly speeds up the shape-based reconstruction. Since the relationship between the shape parameters and the boundary measurements is highly nonlinear, the shape-based reconstruction speed is relatively low when executed only on CPU. With the GPU-accelerated operator, the Jacobian matrix computation is speedup several tenfold, where the concrete value depends on the target size and number. With the acceleration, the demonstrated total optimization time was reduced from around 10 min to less than 1 min by using an NVIDIA GTX-480 graphics card. The time of the one-time computed weight matrix was not included in the mentioned total optimization time above, which was around 54 s and included finite element meshing, stiff matrix forming, Green's functions solving, and weight matrix assembling. GPU acceleration of this part is feasible [29], but is not the main scope of this article.

In this study, we have shown that the proposed method works with experimental measurements. In our further work, we will apply it to preclinical applications. Moreover, although the ellipsoid shape approximation is suitable for many practical applications and provides much valuable information, more complex shape parameterization such as spherical harmonics may better model large irregular targets. Similar to this study, particular consideration in optimization procedure may be needed, which will be investigated in our forthcoming work.

The work was supported by the State Key Laboratory of Software Development Environment (No. SKLSDE-2011ZX-12), the National Natural Science Foundation of China (Nos. 61108084 and 81101123), the Research Fund for the Doctoral Program of Higher Education of China (No. 20111102120039), the Key Laboratory for Biomechanics and Mechanobiology of Ministry of Education, and the National Science and Technology Support Program (No. 2011AA02A104).

References

1. E. E. Graves, J. Ripoll, R. Weissleder, and V. Ntziachristos, "A sub-millimeter resolution fluorescence molecular imaging system for small animal imaging," *Med. Phys.* **30**, 901–911 (2003).
2. F. Leblond, S. C. Davis, P. A. Valdés, and B. W. Pogue, "Pre-clinical whole-body fluorescence imaging: review of instruments, methods, and applications," *J. Photochem. Photobiol. B* **98**, 77–94 (2010).
3. Y. Lin, H. Yan, O. Nalcioglu, and G. Gulsen, "Quantitative fluorescence tomography with functional and structural a priori information," *Appl. Opt.* **48**, 1328–1336 (2009).
4. S. C. Davis, H. Dehghani, J. Wang, S. Jiang, B. W. Pogue, and K. D. Paulsen, "Image-guided diffuse optical fluorescence tomography implemented with Laplacian-type regularization," *Opt. Express* **15**, 4066–4082 (2007).
5. D. Hyde, E. L. Miller, D. H. Brooks, and V. Ntziachristos, "Data specific spatially varying regularization for multi-modal fluorescence molecular tomography," *IEEE Trans. Med. Imaging* **29**, 365–374 (2010).
6. M. Li, X. Cao, F. Liu, B. Zhang, J. Luo, and J. Bai, "Reconstruction of fluorescence molecular tomography using a neighborhood regularization," *IEEE Trans. Biomed. Eng.* **59**, 1799–1803 (2012).
7. J. Dutta, S. Ahn, C. Li, S. R. Cherry, and R. M. Leahy, "Joint L1 and total variation regularization for fluorescence molecular tomography," *Phys. Med. Biol.* **57**, 1459–1476 (2012).
8. P. Mohajerani, A. A. Eftekhari, J. Huang, and A. Adibi, "Optimal sparse solution for fluorescent diffuse optical tomography: theory and phantom experimental results," *Appl. Opt.* **46**, 1679–1685 (2007).
9. D. Han, J. Tian, S. Zhu, J. Feng, C. Qin, B. Zhang, and X. Yang, "A fast reconstruction algorithm for fluorescence molecular tomography with sparsity regularization," *Opt. Express* **18**, 8630–8646 (2010).
10. M. Schweiger, S. R. Arridge, O. Dorn, A. Zacharopoulos, and V. Kolehmainen, "Reconstructing absorption and diffusion shape profiles in optical tomography using a level set technique," *Opt. Lett.* **31**, 471–473 (2006).
11. M. Schweiger, O. Dorn, A. Zacharopoulos, I. Nissila, and S. R. Arridge, "3D level set reconstruction of model and experimental data in diffuse optical tomography," *Opt. Express* **18**, 150–164 (2010).
12. K. Liu, X. Yang, D. Liu, C. Qin, J. Liu, Z. Chang, M. Xu, and J. Tian, "Spectrally resolved three-dimensional bioluminescence tomography with a level-set strategy," *J. Opt. Soc. Am. A* **27**, 1413–1423 (2010).
13. D. Álvarez, P. Medina, and M. Moscoso, "Fluorescence lifetime imaging from time resolved measurements using a shape-based approach," *Opt. Express* **17**, 8843–8855 (2009).
14. M. E. Kilmer, E. L. Miller, A. Barbaro, and D. Boas, "Three-dimensional shape-based imaging of absorption perturbation for diffuse optical tomography," *Appl. Opt.* **42**, 3129–3144 (2003).
15. A. Zacharopoulos, M. Schweiger, V. Kolehmainen, and S. Arridge, "3D shape based reconstruction of experimental data in diffuse optical tomography," *Opt. Express* **17**, 18940–18956 (2009).
16. G. Boverman, E. L. Miller, D. H. Brooks, D. Isaacson, Q. Fang, and D. A. Boas, "Estimation and statistical bounds for three-dimensional polar shapes in diffuse optical tomography," *IEEE Trans. Med. Imaging* **27**, 752–765 (2008).
17. S. Wang and A. P. Dhawan, "Shape-based multi-spectral optical image reconstruction through genetic algorithm based optimization," *Comput. Med. Imaging Graph.* **32**, 429–441 (2008).
18. S. Babaeizadeh and D. H. Brooks, "Electrical impedance tomography for piecewise constant domains using boundary element shape-based inverse solutions," *IEEE Trans. Med. Imaging* **26**, 637–647 (2007).
19. A. D. Zacharopoulos, S. R. Arridge, O. Dorn, V. Kolehmainen, and J. Sikora, "Three-dimensional reconstruction of shape and piecewise constant region values for optical tomography using spherical harmonic parametrization and a boundary element method," *Inverse Problems* **22**, 1509–1532 (2006).
20. P. Venkataraman, *Applied Optimization with Matlab Programming* (Wiley, 2002).
21. H. Gao, H. Zhao, W. Cong, and G. Wang, "Bioluminescence tomography with Gaussian prior," *Biomed. Opt. Express* **1**, 1259–1277 (2010).
22. A. Soubret, J. Ripoll, and V. Ntziachristos, "Accuracy of fluorescent tomography in the presence of heterogeneities: study of the normalized born ratio," *IEEE Trans. Med. Imag.* **24**, 1377–1386 (2005).
23. X. Song, D. Wang, N. Chen, J. Bai, and H. Wang, "Reconstruction for free-space fluorescence tomography using a novel hybrid adaptive finite element algorithm," *Opt. Express* **15**, 18300–18317 (2007).
24. M. Schweiger, S. R. Arridge, M. Hiraoka, and D. T. Delpy, "The finite element method for the propagation of light in scattering media: boundary and source conditions," *Med. Phys.* **22**, 1779–1792 (1995).
25. NVIDIA Corporation, *NVIDIA CUDA C Programming Guide 4.0* (2011).
26. Q. Fang and D. A. Boas, "Monte Carlo simulation of photon migration in 3D turbid media accelerated by graphics processing units," *Opt. Express* **17**, 20178–20190 (2009).

27. E. Alerstam, W. C. Y. Lo, T. D. Han, J. Rose, S. Andersson-Engels, and L. Lilge, "Next-generation acceleration and code optimization for light transport in turbid media using GPUs," *Biomed. Opt. Express* **1**, 658–675 (2010).
28. A. Sassaroli, "Fast perturbation Monte Carlo method for photon migration in heterogeneous turbid media," *Opt. Lett.* **36**, 2095–2097 (2011).
29. B. Zhang, X. Yang, F. Yang, C. Qin, D. Han, X. Ma, K. Liu, and J. Tian, "The CUBLAS and CULA based GPU acceleration of adaptive finite element framework for bioluminescence tomography," *Opt. Express* **18**, 20201–20214 (2010).
30. NVIDIA Corporation, NVIDIA's Next Generation CUDA Compute Architecture: Fermi (2010).
31. NVIDIA Corporation, CUDA Toolkit 4.0 CUBLAS Library (2011).
32. A. Kak and M. Slaney, *Computerized Tomographic Imaging* (IEEE, 1987).
33. N. Deliolanis, T. Lasser, D. Hyde, A. Soubret, J. Ripoll, and V. Ntziachristos, "Free-space fluorescence molecular tomography utilizing 360° geometry projections," *Opt. Lett.* **32**, 382–384 (2007).
34. D. Wang, X. Liu, F. Liu, and J. Bai, "Full-angle fluorescence diffuse optical tomography with spatially coded parallel excitation," *IEEE Trans. Inf. Technol. Biomed.* **14**, 1346–1354 (2010).
35. D. Wang, X. Liu, Y. Chen, and J. Bai, "In-vivo fluorescence molecular tomography based on optimal small animal surface reconstruction," *Chin. Opt. Lett.* **8**, 82–85 (2010).
36. T. Lasser and V. Ntziachristos, "Optimization of 360° projection fluorescence molecular tomography," *Medical Image Anal.* **11**, 389–399 (2007).
37. H. Dehghani, S. R. Arridge, M. Schweiger, and D. T. Depledge, "Optical tomography in the presence of void regions," *J. Opt. Soc. Am. A* **17**, 1659–1670 (2000).

Full-Angle Fluorescence Diffuse Optical Tomography With Spatially Coded Parallel Excitation

Daifa Wang, Xin Liu, Fei Liu, and Jing Bai, *Fellow, IEEE*

Abstract—Challenges remain in imaging fast biological activities through whole small animal using fluorescence diffuse optical tomography (FDOT). In this study, a novel full-angle FDOT with spatially coded parallel excitation (SC-FDOT) is proposed, which provides much better image qualities than our previous FDOT with multiple-points illumination (MP-FDOT) while maintaining comparable temporal resolution. Singular-value analysis and numerical simulations are used to obtain the key experimental parameters including the optimal point sources number and the optimal projections number, and to compare the performances of SC-FDOT, MP-FDOT and the conventional FDOT with single-point illumination. Results demonstrate that SC-FDOT has the best spatial-temporal performances in imaging fast biological activities through whole body. Physical phantom experiments are performed to evaluate the spatial performance of SC-FDOT in practical experimental applications. Utilizing the proposed system, a nude mouse implanted with a small fluorescent inclusion is also imaged. The preliminary result demonstrates the feasibility of SC-FDOT in *in vivo* applications.

Index Terms—Diffusion equations, finite-element methods, fluorescence, optical tomography.

I. INTRODUCTION

OPTICAL tomography using near-infrared light provides a quantitative way to three-dimensionally visualize tissue function in small animals or human organs [1]–[4] at physiological, metabolic, or molecular level. Fluorescence diffuse optical tomography (FDOT) is one of the optical tomography methods, which is mainly referred to small animal imaging in this paper. In FDOT, fluorescent agents are used to label the object of interest, such as cells, proteins, and drug molecules. Then, by

mathematically modeling the light transportation in diffuse tissues, the 3-D distribution of fluorescent agents inside live small animal is reconstructed from different fluorescence projections.

In past years, FDOT systems have evolved from those [5], [6] using optical fibers and matching fluids to those operating in free-space geometries with limited-/full-angle projections [7]–[11]. With these progresses in imaging systems, mathematical models [12]–[14], and fluorescent agents [15], FDOT have been applied in basic research [16]–[19].

Despite these advances, challenges still remain in imaging fast biological activities through whole body, such as pharmacokinetics, where good whole-body image quality and short data-acquisition time should be considered simultaneously. A slab-geometry-based imaging system with limited projection angles and matching fluid was developed for real-time whole-body imaging [20], where the switching time between continuous-wave point sources was decreased using galvanometer-controlled mirrors and the data-acquisition rate was increased using a high-frame-rate electron-multiplying charge-coupled device (EMCCD). Modern FDOT systems typically operate in free-space geometries with full-angle projections and avoid the use of matching fluid [9]. These modern systems are expected to yield significant improvements in image quality compared to matching fluid or fixed-geometry-based systems [11]. Here, we call these reported full-angle FDOT systems as P-FDOT for simplification with symbol P indicating single-point illumination. However, scanning along axial direction is needed in P-FDOT to provide whole-body imaging ability, which near linearly increases the data-acquisition time and limits the application of P-FDOT in imaging fast biological activities. In our earlier study [21], we have proposed and analyzed a kind of full-angle FDOT systems with beam-forming illumination (BF-FDOT). The BF-FDOT systems utilize the advantages of full-angle projections and provide whole-body imaging without scanning along axial direction. These BF-FDOT systems provide the potential in real-time whole-body imaging.

The main strategy of BF-FDOT is using parallel excitation (illumination) instead of the conventional single-point excitation in full-angle imaging systems. However, some tradeoff in spatial resolution along axial direction exists in BF-FDOT system to offer a significant reduction in data-acquisition time. The spatial resolution degradation is caused by no variation in excitation modes along axial direction. A novel full-angle FDOT system with spatially coded parallel excitation (SC-FDOT) is proposed in this paper. With the novel spatially coded parallel excitation strategy, SC-FDOT will provide more varied parallel

Manuscript received January 12, 2010; revised June 28, 2010; accepted September 5, 2010. Date of publication September 20, 2010; date of current version November 5, 2010. This work was supported by the National Natural Science Foundation of China under Grant 30670577, Grant 60831003, Grant 30930092, and Grant 30872633; by the Tsinghua-Yue-Yuen Medical Science Foundation; by the National Basic Research Program of China (973) under Grant 2006CB705700; and by the National High-Tech Research and Development Program of China (863) under Grant 2006AA020803.

D. Wang was with the Department of Biomedical Engineering, School of Medicine, Tsinghua University, Beijing 100084, China. He is now with the School of Biological Science and Medical Engineering, Beihang University, Beijing 100191, China (e-mail: daifa.wang@buaa.edu.cn).

X. Liu, F. Liu, and J. Bai (corresponding author) are with the Department of Biomedical Engineering, School of Medicine, Tsinghua University, Beijing 100084, China (e-mail: deabj@tsinghua.edu.cn).

Color versions of one or more of the figures in this paper are available online at <http://ieeexplore.ieee.org>.

Digital Object Identifier 10.1109/TITB.2010.2077306

excitation modes along axial direction while maintaining the temporal resolution. The strategy is as follows: for each projection, the excitation light is provided by multiple point sources at different height positions; the positions of these point sources between neighboring projections are varied, which leads to more excitation modes along axial direction; the switching or movement of these point-illumination sources is performed along with the rotation of the image object, which, therefore, does not need additional time. The parallel excitation modes are dependent on the projection angles. In other words, they can be seen as a spatially coded function of the projection angles. That is why we call the strategy as spatially coded parallel excitation.

The spatial-temporal performances of the proposed SC-FDOT depend on its key experimental parameters, such as the distribution of point sources. It is obvious that SC-FDOT provides similar image quality as L-FDOT or multiple-point FDOT (MP-FDOT) (two typical BF-FDOT systems with line or multiple points illuminations) when too many point-illumination sources are used for spatially coded parallel excitation. Therefore, studies should be performed to obtain key parameters for SC-FDOT.

In this paper, four categories of experiments were designed. First, singular-value analysis (SVA) can condense the information of different imaging systems into a spectrum vector and has been widely used in analyzing different DOT/FDOT systems [11], [21]–[25]. Herein, SVA was used to 1) determine the optimal experimental parameters for SC-FDOT, including projections number and the distribution of point illumination sources; and 2) compare the performances of MP-FDOT, P-FDOT, and SC-FDOT. Second, a series of numerical simulations were performed to confirm the key findings obtained by SVA, and analyze the upper limit of spatial resolution of SC-FDOT. In addition, a fast biological activity through whole body was numerically simulated and imaged using different full-angle FDOT systems to demonstrate the advantages of SC-FDOT. Third, physical phantom experiments were performed to further demonstrate the performances SC-FDOT. Finally, an *in vivo* experiment was performed to verify the feasibility of SC-FDOT in imaging live small animals.

The outline of this paper is presented as follows. Section II details the methods used. In Section III, we detail and analyze the results. In Section IV, we discuss and conclude this study.

II. METHODS

A. Instrumentation

1) *Full-Angle FDOT System*: The schematic of our full-angle system is shown in Fig. 1(a). The imaged mouse is placed on a rotation stage with its four legs fixed on a suspension bracket. The maximum speed of the rotation stage is set to $6^\circ/\text{s}$ to prevent possible skew and internal mouse organ movement. In each projection, the excitation light is simultaneously provided by several collimated laser diodes (785 nm) that are fixed at different heights on the axial one of 2-D translation stages. The transversal translation stage used is to adjust the transversal positions of these diodes before an experiment. The focuses of these collimators are close to back surface of the imaged object.

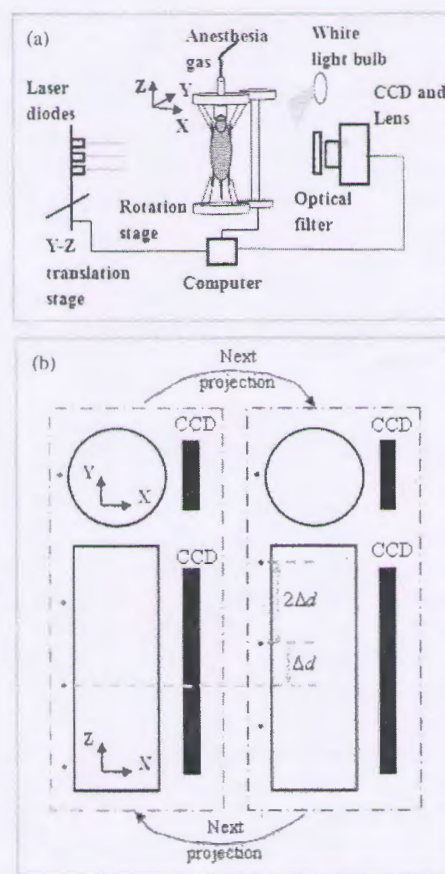


Fig. 1. SC-FDOT. (a) Schematic of the SC-FDOT system. (b) Strategy of spatially coded parallel excitation.

The power of each laser diode is tuned to 8.0 mW in this paper. The number of laser diodes and the distance between neighboring laser diodes depend on the imaged object and will be discussed in following sections.

In each projection angle, the photons propagating through the mouse front surface are collected by a 512×512 pixels, -70°C cooled CCD array (Andor, Belfast, Northern Ireland, U.K.) coupled with a Nikkor 60-mm f/2.8D lens (Nikon, Melville, NY). When collecting fluorescence images, a 840 ± 6 nm bandpass filter (Semrock, Rochester, NY) is placed in front of the lens to allow photons at emission wavelength. When collecting the excitation light images, a neutral density filter (1% transmittance, Daheng, Beijing, China) is used to prevent possible high light damage to CCD or saturation. Mouse 3-D surface is essential for FDOT reconstruction, which can be recovered with back-projection-based technique [26] from white light images at different projection angles. When collecting these white light images, the mouse front surface is illuminated by a white light bulb and the neutral density filter is still used. Seventy-two white light projections evenly distributed over 360° are typically enough.

2) *Spatially Coded Parallel Excitation*: The strategy of spatially coded parallel excitation is illustrated in Fig. 1(b). Assume that the distance between neighboring laser diodes is $2\Delta d$. In

one projection, these diodes are at some heights to illuminate the imaged object, as depicted by the red point in Fig. 1(b). Then, before collecting the next projection, the imaged object is rotated to the next projection angle by the rotation stage. At the same time, these laser diodes are moved with a distance of Δd by the Z translation stage, which are finally depicted by the blue points in Fig. 1(b). It should be noted that high-resolution translation stage typically has slow translation speed, such as 1-cm/s maximum translation speed of the one used in our system. However, the time taken in translating these laser diodes is still shorter than the rotation time between neighboring projections. Therefore, the spatially coded parallel excitation provides more excitation modes along axial direction, least correlated, while no additional time is needed to switching different excitation modes.

B. Reconstruction Method

Light propagation in highly scattering media due to a continuous-wave source term $S(r)$ is modeled using the diffusion equation [27] as follows:

$$-\nabla[D(r)\nabla G(r)] + \mu_a(r)G(r) = S(r)r \in \Omega. \quad (1)$$

In (1), $D(r) = 1/(3\mu'_s(r))$ is the possibly spatially varying diffusion coefficient at position r with reduced scattering coefficient $\mu'_s(r)$. $\mu_a(r)$ is the possibly spatially varying absorption coefficient. $G(r)$ describing light propagation inside the domain Ω of imaged object. Typically, Robin-type boundary condition [27] is couple to (1) on the boundary of Ω . Finite-element method is used to discretize (1), where a commercial software package COMSOL is used to discretize the domain Ω to a finite-element mesh. The edge size of tetrahedron finite element is controlled less than or equal to 2.3 mm, which is considered accurate enough for FMT applications. Then, (1) is transformed to a linear equation as follows [27]:

$$KG = b \quad (2)$$

where stiffness matrix K is a positive definite matrix containing the contribution of tissue diffusion and absorption, and b is a vector corresponding to the source term. By solving (2), G , the vector of light distribution values at finite-element nodes, is obtained, which can be then used to interpolate the value at arbitrary point inside Ω . For SC-FDOT, the source term $SC(r)$ due to the N laser spots are modeled as follows:

$$SC(r) = \frac{1}{N} \sum_{i=1}^N \delta(r - r_i) \quad (3)$$

where $\delta(r - r_i)$ is an isotropic point source at position r_i , which is one transport mean free path into medium from these laser spots [27]. Based on Normalized Born approximation [28], which reduces the mouse tissue heterogeneity influences, the ratio of the measured emission $\Phi_m(r_d)$ and the corresponding excitation $\Phi_x(r_d)$ at detector point r_d can be written as

$$\frac{\Phi_m(r_d)}{\Phi_x(r_d)} = \Theta_m \int_{r_p \in V} \frac{G_{S(r)}(r_p)G_{\delta(r-r_d)}(r_p)}{G_{S(r)}(r_d)} n(r_p) dr_p \quad (4)$$

where $G_{\delta(r-r_d)}$ is the fluorescence light distribution due to an isotropic point source $\delta(r - r_d)$ and $G_{S(r)}$ is the excitation light distribution due to a source term $S(r)$. $n(r_p)$ is the unknown fluorescence yield at point r_p in the volume of interest V ($V \subset \Omega$). Θ_m is a unitless constant taking account of the unknown gain and attenuation factors of the system. Accounting for data from all source-detector pairs, (4) is discretized to a linear system $\Phi_m/\Phi_x = Wn$, with weight matrix W containing the contribution of the integral over volume V , n being the discretized vector of fluorescence yield, and Φ_m/Φ_x being the vectors of normalized Born ratio. The reconstruction of n is carried out using algebraic reconstruction technique (ART) [29] with non-negative constraints.

C. Singular-Value Analysis (SVA)

SVA has been successfully used in comparing the performances of different DOT/FDOT imaging systems or determining optimal experimental parameters [11], [21]–[25]. In SVA, the information contained in a weight matrix W is condensed to a singular-value spectrum. The number of singular values above a specific threshold (NSVAT) represents the useable image-space modes, which can be detected in the experimental setup. More detailed descriptions on SVA in the context of DOT/FDOT were given in [21] and [22]. In this study, a singular-value spectrum was normalized by its largest element. Then, the normalized singular-value spectrum was truncated at a series of thresholds from 10^{-3} to 10^{-5} , where 10^{-4} was chosen as the main threshold for analysis.

In this section, SVA was used to analyze the SC-FDOT in 1) determining how many point sources will lead to the best image quality; 2) determining how many projections will lead to the optimal spatial-temporal performance; and 3) comparing the performances among MP-FDOT, P-FDOT, and the proposed SC-FDOT.

There are different kinds of full-angle FDOT systems discussed in this paper. Some concepts are clarified here. In P-FDOT, scanning along axial direction at one projection angle is needed to provide whole-body imaging ability. There will be different scanning positions along axial directions in P-FDOT, which will be described as different cycles of projections. Then, assuming P-FDOT with C scanning positions along axial direction, we will call it P-FDOT with C cycles of projections. When there are P projection angles for each scanning position, we will call it P-FDOT with $C \times P$ projections. In MP-FDOT, several point sources along axial direction will illuminate the imaged object simultaneously. Then, assuming MP-FDOT with M point sources and P projection angles, we will call it MP-FDOT with M point sources and P projections. Similar as MP-FDOT, for SC-FDOT with N point sources and P projection angles, we will call it SC-FDOT with N point sources and P projections.

Then, there are different height positions along axial direction, where a point source is located. For example, there are C different height positions in P-FDOT with C cycles of projections, M different height positions in MP-FDOT with M point sources, or $2N$ different height positions in SC-FDOT with N point sources. Obviously, the distribution of these height

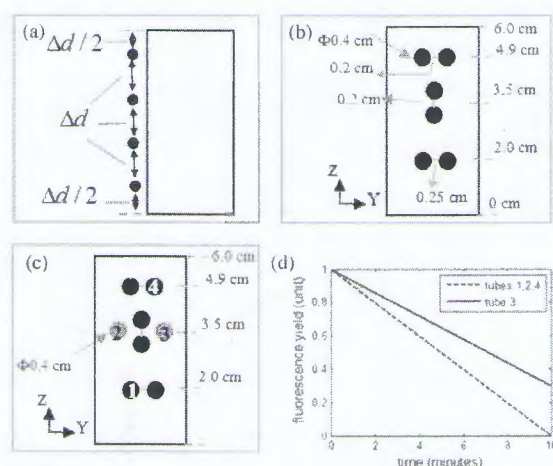


Fig. 2. Settings of phantom and tubes for numerical simulations. (a) Heights distribution along axial direction for full-angle FDOT. Δd is the distance between neighboring heights. (b) Simulations of a static biological activity. The six black circles represent spherical fluorescent inclusions (0.4 cm diameter, 1 unit fluorescence yield) placed inside a cylinder phantom (6.0 cm length, 2.0 cm diameter). The edge-to-edge distance in each group of spheres (connected with gray lines) was 0.2 cm or 0.25 cm. (c)–(d) Simulations of a fast biological activity. The eight circles represent spherical fluorescent inclusions (0.4 cm diameter), where the black ones had the same geometrical settings, as in (b). The fluorescence yields of the numbered spheres were time variant, as depicted in (d). The fluorescence yields of other spheres were time invariant (1 unit).

positions influences the spatial performances of these full-angle FDOT systems. In this paper, for simplification, these height positions are assumed evenly distributed along axial direction, as shown in Fig. 2(a). In other words, for a L -cm-long object imaged and C different heights, the distance Δd between neighboring heights is L/C cm.

In SVA and following numerical simulations, a homogeneous phantom (6.0 cm length and 2.0 cm diameter) with $\mu'_s = 10.0 \text{ cm}^{-1}$, $\mu_a = 0.58 \text{ cm}^{-1}$ optical properties was investigated. The optical properties were close to the mean optical properties of the mouse mid-torso [11], while the geometry sizes were close to the mean one during our earlier *in vivo* experiments. In this paper, most experimental parameters used were based on [21], where the optimal experimental parameters were determined for BF-FDOT. The detector spacing was 0.2 cm; 1.8 cm detector horizontal field of view (FOV) was used. As detector points with ultralow excitation light do not contain information but typically induce artifacts, the detector FOV along vertical direction (VFOV) was determined as region with excitation light above 5% of the maximum excitation light intensity. For example, the VFOV was 2.4 cm for P-FDOT and 5.8 cm for SC-FDOT with three point sources. The reconstruction mesh was over $2.0 \text{ cm} \times 2.0 \text{ cm} \times 5.8 \text{ cm}$ with 0.1 cm mesh spacing, and only the voxels inside imaged object were considered for analysis.

D. Simulations

Data were synthesized on the described phantom in Section II-C for SC-FDOT with point sources from 2 to 4, MP-FDOT with point sources from 4 to 8, and P-FDOT with 1 to 6 cycles of projections.

1) *Simulations of Static Biological Activity:* The simulations in this section were performed to evaluate the spatial resolution of SC-FDOT and confirm the key findings obtained by SVA.

As shown in Fig. 2(b), six small spherical fluorescent inclusions with 0.4 cm diameter were embedded inside the cylinder phantom. These six spheres were divided to three groups, where the edge-to-edge distance inside each group was 0.2 cm or 0.25 cm. The fluorescence yields were assumed as 1 unit inside the spheres and 0 inside the background. The excitation and fluorescence photon densities were synthesized using finite-element method. Seven percent of poisson noise was then added to the synthetic data.

2) *Simulations of Dynamic Biological Activity:* A fast biological activity through whole body was simulated and imaged to further verify the feasibility of SC-FDOT and demonstrate its advantages over MP-FDOT and P-FDOT.

As shown in Fig. 2(c), eight spherical fluorescent inclusions with 0.4 cm diameter were embedded inside the cylinder phantom. Among these spheres, the six black ones have the same geometrical settings as in Fig. 2(b), while the remaining two gray ones were placed at $x = 0.0 \text{ cm}$, $y = \pm 0.5 \text{ cm}$, and $z = 3.5 \text{ cm}$. The fluorescence yields of the numbered spheres were time variant, as depicted in Fig. 2(d). The remaining spheres had time-invariant fluorescence yields (1 unit).

Before synthesizing the data, we should analyze the imaging time of these full-angle FDOT at first. The imaging time of one frame for full-angle FDOT consists of the total exposure time of all projections, the rotation time (1 min), and the total switching time between illumination sources (0 min for SC-FDOT and MP-FDOT). As mentioned in Section II-A, the high-resolution mechanical translation stage, for switching illumination points at different heights and at the same projection angle in our full-angle FDOT system, has a maximum translation of 1 cm/s. Assume that each projection takes 3.0 s, which is typical in our previous *in vivo* experiments. Based on these assumptions, data were synthesized for the dynamic process. The synthetic process was similar as in the previous section except that the fluorescence yields of these time-variant fluorescent inclusions were different for each projection.

E. Physical Phantom Experiment

Physical phantom experiments were performed to verify the feasibility of SC-FDOT in practical experimental applications. The phantom was made of a glass cylinder (2.2 cm diameter and 6.7 cm length) filled with matching fluid ($\mu'_s = 10.0 \text{ cm}^{-1}$, $\mu_a = 0.58 \text{ cm}^{-1}$). Two transparent glass tubes (0.3 cm diameter) were filled with 0.26-nmol indocyanine green (ICG), respectively, providing fluorescent inclusions of 0.4 cm length. First, to demonstrate the radial spatial performance of our SC-FDOT, the two fluorescent inclusions were placed close to each other, with their centers at the same height and 0.5 cm edge-to-edge distance, as shown in Fig. 3(a). Second, to demonstrate the axial spatial performance of our SC-FDOT, we wanted to place two fluorescent inclusions at different heights and close to each other. As it was not easy to implement such settings, instead, one fluorescent inclusion was placed

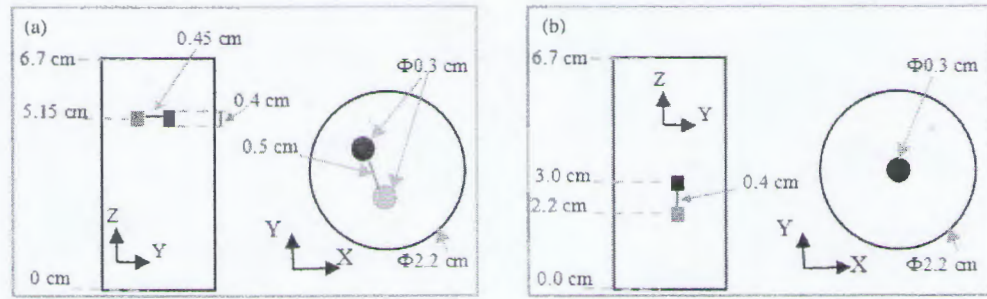


Fig. 3. Setup of physical phantom experiment. Fluorescent inclusions (0.3 cm diameter and 0.4 cm length) were embedded in a cylinder phantom (2.2 cm diameter and 6.7 cm length). (a) Phantom for evaluating radial spatial performance. The two fluorescent inclusions were closely placed with their centers at the same height and edge-to-edge distance of 0.5 cm. (b) Phantom for evaluating axial spatial performance. One fluorescent inclusion was placed at different heights and imaged respectively to simulate two closely placed inclusions along axial direction. The edge-to-edge distance was 0.4 cm.

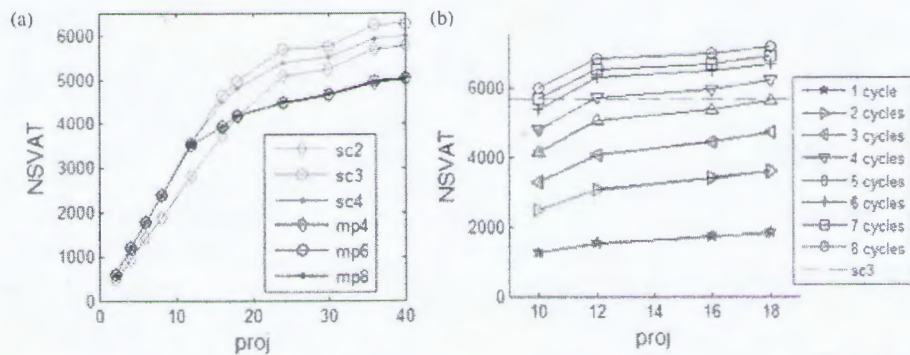


Fig. 4. SVA for full-angle FDOT systems, especially for SC-FDOT. The legends sc2 to sc4 represent SC-FDOT with 2 to 4 point sources. The legends mp4 to mp8 represent MP-FDOT with 4 to 8 point sources. The legends one cycle to eight cycles represent P-FDOT with 1–8 cycles of projections. (a) SVA of the projections number for SC-FDOT (red lines) and MP-FDOT (blue lines). (b) SVA of the projections number and the cycles number for P-FDOT (black lines). Corresponding NSVAT of SC-FDOT with three point sources and 24 projections are plotted as a red line.

at two different heights and imaged, respectively. Then, by summing the acquired signals, we simulated two close fluorescent inclusions along axial direction (0.4 cm edge-to-edge distance), as shown in Fig. 3(b). In the second experiment, the positions of fluorescent inclusions were far away from those in the first experiment. Those four fluorescent inclusions together could mimic one whole-body distribution. Then, we can verify the whole-body performance of our SC-FDOT, if those fluorescent inclusions were all well reconstructed. In the experiments, three laser diodes spaced with 2.0 cm distance were used. To image whole body, the CCD FOV was 8.6 cm \times 8.6 cm. Twenty-four excitation projections were collected every 15°. Twenty-four fluorescence images were collected every 15°, with 3 s exposure time and 4 \times 4 CCD binning, taking approximate 2.3 min imaging time.

F. In Vivo Experiment

A preliminary *in vivo* experiment was performed to demonstrate the feasibility of the SC-FDOT in *in vivo* application. One nude mouse was anesthetized under isoflurane–oxygen gas mixture and suspended on the rotation stage. A transparent glass tube (0.3 cm diameter) was filled with 0.13-nmol ICG, producing a fluorescent inclusion of 0.2 cm length. By inserting the glass tube through mouse anal, the small fluorescent inclusion was finally implanted inside mouse liver region. Three laser diodes

spaced with 2.0 cm distance were used to provide the excitation light. The CCD FOV was 10.7 cm \times 10.7 cm. Twenty-four fluorescence projection were collected every 15° with exposure time 3.0 s and 4 \times 4 CCD binning, taking approximate 2.3 min imaging time. Twenty-four excitation projections were collected every 15°.

III. RESULTS

A. Singular Value Analysis (SVA)

The following SVA results shown are of the threshold 10^{-4} . The studies were also repeated with other thresholds from 10^{-3} to 10^{-5} . Although the absolute value of NSVAT changed with different thresholds, the general trends in imaging performances were independent of the thresholds chosen.

As shown in Fig. 4(a), the NSVAT is plotted as a function against projections number for SC-FDOT with 2–4 point sources (red lines). An initial sharp increase is observed up to 24 projections for SC-FDOT. Relatively much smaller increase speed is observed for projections number over 24. The increase in NSVAT corresponds to more useable image-space modes (better spatial resolution). However, increasing the projections number increases the imaging time (lower temporal resolution) near linearly. When compromising between the increase speed in NSVAT and the near linearly increased imaging time, 24 projections are considered optimal.

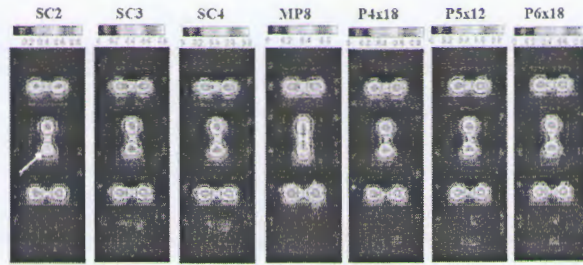


Fig. 5. Reconstructions of simulated data of a static biological activity. The black circles in the images represent the actual tubes. The images are at slice $X = 0$. The first three subimages are for SC-FDOT with 2 (SC2)–4 (SC4) point sources and 24 projections. The fourth subimage is for MP-FDOT with eight point sources and 24 projections. The remaining subimages are for P-FDOT with different projections (4×18 , 5×12 , 6×18). The black circles in the images represent the actual fluorescent inclusions. The color scale of each subimage corresponds to the reconstructed value range from 0 to maximum.

It can be seen that three point sources yield the largest NSVAT, especially after the optimal projections number. Therefore, three point sources spaced with 2 cm distance are optimal for SC-FDOT.

As shown in Fig. 4(a), the NSVAT of MP-FDOT is also plotted (blue lines). For projections number over 18 (the optimal projections number for MP-FDOT [21]), much larger NSVAT are observed for SC-FDOT with three point sources. Therefore, SC-FDOT has better performances than MP-FDOT.

As shown in Fig. 4(b), the NSVAT is plotted as a function against projections number for P-FDOT with different cycles of projections (black lines). The NSVAT of SC-FDOT with three point sources and 24 projections is also plotted as a red line. It can be seen that SC-FDOT with 24 projections has comparable NSVAT to P-FDOT with 4×18 projections or 5×12 projections.

B. Reconstructions of Simulated Data

Reconstructions were carried out using 1000 ART iterations and relaxation parameter of 0.1.

The reconstructed images from 24 projections in SC-FDOT are shown in Fig. 5. The target, highlighted by a white arrow, is reconstructed with lower value than other targets, when using SC-FDOT with two point sources. In contrast, better image quality with more consistent quantification is demonstrated for SC-FDOT with three point sources. These results are consistent with the optimal point sources number obtained using SVA in Section III-A.

The reconstructed images for MP-FDOT and P-FDOT are also shown in Fig. 5. Compared with MP-FDOT with eight point sources, the axial resolution is significantly improved in SC-FDOT with three point sources. The image quality of SC-FDOT with three point sources and 24 projections is comparable to those of P-FDOT with 4×18 or 5×12 projections. All these results are consistent with the conclusions obtained using SVA in Section III-A.

The reconstructed fluorescence yields of a fast biological activity at start point (0 min) are shown in Fig. 6(a). Among these three full-angle FDOT systems, SC-FDOT with three

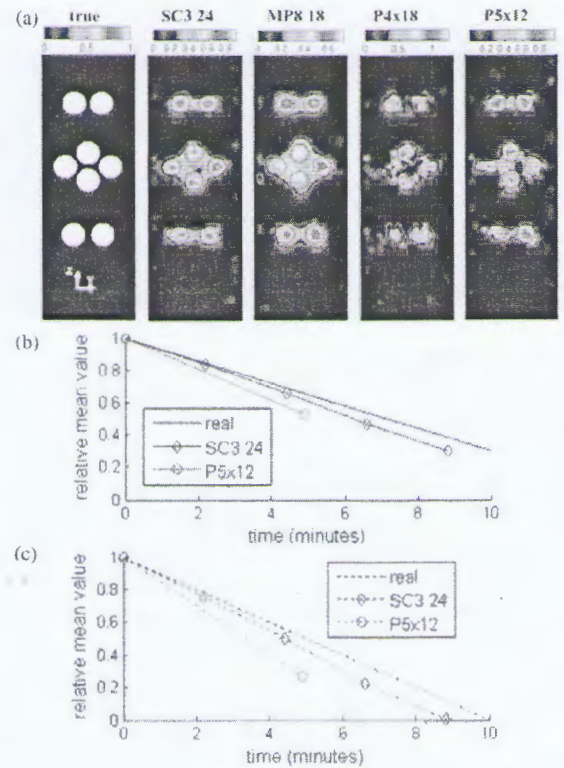


Fig. 6. Reconstructions of simulated data of a dynamic biological activity. (a) Reconstructed images at start point (0 min) and at slice $X = 0$. The first subimage is the true image. The second subimage is for SC-FDOT with three point sources and 24 projections, the third subimage is for MP-FDOT with eight point sources and 18 projections, while the remaining subimages are for P-FDOT with different projections (4×18 , 5×12). The black circles in the subimages represent the actual fluorescent inclusions. The color scale of each subimage corresponds to the reconstructed value range from 0 to maximum. (b) Relative mean value of tube 3. (c) Relative mean value of tube 4.

point sources demonstrated the best image quality. The same conclusion can be made from the reconstructed fluorescence yields over time. The relative mean values of tubes 3 and 4 in Fig. 6(b) and (c) are the mean fluorescence yields inside tubes, and are normalized by those values at start point. For both tubes, it is seen that, compared to P-FDOT, the relatively changing speeds of fluorescence yields reconstructed from SC-FDOT are closer to the real ones. Therefore, SC-FDOT has the best spatial-temporal performance in imaging fast biological activities through whole body.

C. Reconstruction of Physical Phantom Data

In the reconstruction, the detectors were distributed over $2.0 \text{ cm} \times 6.0 \text{ cm}$ FOV with 0.1 cm spacing. The reconstruction mesh was over $2.6 \text{ cm} \times 2.6 \text{ cm} \times 6.0 \text{ cm}$ 3-D region with 0.2 cm mesh spacing and only the mesh inside the imaged object was considered for reconstruction. 100 ART iterations and relaxation parameter 0.1 were used in the reconstructions.

From Fig. 7(a) and (b), it can be seen that the two closely placed fluorescent inclusions, inside radial plane or axial plane, were clearly resolved and well localized. Near-consistent quantification was observed for all these fluorescent inclusions. It

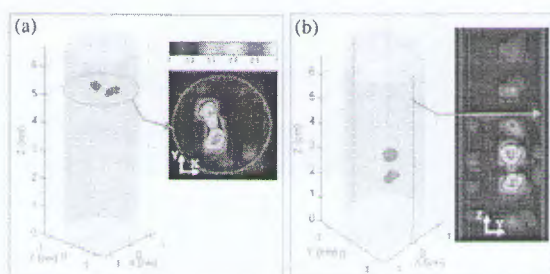


Fig. 7. Reconstruction of physical phantom data for SC-FDOT. (a) Reconstruction for two closely placed fluorescent inclusions at radial plane. (b) Reconstruction for two closely placed fluorescent inclusions at axial plane. Top 50% of the contour levels of reconstructed fluorescence yields are shown in the 3-D view. The red curves on the section images represent the phantom boundary and the small black circles/rectangles represent the actual fluorescent targets. The section images are in the same color scale corresponding to the reconstructed value range from 0 to maximum.

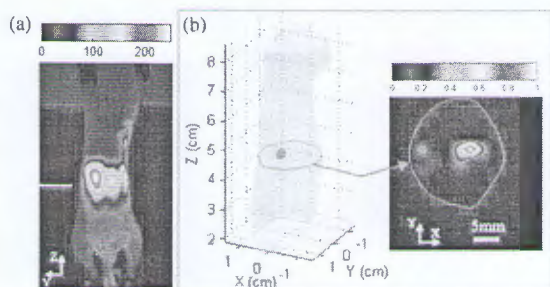


Fig. 8. Reconstruction of *in vivo* data for SC-FDOT. (a) Measured fluorescence projection at 0° . (b) Reconstructed FDOT image. Top 50% of the contour levels of reconstructed target is shown in 3-D view. The cross image corresponds to height slice depicted as the white line in (a). The red curve in cross image denotes mouse boundary. The color scale of the cross image corresponds to the reconstructed value range from 0 to maximum.

should be noted that some of these fluorescent inclusions were far away from each other, which could mimic a distribution inside whole body. Therefore, these results demonstrate that SC-FDOT has good whole-body performance in practical experimental applications.

D. Reconstruction of In Vivo Data

The detectors were first meshed with 0.1 cm spacing over $2.8 \text{ cm} \times 5.7 \text{ cm}$ FOV for each projection. Then, we selected those detectors for reconstruction 1) which covered the animal and were more than 0.2 cm away from the boundary and 2) where the intensities of fluorescence and excitation light reached above a threshold 30 CCD counts. The reconstruction meshes for FDOT were over $3.0 \text{ cm} \times 3.0 \text{ cm} \times 5.7 \text{ cm}$ 3-D regions with 0.2 cm spacing and inside the imaged object. Optical properties of $\mu'_s = 10.0 \text{ cm}^{-1}$, $\mu_a = 0.58 \text{ cm}^{-1}$ were used. The FDOT reconstruction was carried out using 100 ART iterations with relaxation parameter 0.1.

From the 3-D view in Fig. 8, it can be seen that one fluorescent target was reconstructed. The position of reconstructed target was approximately in agreement with the tube position maintained in the experiment. From the preliminary result, we can see the feasibility of SC-FDOT in *in vivo* applications.

IV. DISCUSSION AND CONCLUSION

Challenges remain in FDOT imaging fast biological activities through whole small animal. Therefore, it is important to design real-time imaging systems with whole-body FOV. In this study, we proposed a novel noncontact, full-angle FDOT with spatially coded parallel excitation. We analyzed the key parameters for the proposed SC-FDOT. Numerical simulations, physical phantom experiments, and *in vivo* experiments were performed to verify the feasibility of the proposed SC-FDOT. Using SVA, we also quantitatively compared the performances of the proposed SC-FDOT, our previous MP-FDOT, and the conventional P-FDOT. Using a numerically simulated fast biological activity, we demonstrated the advantage of SC-FDOT in imaging fast biological activities through whole body over the other two full-angle FDOT.

For SC-FDOT, the spatial-temporal performances depend on the projections number and the distribution of point sources. For a phantom with typical optical geometry size and optical properties, 24 projections are considered to yield the optimal spatial-temporal performances. Three point sources spaced with 2 cm distance are considered as optimal for SC-FDOT, which were also verified in numerical simulations. Based the obtained parameters, physical phantom and *in vivo* experiments were also performed.

Comparisons were made between SC-FDOT and our earlier MP-FDOT using SVA, numerical simulations of static or dynamic biological activities. Results demonstrate that SC-FDOT has much better axial resolution than MP-FDOT. In contrast, the radial resolution and the temporal resolution are comparable. Therefore, SC-FDOT is more suitable for imaging fast biological activities through whole body than MP-FDOT.

Comparisons were also made between SC-FDOT and P-FDOT. When imaging a static biological activity inside the simulated phantom, SC-FDOT with three point sources and 24 projections yielded comparable image quality to P-FDOT with 4×18 or 5×12 projections. Let us analyze the temporal resolution between the two FDOT systems based on the description in Section II-D2. Assume that each projection takes 3 s. Then, SC-FDOT with 24 projections will spend 2.2 min in obtaining one frame. In contrast, P-FDOT with $4 \times 18/5 \times 12$ projections will spend 5.9/4.9 min (our P-FDOT with slow switching by mechanical translation stage) or 4.6/4.0 min (P-FDOT with fast switching by galvanometer-controlled mirrors), respectively. Then, we can see that SC-FDOT has much better spatial-temporal resolutions than P-FDOT, which were also verified in imaging a numerically simulated dynamic biological activity.

The proposed SC-FDOT is rotation based. The rotation time is one big portion in obtaining one frame. In the proposed SC-FDOT, by taking the advantage of simultaneously translating the point sources and rotating the imaged object, we save much time. Assume 24 projections in SC-FDOT with point sources spaced with 2 cm distance, the switching time will be 24 s. Then, there are still 36 s spent just for rotation. Recently, conical-mirror-based full-angle FDOT and bioluminescence tomography were reported [30], [31], which allowed collecting

full-angle projections without rotation. By incorporating parallel excitation, the kind of systems may provide another way in further enhancing the temporal resolution. However, it is out of the focus of our current rotation-based imaging modalities.

In this paper, the scanning distance along axial direction between neighbor projections is half the space between point sources. It is mainly because we focus on spatial-temporal performance. In other words, we want to obtain as many as useable image-space modes while maintaining the temporal resolution. When imaging slow biological activities inside whole body, more scanning positions along axial direction ($S(S \geq 3)$ scanning positions with scanning distance of $2\Delta d/S$) are recommended, which will lead to better spatial performance. In this situation, the spatially coded parallel-excitation strategy is still helpful in enhancing the system-imaging speed or throughput. However, it is out of the scope of this paper and will be investigated in our future research.

Although mechanical scanned laser diodes are selected to provide spatially coded parallel excitation in this paper, other type of illumination light source can also be used. However, two following issues should be considered during selection. The first is to eliminate the probability of direct illumination light transportation to CCD, which otherwise results in CCD saturation. That means, wide excitation patterns along transversal direction are not recommended. The second is the availability and simplicity of the light source. With the two considerations, better illumination light source or scheme based on the strategy of spatially coded parallel excitation may be selected or developed, which will further improve the spatial-temporal performance of FDOT.

In summary, the development of SC-FDOT consists of 1) using parallel excitation instead of the conventional single-point illumination in P-FDOT; 2) using varied parallel excitation modes along axial direction instead of unvaried parallel excitation mode in our previous BF-FDOT; and 3) using spatially coded method to eliminate the switching time caused by slow switching device. Results demonstrate that the strategy is feasible and helpful in designing real-time FDOT system. Future research will be focused on applying SC-FDOT in observing pharmacokinetics and developing possible better FDOT systems.

REFERENCES

- [1] V. Ntziachristos, J. Ripoll, L. Wang, and R. Weissleder, "Looking and listening to light: The evolution of whole-body photonic imaging," *Nat. Biotechnol.*, vol. 23, no. 3, pp. 313–320, Mar. 2005.
- [2] G. Wang, W. Cong, H. Shen, X. Qian, M. Henry, and Y. Wang, "Overview of bioluminescence tomography—A new molecular imaging modality," *Front. Biosci.*, vol. 13, pp. 1281–1293, 2008.
- [3] B. J. Tromberg, B. W. Pogue, K. D. Paulsen, A. G. Yodh, D. A. Boas, and A. E. Cerussi, "Assessing the future of diffuse optical imaging technologies for breast cancer management," *Med. Phys.*, vol. 35, no. 6, pp. 2443–2451, 2008.
- [4] A. P. Gibson, J. C. Hebden, and S. R. Arridge, "Recent advances in diffuse optical tomography," *Phys. Med. Biol.*, vol. 50, pp. R1–R43, Feb. 2005.
- [5] V. Ntziachristos and R. Weissleder, "Charge-coupled-device based scanner for tomography of fluorescent near-infrared probes in turbid media," *Med. Phys.*, vol. 29, no. 5, pp. 803–809, May 2002.
- [6] H. Feng, J. Bai, X. Song, G. Hu, and J. Yao, "A near-infrared optical tomography system based on photomultiplier tube," *Int. J. Biomed. Imag.*, vol. 2007, pp. 28387–1–28387-9, 2007.
- [7] R. B. Schulz, J. Ripoll, and V. Ntziachristos, "Experimental fluorescence tomography of tissues with noncontact measurements," *IEEE Trans. Med. Imag.*, vol. 23, no. 4, pp. 492–500, Apr. 2004.
- [8] G. Zavattini, S. Vecchi, G. Mitchell, U. Weisser, R. Leahy, B. Pichler, D. Smith, and S. Cherry, "A hyperspectral fluorescence system for 3D in vivo optical imaging," *Phys. Med. Biol.*, vol. 51, no. 8, pp. 2029–2043, Apr. 2006.
- [9] N. Deliolanis, T. Lasser, D. Hyde, A. Soubret, J. Ripoll, and V. Ntziachristos, "Free-space fluorescence molecular tomography utilizing 360° geometry projections," *Opt. Lett.*, vol. 32, no. 4, pp. 382–384, Feb. 2007.
- [10] G. Hu, J. Yao, and J. Bai, "Full-angle optical imaging of near-infrared fluorescent probes implanted in small animals," *Prog. Nat. Sci.*, vol. 18, no. 6, pp. 707–711, 2008.
- [11] T. Lasser and V. Ntziachristos, "Optimization of 360° projection fluorescence molecular tomography," *Med. Image Anal.*, vol. 11, no. 4, pp. 389–399, 2007.
- [12] A. Joshi, J. C. Rasmussen, E. M. Sevick-Muraca, T. A. Wareing, and J. McGhee, "Radiative transport-based frequency-domain fluorescence tomography," *Phys. Med. Biol.*, vol. 53, no. 8, pp. 2069–2088, Apr. 2008.
- [13] K. Ren, G. Bal, and A. H. Hielscher, "Transport- And diffusion-based optical tomography in small domains: A comparative study," *Appl. Opt.*, vol. 46, no. 27, pp. 6669–6679, Sep. 2007.
- [14] Y. Lu, H. B. Machado, A. Douraghy, D. Stout, H. Herschman, and A. F. Chatziioannou, "Experimental bioluminescence tomography with fully parallel radiative-transfer-based reconstruction framework," *Opt. Exp.*, vol. 17, no. 19, pp. 16681–16695, Sep. 2009.
- [15] M. C. Pierce, D. J. Javier, and R. Richards-Kortum, "Optical contrast agents and imaging systems for detection and diagnosis of cancer," *Int. J. Cancer*, vol. 123, no. 9, pp. 1979–1990, 2008.
- [16] A. Koenig, L. Hervé, V. Jossierand, M. Berger, J. Boutet, A. D. Silva, J. Dinten, P. Peltié, J. Coll, and P. Rizo, "In vivo mice lung tumor follow-up with fluorescence diffuse optical tomography," *J. Biomed. Opt.*, vol. 13, no. 1, pp. 011008-1–011008-9, Feb. 2008.
- [17] D. S. Kepshire, S. L. Gibbs-Struass, J. A. O'Hara, M. Hutchins, N. Mincu, F. Leblond, M. Khayat, H. Dehghani, S. Srinivasan, and B. W. Pogue, "Imaging of glioma tumor with endogenous fluorescence tomography," *J. Biomed. Opt.*, vol. 14, no. 3, pp. 030501-1–030501-3, Jun. 2009.
- [18] V. Ntziachristos, E. A. Schellenberger, J. Ripoll, D. Yessayan, E. Graves, A. Bogdanov, L. Josephson, and R. Weissleder, "Visualization of antitumor treatment by means of fluorescence molecular tomography with an annexin V-Cy5.5 conjugate," *PNAS*, vol. 101, no. 33, pp. 12294–12299, Aug. 2004.
- [19] J. Haller, D. Hyde, N. Deliolanis, R. d. Kleine, M. Niedre, and V. Ntziachristos, "Visualization of pulmonary inflammation using noninvasive fluorescence molecular imaging," *J. Appl. Phys.*, vol. 104, pp. 795–802, Jan. 2008.
- [20] S. V. Patwardhan, S. R. Bloch, S. Achilefu, and J. P. Culver, "Time-dependent whole-body fluorescence tomography of probe bio-distributions in mice," *Opt. Exp.*, vol. 13, no. 7, pp. 2564–2577, Apr. 2005.
- [21] D. Wang, X. Liu, and J. Bai, "Analysis of fast full angle fluorescence diffuse optical tomography with beam-forming illumination," *Opt. Exp.*, vol. 17, no. 24, pp. 21376–21395, Nov. 2009.
- [22] J. P. Culver, V. Ntziachristos, M. J. Holbake, and A. G. Yodh, "Optimization of optode arrangements for diffuse optical tomography: A singular-value analysis," *Opt. Lett.*, vol. 26, no. 10, pp. 701–703, May 2001.
- [23] H. Xu, H. Dehghani, B. W. Pogue, R. Springett, K. D. Paulsen, and J. F. Dunn, "Near-infrared imaging in the small animal brain: Optimization of fiber positions," *J. Biomed. Opt.*, vol. 8, no. 1, pp. 102–110, Jan. 2003.
- [24] E. E. Graves, J. P. Culver, J. Ripoll, R. Weissleder, and V. Ntziachristos, "Singular-value analysis and optimization of experimental parameters in fluorescence molecular tomography," *J. Opt. Soc. Amer. A*, vol. 21, no. 2, pp. 231–241, Feb. 2004.
- [25] X. Zhang and C. Badea, "Effects of sampling strategy on image quality in noncontact panoramic fluorescence diffuse optical tomography for small animal imaging," *Opt. Exp.*, vol. 17, no. 7, pp. 5125–5138, Mar. 2009.
- [26] D. Wang, X. Liu, Y. Chen, and J. Bai, "In-vivo fluorescence molecular tomography based on optimal small animal surface reconstruction," *Chin. Opt. Lett.*, vol. 8, no. 1, pp. 82–85, Jan. 2010.
- [27] M. Schweiger, S. R. Arridge, M. Hiraoka, and D. T. Delpy, "The finite element method for the propagation of light in scattering media: Boundary and source conditions," *Med. Phys.*, vol. 22, no. 11, pp. 1779–1792, Nov. 1995.

- [28] A. Soubret, J. Ripoll, and V. Ntziachristos, "Accuracy of fluorescent tomography in the presence of heterogeneities: Study of the normalized Born ratio," *IEEE Trans. Med. Imag.*, vol. 24, no. 10, pp. 1377–1386, Oct. 2005.
- [29] A. Kak and M. Slaney, *Computerized Tomographic Imaging*. New York: IEEE Press, 1987, ch. 7.
- [30] G. Wang, H. Shen, K. Duraiaj, X. Qian, and W. Cong, "The first bioluminescence tomography system for simultaneous acquisition of multiview and multispectral Data," *Int. J. Biom. Imag.*, vol. 2006, pp. 58601–1–58601–8, Sep. 2006.
- [31] C. Li, G. S. Mitchell, J. Dutta, S. Ahn, R. M. Leahy, and S. R. Cherry R. "A three-dimensional multispectral fluorescence optical tomography imaging system for small animals based on a conical mirror design," *Opt. Exp.*, vol. 17, no. 9, pp. 7571–7585, Apr. 2009.



Daifa Wang received the Bachelor's degree and the Ph.D. degree from the Department of Biomedical Engineering, Tsinghua University, Beijing, China, in 2005 and 2010, respectively.

He is currently an Assistant Professor in the School of Biological Science and Medical Engineering, Beihang University, Beijing. He is the author or coauthor of more than 15 research papers. His research interests include the diffuse optical tomography and fluorescence molecular tomography.



Xin Liu received the Bachelor's and Master's degrees in biomedical engineering from Fourth Military Medical University, Xi'an, Shaanxi, China, in 2001 and 2006, respectively. Since 2008, he has been working toward the Ph.D. degree in the Biomedical Engineering Department, Tsinghua University, Beijing, China.

His current research interests include the fluorescence molecular tomography and medical image processing.



Fei Liu received the Bachelor's degree in biomedical engineering from Zhejiang University, Hangzhou, Zhejiang, China, in 2008. Since 2008, she has been working toward the Ph.D. degree in the Biomedical Engineering Department, Tsinghua University, Beijing, China.

Her research interest include the fluorescence molecular tomography.



Jing Bai (F'01) received the M.S. and Ph.D. degrees from Drexel University, Philadelphia, PA, in 1983 and 1985, respectively.

From 1985 to 1987, she was a Research Associate and Assistant Professor at the Biomedical Engineering and Science Institute, Drexel University. She is currently at the Biomedical Engineering Department, Tsinghua University, Beijing, China, where she was an Associate Professor, Professor, and Cheung Kong Chair Professor, respectively, during 1988, 1991, and 2000. She is the author or coauthor of four books

and more than 200 journal papers. Her research interests include mathematical modeling and simulation of cardiovascular system, optimization of cardiac assist devices, medical ultrasound, telemedicine, home health-care network and home-monitoring devices, and infrared imaging.

Dr. Bai is a Fellow of American Institute for Medical & Biological Engineering. Since 1997, she has been an Associate Editor of the IEEE TRANSACTIONS ON INFORMATION TECHNOLOGY IN BIOMEDICINE.



期刊影响因子证明

经检索“期刊引证报告（Journal Citation Reports）”数据库，下列 3 种期刊的影响因子及学科排名：

检索结果见附件，共 1 页。

检索时间为 2016 年 5 月 20 日。

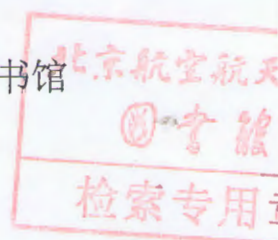
特此证明！



证明人（签字）：姜成林

证明单位（盖章）：北京航空航天大学图书馆

二〇一六年五月二十日





附件:

1. 期刊名称: **APPLIED OPTICS**

ISSN: 1559-128X

影响因子 (2014 年): **1.784**

所属学科及排名:

JCR® Category	Rank in Category	Quartile in Category
OPTICS	36 of 87	Q2

2. 期刊名称: **PLOS ONE**

ISSN: 1932-6203

影响因子 (2014 年): **3.234**

所属学科及排名:

JCR® Category	Rank in Category	Quartile in Category
MULTIDISCIPLINARY SCIENCES	9 of 57	Q1

3. 期刊名称: **IEEE TRANSACTIONS ON INFORMATION TECHNOLOGY IN BIOMEDICINE**

ISSN: 1089-7771

影响因子 (2014 年): **2.493**

所属学科及排名:

JCR® Category	Rank in Category	Quartile in Category
COMPUTER SCIENCE, INFORMATION SYSTEMS	14 of 139	Q1
COMPUTER SCIENCE, INTERDISCIPLINARY APPLICATIONS	17 of 102	Q1
MATHEMATICAL & COMPUTATIONAL BIOLOGY	12 of 57	Q1
MEDICAL INFORMATICS	5 of 24	Q1



文献收录检索证明

作者姓名: 汪待发(Wang, Daifa)

经检索“网络版科学引文索引 (SCI-EXPANDED)”数据库, 该作者发表的论文 (2010-2016 年), 被收录 10 篇。

检索结果见附件, 共 5 页。

检索时间为 2016 年 5 月 20 日。

特此证明!

证明人 (签字):

姜成林

证明单位 (盖章): 北京航空航天大学图书馆

检索专用章

二〇一六年五月三十日



附件:

Record 1 of 10

第一作者

Title: Focusing through dynamic tissue with millisecond digital optical phase conjugation

Author(s): Wang, DF (Wang, Daifa); Zhou, EH (Zhou, Edward Haojiang); Brake, J (Brake, Joshua); Ruan, HW (Ruan, Haowen); Jang, M (Jang, Mooseok); Yang, CH (Yang, Changhui)

Source: OPTICA Volume: 2 Issue: 8 Pages: 728-735 DOI: 10.1364/OPTICA.2.000728 Published: AUG 20 2015

Times Cited in Web of Science Core Collection: 8

Total Times Cited: 8

Accession Number: WOS:000364484600012

Language: English

Document Type: Article

Addresses: [Wang, Daifa; Zhou, Edward Haojiang; Brake, Joshua; Ruan, Haowen; Jang, Mooseok; Yang, Changhui] CALTECH, Dept Elect Engr, Pasadena, CA 91125 USA.

[Wang, Daifa; Zhou, Edward Haojiang; Brake, Joshua; Ruan, Haowen; Jang, Mooseok; Yang, Changhui] CALTECH, Dept Bioengn, Pasadena, CA 91125 USA.

[Wang, Daifa] Beihang Univ, Sch Biol Sci & Med Engr, Minist Educ, Key Lab Biomech & Mechanobiol, Beijing 100191, Peoples R China.

Reprint Address: Yang, CH (reprint author), CALTECH, Dept Elect Engr, Pasadena, CA 91125 USA.

E-mail Addresses: chyang@caltech.edu

IDS Number: CV7VV

ISSN: 2334-2536

Source Item Page Count: 8

Record 2 of 10

第一作者

Title: Noncontact full-angle fluorescence molecular tomography system based on rotary mirrors

Author(s): Wang, DF (Wang, Daifa); He, J (He, Jin); Qiao, HT (Qiao, Huiting); Li, P (Li, Ping); Fan, YB (Fan, Yubo); Li, DY (Li, Deyu)

Source: APPLIED OPTICS Volume: 54 Issue: 23 Pages: 7062-7070 DOI: 10.1364/AO.54.007062 Published: AUG 10 2015

Times Cited in Web of Science Core Collection: 0

Total Times Cited: 0

Accession Number: WOS:000359356400016

Language: English

Document Type: Article

Addresses: [Wang, Daifa; He, Jin; Qiao, Huiting; Li, Ping; Fan, Yubo; Li, Deyu] Beihang Univ, Sch Biol Sci & Med Engr, Key Lab Biomech & Mechanobiol, Minist Educ, Beijing 100191, Peoples R China.

Reprint Address: Li, DY (reprint author), Beihang Univ, Sch Biol Sci & Med Engr, Key Lab Biomech & Mechanobiol, Minist Educ, Beijing 100191, Peoples R China.

E-mail Addresses: deyuli@buaa.edu.cn

IDS Number: CO7QR

ISSN: 1559-128X

eISSN: 2155-3165

Source Item Page Count: 9

Record 3 of 10

Title: The Transport and Deposition of Nanoparticles in Respiratory System by Inhalation

Author(s): Qiao, HT (Qiao, Huiting); Liu, WY (Liu, Wenyong); Gu, HY (Gu, Hongyu); Wang, DF (Wang, Daifa); Wang, Y (Wang, Yu)

Source: JOURNAL OF NANOMATERIALS Article Number: 394507 DOI: 10.1155/2015/394507 Published: 2015



Times Cited in Web of Science Core Collection: 1

Total Times Cited: 1

Accession Number: WOS:000355431300001

Language: English

Document Type: Review

Addresses: [Qiao, Huiting; Liu, Wenyong; Gu, Hongyu; Wang, Daifa; Wang, Yu] Beihang Univ, Sch Biol Sci & Med Engn, Key Lab Biomech & Mechanobiol, Minist Educ, Beijing 100191, Peoples R China.

[Qiao, Huiting] Drexel Univ, Sch Biomed Engn Sci & Hlth Syst, Philadelphia, PA 19104 USA.

Reprint Address: Wang, Y (reprint author), Beihang Univ, Sch Biol Sci & Med Engn, Key Lab Biomech & Mechanobiol, Minist Educ, Beijing 100191, Peoples R China.

E-mail Addresses: wangyu@buaa.edu.cn

IDS Number: CJ4CG

ISSN: 1687-4110

eISSN: 1687-4129

Source Item Page Count: 8

Record 4 of 10

第一作者

Title: High-Performance Fluorescence Molecular Tomography through Shape-Based Reconstruction Using Spherical Harmonics Parameterization

Author(s): Wang, DF (Wang, Daifa); He, J (He, Jin); Qiao, HT (Qiao, Huiting); Song, XL (Song, Xiaolei); Fan, YB (Fan, Yubo); Li, DY (Li, Deyu)

Source: PLOS ONE Volume: 9 Issue: 4 Article Number: e94317 DOI: 10.1371/journal.pone.0094317 Published: APR 14 2014

Times Cited in Web of Science Core Collection: 4

Total Times Cited: 4

Accession Number: WOS:000336970400030

Language: English

Document Type: Article

Addresses: [Wang, Daifa] Beihang Univ, State Key Lab Software Dev Environm, Beijing, Peoples R China.

[Wang, Daifa; He, Jin; Qiao, Huiting; Fan, Yubo; Li, Deyu] Beihang Univ, Sch Biol Sci & Med Engn, Minist Educ, Key Lab Biomech & Mechanobiol, Beijing, Peoples R China.

[Song, Xiaolei] Johns Hopkins Univ, Sch Med, Russell H Morgan Dept Radiol & Radiol Sci, Div MR Res, Baltimore, MD USA.

Reprint Address: Li, DY (reprint author), Beihang Univ, Sch Biol Sci & Med Engn, Minist Educ, Key Lab Biomech & Mechanobiol, Beijing, Peoples R China.

E-mail Addresses: deyuli@buaa.edu.cn

IDS Number: AI6GP

ISSN: 1932-6203

Source Item Page Count: 11

Record 5 of 10

Title: A study of the metabolism of transplanted tumor in the lung by micro PET/CT in mice

Author(s): Qiao, HT (Qiao, Huiting); Li, J (Li, Jun); Chen, YM (Chen, Yingmao); Wang, DF (Wang, Daifa); Han, JT (Han, Jintao); Mei, MQ (Mei, Mengqi); Li, DY (Li, Deyu)

Source: MEDICAL ENGINEERING & PHYSICS Volume: 36 Issue: 3 Pages: 294-299 DOI: 10.1016/j.medengphy.2013.11.012 Published: MAR 2014

Times Cited in Web of Science Core Collection: 0

Total Times Cited: 0

Accession Number: WOS:000334008700003

Language: English



Document Type: Article

Addresses: [Qiao, Huiting; Wang, Daifa; Mei, Mengqi; Li, Deyu] Beihang Univ, Minist Educ, Sch Biol Sci & Med Engr, Key Lab Biomech & Mechanobiol, Beijing 100191, Peoples R China.

[Li, Jun] Peking Univ, Lab Anim Ctr, Beijing 100871, Peoples R China.

[Chen, Yingmao] Gen Hosp PLA, Dept Nucl Med, Beijing 100853, Peoples R China.

[Han, Jintao] Peking Univ, Hosp 3, Dept Intervent Radiol & Vasc Surg, Beijing 100191, Peoples R China.

Reprint Address: Li, DY (reprint author), Beihang Univ, Minist Educ, Sch Biol Sci & Med Engr, Key Lab Biomech & Mechanobiol, Beijing 100191, Peoples R China.

E-mail Addresses: deyuli@buaa.edu.cn

IDS Number: AE5DT

ISSN: 1350-4533

eISSN: 1873-4030

Source Item Page Count: 6

Record 6 of 10

Title: The effect of tumor size on the imaging diagnosis: A study based on simulation

Author(s): Qiao, HT (Qiao, Huiting); Wang, LB (Wang, Libin); Li, DY (Li, Deyu); Wang, DF (Wang, Daifa); Wang, Y (Wang, Yu)

Source: BIO-MEDICAL MATERIALS AND ENGINEERING Volume: 24 Issue: 6 Pages: 3129-3136 DOI: 10.3233/BME-141135 Published: 2014

Times Cited in Web of Science Core Collection: 0

Total Times Cited: 0

Accession Number: WOS:000343005700138

Language: English

Document Type: Article

Addresses: [Qiao, Huiting; Wang, Libin; Li, Deyu; Wang, Daifa; Wang, Yu] Beihang Univ, Sch Biol Sci & Med Engr, Beijing 100191, Peoples R China.

Reprint Address: Wang, Y (reprint author), Beihang Univ, Sch Biol Sci & Med Engr, Beijing 100191, Peoples R China.

E-mail Addresses: wangyu@buaa.edu.cn

IDS Number: AQ7NW

ISSN: 0959-2989

eISSN: 1878-3619

Source Item Page Count: 8

Record 7 of 10

Title: The Mutual Beneficial Effect between Medical Imaging and Nanomedicine

Author(s): Qiao, HT (Qiao, Huiting); Wang, LB (Wang, Libin); Han, JT (Han, Jintao); Chen, YM (Chen, Yingmao); Wang, DF (Wang, Daifa); Li, DY (Li, Deyu)

Source: JOURNAL OF NANOMATERIALS Article Number: 764095 DOI: 10.1155/2013/764095 Published: 2013

Times Cited in Web of Science Core Collection: 0

Total Times Cited: 0

Accession Number: WOS:000323964200001

Language: English

Document Type: Review

Addresses: [Qiao, Huiting; Wang, Libin; Wang, Daifa; Li, Deyu] Beihang Univ, Key Lab Biomech & Mechanobiol, Minist Educ, Sch Biol Sci & Med Engr, Beijing 100191, Peoples R China.

[Han, Jintao] Peking Univ, Dept Intervent Radiol & Vasc Surg, Hosp 3, Beijing 100871, Peoples R China.

[Chen, Yingmao] Gen Hosp PLA, Dept Nucl Med, Beijing 100853, Peoples R China.

Reprint Address: Li, DY (reprint author), Beihang Univ, Key Lab Biomech & Mechanobiol, Minist Educ, Sch Biol Sci & Med Engr, Beijing 100191, Peoples R China.



E-mail Addresses: deyuli@buaa.edu.cn

IDS Number: 212ED

ISSN: 1687-4110

eISSN: 1687-4129

Source Item Page Count: 7

Record 8 of 10

第1作者

Title: Fluorescence molecular tomography using a two-step three-dimensional shape-based reconstruction with graphics processing unit acceleration

Author(s): Wang, DF (Wang, Daifa); Qiao, HT (Qiao, Huiting); Song, XL (Song, Xiaolei); Fan, YB (Fan, Yubo); Li, DY (Li, Deyu)

Source: APPLIED OPTICS Volume: 51 Issue: 36 Pages: 8731-8744 DOI: 10.1364/AO.51.008731 Published: DEC 20 2012

Times Cited in Web of Science Core Collection: 6

Total Times Cited: 7

Accession Number: WOS:000312783700027

Language: English

Document Type: Article

Addresses: [Wang, Daifa; Qiao, Huiting; Fan, Yubo; Li, Deyu] Beihang Univ, Sch Biol Sci & Med Engr, Minist Educ, Key Lab Biomech & Mechanobiol, Beijing 100191, Peoples R China.

[Wang, Daifa] Beihang Univ, State Key Lab Software Dev Environm, Beijing 100191, Peoples R China.

[Song, Xiaolei] Johns Hopkins Univ, Russell H Morgan Dept Radiol & Radiol Sci, Div MR Res, Sch Med, Baltimore, MD 21287 USA.

Reprint Address: Li, DY (reprint author), Beihang Univ, Sch Biol Sci & Med Engr, Minist Educ, Key Lab Biomech & Mechanobiol, Beijing 100191, Peoples R China.

E-mail Addresses: deyuli@buaa.edu.cn

IDS Number: 060MZ

ISSN: 1559-128X

eISSN: 2155-3165

Source Item Page Count: 14

Record 9 of 10

第1作者

Title: Full-Angle Fluorescence Diffuse Optical Tomography With Spatially Coded Parallel Excitation

Author(s): Wang, DF (Wang, Daifa); Liu, X (Liu, Xin); Liu, F (Liu, Fei); Bai, J (Bai, Jing)

Source: IEEE TRANSACTIONS ON INFORMATION TECHNOLOGY IN BIOMEDICINE Volume: 14 Issue: 6 Pages: 1346-1354 DOI: 10.1109/TITB.2010.2077306 Published: NOV 2010

Times Cited in Web of Science Core Collection: 5

Total Times Cited: 5

Accession Number: WOS:000283982200005

Language: English

Document Type: Article

Addresses: [Wang, Daifa; Liu, Xin; Liu, Fei; Bai, Jing] Tsinghua Univ, Sch Med, Dept Biomed Engr, Beijing 100084, Peoples R China.

Reprint Address: Bai, J (reprint author), Tsinghua Univ, Sch Med, Dept Biomed Engr, Beijing 100084, Peoples R China.

E-mail Addresses: daifa.wang@buaa.edu.cn; daifa.wang@buaa.edu.cn

IDS Number: 677II

ISSN: 1089-7771

Source Item Page Count: 9

Record 10 of 10



Title: Medical image retrieval based on unclean image bags

Author(s): Huang, YG (Huang, Yonggang); Zhang, J (Zhang, Jun); Huang, HY (Huang, Heyan); Wang, DF (Wang, Daifa)

Source: MULTIMEDIA TOOLS AND APPLICATIONS Volume: 72 Issue: 3 Pages: 2977-2999 DOI: 10.1007/s11042-013-1589-3 Published: OCT 2014

Times Cited in Web of Science Core Collection: 0

Total Times Cited: 0

Accession Number: WOS:000340550300038

Language: English

Document Type: Article

Addresses: [Huang, Yonggang; Huang, Heyan] Beijing Inst Technol, Beijing Engn Res Ctr High Volume Language Informa, Beijing 100081, Peoples R China.

[Huang, Yonggang; Huang, Heyan] Beijing Inst Technol, Sch Comp Sci & Technol, Beijing 100081, Peoples R China.

[Zhang, Jun] Deakin Univ, Sch Informat Technol, Geelong, Vic 3217, Australia.

[Wang, Daifa] Beihang Univ, Sch Biol Sci & Med Engn, Beijing 100191, Peoples R China.

Reprint Address: Huang, YG (reprint author), Beijing Inst Technol, Beijing Engn Res Ctr High Volume Language Informa, Beijing 100081, Peoples R China.

E-mail Addresses: yonggang.h@gmail.com; jun.zhang@deakin.edu.au; daifa.wang@buaa.edu.cn

IDS Number: AN4IE

ISSN: 1380-7501

eISSN: 1573-7721

Source Item Page Count: 23

文献引用检索证明

作者姓名：汪待发(Wang, Daifa)

经检索“Web of Science 引文索引数据库”，该作者发表的 5 篇论文被引用 **22** 次(in SCIE/SSCI/CPCI-S)，其中他引 **17** 次。

(他引定义：引用文献中不包含被检索作者的引用视为他引。)

检索结果见附件，共 6 页。

检索时间为 2016 年 5 月 20 日。

特此证明！

证明人(签字):

姜成林

证明单位(盖章): 北京航空航天大学图书馆

二〇一六年五月二十日

附件:

Record 1 of 5

Title: Focusing through dynamic tissue with millisecond digital optical phase conjugation

Author(s): Wang, DF (Wang, Daifa); Zhou, EH (Zhou, Edward Haojiang); Brake, J (Brake, Joshua); Ruan, HW (Ruan, Haowen); Jang, M (Jang, Mooseok); Yang, CH (Yang, Changhui)

Source: OPTICA Volume: 2 Issue: 8 Pages: 728-735 DOI: 10.1364/OPTICA.2.000728 Published: AUG 20 2015

Times Cited in Web of Science Core Collection: 8

Total Times Cited: 8

Accession Number: WOS:000364484600012

引证文献共计 7 篇(in SCIE/SSCI/CPCI-S), 其中他引 7 次

Record 1 of 7

Title: Bit-efficient, sub-millisecond wavefront measurement using a lock-in camera for time-reversal based optical focusing inside scattering media

Author(s): Liu, Y (Liu, Yan); Ma, C (Ma, Cheng); Shen, YC (Shen, Yuecheng); Wang, LHV (Wang, Lihong V.)

Source: OPTICS LETTERS Volume: 41 Issue: 7 Pages: 1321-1324 DOI: 10.1364/OL.41.001321 Published: APR 1 2016

Accession Number: WOS:000373225400004

ISSN: 0146-9592

eISSN: 1539-4794

Record 2 of 7

Title: Focusing light through scattering media by full-polarization digital optical phase conjugation

Author(s): Shen, YC (Shen, Yuecheng); Liu, Y (Liu, Yan); Ma, C (Ma, Cheng); Wang, LV (Wang, Lihong V.)

Source: OPTICS LETTERS Volume: 41 Issue: 6 Pages: 1130-1133 DOI: 10.1364/OL.41.001130 Published: MAR 15 2016

Accession Number: WOS:000373042600015

PubMed ID: 26977651

ISSN: 0146-9592

eISSN: 1539-4794

Record 3 of 7

Title: Analyzing the relationship between decorrelation time and tissue thickness in acute rat brain slices using multispeckle diffusing wave spectroscopy

Author(s): Brake, J (Brake, Joshua); Jang, M (Jang, Mooseok); Yang, CH (Yang, Changhui)

Source: JOURNAL OF THE OPTICAL SOCIETY OF AMERICA A-OPTICS IMAGE SCIENCE AND VISION Volume: 33 Issue: 2 Pages: 270-275 DOI: 10.1364/JOSAA.33.000270 Published: FEB 1 2016

Accession Number: WOS:000369098200013

PubMed ID: 26831778

ISSN: 1084-7529

eISSN: 1520-8532

Record 4 of 7

Title: Optical imaging through dynamic turbid media using the Fourier-domain shower-curtain effect

Author(s): Edrei, E (Edrei, Eitan); Scarcelli, G (Scarcelli, Giuliano)

Source: OPTICA Volume: 3 Issue: 1 Pages: 71-74 DOI: 10.1364/OPTICA.3.000071 Published: JAN 20 2016

Accession Number: WOS:000370815300013

ISSN: 2334-2536

Record 5 of 7

Title: Effect of experimental parameters on optimal reflection of light from opaque media

Author(s): Anderson, BR (Anderson, Benjamin R.); Gunawidjaja, R (Gunawidjaja, Ray); Eilers, H (Eilers, Hergen)

Source: PHYSICAL REVIEW A Volume: 93 Issue: 1 Article Number: 013813 DOI:

10.1103/PhysRevA.93.013813 Published: JAN 11 2016

Accession Number: WOS:000367890100017

Author Identifiers:

Author ResearcherID Number ORCID Number

Anderson, Benjamin A-4981-2015 0000-0003-1403-970X

ISSN: 1050-2947

eISSN: 1094-1622

Record 6 of 7

Title: Optical focusing inside scattering media with time-reversed ultrasound microbubble encoded light

Author(s): Ruan, HW (Ruan, Haowen); Jang, M (Jang, Mooseok); Yang, CH (Yang, Changhuei)

Source: NATURE COMMUNICATIONS Volume: 6 Article Number: 8968 DOI: 10.1038/ncomms9968 Published: NOV 2015

Accession Number: WOS:000366382800001

PubMed ID: 26597439

ISSN: 2041-1723

Record 7 of 7

Title: Single-exposure optical focusing inside scattering media using binarized time-reversed adapted perturbation

Author(s): Ma, C (Ma, Cheng); Zhou, FB (Zhou, Fengbo); Liu, Y (Liu, Yan); Wang, LHV (Wang, Lihong V.)

Source: OPTICA Volume: 2 Issue: 10 Pages: 869-876 DOI: 10.1364/OPTICA.2.000869 Published: OCT 20 2015

Accession Number: WOS:000364485100008

Author Identifiers:

Author ResearcherID Number ORCID Number

Wang, Lihong A-7147-2009 0000-0001-9783-4383

ISSN: 2334-2536

Record 2 of 5

Title: Noncontact full-angle fluorescence molecular tomography system based on rotary mirrors

Author(s): Wang, DF (Wang, Daifa); He, J (He, Jin); Qiao, HT (Qiao, Huiting); Li, P (Li, Ping); Fan, YB (Fan, Yubo); Li, DY (Li, Deyu)

Source: APPLIED OPTICS Volume: 54 Issue: 23 Pages: 7062-7070 DOI: 10.1364/AO.54.007062 Published: AUG 10 2015

Times Cited in Web of Science Core Collection: 0

Total Times Cited: 0

Accession Number: WOS:000359356400016

引证文献共计 0 篇(in SCIE/SSCI/CPCI-S)

Record 3 of 5

Title: High-Performance Fluorescence Molecular Tomography through Shape-Based Reconstruction Using Spherical Harmonics Parameterization

Author(s): Wang, DF (Wang, Daifa); He, J (He, Jin); Qiao, HT (Qiao, Huiting); Song, XL (Song, Xiaolei); Fan, YB (Fan, Yubo); Li, DY (Li, Deyu)

Source: PLOS ONE Volume: 9 Issue: 4 Article Number: e94317 DOI: 10.1371/journal.pone.0094317 Published: APR 14 2014

Times Cited in Web of Science Core Collection: 4

Total Times Cited: 4

Accession Number: WOS:000336970400030

引证文献共计 4 篇(in SCIE/SSCI/CPCI-S), 其中他引 3 次

Record 1 of 4

Title: Noncontact full-angle fluorescence molecular tomography system based on rotary mirrors

Author(s): Wang, DF (Wang, Daifa); He, J (He, Jin); Qiao, HT (Qiao, Huiting); Li, P (Li, Ping); Fan, YB (Fan, Yubo); Li,

DY (Li, Deyu)

Source: APPLIED OPTICS Volume: 54 Issue: 23 Pages: 7062-7070 DOI: 10.1364/AO.54.007062 Published: AUG 10 2015

Accession Number: WOS:000359356400016

PubMed ID: 26368376

ISSN: 1559-128X

eISSN: 2155-3165

Record 2 of 4

Title: Fluorescence molecular tomography reconstruction via discrete cosine transform-based regularization

Author(s): Shi, JW (Shi, Junwei); Liu, F (Liu, Fei); Zhang, JL (Zhang, Jiulou); Luo, JW (Luo, Jianwen); Bai, J (Bai, Jing)

Source: JOURNAL OF BIOMEDICAL OPTICS Volume: 20 Issue: 5 Article Number: 055004 DOI: 10.1117/1.JBO.20.5.055004 Published: MAY 2015

Accession Number: WOS:000356241900052

PubMed ID: 25970083

Author Identifiers:

Author ResearcherID Number ORCID Number

Luo, Jianwen D-5612-2011 0000-0001-9215-5568

ISSN: 1083-3668

eISSN: 1560-2281

Record 3 of 4

Title: A modularly designed fluorescence molecular tomography system for multi-modality imaging

Author(s): Wang, GH (Wang, Guohe); Zhang, B (Zhang, Bin); Ding, YC (Ding, Yichen); He, Y (He, Yun); Chen, JS (Chen, Jingsong); Lu, YY (Lu, Yanye); Jiang, XY (Jiang, Xiaoyun); Shi, JW (Shi, Junwei); Bai, J (Bai, Jing); Ren, QS (Ren, Qiushi); Li, CH (Li, Changhui)

Source: JOURNAL OF X-RAY SCIENCE AND TECHNOLOGY Volume: 23 Issue: 2 Pages: 147-156 DOI: 10.3233/XST-150478 Published: 2015

Accession Number: WOS:000353063200004

PubMed ID: 25882728

ISSN: 0895-3996

eISSN: 1095-9114

Record 4 of 4

Title: Shape-parameterized diffuse optical tomography holds promise for sensitivity enhancement of fluorescence molecular tomography

Author(s): Wu, LH (Wu, Linhui); Wan, WB (Wan, Wenbo); Wang, X (Wang, Xin); Zhou, ZX (Zhou, Zhongxing); Li, J (Li, Jiao); Zhang, LM (Zhang, Limin); Zhao, HJ (Zhao, Huijuan); Gao, F (Gao, Feng)

Source: BIOMEDICAL OPTICS EXPRESS Volume: 5 Issue: 10 Pages: 3640-3659 DOI: 10.1364/BOE.5.003640 Published: OCT 1 2014

Accession Number: WOS:000343135200031

PubMed ID: 25360379

ISSN: 2156-7085

Record 4 of 5

Title: Fluorescence molecular tomography using a two-step three-dimensional shape-based reconstruction with graphics processing unit acceleration

Author(s): Wang, DF (Wang, Daifa); Qiao, HT (Qiao, Huiting); Song, XL (Song, Xiaolei); Fan, YB (Fan, Yubo); Li, DY (Li, Deyu)

Source: APPLIED OPTICS Volume: 51 Issue: 36 Pages: 8731-8744 DOI: 10.1364/AO.51.008731 Published: DEC 20 2012

Times Cited in Web of Science Core Collection: 6

Total Times Cited: 7

Accession Number: WOS:000312783700027

引证文献共计 6 篇(in SCIE/SSCI/CPCI-S), 其中他引 5 次

Record 1 of 6

Title: Generalized total variation iterative constraint strategy in limited angle optical diffraction tomography

Author(s): Krauze, W (Krauze, Wojciech); Makowski, P (Makowski, Piotr); Kujawska, M (Kujawska, Malgorzata); Kus, A (Kus, Arkadiusz)

Source: OPTICS EXPRESS Volume: 24 Issue: 5 Pages: 4924-4936 DOI: 10.1364/OE.24.004924 Published: MAR 7 2016

Accession Number: WOS:000371435000058

ISSN: 1094-4087

Record 2 of 6

Title: Spectral selective fluorescence molecular imaging with volume holographic imaging system

Author(s): Lv, YL (Lv, Yanlu); Zhang, JL (Zhang, Jiulou); Liu, F (Liu, Fei); Shi, JW (Shi, Junwei); Guang, HZ (Guang, Huizhi); Bai, J (Bai, Jing); Luo, JW (Luo, Jianwen)

Source: JOURNAL OF INNOVATIVE OPTICAL HEALTH SCIENCES Volume: 9 Issue: 2 Article Number: 1650010 DOI: 10.1142/S1793545816500103 Published: MAR 2016

Accession Number: WOS:000374134100006

ISSN: 1793-5458

eISSN: 1793-7205

Record 3 of 6

Title: A reconstruction approach in wavelet domain for fluorescent molecular tomography via rotated sources illumination

Author(s): Zou, W (Zou, Wei); Wang, JJ (Wang, Jiajun); Hu, DF (Hu, Danfeng); Wang, WX (Wang, Wenxia)

Source: BIOMEDICAL ENGINEERING ONLINE Volume: 14 Article Number: 86 DOI: 10.1186/s12938-015-0080-y Published: SEP 30 2015

Accession Number: WOS:000361936400001

PubMed ID: 26419738

ISSN: 1475-925X

Record 4 of 6

Title: Full domain-decomposition scheme for diffuse optical tomography of large-sized tissues with a combined CPU and GPU parallelization

Author(s): Yi, X (Yi, Xi); Wang, X (Wang, Xin); Chen, WT (Chen, Weiting); Wan, WB (Wan, Wenbo); Zhao, HJ (Zhao, Huijuan); Gao, F (Gao, Feng)

Source: APPLIED OPTICS Volume: 53 Issue: 13 Pages: 2754-2765 DOI: 10.1364/AO.53.002754 Published: MAY 1 2014

Accession Number: WOS:000335493000011

PubMed ID: 24921857

ISSN: 1559-128X

eISSN: 2155-3165

Record 5 of 6

Title: High-Performance Fluorescence Molecular Tomography through Shape-Based Reconstruction Using Spherical Harmonics Parameterization

Author(s): Wang, DF (Wang, Daifa); He, J (He, Jin); Qiao, HT (Qiao, Huiting); Song, XL (Song, Xiaolei); Fan, YB (Fan, Yubo); Li, DY (Li, Deyu)

Source: PLOS ONE Volume: 9 Issue: 4 Article Number: e94317 DOI: 10.1371/journal.pone.0094317 Published: APR 14 2014

Accession Number: WOS:000336970400030

PubMed ID: 24732826

Author Identifiers:

Author ResearcherID Number ORCID Number

Song, Xiaolei B-3000-2014



ISSN: 1932-6203

Record 6 of 6

Title: Three-dimensional photoacoustic tomography based on graphics-processing-unit-accelerated finite element method

Author(s): Peng, K (Peng, Kuan); He, L (He, Ling); Zhu, ZQ (Zhu, Ziqiang); Tang, JT (Tang, Jingtian); Xiao, JY (Xiao, Jiaying)

Source: APPLIED OPTICS Volume: 52 Issue: 34 Pages: 8270-8279 DOI: 10.1364/AO.52.008270 Published: DEC 1 2013

Accession Number: WOS:000328449900014

PubMed ID: 24513828

ISSN: 1559-128X

eISSN: 2155-3165

Record 5 of 5

Title: Full-Angle Fluorescence Diffuse Optical Tomography With Spatially Coded Parallel Excitation

Author(s): Wang, DF (Wang, Daifa); Liu, X (Liu, Xin); Liu, F (Liu, Fei); Bai, J (Bai, Jing)

Source: IEEE TRANSACTIONS ON INFORMATION TECHNOLOGY IN BIOMEDICINE Volume: 14 Issue: 6
Pages: 1346-1354 DOI: 10.1109/TITB.2010.2077306 Published: NOV 2010

Times Cited in Web of Science Core Collection: 5

Total Times Cited: 5

Accession Number: WOS:000283982200005

引证文献共计 5 篇(in SCIE/SSCI/CPCI-S), 其中他引 2 次

Record 1 of 5

Title: Noncontact full-angle fluorescence molecular tomography system based on rotary mirrors

Author(s): Wang, DF (Wang, Daifa); He, J (He, Jin); Qiao, HT (Qiao, Huiting); Li, P (Li, Ping); Fan, YB (Fan, Yubo); Li, DY (Li, Deyu)

Source: APPLIED OPTICS Volume: 54 Issue: 23 Pages: 7062-7070 DOI: 10.1364/AO.54.007062 Published: AUG 10 2015

Accession Number: WOS:000359356400016

PubMed ID: 26368376

ISSN: 1559-128X

eISSN: 2155-3165

Record 2 of 5

Title: High-Performance Fluorescence Molecular Tomography through Shape-Based Reconstruction Using Spherical Harmonics Parameterization

Author(s): Wang, DF (Wang, Daifa); He, J (He, Jin); Qiao, HT (Qiao, Huiting); Song, XL (Song, Xiaolei); Fan, YB (Fan, Yubo); Li, DY (Li, Deyu)

Source: PLOS ONE Volume: 9 Issue: 4 Article Number: e94317 DOI: 10.1371/journal.pone.0094317 Published: APR 14 2014

Accession Number: WOS:000336970400030

PubMed ID: 24732826

Author Identifiers:

Author ResearcherID Number ORCID Number

Song, Xiaolei B-3000-2014

ISSN: 1932-6203

Record 3 of 5

Title: On the use of the Cramer-Rao lower bound for diffuse optical imaging system design

Author(s): Pera, V (Pera, Vivian); Brooks, DH (Brooks, Dana H.); Niedre, M (Niedre, Mark)

Source: JOURNAL OF BIOMEDICAL OPTICS Volume: 19 Issue: 2 Article Number: 025002 DOI: 10.1117/1.JBO.19.2.025002 Published: FEB 2014

Accession Number: WOS:000332830900015



PubMed ID: 24503635

ISSN: 1083-3668

eISSN: 1560-2281

Record 4 of 5

Title: Fluorescence molecular tomography using a two-step three-dimensional shape-based reconstruction with graphics processing unit acceleration

Author(s): Wang, DF (Wang, Daifa); Qiao, HT (Qiao, Huiting); Song, XL (Song, Xiaolei); Fan, YB (Fan, Yubo); Li, DY (Li, Deyu)

Source: APPLIED OPTICS Volume: 51 Issue: 36 Pages: 8731-8744 DOI: 10.1364/AO.51.008731 Published: DEC 20 2012

Accession Number: WOS:000312783700027

PubMed ID: 23262613

Author Identifiers:

Author ResearcherID Number ORCID Number

Song, Xiaolei B-3000-2014

ISSN: 1559-128X

eISSN: 2155-3165

Record 5 of 5

Title: Optical Tomography

Author(s): Haisch, C (Haisch, Christoph)

Edited by: Cooks RG; Yeung ES

Source: ANNUAL REVIEW OF ANALYTICAL CHEMISTRY, VOL 5 Book Series: Annual Review of Analytical Chemistry Volume: 5 Pages: 57-77 DOI: 10.1146/annurev-anchem-062011-143138 Published: 2012

Accession Number: WOS:000307956200005

PubMed ID: 22524216

Author Identifiers:

Author ResearcherID Number ORCID Number

Haisch, Christoph I-3591-2012 0000-0002-6344-6750

ISSN: 1936-1327

ISBN: 978-0-8243-4405-4



文献收录检索证明

作者姓名: 汪待发(Wang, Daifa)

经检索“网络版工程索引(EI Compendex)”数据库, 该作者发表的
论文(2010-2016年), 被收录3篇。

检索结果见附件, 共1页。

检索时间为2016年5月20日。

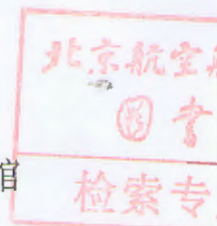
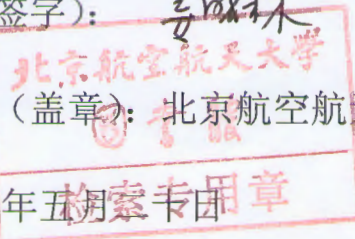
特此证明!

证明人(签字):

姜成林

证明单位(盖章): 北京航空航天大学图书馆

二〇一六年五月二十日





附件:

1. Performance of fluorescence molecular tomography with hybrid diffuse optical tomography guidance and normalized born method ^{第1作者}

Wang, Daifa (State Key Laboratory of Software Development Environment, Beihang University, Beijing 100191, China); Wang, Ling; Fan, Yubo; Li, Deyu Source: Proceedings - 2011 4th International Conference on Biomedical Engineering and Informatics, BMEI 2011, v 1, p 434-438, 2011, Proceedings - 2011 4th International Conference on Biomedical Engineering and Informatics, BMEI 2011

Database: Compendex

Accession number: 20120314690514

2. Optical tomography for dense scattering media using DLP based structured illumination ^{第1作者}

Wang, Daifa (Key Laboratory for Biomechanics and Mechanobiology, School of Biological Science and Medical Engineering, Beihang University, XueYuan Road No.37, HaiDian District, Beijing 100191, China); He, Jin; Li, Deyu Source: Asia Communications and Photonics Conference, ACP, 2013, Asia Communications and Photonics Conference, ACP 2013

Database: Compendex

Accession number: 20142017711215

3. 2D shape-based fluorescence molecular tomography through hybrid genetic algorithm based optimization ^{第1作者}

Wang, Daifa (State Key Laboratory of Software Development Environment, Beihang University, Beijing, China); Wang, Ling; Fan, Yubo; Li, Deyu Source: IFMBE Proceedings, v 39 IFMBE, p 1018-1021, 2013, World Congress on Medical Physics and Biomedical Engineering

Database: Compendex

Accession number: 20131616209591





中文核心期刊检索证明

经检索《中文核心期刊要目总览（2014年版）》（朱强、何峻、蔡蓉华主编，北京大学出版社，ISBN: 978-7-301-26189-7），下列1种期刊为核心期刊：

1.【期刊名称】中国科技论文在线

【ISSN】1673-7180

【核心期刊版次】2011/2014

注：该刊2012年起改名为《中国科技论文》，ISSN为2095-2783。

检索时间为2016年5月20日。

特此证明！

证明人（签字）

姜树林

证明单位（盖章）：北京航空航天大学图书馆

检索专用章

二〇一六年五月二十日

2016年专业技术职务评聘论文发表及收录情况证明表

单位：生物与医学工程学院

姓名	汪待发	工作证号	09259	现任职称	讲师	任职时间	2010年10月	
任现职以来发表论文及收录情况：收录类别、作者贡献（第一、通讯等）仅计算1次；论文收录以图书馆检索证明为准，未检索到的来源刊论文仅计算1篇								
类别	合计	SCI	SSCI	CSSCI	EI	ISTP	中文核心期刊	其他
一、符合职称申报条件论文	10	5			3		2	0
其中：1. 第一作者	8	5			3			0
2. 学生第一本人第二作者								
3. 通讯作者	2						2	
二、其他	5	5						

本人承诺以上所填属实，如与事实不符，本人愿承担一切责任。

本人签字：汪待发

日期：2016年06月01日

单位负责人签字（加盖公章）：姜成林

日期： 年 月 日

图书馆意见：

经检索，上表所列论文发表及收录情况属实。

经检索，上表中被SCI/EI数据库收录的文章数量情况属实。

经检索，北大版核心期刊之刊物种数情况属实。

证明人：

姜成林 盖章：

日期：2016年6月2日

检索专用章

注：1. 申请人认真如实填写相关信息后A4纸单面打印；

2. 对于学生第一本人第二作者的论文需填写《2016年专业技术职务评聘研究生指导情况证明表》由所在单位认定，主管副院长签字，学院盖章，研究生院审定，一并去图书馆认定。

北京航空航天大学专业技术职务评审 任现职以来主要教学业绩水平证明表

姓 名 汪待发
 现任专业技术职务 讲师
 申请专业技术职务 副教授

单位 生物与医学工程学院
 任现职时间 2010.10
 填表日期 2016.05.17

一、教学总体情况

任现职以来，独立指导硕士研究生 4 届 5 人，其中毕业 1 人，在读 4 人；指导本科毕设 4 人，主讲本科生课 2 门，其中必修课 0 门；主讲研究生课 1 门、其中学位课 1 门。年均授课 50 学时。

二、本科教学工作量

教学工作量	课程代码	课程名称	学年-学期	课程学时	本人授课学时	授课对象 (本科生/留学生等)	授课次数 (几轮次)	课程性质
	F10D 3250	数值计算方法	2011-2012-1 2012-2013-1 2013-2014-1	32	30	本科生	3	选修
	E10B 3320	生物医学信号处理	2011-2012-1 2012-2013-1 2013-2014-1	48	8	本科生	3	必修
	E10B 3330	生物医学图像处理	2010-2011-2 2011-2012-2	52	7	本科生	2	必修
	C10D 1110	C 语言程序设计	2010-2011-2	48	2	本科生	1	必修
	F10C 3141	临检测试技术及装备	2015-2016-2	32	32	本科生	1	必修
	F10C 3911	生物医学仪器	2015-2016-2	32	8	本科生	1	必修
	G10C 4430	专业综合实验	2012-2013-1 2013-2014-1 2015-2016-1	16 周	40	本科生	3	必修

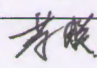
注：课程性质为校级核心、专业基础核心、专业方向核心、必修、选修、公共选修等。

院(系)确认人签字：


教务处确认人签字：

教学含 成果材 奖	获奖时间	获奖项目名称	获奖等级	本人排名
	无			

教学研究	起止时间	教改立项项目名称(含编写教材、讲义)	项目来源	完成情况	本人作用
	无				
其它	任务完成情况(含辅导员、军训、学生工作论文、指导青年教师及青年技术人员社会实践等)				本人作用
	指导3届本科生毕业设计, 合计4名本科生(魏俊生、贺进、张烨、祝永强)				指导教师
	指导3届本科生冯如杯竞赛, 获得一等和二等奖(祝永强、曹桂明、李秦、苑译; 朱君、郑燕春、谢风华)				指导教师
	指导一届本科生 SRTP (朱君、郑燕春、谢风华)				指导教师

院(系)确认人签字: 

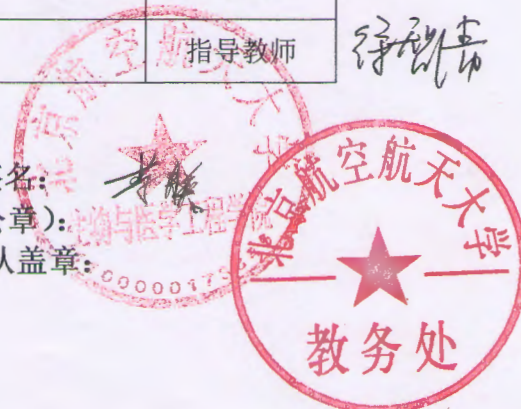
教务处确认人签字:

本人确认表内所填内容属实 签名: 

院(系)确认人签字(公章):

教务处确认盖章:

日期:



三、研究生教学工作量

教学工作量	课程名称	起止时间	课程学时	本人授课学时	授课对象 (研究生/留学生等)	授课次数 (几轮次)	课程类型
	生理信号检测与处理实验	2013.04-2013.05	18	9	研究生	1	学位课
	生物医学图像分析	2013.03-2013.07	32	4	研究生	1	学位课
	生物医学成像技术	2013.03-2013.07	32	2	研究生	1	学位课

院(系)确认人签字:

研究生院确认人签字:

教学成果奖	获奖时间	获奖项目名称		获奖等级	本人排名
	无				
教学研究	时间	项目名称	项目来源	完成情况	本人作用
	无				
其它	任务完成情况(含辅导员、学生工作论文、指导青年教师及青年技术人员社会实践等)				本人作用
	指导5名硕士生(孟云、贺进、祝永强、张岫、宋超)				指导教师

院(系)确认人签字:

研究生院确认人签字:

本人确认表内所填内容属实 签名:

院(系)确认人签字(公章):

研究生院确认人签字(公章):

日期:

2016年专业技术职务评聘专利与获奖情况认定表


单位	生物与医学工程学院	姓名	汪待发	工作证号	9259	任职时间	2010年10月		
1. 获批专利情况									
任现职以来以第一享有人(含学生第一本人第二)名义共授权专利 <u>4</u> 项; 任现职以来共获得已授权专利情况:									
类别	专利数	发明专利		实用新型		外观设计			
第一享有人	4	4		0		0			
总数量	6	6		0		0			
序号	专利名称	专利类型	授权日期	批准机构	专利号	仅限首次授权			
						权利单位	人数	本人排名	
1	一种多光学信息同步检测的双参数荧光分子断层成像装置及方法	中国发明专利	2012.07.04	中华人民共和国国家知识产权局	CN201110090186.0	北京航空航天大学	3	1	
2	一种基于旋转镜的全角度荧光分子断层成像装置	中国发明专利	2014.04.16	中华人民共和国国家知识产权局	CN201210394893.3	北京航空航天大学	6	1	
3	一种基于单滑环和无线控制激发光扫描的荧光分子断层成像装置及方法	中国发明专利	2015.11.04	中华人民共和国国家知识产权局	CN201310740964.5	北京航空航天大学	4	1	
4	基于生物电阻抗的全视角椎弓根手术辅助导航装置及方法	中国发明专利	2016.01.13	中华人民共和国国家知识产权局	CN103750895B	北京航空航天大学	3	1	
5	一种基于彩色探测器的体外过敏原定量检测装置及其方法	中国发明专利	2015.04.15	中华人民共和国国家知识产权局	CN201310163680	北京航空航天大学	5	3	
6	一种基于多光谱成像的体外过敏原定量检测装置及其方法	中国发明专利	2014.07.16	中华人民共和国国家知识产权局	CN201210064231	北京航空航天大学	5	3	
7									
8									
本人承诺以上所填属实。									
承诺人: 汪待发				学院审核人(盖章): 史永青					
科研部门审核意见:									
经审核, 上表所列奖项中, 符合首次授权状态的归档专利共 <u>6</u> 项(序号: 1-6)。									
审核人: 史永青 2016.5.30.				盖章: [红色印章]					

2.获奖情况

任现职以来获得国家级教学/科研成果奖 0 项；省部级教学/科研成果一等奖前五名、二等奖前三名或三等奖第一完成人共 0 项。请填写任现职以来获得教学、科研、管理奖励情况。


序号	奖励名称	颁奖部门	奖励级别	获奖时间	人数	本人排名
1	无					
2						
3						
4						
5						
6						

本人承诺以上所填属实。

承诺人: 汪待发 学院审核人 (盖章): 

科研部门审核意见:

经审核, 上表所列奖项中, 情况属实的国家级科研成果奖 项 (序号:), 省部级科研成果 项 (序号:)。

审核人: 盖章: 

注: 1. 申请人认真如实填写相关信息后A4纸单面打印;
2. 申请人签字确认后将此表及相关证明材料交至所在学院, 由学院统一送至科研院审核;
3. 申请人填写申报材料时以审核后的信息为准。

课题信息查询

经费负责人：汪待发

工作证号：09259

查询范围：2010-07-23到2016-05-23

总实到经费：159

单位：万元

编号	经费号	项目名称	项目来源	实到经费	设备费	外协费	课题性质	项目负责人
1	30-4511-01	基于近红外光谱脑功能成像的新生儿情绪加工脑机制研究	教育部	8	0	0.9	非51合同	汪待发
2	54-2401	多通道近红外光脑功能成像仪NIR-BRAIN研制	北京心灵方舟科技发展有限公司	95	2.3	40	技术开发	汪待发
3	30-2147	双源智能型负压创口治疗仪的研发	教育部	3	0	0	非51合同	汪待发
4	36-0380	融合多光学信息的双参数荧光分子断层成像的理论和算法研究	博士点基金	4	0	0	非51合同	汪待发
5	37-5411	融合多光学信息的双参数荧光分子断层成像方法的研究	国家自然科学基金	32	0	5.3	非51合同	汪待发
6	30-1315	多光学信息融合的双参数荧光分子断层成像的理论研究	工信部：“唯实”人才培育基金	2	0	0	非51合同	汪待发
7	27-0382	科研项目	工信部	15	0	0	非51合同	李未

科学技术研究院

查询日期：2016年05月24日

国家自然科学基金资助项目批准通知

北京航空航天大学 汪待发同志：

根据《国家自然科学基金条例》的规定和专家评审意见，国家自然科学基金委员会决定资助您的申请项目。请您登录科学基金项目管理 ISIS 网络信息系统 (<https://isis.nsfc.gov.cn>)，获取《国家自然科学基金资助项目研究计划书》（以下简称计划书）。您登录该系统的用户名和密码已通过电子邮件方式发送至您在申请书中填写的电子邮箱。

请您按照本通知的研究期限、资助金额和修改意见填写计划书，要求纸质原件（一式两份）和电子文档同时报送（请保证电子文档和纸质文件内容一致）。电子文档由申请人上传到科学基金网络信息系统 (<https://isis.nsfc.gov.cn>)，或用电子邮件发送到：report@pro.nsfc.gov.cn 信箱，电子文档报送截止日期为 9 月 12 日；纸质原件送所在单位审核盖章后，由依托单位在 9 月 12 日前统一报送。

如对批准意见有异议，须在上述电子文档报关截止日期前提出；未说明理由逾期不报计划书者，视为自动放弃接受资助。



附：批准意见表（见背面）

77

附：批准意见表

项目批准号	61108084	归口管理部门	信息科学部	资助领域 分类代码	F051206
项目名称	融合多光学信息的双参数荧光分子断层成像方法的研究				
资助类别	青年科学基金项目	亚类说明			
附注说明					
项目负责人	汪待发	依托单位	北京航空航天大学		
资助金额	32.00 万元	研究期限	2012.01 至 2014.12		
对研究方案的修改意见：					

课题编号: 2011AA02A104

密 级: 公开级

国家高技术研究发展计划(863 计划) 课题任务书

课题名称:	基于免疫学方法的自动化专用检测分析仪器研制
所属项目:	体外诊断技术产品开发
所属技术领域:	生物和医药技术领域
课题管理单位:	中国生物技术发展中心
课题承担单位:	北京航空航天大学
起止年限:	2011 年至 2012 年

中华人民共和国科学技术部

2012 年 03 月 06 日

003 2011AA02A104



六、课题参加人员基本情况表

填表说明：1、职称分类：A、正高级 B、副高级 C、中级 D、初级 E、其他；

2、投入本课题的全时工作时间（人月）是指在课题实施期间该人总共为课题工作的满月度工作量；累计是指课题组所有人员投入人月之合。

3、课题固定研究人员需填写人员明细；

4、是否有工资性收入：Y、是 N、否；

5、人员分类代码：A、课题负责人 B、课题骨干 C、其他研究人员；

序号	姓名	性别	出生日期	证件类型	证件号码	技术职称	职务	专业	投入本课题的全时工作时间（人月）	人员分类	在课题中分担的任务	是否有工资性收入	工作单位
1	李德玉	男	1967-03-21	身份证	510102196703218475	正高级	副院长	工学	12	课题负责人	总体负责	是	北京航空航天大学
2	孙建堂	男	1977-01-08	身份证	370102197701084512	正高级	无	工学	14	其他研究人员	全自动血型配血系统部分负责	是	苏州生物医学工程技术研究所
3	蒲放	男	1973-10-28	身份证	512930197310280257	副高级	系主任	工学	8	其他研究人员	算法研究	是	北京航空航天大学
4	汪待发	男	1984-04-21	身份证	340824198404212819	中级	讲师	工学	16	其他研究人员	系统研制	是	北京航空航天大学
5	吴再辉	男	1980-06-25	身份证	220104198006250333	副高级	副研究员	电子与信息类	20	其他研究人员	电子学设计	是	苏州生物医学工程技术研究所
6	刘铁梅	女	1965-07-23	身份证	220104196507233321	正高级	科主任	临床医学与医学技术类	12	其他研究人员	临床测试评价负责	是	吉林大学
7	赵国庆	男	1965-11-20	身份证	220104196511201314	正高级	副院长	临床医学与医学技术类	12	其他研究人员	临床样本制备	是	吉林大学
8	王玲	女	1983-01-09	身份证	513821198301090201	中级	讲师	工学	16	其他研究人员	系统与仪器研制	是	北京航空航天大学
9	刘广兴	男	1983-07-23	身份证	650103198307231818	中级	无	工学	8	其他研究人员	实验室样本采集与处理	是	苏州生物医学工程技术研究所

10	郑丽沙	女	1979-03-20	身份证	510282197903203800	中级	讲师	医学	6	其他研究人员	方法学设计	是	北京航空航天大学
11	易宗春	男	1971-01-03	身份证	420104197101031633	副高级	系主任	生物科学类	16	其他研究人员	过敏原检测基础研究	是	北京航空航天大学
12	魏仲航	女	1964-05-20	身份证	220102196405203401	正高级	副院长	临床医学与医学技术类	12	其他研究人员	临床对比试验	是	吉林大学
13	王海兵	男	1974-07-25	身份证	230202197407250633	中级	生产总监	生物科学类	12	其他研究人员	过敏原试剂条部分总体协调	是	苏州浩欧博生物医药有限公司
14	姜洋	男	1975-05-05	身份证	220104197505051334	中级	无	临床医学与医学技术类	16	其他研究人员	临床试验	是	吉林大学
15	张晓阳	女	1981-11-27	身份证	210311198111270929	初级	工艺工程师	生物科学类	12	其他研究人员	过敏原试剂条测试	是	苏州浩欧博生物医药有限公司
16	袁春辉	男	1979-08-30	身份证	150429197908301233	其他	工程师	工学	20	其他研究人员	光学设计	是	苏州长光华医生物医学工程有限公司
17	陈卿	男	1984-12-26	身份证	320581198412261710	中级	无	工学	14	其他研究人员	软件设计	是	苏州生物医学工程技术研究所
18	尹焕才	男	1982-01-05	身份证	22042119820105271x	其他	助理研究员	生物科学类	8	其他研究人员	免疫学试验	是	苏州生物医学工程技术研究所
19	陈小三	男	1976-03-13	身份证	37012119760313743X	其他	技术总监	生物科学类	12	其他研究人员	过敏原试剂条研发	是	苏州浩欧博生物医药有限公司
20	程文播	男	1984-12-31	身份证	460036198412315518	其他	助理研究员	工学	20	其他研究人员	电子学设计	是	苏州生物医学工程技术研究所
21	吴利娅	女	1971-11-18	身份证	330323197111180024	其他	副总经理	预防医学类	12	其他研究人员	方法学设计	是	苏州浩欧博生物医药有限公司
22	孙海旋	男	1985-09-01	身份证	320323198509010714	其他	实习研究员	机械类	20	其他研究人员	机械设计	是	苏州生物医学工程技术研究所
23	赵文姬	女	1978-09-18	身份证	130228197809182047	中级	研发工程师	生物科学类	12	其他研究人员	过敏原试剂条研发	是	苏州浩欧博生物医药有限公司
24	吴冬	男	1984-05-05	身份证	220721198405050012	其他	工程师	机械类	20	其他研究人员	机械设计	是	苏州长光华医生物医学工程有限公司

25	钱俊	男	1983-08-05	身份证	320981198308051970	其他	实习研究员	工学	20	其他研究人员	电子学设计	是	苏州生物医学工程技术研究所
26	李慧	女	1984-08-02	身份证	220204198408022144	其他	学生	工学	16	其他研究人员	过敏原原理基础研究	否	北京航空航天大学
27	李双	男	1984-01-25	身份证	220323198401254510	其他	学生	工学	8	其他研究人员	机械设计	否	北京航空航天大学
28	郭萌	男	1988-09-28	身份证	131125198809280035	其他	学生	工学	8	其他研究人员	电子电路开发	否	北京航空航天大学
29	李琦	男	1981-11-12	身份证	420111198111124057	其他	学生	工学	16	其他研究人员	过敏原系统研发	否	北京航空航天大学
30	杨京芸	女	1987-04-06	身份证	620102198704065022	其他	学生	工学	8	其他研究人员	光学设计	否	北京航空航天大学
31	王颖	女	1988-05-12	身份证	110105198805127324	其他	学生	工学	8	其他研究人员	电子电路开发	否	北京航空航天大学
32	王典	女	1986-02-15	身份证	230206198602150929	其他	学生	工学	8	其他研究人员	测试软件开发及测试	否	北京航空航天大学
33	陈颀	女	1988-12-11	身份证	360622198812110029	其他	学生	工学	20	其他研究人员	软件开发	否	北京航空航天大学
34	吴帆	男	1987-09-21	身份证	110103198709210950	其他	学生	工学	8	其他研究人员	机械传动	否	北京航空航天大学
					固定研究人员合计				450	/	/	/	/
					流动人员或临时聘用人员合计				0	/	/	/	/
					累计				450	/	/	/	/

密级：公开级

国家科技支撑计划课题任务书

项目 编号： 2012BAI19B00

项目 名称： 重大慢病筛查和监测新设备研发

项目组织单位： 医疗器械产业技术创新战略联盟、中国医疗器械行业协会

课题 编号： 2012BAI19B04

课题 名称： 心脑血管硬化与狭窄预警和诊断技术与设备开发

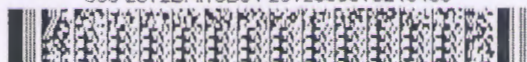
课题承担单位： 北京麦邦光电仪器有限公司、北京航空航天大学

课题起止日期： 2012 年 01 月 01 日至 2015 年 12 月 31 日

编制 日期： 2012 年 02 月 20 日

中华人民共和国科学技术部制

009 2012BAI19B04 2012030519240458



五、课题的承担单位、参加单位及主要研究人员

填表说明：1. 职称分类：A、正高级 B、副高级 C、中级 D、初级 E、其他；
2. 人员分类代码：A、课题负责人 B、课题骨干 C、其他研究人员；
3. 是否有工资性收入：Y、是 N、否；
4. 课题固定研究人员需填写人员名单；

序号	姓 名	证件类型	证件号码	工作单位	技术职称	投入本课题的全时 工作时间（人月）	是否有工 资性收入	人员分类
1	李淑宇	身份证	41290119760822050X	北京航空航天大学	副高级	30	是	课题负责人
2	吴豪杰	身份证	360124198302010015	北京麦邦光电仪器有限公司	初级	32	是	课题骨干
3	李晓明	身份证	132521197704245711	北京航空航天大学	副高级	20	是	课题骨干
4	王玲	身份证	513821198301090201	北京航空航天大学	中级	32	是	课题骨干
5	汪待发	身份证	340824198404212819	北京航空航天大学	中级	32	是	课题骨干
6	刘洪运	军官证	2426071	中国人民解放军总医院	中级	20	是	课题骨干
7	郭萌	身份证	131125198809280035	北京航空航天大学	其他	20	否	课题骨干
8	李双	身份证	220323198401254510	北京航空航天大学	其他	32	否	课题骨干
9	杨世胜	身份证	140225198012083719	北京麦邦光电仪器有限公司	初级	40	是	课题骨干
10	刘忠英	身份证	110108196310123815	北京麦邦光电仪器有限公司	副高级	32	是	课题骨干
11	刘光荣	军官证	2404312	中国人民解放军总医院	副高级	20	是	其他研究人员
12	刘美丽	身份证	142431197604050027	北京航空航天大学	中级	32	是	其他研究人员
13	王典	身份证	230206198602150929	北京航空航天大学	其他	32	否	其他研究人员
14	费蔚春	身份证	110105197410055317	北京麦邦光电仪器有限公司	初级	40	是	其他研究人员
15	王颖	身份证	110105198805127324	北京航空航天大学	其他	40	否	其他研究人员
16	王秀清	身份证	152631198009083016	北京麦邦光电仪器有限公司	初级	40	是	其他研究人员

课题固定研究人员合计全时工作时间(人月): 494

证明

兹证明生物与医学工程学院汪待发同志（职工编号：09259），
于 2010 年获批北航“蓝天新秀”称号。

特此证明。



证 明

兹证明汪待发于 2011、2012、2013、2015 年终考核被评为
院优秀。

特此证明。



荣誉证书

HONORARY CREDENTIAL

汪待发 老师：

在第23届“冯如杯”学生学术科技作品竞赛中，您指导的《脑皮层血流实时监测的近红外功能成像系统》荣获一等奖。为表彰您的辛勤劳动，特将您评为优秀指导教师。

特发此证，以资鼓励。

北京航空航天大学

二〇一六年六月

⑫

留学回国人员证明

(2015) 洛 教(文) 证字 1676 号

兹证明 汪待发 (男 ☒、女 ☐) 护照号码 E30087694) 系我国

CALIFORNIA INSTITUTE OF TECHNOLOGY

在 美 国 加州理工学院 学校(单位)

的高级研究学者 ☐、访问学者 ☒、博士后 ☐、博士研究生 ☐、硕士研究生 ☐、

本科生 ☐、大专生 ☐、其他留学人员 ☐

在我驻外使(领)馆报到日期 2014 年 04 月 03 日

注册入学日期 2014 年 04 月 03 日

毕(结)业日期 2015 年 09 月 19 日

拟回国日期 2015 年 09 月 19 日

毕(结)业证书名称 _____ 号码 _____

备注(留学经历描述) _____

留学回国人员签字:

经办人签字:

负责人签字:

教育(文化)处(组)公章

2015 年 08 月 10 日

第一联:交留学回国人员

教育部国际合作与交流司 2012 年制表

注意事项

1. 本证明只为学成回国工作的留学人员开具。
2. 本证明由我驻外使(领)馆教育(文化)处(组)在留学人员回国时填写,不得涂改。
3. 本证明经使(领)馆教育(文化)处(组)经办人、负责人签字并在第一、第二联加盖公章方为有效。
4. 第一联由留学人员保存,其他单位可查验原件,留存复印件,不得收取原件。

89



全国英语等级考试

五级合格证书

汪待发

证书编号: 99122990200222

身份证件号: 340824198404212819

参加 2012 年 12 月全国英语等级考试第五级考试, 成绩合格, 特发此证。

CERTIFICATE OF PETS LEVEL 5

This is to certify that the bearer has passed Level 5 of the Public English Test System (PETS).

Certificate Number: 99122990200222

ID Number: 340824198404212819

NATIONAL EDUCATION EXAMINATIONS AUTHORITY (NEEA)

MINISTRY OF EDUCATION OF CHINA

教育部考试中心

No.10-A00006489

全国外语水平考试
(WSK)
成绩通知单

考生姓名：汪待发

身份证件号码：340824198404212819

准考证号：990212200222

考试时间：2012年12月8日

考试语种：英语(PETS-5)

考试成绩：笔试总分 63 分
听力部分 19 分
口试总分 3 分



No. 11_W 00042314

证书号第986740号



发明专利证书

发明名称：一种多光学信息同步检测的双参数荧光分子断层成像装置及方法

发明人：汪待发；李德玉；樊瑜波

专利号：ZL 2011 1 0090186.0

专利申请日：2011年04月12日

专利权人：北京航空航天大学

授权公告日：2012年07月04日

本发明经过本局依照中华人民共和国专利法进行审查，决定授予专利权，颁发本证书并在专利登记簿上予以登记。专利权自授权公告之日起生效。

本专利的专利权期限为二十年，自申请日起算。专利权人应当依照专利法及其实施细则规定缴纳年费。本专利的年费应当在每年04月12日前缴纳。未按照规定缴纳年费的，专利权自应当缴纳年费期满之日起终止。

专利证书记载专利权登记时的法律状况。专利权的转移、质押、无效、终止、恢复和专利权人的姓名或名称、国籍、地址变更等事项记载在专利登记簿上。



局长

田力普



证书号第1384760号



发明专利证书

发明名称：一种基于旋转镜的全角度荧光分子断层成像装置

发明人：汪待发；李德玉；贺进；樊瑜波；唐桥虹；刘文勇

专利号：ZL 2012 1 0394893.3

专利申请日：2012年10月17日

专利权人：北京航空航天大学

授权公告日：2014年04月16日

本发明经过本局依照中华人民共和国专利法进行审查，决定授予专利权，颁发本证书并在专利登记簿上予以登记。专利权自授权公告之日起生效。

本专利的专利权期限为二十年，自申请日起算。专利权人应当依照专利法及其实施细则规定缴纳年费。本专利的年费应当在每年10月17日前缴纳。未按照规定缴纳年费的，专利权自应当缴纳年费期满之日起终止。

专利证书记载专利权登记时的法律状况。专利权的转移、质押、无效、终止、恢复和专利权人的姓名或名称、国籍、地址变更等事项记载在专利登记簿上。



局长
申长雨

申长雨



证书号第 1836955 号



发明专利证书

发明名称：一种基于单滑环和无线控制激发光扫描的荧光分子断层成像装置及方法

发明人：汪待发；贺进；李德玉；樊瑜波

专利号：ZL 2013 1 0740964.5

专利申请日：2013 年 12 月 27 日

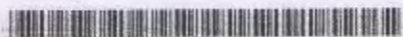
专利权人：北京航空航天大学

授权公告日：2015 年 11 月 04 日

本发明经过本局依照中华人民共和国专利法进行审查，决定授予专利权，颁发本证书并在专利登记簿上予以登记。专利权自授权公告之日起生效。

本专利的专利权期限为二十年，自申请日起算。专利权人应当依照专利法及其实施细则规定缴纳年费。本专利的年费应当在每年 12 月 27 日前缴纳。未按照规定缴纳年费的，专利权自应当缴纳年费期满之日起终止。

专利书记载专利权登记时的法律状况。专利权的转移、质押、无效、终止、恢复和专利权人的姓名或名称、国籍、地址变更等事项记载在专利登记簿上。



局长
申长雨

申长雨



第 1 页 (共 1 页)

95

证书号第 1634578 号



发明专利证书

发明名称：一种基于彩色探测器的体外过敏原定量检测装置及其方法

发明人：李德玉；王典；汪待发；樊瑜波；蒲放

专利号：ZL 2013 1 0163680.4

专利申请日：2013 年 05 月 07 日

专利权人：北京航空航天大学

授权公告日：2015 年 04 月 15 日

本发明经过本局依照中华人民共和国专利法进行审查，决定授予专利权，颁发本证书并在专利登记簿上予以登记。专利权自授权公告之日起生效。

本专利的专利权期限为二十年，自申请日起算。专利权人应当依照专利法及其实施细则规定缴纳年费。本专利的年费应当在每年 05 月 07 日前缴纳。未按照规定缴纳年费的，专利权自应当缴纳年费期满之日起终止。

专利证书记载专利权登记时的法律状况。专利权的转移、质押、无效、终止、恢复和专利权人的姓名或名称、国籍、地址变更等事项记载在专利登记簿上。



局长
申长雨

申长雨



证书号第 1443858 号



发明专利证书

发明名称：一种基于多光谱成像的体外过敏原定量检测方法

发明人：李德玉；韩冬宜；汪待发；樊瑜波；蒲放

专利号：ZL 2012 1 0064231.X

专利申请日：2012 年 03 月 13 日

专利权人：北京航空航天大学

授权公告日：2014 年 07 月 16 日

本发明经过本局依照中华人民共和国专利法进行审查，决定授予专利权，颁发本证书并在专利登记簿上予以登记。专利权自授权公告之日起生效。

本专利的专利权期限为二十年，自申请日起算。专利权人应当依照专利法及其实施细则规定缴纳年费。本专利的年费应当在每年 03 月 13 日前缴纳。未按照规定缴纳年费的，专利权自应当缴纳年费期满之日起终止。

专利证书记载专利权登记时的法律状况。专利权的转移、质押、无效、终止、恢复和专利权人的姓名或名称、国籍、地址变更等事项记载在专利登记簿上。



局长
申长雨

申长雨



证书号第1922349号



发明专利证书

发明名称：基于生物电阻抗的全视角椎弓根手术辅助导航装置及方法

发明人：汪待发；孟云；周蓉

专利号：ZL 2014 1 0007144.X

专利申请日：2014年01月07日

专利权人：北京航空航天大学

授权公告日：2016年01月13日

本发明经过本局依照中华人民共和国专利法进行审查，决定授予专利权，颁发本证书并在专利登记簿上予以登记。专利权自授权公告之日起生效。

本专利的专利权期限为二十年，自申请日起算。专利权人应当依照专利法及其实施细则规定缴纳年费。本专利的年费应当在每年01月07日前缴纳，未按照规定缴纳年费的，专利权自应当缴纳年费期满之日起终止。

专利证书记载专利权登记时的法律状况。专利权的转移、质押、无效、终止、恢复和专利权人的姓名或名称、国籍、地址变更等事项记载在专利登记簿上。



局长
申长雨

申长雨



Comments to "Focusing through dynamic tissue with millisecond digital optical phase conjugation" by D. Wang, *et al.*

Wavefront shaping is capable of sending light deep inside biological tissues by compensating scattering. However, *in vivo* application of the technology is hindered by factors such as slow response, insufficient control complexity, and limited energy gain. Among all wavefront shaping techniques developed to date, digital time reversal is the most successful as measured by the key criteria above. The work reported in this submission clearly made digital time reversal more practical—the response speed has been improved by two orders of magnitude, allowing light to be focused through unclamped living tissue. As such, this reviewer deems the work as a technological breakthrough, and strongly recommends its publication in *Optica*. The manuscript is well-written, but can be further improved by addressing my following concerns.

1. Abstract. Line 5: "fast playback latency" doesn't make sense. Line 9, DMD is commonly termed "digital micromirror device".
2. Page 1, column 2, second paragraph. The full name of "TRAP" should be accompanied by a noun (e.g., focusing).
3. Page 2, figure 1(b). The arrows and text associated with the playback beam should be removed.
4. Page 2, figure 1 caption. "Collimated by L3" should be "collected by L3". Strictly speaking scattered light cannot be collimated.
5. Page 2, column 1, first paragraph. The number of spatial modes (2 million) does not consider spatial sampling. Each spatial mode is typically sampled by at least 4 pixels.
6. Page 2, column 1, second paragraph, definition of fluence reflectivity. It makes more sense to use sample beam fluence instead of the total fluence in the recording phase as the denominator.
7. Page 2, column 1, third paragraph. The fastest realization using nonlinear crystal for phase conjugation achieved 0.1 ms latency (Jayet, B., J-P. Huignard, and F. Ramaz. "Optical phase conjugation in Nd: YVO 4 for acousto-optic detection in scattering media." *Optics letters* 38.8 (2013): 1256-1258).
8. Page 2-3, Methods section. In order for others to repeat the experiment, model numbers of key components are needed (e.g., laser, DMD kit, cameras etc.).
9. Page 3, Section 2A. For single-shot phase retrieval, $I_{\text{sam}} \ll I_{\text{ref}}$ is required. The authors should state the real experimental beam ratio, and discuss how camera dynamic range affects the accuracy of phase measurement (also, see comments 29 & 30).
10. Page 3, Section 2B. To achieve phase map transfer in 1.56 ms (1.8 Gb/s), the phase map data should be compressed to 1 bit/pixel. As far as I know, DMD receives 1 frame of data containing 24 bit-planes over HDMI. Did the authors program the FPGA of the DMD controller board to enable single-bit image transfer (instead of a 24 bit) via HDMI? If yes, they should state this in the paper. The authors should also state how long it takes for stable display after data is received (does it take $1/(23k)$ of a second?).
11. Page 3, figure 2. The texts in the figure need to be enlarged. Also, 'communication' is misspelled.
12. Page 3, Section 2C. I suggest that the authors provide measured reflectivity (into the desired order) of the DMD, which implies the efficiency of the device. Moreover, how does this

From: OSA Journals
Date sent: 10/13/2015 08:10:49 am
Subject: Top Downloads in Optica

[Print This](#)

[View Online](#) | [Forward](#) | [Share this email:](#)



OSA | The Optical Society



optica

TOP DOWNLOADS

[Author Information](#) | [Submit Your Manuscript](#) | [Create E-alerts](#)

View Top Downloads from July-September 2015

Stay current on the latest research by reviewing the most downloaded articles in the 3rd quarter (July-September 2015) from OSA's *Optica*. *Optica* is an Open-Access journal so the articles below are freely accessible.

JOURNAL NEWS AND ANNOUNCEMENTS

OSA Launches Solution to Enable Public Access of U.S. Federally Funded Research Articles

OSA has implemented a technology solution that effectively supports U.S. federal agency public access requirements and helps authors comply with governmental mandates to make their federally funded articles publicly available after a 12-month embargo.

Perfect optics with imperfect components

David A. B. Miller

Optica 2(8) 747-750 (2015) View: [HTML](#) | [PDF](#) [Suppl. Mat. (1)]

Learning approach to optical tomography

Ulugbek S. Kamilov, Ioannis N. Papadopoulos, Morteza H. Shoreh, Alexandre Goy, Cedric Vonesch, Michael Unser, and Demetri Psaltis

Optica 2(6) 517-522 (2015) View: [HTML](#) | [PDF](#) [Suppl. Mat. (2)]

Shifting the quantum-classical boundary: theory and experiment for statistically classical optical fields

Xiao-Feng Qian, Bethany Little, John C. Howell, and J. H. Eberly

Optica 2(7) 611-615 (2015) View: [HTML](#) | [PDF](#) [Suppl. Mat. (1)]

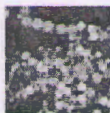
Femtosecond fiber lasers reach the mid-infrared

Simon Duval, Martin Bernier, Vincent Fortin, Jérôme Genest, Michel Piché, and Réal Vallée

Optica 2(7) 623-626 (2015) View: [HTML](#) | [PDF](#)

Gigapixel multispectral microscopy

(100)



Antony Orth, Monica Jo Tomaszewski, Richik N. Ghosh, and Ethan Schonbrun

Optica 2(7) 654-662 (2015) View: [HTML](#) | [PDF](#) [Suppl. Mat. (2)]



Quantum teleportation over 100 km of fiber using highly efficient superconducting nanowire single-photon detectors

Hiroki Takesue, Shellee D. Dyer, Martin J. Stevens, Varun Verma, Richard P. Mirin, and Sae Woo Nam

Optica 2(10) 832-835 (2015) View: [HTML](#) | [PDF](#) [Suppl. Mat. (1)]



Midinfrared supercontinuum generation from 2 to 6 μm in a silicon nanowire

Neetesh Singh, Darren D. Hudson, Yi Yu, Christian Grillet, Stuart D. Jackson, Alvaro Casas-Bedoya, Andrew Read, Petar Atanackovic, Steven G. Duvall, Stefano Palomba, Barry Luther-Davies, Stephen Madden, David J. Moss, and Benjamin J. Eggleton

Optica 2(9) 797-802 (2015) View: [HTML](#) | [PDF](#) [Suppl. Mat. (1)]



Decoupled illumination detection in light sheet microscopy for fast volumetric imaging

Omar E. Olarte, Jordi Andilla, David Artigas, and Pablo Loza-Alvarez

Optica 2(8) 702-705 (2015) View: [HTML](#) | [PDF](#) [Suppl. Mat. (6)]

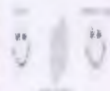


Image translation for single-shot focal tomography

Patrick Llull, Xin Yuan, Lawrence Carin, and David J. Brady

Optica 2(9) 822-825 (2015) View: [HTML](#) | [PDF](#) [Suppl. Mat. (2)]



Focusing through dynamic tissue with millisecond digital optical phase conjugation

Daifa Wang, Edward Haojiang Zhou, Joshua Brake, Haowen Ruan, Mooseok Jang, and Changhui Yang

Optica 2(8) 728-735 (2015) View: [HTML](#) | [PDF](#) [Suppl. Mat. (2)]

You are receiving this email because you are a member or are otherwise affiliated with The Optical Society (OSA), the publisher of this journal.

This Journal is an Open-Access journal that provides public access to all published articles once the Article Processing Charge has been paid. For author submission information, please visit <https://www.osapublishing.org/author/author.cfm>.

Privacy - OSA respects your privacy and does not disclose or sell your personal information to any unaffiliated third parties. Please see OSA's [privacy policy](#) for additional information.

© Copyright 2015 The Optical Society
All Rights Reserved | [Privacy Statement](#) | [Terms of Use](#)

Join the global movement to celebrate light

OSA
The Optical Society



**INTERNATIONAL
YEAR OF LIGHT
2015**

The Optical Society (OSA)
2010 Massachusetts Ave., N.W.
Washington, D.C. 20036 USA

www.osa.org
+1 202.223.8130

101

optica

Volume 2 • Issue 8 • August 2015



OSA[®]
The Optical Society

ISSN: 2334-2536

optica.osa.org

102



(<https://www.osapublishing.org>)

Optica

Alex Gaeta, Editor-in-Chief

([home.cfm](#))

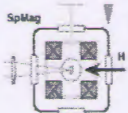
Issues in Progress ([/optica/upcomingissue.cfm](#))

Current Issue ([/optica/issue.cfm](#))

All Issues ([/optica/browse.cfm](#))

20 August 2015, Volume 2, Issue 8, pp. 663-772 19 articles

Sort: Topic Page Number



Magnetic circular polarization of luminescence in bismuth-doped silica glass
([/abstract.cfm?uri=optica-2-8-663](#))

Oleksii Laguta, Hicham El Hamzaoui, Mohamed Bouazaoui, Vladimir B. Arion, and Igor Razdobreev

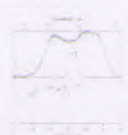
Optica 2(8), 663-666 (2015) View: HTML ([/viewmedia.cfm?uri=optica-2-8-663&seq=0&html=true](#)) | PDF ([/viewmedia.cfm?uri=optica-2-8-663&seq=0](#))



Femtosecond mode locking based on adiabatic excitation of quadratic solitons
([/abstract.cfm?uri=optica-2-8-667](#))

C. R. Phillips, A. S. Mayer, A. Klenner, and U. Keller

Optica 2(8), 667-674 (2015) View: HTML ([/viewmedia.cfm?uri=optica-2-8-667&seq=0&html=true](#)) | PDF ([/viewmedia.cfm?uri=optica-2-8-667&seq=0](#)) [Suppl. Mat. (1)]



Chirped-pulse amplification in a CO₂ laser ([/abstract.cfm?uri=optica-2-8-675](#))

Mikhail N. Polyanskiy, Marcus Babzien, and Igor V. Pogorelsky

Optica 2(8), 675-681 (2015) View: HTML ([/viewmedia.cfm?uri=optica-2-8-675&seq=0&html=true](#)) | PDF ([/viewmedia.cfm?uri=optica-2-8-675&seq=0](#))

103



Conjugate adaptive optics in widefield microscopy with an extended-source wavefront sensor (/abstract.cfm?uri=optica-2-8-682)

Jiang Li, Devin R. Beaulieu, Hari Paudel, Roman Barankov, Thomas G. Bifano, and Jerome Mertz
Optica 2(8), 682-688 (2015) View: HTML (/viewmedia.cfm?uri=optica-2-8-682&seq=0&html=true) | PDF (/viewmedia.cfm?uri=optica-2-8-682&seq=0) [Suppl. Mat. (1)]



Spectral multiphoton effects and quantum anharmonicities in dissipative cavity-QED systems via off-resonant coherent excitation (/abstract.cfm?uri=optica-2-8-689)

E. Illes, C. Roy, and S. Hughes

Optica 2(8), 689-697 (2015) View: HTML (/viewmedia.cfm?uri=optica-2-8-689&seq=0&html=true) | PDF (/viewmedia.cfm?uri=optica-2-8-689&seq=0) [Suppl. Mat. (1)]



Second harmonic generation spectroscopy on second harmonic resonant plasmonic metamaterials (/abstract.cfm?uri=optica-2-8-698)

Heiko Linnenbank and Stefan Linden

Optica 2(8), 698-701 (2015) View: HTML (/viewmedia.cfm?uri=optica-2-8-698&seq=0&html=true) | PDF (/viewmedia.cfm?uri=optica-2-8-698&seq=0)



Decoupled illumination detection in light sheet microscopy for fast volumetric imaging (/abstract.cfm?uri=optica-2-8-702)

Omar E. Olarte, Jordi Andilla, David Artigas, and Pablo Loza-Alvarez

Optica 2(8), 702-705 (2015) View: HTML (/viewmedia.cfm?uri=optica-2-8-702&seq=0&html=true) | PDF (/viewmedia.cfm?uri=optica-2-8-702&seq=0) [Suppl. Mat. (6)]



Counting the cycles of light using a self-referenced optical microresonator (/abstract.cfm?uri=optica-2-8-706)

J. D. Jost, T. Herr, C. Lecaplain, V. Brasch, M. H. P. Pfeiffer, and T. J. Kippenberg

Optica 2(8), 706-711 (2015) View: HTML (/viewmedia.cfm?uri=optica-2-8-706&seq=0&html=true) | PDF (/viewmedia.cfm?uri=optica-2-8-706&seq=0)



Topological phase transitions in superradiance lattices (/abstract.cfm?uri=optica-2-8-712)

Da-Wei Wang, Han Cai, Luqi Yuan, Shi-Yao Zhu, and Ren-Bao Liu

Optica 2(8), 712-715 (2015) View: HTML (/viewmedia.cfm?uri=optica-2-8-712&seq=0&html=true) | PDF (/viewmedia.cfm?uri=optica-2-8-712&seq=0) [Suppl. Mat. (1)]

104



Plasmonic metagratings for simultaneous determination of Stokes parameters

(/abstract.cfm?uri=optica-2-8-716)

Anders Pors, Michael G. Nielsen, and Sergey I. Bozhevolnyi

Optica 2(8), 716-723 (2015) View: HTML (/viewmedia.cfm?uri=optica-2-8-

716&seq=0&html=true) | PDF (/viewmedia.cfm?uri=optica-2-8-716&seq=0) [Suppl. Mat. (1)]



Compact and reconfigurable silicon nitride time-bin entanglement circuit

(/abstract.cfm?uri=optica-2-8-724)

C. Xiong, X. Zhang, A. Mahendra, J. He, D.-Y. Choi, C. J. Chae, D. Marpaung, A. Leinse, R. G. Heideman, M. Hoekman, C. G. H. Roeloffzen, R. M. Oldenbeuving, P. W. L. van Dijk, C. Taddei, P. H. W. Leong, and B. J. Eggleton

Optica 2(8), 724-727 (2015) View: HTML (/viewmedia.cfm?uri=optica-2-8-

724&seq=0&html=true) | PDF (/viewmedia.cfm?uri=optica-2-8-724&seq=0)

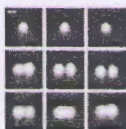


Focusing through dynamic tissue with millisecond digital optical phase conjugation (/abstract.cfm?uri=optica-2-8-728)

Daifa Wang, Edward Haojiang Zhou, Joshua Brake, Haowen Ruan, Mooseok Jang, and Changhui Yang

Optica 2(8), 728-735 (2015) View: HTML (/viewmedia.cfm?uri=optica-2-8-

728&seq=0&html=true) | PDF (/viewmedia.cfm?uri=optica-2-8-728&seq=0) [Suppl. Mat. (2)]



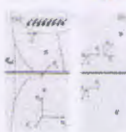
Equivalent of the point spread function for partially coherent imaging

(/abstract.cfm?uri=optica-2-8-736)

Shalin B. Mehta and Colin J. R. Sheppard

Optica 2(8), 736-739 (2015) View: HTML (/viewmedia.cfm?uri=optica-2-8-

736&seq=0&html=true) | PDF (/viewmedia.cfm?uri=optica-2-8-736&seq=0) [Suppl. Mat. (3)]



Two-dimensional exciton-polariton—light guiding by transition metal dichalcogenide monolayers (/abstract.cfm?uri=optica-2-8-740)

Jacob B. Khurgin

Optica 2(8), 740-742 (2015) View: HTML (/viewmedia.cfm?uri=optica-2-8-

740&seq=0&html=true) | PDF (/viewmedia.cfm?uri=optica-2-8-740&seq=0)



Nanoimprinted superlattice metallic photonic crystal as ultrasensitive solar absorber (/abstract.cfm?uri=optica-2-8-743)

V. Rinnerbauer, E. Lausecker, F. Schäffler, P. Reininger, G. Strasser, R. D. Geil, J. D. Joannopoulos, M. Soljačić, and I. Celanovic

Optica 2(8), 743-746 (2015) View: HTML (/viewmedia.cfm?uri=optica-2-8-743&seq=0&html=true) | PDF (/viewmedia.cfm?uri=optica-2-8-743&seq=0)



Perfect optics with imperfect components (/abstract.cfm?uri=optica-2-8-747)

David A. B. Miller

Optica 2(8), 747-750 (2015) View: HTML (/viewmedia.cfm?uri=optica-2-8-747&seq=0&html=true) | PDF (/viewmedia.cfm?uri=optica-2-8-747&seq=0) [Suppl. Mat. (1)]



Low-error and broadband microwave frequency measurement in a silicon chip (/abstract.cfm?uri=optica-2-8-751)

Mattia Pagani, Blair Morrison, Yanbing Zhang, Alvaro Casas-Bedoya, Timo Aalto, Mikko Harjanne, Markku Kapulainen, Benjamin J. Eggleton, and David Marpaung
Optica 2(8), 751-756 (2015) View: HTML (/viewmedia.cfm?uri=optica-2-8-751&seq=0&html=true) | PDF (/viewmedia.cfm?uri=optica-2-8-751&seq=0)



Supercontinuum generation as a signal amplifier (/abstract.cfm?uri=optica-2-8-757)

Lasse Orsila, Johan Sand, Mikko Närhi, Goëry Genty, and Günter Steinmeyer
Optica 2(8), 757-764 (2015) View: HTML (/viewmedia.cfm?uri=optica-2-8-757&seq=0&html=true) | PDF (/viewmedia.cfm?uri=optica-2-8-757&seq=0) [Suppl. Mat. (1)]



Relaxation dynamics of nanosecond laser superheated material in dielectrics (/abstract.cfm?uri=optica-2-8-765)

Stavros G. Demos, Raluca A. Negres, Rajesh N. Raman, Michael D. Feit, Kenneth R. Manes, and Alexander M. Rubenchik
Optica 2(8), 765-772 (2015) View: HTML (/viewmedia.cfm?uri=optica-2-8-765&seq=0&html=true) | PDF (/viewmedia.cfm?uri=optica-2-8-765&seq=0)



See Wang *et al.*, pp. 712-715 (<https://www.osapublishing.org/optica/abstract.cfm?uri=optica-2-8-712>). See print version (<https://www.osapublishing.org/optica/journal/optica/toc/cover-optica-2-8.pdf>) of the cover.

Today's Top Downloads

1. Blind and reference-free fluorescence lifetime estimation via consumer time-of-flight sensors (<https://www.osapublishing.org/optica/abstract.cfm?URI=optica-2-11-965>)
2. Correcting field-dependent aberrations with nanoscale accuracy in three-dimensional single-molecule localization microscopy (<https://www.osapublishing.org/optica/abstract.cfm?URI=optica-2-11-985>)
3. Measurement of flow vorticity with helical beams of light (<https://www.osapublishing.org/optica/abstract.cfm?URI=optica-2-11-1002>)
4. Fabrication of ideal geometric-phase holograms with arbitrary wavefronts (<https://www.osapublishing.org/optica/abstract.cfm?URI=optica-2-11-958>)
5. Ultra-high-sensitivity color imaging via a transparent diffractive-filter array and computational optics (<https://www.osapublishing.org/optica/abstract.cfm?URI=optica-2-11-933>)

[Home \(/\)](#)

[To Top ↑](#)

[◀ Previous Issue \(/optica/issue.cfm?volume=2&issue=7\)](#)

[Next Issue ▶ \(/optica/issue.cfm?volume=2&issue=9\)](#)

[My Favorites ▼](#)

[Recent Pages ▼](#)

[Journals \(/about.cfm\)](#)

[Proceedings \(/conferences.cfm\)](#)

[Information for](#)

[Authors \(/author/author.cfm\)](#)

[Reviewers \(/submit/review/peer_review.cfm\)](#)

Focusing through dynamic tissue with millisecond digital optical phase conjugation

DAIFA WANG,^{1,2,†} EDWARD HAOJIANG ZHOU,^{1,†} JOSHUA BRAKE,¹ HAOWEN RUAN,¹
MOOSEOK JANG,¹ AND CHANGHUEI YANG^{1,*}

¹Departments of Electrical Engineering and Bioengineering, California Institute of Technology, Pasadena, California 91125, USA

²Key Laboratory for Biomechanics and Mechanobiology of Ministry of Education, School of Biological Science and Medical Engineering, Beihang University, Beijing, China

*Corresponding author: chyang@caltech.edu

Received 18 May 2015; revised 16 July 2015; accepted 21 July 2015 (Doc. ID 240996); published 7 August 2015

Digital optical phase conjugation (DOPC) is a new technique employed in wavefront shaping and phase conjugation for focusing light through or within scattering media such as biological tissues. DOPC is particularly attractive as it intrinsically achieves a high fluence reflectivity in comparison to nonlinear optical approaches. However, the slow refresh rate of liquid crystal spatial light modulators and limitations imposed by computer data transfer speeds have thus far made it difficult for DOPC to achieve a playback latency of shorter than ~ 200 ms and, therefore, prevented DOPC from being practically applied to thick living samples. In this paper, we report a novel DOPC system that is capable of 5.3 ms playback latency. This speed improvement of almost 2 orders of magnitude is achieved by using a digital micromirror device, field programmable gate array (FPGA) processing, and a single-shot binary phase retrieval technique. With this system, we are able to focus through 2.3 mm living mouse skin with blood flowing through it (decorrelation time ~ 30 ms) and demonstrate that the focus can be maintained indefinitely—an important technological milestone that has not been previously reported, to the best of our knowledge. © 2015 Optical Society of America

OCIS codes: (110.0113) Imaging through turbid media; (070.5040) Phase conjugation; (110.0180) Microscopy.

<http://dx.doi.org/10.1364/OPTICA.2.000728>

1. INTRODUCTION

Focusing light through tissues has long been a challenge for biomedical optics. The turbid nature of tissues strongly scatters light and hinders the formation of a sharp focus. Recently, research in the field of wavefront shaping has shown that by correcting the wavefront incident on scattering media, focus can be constructed at an arbitrary location behind the sample [1,2]. Different strategies have been developed to realize this process including iterative wavefront optimization [1,3–5], transmission matrix measurement [6–8], and optical phase conjugation (OPC) [9–11]. Among these, OPC implements the corrected wavefront by recording the scattered light field globally and then playing back the conjugate light field by a phase conjugate mirror (PCM) without time-consuming iterations. Since the process of elastic light scattering is time symmetric, by playing a conjugate version of the scattered wavefront back through the scattering medium, the conjugate input wavefront can be recovered.

By employing OPC, a number of novel techniques for focusing light through or within a scattering medium have recently been developed. These include time-reversed ultrasonically encoded light (TRUE) [12,13], time reversal of variance-encoded light (TROVE) [14], time reversal by analysis of changing wavefronts from kinetic targets (TRACK) [15], and time-reversed adapted-perturbation (TRAP) focusing [16]. These methods have


the potential to improve or enable biomedical applications such as deep tissue imaging, photodynamic therapy, and noninvasive cytometry.

There are two major advantages of OPC compared to other wavefront shaping techniques. First, it is able to arrive at the correct wavefront solution without iteration. Second, the number of controllable optical modes in the playback wavefront can be very high, $\sim 5 \times 10^5$ modes or more. Optical phase conjugation methods can be categorized into two primary groups. Nonlinear OPC methods [12,17,18] employ nonlinear crystals to store the scattered field and propagate the phase conjugate field. In contrast, the digital optical phase conjugation (DOPC) method [13–16] uses an electronic camera in an interferometric setup to capture the optical wavefront information and subsequently produce a suitable OPC field by using that information to pattern a spatial light modulator (SLM).

The DOPC method has several intrinsic advantages over nonlinear OPC methods. First, whereas nonlinear crystals are strongly dependent on wavelength, DOPC can freely work with a broad range of wavelengths. Second, DOPC provides the flexibility to render wavefront playback beyond a single QPC field. In fact, TROVE, TRACK, and TRAP all exploit this unique capability of DOPC to render complex and nuanced wavefronts. In the case of TRACK and TRAP, for example, the rendered wavefront is

Open Access 期刊, 无封面与目录

High-Performance Fluorescence Molecular Tomography through Shape-Based Reconstruction Using Spherical Harmonics Parameterization

Daifa Wang, Jin He, Huiting Qiao, Xiaolei Song, Yubo Fan, Deyu Li 

Published: April 14, 2014 • DOI: 10.1371/journal.pone.0094317

Article

About the Authors

Metrics

Comments

Related Content

Download PDF 

Print

Share

 CrossMark

Subject Areas 

Ellipsoids

Fluorescence

Fluorescence imaging

Optical properties

About the Authors

Daifa Wang

State Key Laboratory of Software Development Environment, Beihang University, Beijing, China

Daifa Wang, Jin He, Huiting Qiao, Yubo Fan, Deyu Li

Key Laboratory for Biomechanics and Mechanobiology of Ministry of Education, School of Biological Science and Medical Engineering, Beihang University, Beijing, China



High-Performance Fluorescence Molecular Tomography through Shape-Based Reconstruction Using Spherical Harmonics Parameterization

Daifa Wang^{1,2}, Jin He², Huiting Qiao², Xiaolei Song³, Yubo Fan², Deyu Li^{2*}

1 State Key Laboratory of Software Development Environment, Beihang University, Beijing, China, **2** Key Laboratory for Biomechanics and Mechanobiology of Ministry of Education, School of Biological Science and Medical Engineering, Beihang University, Beijing, China, **3** The Russell H. Morgan Department of Radiology and Radiological Sciences, Division of MR Research, Johns Hopkins University School of Medicine, Baltimore, Maryland, United States of America

Abstract

Fluorescence molecular tomography in the near-infrared region is becoming a powerful modality for mapping the three-dimensional quantitative distributions of fluorochromes in live small animals. However, wider application of fluorescence molecular tomography still requires more accurate and stable reconstruction tools. We propose a shape-based reconstruction method that uses spherical harmonics parameterization, where fluorophores are assumed to be distributed as piecewise constants inside disjointed subdomains and the remaining background. The inverse problem is then formulated as a constrained nonlinear least-squares problem with respect to shape parameters, which decreases ill-posedness because of the significantly reduced number of unknowns. Since different shape parameters contribute differently to the boundary measurements, a two-step and modified block coordinate descent optimization algorithm is introduced to stabilize the reconstruction. We first evaluated our method using numerical simulations under various conditions for the noise level and fluorescent background; it showed significant superiority over conventional voxel-based methods in terms of the spatial resolution, reconstruction accuracy with regard to the morphology and intensity, and robustness against the initial estimated distribution. In our phantom experiment, our method again showed better spatial resolution and more accurate intensity reconstruction. Finally, the results of an *in vivo* experiment demonstrated its applicability to the imaging of mice.

Citation: Wang D, He J, Qiao H, Song X, Fan Y, et al. (2014) High-Performance Fluorescence Molecular Tomography through Shape-Based Reconstruction Using Spherical Harmonics Parameterization. PLoS ONE 9(4): e94317. doi:10.1371/journal.pone.0094317

Editor: Jonathan A. Coles, Glasgow University, United Kingdom

Received: November 11, 2013; **Accepted:** March 14, 2014; **Published:** April 14, 2014

Copyright: © 2014 Wang et al. This is an open-access article distributed under the terms of the Creative Commons Attribution License, which permits unrestricted use, distribution, and reproduction in any medium, provided the original author and source are credited.

Funding: This study was funded by the State Key Laboratory of Software Development Environment (No. SKLSDE-2011ZX-12), the National Natural Science Foundation of China (Nos. 61108084, 81101123), Research Fund for the Doctoral Program of Higher Education of China (No. 20111102120039), Key Laboratory for Biomechanics and Mechanobiology of Ministry of Education. The funders had no role in study design, data collection and analysis, decision to publish, or preparation of the manuscript.

Competing Interests: The authors have declared that no competing interests exist.

* E-mail: deyuli@buaa.edu.cn

Introduction

Near-infrared fluorescence molecular tomography (FMT) is used for the three-dimensional (3D) localization and quantification of fluorescent targets deep inside turbid tissue. As a convenient and cost-effective small animal imaging modality, it can provide accurate visualization and quantification of the distribution of fluorescent tracers. Various applications have been proposed or carried out using this tool to monitor diseases at the molecular level, such as enzyme activity [1], mapping expressions of cancer markers [2], [3], and monitoring targeted drug delivery [4]. Davis *et al.* recently presented multicolor imaging to monitor two cancer markers simultaneously [5]. Although some devices for FMT are commercially available, the need for higher spatial resolution and more quantitative and reliable reconstruction hinders the wider application of this technique.

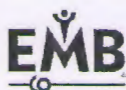
The recovery of 3D fluorescence distribution from boundary measurements is a nonlinear inverse problem. Because of the scattered light propagation inside turbid tissue media, the problem is highly ill posed and thus susceptible to data noise and model errors. The ill-posedness makes FMT reconstruction a significant

challenge. As a solution, additional prior information is generally applied through different regularization techniques. Smooth distribution constraints are typically imposed through methods such as Tikhonov regularization [6]. Information on the sparse distribution is utilized through different compressed sensing techniques [7], [8]. Edge enhancement priors are utilized by penalizing the fluorescence intensity gradient as a regularized term, such as in the total variation method [9], [10], [11], [12]. The development of multimodality FMT systems [13], [14] has boosted the fusion of information derived from anatomical structures [15], [16]. High-density sampling [17], which increases the amount of boundary measurements, has also proven effective, and several studies have focused on investigating the optimal source-detector configurations for different kinds of FMT imaging systems [18], [19]. Although these advances have been critical to moving FMT from the laboratory to commercial applications, great challenges remain in order to obtain 3D fluorescence distributions stably and accurately.

In many specific applications, the distribution of fluorescent targets can be well described as the sum of a small number of subdomains (shapes) with constant piecewise intensities. This

IEEE TRANSACTIONS ON INFORMATION TECHNOLOGY IN BIOMEDICINE

A PUBLICATION OF THE IEEE ENGINEERING IN MEDICINE AND BIOLOGY SOCIETY



TECHNICALLY COSPONSORED BY THE IEEE COMPUTER SOCIETY



Indexed in PubMed® and MEDLINE®, products of the United States National Library of Medicine



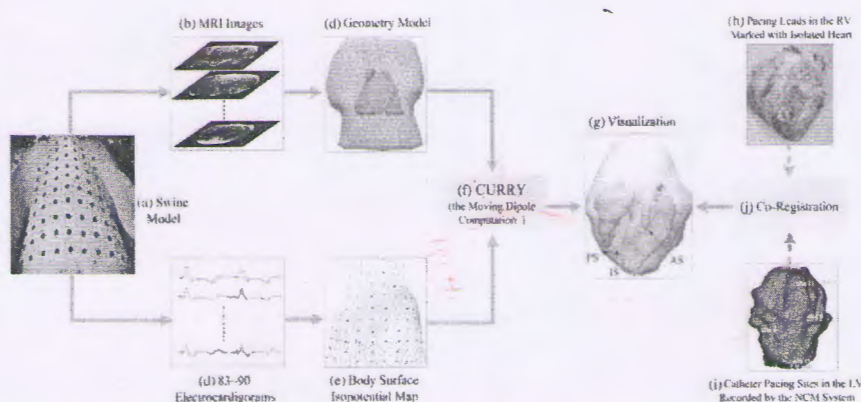
NOVEMBER 2010

VOLUME 14

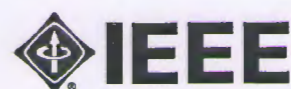
NUMBER 6

ITIBFX

(ISSN 1089-7771)



Schematic diagram of electrocardiogram inverse solution and evaluation procedure. IS represents the estimated “initiation site” of the ectopic activity, PS represents the “pacing site” recorded by the intracavitary NCM system, and AS represents the estimated “activation sequence” of the ectopic activity using a dipole trajectory. As shown in “Equivalent Moving Dipole Localization of Cardiac Ectopic Activity in a Swine Model During Pacing,” by Dakun Lai, Chenguang Liu, Michael D. Eggen, Paul A. Iaizzo, and Bin He on page 1319.



IEEE TRANSACTIONS ON INFORMATION TECHNOLOGY IN BIOMEDICINE

NOVEMBER 2010

VOLUME 14

NUMBER 6

ITIBFX

(ISSN 1089-7771)

Interoperability in Digital Electrocardiography: Harmonization of ISO/IEEE x73-PHD and SCP-ECG	J. D. Trigo, F. Chiarugi, Á. Alesanco, M. Martínez-Espronedá, L. Serrano, C. E. Chronaki, J. Escayola, I. Martínez, and J. García	1303
Equivalent Moving Dipole Localization of Cardiac Ectopic Activity in a Swine Model During Pacing	D. Lai, C. Liu, M. D. Eggen, P. A. Iaizzo, and B. He	1318
Data-Centric Privacy Protocol for Intensive Care Grids	J. Luna, M. Dikaiakos, M. Marazakis, and T. Kyprianou	1327
Real-Time Visualized Freehand 3D Ultrasound Reconstruction Based on GPU	Y. Dai, J. Tian, D. Dong, G. Yan, and H. Zheng	1338
Full-Angle Fluorescence Diffuse Optical Tomography With Spatially Coded Parallel Excitation	D. Wang, X. Liu, F. Liu, and J. Bai	1346
An Optimized Tongue Image Color Correction Scheme	X. Wang and D. Zhang	1355
@neurIST: Infrastructure for Advanced Disease Management Through Integration of Heterogeneous Data, Computing, and Complex Processing Services	S. Benkner, A. Arbona, G. Berti, A. Chiarini, R. Dunlop, G. Engelbrecht, A. F. Frangi, C. M. Friedrich, S. Hanser, P. Hasselmeyer, R. D. Hose, J. Iavindrasana, M. Köhler, L. L. Iacono, G. Lonsdale, R. Meyer, B. Moore, H. Rajasekaran, P. E. Summers, A. Wöhrer, and S. Wood	1365
Searching Protein 3-D Structures for Optimal Structure Alignment Using Intelligent Algorithms and Data Structures	T. Novosád, V. Snášel, A. Abraham, and J. Y. Yang	1378
A Low-Power RFID Integrated Circuits for Intelligent Healthcare Systems	S.-Y. Lee, L.-H. Wang, and Q. Fang	1387
Trustworthy Data Collection From Implantable Medical Devices Via High-Speed Security Implementation Based on IEEE 1363	F. Hu, Q. Hao, M. Lukowiak, Q. Sun, K. Wilhelm, S. Radziszowski, and Y. Wu	1397
Active Learning Methods for Electrocardiographic Signal Classification	E. Pasolli and F. Melgani	1405
GPGPU-Aided Ensemble Empirical-Mode Decomposition for EEG Analysis During Anesthesia	D. Chen, D. Li, M. Xiong, H. Bao, and X. Li	1417
Sleep-States-Transition Model by Body Movement and Estimation of Sleep-Stage-Appearance Probabilities by Kalman Filter	Y. Kurihara, K. Watanabe, and H. Tanaka	1428
Estimating Posture-Recognition Performance in Sensing Garments Using Geometric Wrinkle Modeling	H. Harms, O. Amft, and G. Tröster	1436
LOBIN: E-Textile and Wireless-Sensor-Network-Based Platform for Healthcare Monitoring in Future Hospital Environments	G. López, V. Custodio, and J. I. Moreno	1446

(Contents Continued on Page 1302)



(Contents Continued from Page 1301)

Applying Wearable Solutions in Dependent Environments	<i>J. A. Fraile, J. Bajo, J. M. Corchado, and A. Abraham</i>	1459
Rhythm of Life Aid (ROLA): An Integrated Sensor System for Supporting Medical Staff During Cardiopulmonary Resuscitation (CPR) of Newborn Infants	<i>W. Chen, S. Bambang Oetomo, L. Feijs, P. Andriessen, F. Kimman, M. Geraets, and M. Thielen</i>	1468
<hr/>		
COMMUNICATIONS		
Detection of Falls Among the Elderly by a Floor Sensor Using the Electric Near Field	<i>H. Rimminen, J. Lindström, M. Linnavuo, and R. Sepponen</i>	1475
<hr/>		
LIST OF EDITORS AND REVIEWERS		1477
<hr/>		
INDEX		1482

Full-Angle Fluorescence Diffuse Optical Tomography With Spatially Coded Parallel Excitation

Daifa Wang, Xin Liu, Fei Liu, and Jing Bai, *Fellow, IEEE*

Abstract—Challenges remain in imaging fast biological activities through whole small animal using fluorescence diffuse optical tomography (FDOT). In this study, a novel full-angle FDOT with spatially coded parallel excitation (SC-FDOT) is proposed, which provides much better image qualities than our previous FDOT with multiple-points illumination (MP-FDOT) while maintaining comparable temporal resolution. Singular-value analysis and numerical simulations are used to obtain the key experimental parameters including the optimal point sources number and the optimal projections number, and to compare the performances of SC-FDOT, MP-FDOT and the conventional FDOT with single-point illumination. Results demonstrate that SC-FDOT has the best spatial-temporal performances in imaging fast biological activities through whole body. Physical phantom experiments are performed to evaluate the spatial performance of SC-FDOT in practical experimental applications. Utilizing the proposed system, a nude mouse implanted with a small fluorescent inclusion is also imaged. The preliminary result demonstrates the feasibility of SC-FDOT in *in vivo* applications.

Index Terms—Diffusion equations, finite-element methods, fluorescence, optical tomography.

I. INTRODUCTION

OPTICAL tomography using near-infrared light provides a quantitative way to three-dimensionally visualize tissue function in small animals or human organs [1]–[4] at physiological, metabolic, or molecular level. Fluorescence diffuse optical tomography (FDOT) is one of the optical tomography methods, which is mainly referred to small animal imaging in this paper. In FDOT, fluorescent agents are used to label the object of interest, such as cells, proteins, and drug molecules. Then, by

mathematically modeling the light transportation in diffuse tissues, the 3-D distribution of fluorescent agents inside live small animal is reconstructed from different fluorescence projections.

In past years, FDOT systems have evolved from those [5], [6] using optical fibers and matching fluids to those operating in free-space geometries with limited-/full-angle projections [7]–[11]. With these progresses in imaging systems, mathematical models [12]–[14], and fluorescent agents [15], FDOT have been applied in basic research [16]–[19].

Despite these advances, challenges still remain in imaging fast biological activities through whole body, such as pharmacokinetics, where good whole-body image quality and short data-acquisition time should be considered simultaneously. A slab-geometry-based imaging system with limited projection angles and matching fluid was developed for real-time whole-body imaging [20], where the switching time between continuous-wave point sources was decreased using galvanometer-controlled mirrors and the data-acquisition rate was increased using a high-frame-rate electron-multiplying charge-coupled device (EMCCD). Modern FDOT systems typically operate in free-space geometries with full-angle projections and avoid the use of matching fluid [9]. These modern systems are expected to yield significant improvements in image quality compared to matching fluid or fixed-geometry-based systems [11]. Here, we call these reported full-angle FDOT systems as P-FDOT for simplification with symbol P indicating single-point illumination. However, scanning along axial direction is needed in P-FDOT to provide whole-body imaging ability, which near linearly increases the data-acquisition time and limits the application of P-FDOT in imaging fast biological activities. In our earlier study [21], we have proposed and analyzed a kind of full-angle FDOT systems with beam-forming illumination (BF-FDOT). The BF-FDOT systems utilize the advantages of full-angle projections and provide whole-body imaging without scanning along axial direction. These BF-FDOT systems provide the potential in real-time whole-body imaging.

The main strategy of BF-FDOT is using parallel excitation (illumination) instead of the conventional single-point excitation in full-angle imaging systems. However, some tradeoff in spatial resolution along axial direction exists in BF-FDOT system to offer a significant reduction in data-acquisition time. The spatial resolution degradation is caused by no variation in excitation modes along axial direction. A novel full-angle FDOT system with spatially coded parallel excitation (SC-FDOT) is proposed in this paper. With the novel spatially coded parallel excitation strategy, SC-FDOT will provide more varied parallel

Manuscript received January 12, 2010; revised June 28, 2010; accepted September 5, 2010. Date of publication September 20, 2010; date of current version November 5, 2010. This work was supported by the National Natural Science Foundation of China under Grant 30670577, Grant 60831003, Grant 30930092, and Grant 30872633; by the Tsinghua-Yue-Yuen Medical Science Foundation; by the National Basic Research Program of China (973) under Grant 2006CB705700; and by the National High-Tech Research and Development Program of China (863) under Grant 2006AA020803.

D. Wang was with the Department of Biomedical Engineering, School of Medicine, Tsinghua University, Beijing 100084, China. He is now with the School of Biological Science and Medical Engineering, Beihang University, Beijing 100191, China (e-mail: daifa.wang@buaa.edu.cn).

X. Liu, F. Liu, and J. Bai (corresponding author) are with the Department of Biomedical Engineering, School of Medicine, Tsinghua University, Beijing 100084, China (e-mail: deabj@tsinghua.edu.cn).

Color versions of one or more of the figures in this paper are available online at <http://ieeexplore.ieee.org>.

Digital Object Identifier 10.1109/TITB.2010.2077306

(<https://www.osapublishing.org>)

Applied Optics

Ronald Driggers, Editor-in-Chief

([home.cfm](#))

Issues in Progress ([/ao/upcomingissue.cfm](#))

Current Issue ([/ao/issue.cfm](#))

All Issues ([/ao/browse.cfm](#))

Early Posting ([/ao/upcoming.cfm](#))

Feature Issues ([/ao/feature.cfm](#))

20 December 2012, Volume 51, Issue 36, pp. 8505-8892 43 articles

Sort:

Optical Technology

Atmospheric and Oceanic Optics



Method of estimation of turbulence characteristic scales ([/ao/abstract.cfm?uri=ao-51-36-8505](#))

Victor Alexeevich Kulikov, Maria Sergeevna Andreeva, Alexander Vasil'evich Koryabin, and Victor Ivanovich Shmalhausen

Appl. Opt. 51(36), 8505-8515 (2012) View: HTML ([/ao/viewmedia.cfm?uri=ao-51-36-8505&seq=0&html=true](#)) | PDF ([/ao/viewmedia.cfm?uri=ao-51-36-8505&seq=0](#))



Production of phase screens for simulation of atmospheric turbulence (/ao/abstract.cfm?uri=ao-51-36-8769)

Rachel Rampy, Don Gavel, Daren Dillon, and Sandrine Thomas

Appl. Opt. 51(36), 8769-8778 (2012) View: HTML (/ao/viewmedia.cfm?uri=ao-51-36-8769&seq=0&html=true) | PDF (/ao/viewmedia.cfm?uri=ao-51-36-8769&seq=0)

Diffraction and Gratings



Dynamic polarization grating based on a dye-doped liquid crystal controllable by a single beam in a homeotropic-planar geometry (/ao/abstract.cfm?uri=ao-51-36-8526)

Hak-Rin Kim, Eunje Jang, Jiyeon Kim, Kyung-Il Joo, and Sin-Doo Lee

Appl. Opt. 51(36), 8526-8534 (2012) View: HTML (/ao/viewmedia.cfm?uri=ao-51-36-8526&seq=0&html=true) | PDF (/ao/viewmedia.cfm?uri=ao-51-36-8526&seq=0)

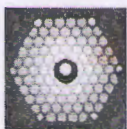
Fiber Optics and Optical Communications



Theoretical and experimental analysis of splicing between the photonic crystal fiber and the conventional fiber using grating fibers (/ao/abstract.cfm?uri=ao-51-36-8516)

De-qin Ouyang, Chun-yu Guo, Shuang-chen Ruan, Yi-ming Wu, Jin-hui Yang, Huai-qin Lin, and Hui-feng Wei

Appl. Opt. 51(36), 8516-8520 (2012) View: HTML (/ao/viewmedia.cfm?uri=ao-51-36-8516&seq=0&html=true) | PDF (/ao/viewmedia.cfm?uri=ao-51-36-8516&seq=0)



Photonic nanojet focusing for hollow-core photonic crystal fiber probes (/ao/abstract.cfm?uri=ao-51-36-8637)

Petru Ghenuche, Hervé Rigneault, and Jérôme Wenger

Appl. Opt. 51(36), 8637-8640 (2012) View: HTML (/ao/viewmedia.cfm?uri=ao-51-36-8637&seq=0&html=true) | PDF (/ao/viewmedia.cfm?uri=ao-51-36-8637&seq=0)



Optical analysis of a photovoltaic V-trough system installed in western India (/ao/abstract.cfm?uri=ao-51-36-8606)

Subarna Maiti, Nabin Sarmah, Pratap Bapat, and Tapas K. Mallick

Appl. Opt. 51(36), 8606-8614 (2012) View: HTML (/ao/viewmedia.cfm?uri=ao-51-36-8606&seq=0&html=true) | PDF (/ao/viewmedia.cfm?uri=ao-51-36-8606&seq=0)



Joint influences of aerodynamic flow field and aerodynamic heating of the dome on imaging quality degradation of airborne optical systems (/ao/abstract.cfm?uri=ao-51-36-8625)

Haosu Xiao, Baojun Zuo, Yi Tian, Wang Zhang, Chenglong Hao, Chaofeng Liu, Qi Li, Fan Li, Li Zhang, and Zhigang Fan

Appl. Opt. 51(36), 8625-8636 (2012) View: HTML (/ao/viewmedia.cfm?uri=ao-51-36-8625&seq=0&html=true) | PDF (/ao/viewmedia.cfm?uri=ao-51-36-8625&seq=0)

Imaging Systems



Experimental demonstration of high-speed full-range Fourier domain optical coherence tomography imaging using orthogonally polarized light and a phase-shifting algorithm (/ao/abstract.cfm?uri=ao-51-36-8762)

Hsu-Chih Cheng and Ming-Shiuan Shiu

Appl. Opt. 51(36), 8762-8768 (2012) View: HTML (/ao/viewmedia.cfm?uri=ao-51-36-8762&seq=0&html=true) | PDF (/ao/viewmedia.cfm?uri=ao-51-36-8762&seq=0)

Instrumentation, Measurement, and Metrology



Application of white-light scanning interferometer on transparent thin-film measurement (/ao/abstract.cfm?uri=ao-51-36-8579)

Meng-Chi Li, Der-Shen Wan, and Cheng-Chung Lee

Appl. Opt. 51(36), 8579-8586 (2012) View: HTML (/ao/viewmedia.cfm?uri=ao-51-36-8579&seq=0&html=true) | PDF (/ao/viewmedia.cfm?uri=ao-51-36-8579&seq=0)



Through-focus response of multifocal intraocular lenses evaluated with a spatial light modulator (/ao/abstract.cfm?uri=ao-51-36-8594)

Laura Remón, Augusto Arias, Arnau Calatayud, Walter D. Furlan, and Juan A. Monsoriu

Appl. Opt. 51(36), 8594-8598 (2012) View: HTML (/ao/viewmedia.cfm?uri=ao-51-36-8594&seq=0&html=true) | PDF (/ao/viewmedia.cfm?uri=ao-51-36-8594&seq=0)



Comparison study of algorithms and accuracy in the wavelength scanning interferometry (/ao/abstract.cfm?uri=ao-51-36-8854)

Hussam Muhamedsalih, Feng Gao, and Xiangqian Jiang

Appl. Opt. 51(36), 8854-8862 (2012) View: HTML (/ao/viewmedia.cfm?uri=ao-51-36-8854&seq=0&html=true) | PDF (/ao/viewmedia.cfm?uri=ao-51-36-8854&seq=0)

Medical Optics and Biotechnology



Time-domain fluorescence-guided diffuse optical tomography based on the third-order simplified harmonics approximation (/ao/abstract.cfm?uri=ao-51-36-8656)

Wenjuan Ma, Wei Zhang, Xi Yi, Jiao Li, Linhui Wu, Xin Wang, Limin Zhang, Zhongxing Zhou, Huijuan Zhao, and Feng Gao

Appl. Opt. 51(36), 8656-8668 (2012) View: HTML (/ao/viewmedia.cfm?uri=ao-51-36-8656&seq=0&html=true) | PDF (/ao/viewmedia.cfm?uri=ao-51-36-8656&seq=0)



Weighted depth compensation algorithm for fluorescence molecular tomography reconstruction (/ao/abstract.cfm?uri=ao-51-36-8883)

Fei Liu, Mingze Li, Bin Zhang, Jianwen Luo, and Jing Bai

Appl. Opt. 51(36), 8883-8892 (2012) View: HTML (/ao/viewmedia.cfm?uri=ao-51-36-8883&seq=0&html=true) | PDF (/ao/viewmedia.cfm?uri=ao-51-36-8883&seq=0)

Optical Design and Fabrication



Design of a compact modified total internal reflection lens for high angular color uniformity (/ao/abstract.cfm?uri=ao-51-36-8557)

Shuiming Li, Fei Chen, Kai Wang, Shuang Zhao, Zhili Zhao, and Sheng Liu

Appl. Opt. 51(36), 8557-8562 (2012) View: HTML (/ao/viewmedia.cfm?uri=ao-51-36-8557&seq=0&html=true) | PDF (/ao/viewmedia.cfm?url=ao-51-36-8557&seq=0)

Optical Devices



Analysis of a color-matching backlight system using a blazed grating and a lenticular lens array (/ao/abstract.cfm?uri=ao-51-36-8615)

Chang-Gyun Son, Jin Seok Gwag, Jong-Hoon Lee, and Jin Hyuk Kwon

Appl. Opt. 51(36), 8615-8620 (2012) View: HTML (/ao/viewmedia.cfm?uri=ao-51-36-8615&seq=0&html=true) | PDF (/ao/viewmedia.cfm?uri=ao-51-36-8615&seq=0)



Nested fiber ring resonator enhanced Mach-Zehnder interferometer for temperature sensing (/ao/abstract.cfm?uri=ao-51-36-8873)

Changqiu Yu, Yundong Zhang, Xuenan Zhang, Kaiyang Wang, Chengbao Yao, Ping Yuan, and Yudong Guan

Appl. Opt. 51(36), 8873-8876 (2012) View: HTML (/ao/viewmedia.cfm?uri=ao-51-36-8873&seq=0&html=true) | PDF (/ao/viewmedia.cfm?uri=ao-51-36-8873&seq=0)

Optics in Computing



Single Mach-Zehnder interferometer based optical Boolean logic gates (/ao/abstract.cfm?uri=ao-51-36-8693)

Cláudia Reis, Tanay Chattopadhyay, Paulo André, and António Teixeira

Appl. Opt. 51(36), 8693-8701 (2012) View: HTML (/ao/viewmedia.cfm?uri=ao-51-36-8693&seq=0&html=true) | PDF (/ao/viewmedia.cfm?uri=ao-51-36-8693&seq=0)

Physical Optics



Effects of thermal gradients on total internal reflection corner cubes (/ao/abstract.cfm?uri=ao-51-36-8793)

Scott D. Goodrow and Thomas W. Murphy

Appl. Opt. 51(36), 8793-8799 (2012) View: HTML (/ao/viewmedia.cfm?uri=ao-51-36-8793&seq=0&html=true) | PDF (/ao/viewmedia.cfm?uri=ao-51-36-8793&seq=0)

Remote Sensing and Sensors



Signal-to-noise performance analysis of streak tube imaging lidar systems. II. Theoretical analysis and discussion (/ao/abstract.cfm?uri=ao-51-36-8836)

Lei Wu, Xiaopeng Wang, Hongru Yang, Bing Yu, Chao Chen, Bin Yang, Liang Yuan, Lipeng Wu, Zhanli Xue, Gaoping Li, and Baoning Wu

Appl. Opt. 51(36), 8836-8847 (2012) View: HTML (/ao/viewmedia.cfm?uri=ao-51-36-8836&seq=0&html=true) | PDF (/ao/viewmedia.cfm?uri=ao-51-36-8836&seq=0)

Scattering



Spectral and geometrical variation of the bidirectional reflectance distribution function of diffuse reflectance standards (/ao/abstract.cfm?uri=ao-51-36-8535)

Alejandro Ferrero, Ana María Rabal, Joaquín Campos, Alicia Pons, and María Luisa Hernanz

Appl. Opt. 51(36), 8535-8540 (2012) View: HTML (/ao/viewmedia.cfm?uri=ao-51-36-8535&seq=0&html=true) | PDF (/ao/viewmedia.cfm?uri=ao-51-36-8535&seq=0)

Thin Films



Polarimetric characterization of bismuth thin films deposited by laser ablation
 (/ao/abstract.cfm?uri=ao-51-36-8549)

Rafael Espinosa-Luna, Enrique Camps, Dagoberto Cardona, and Elder De la Rosa
 Appl. Opt. 51(36), 8549-8556 (2012) **View:** HTML (/ao/viewmedia.cfm?uri=ao-51-36-8549&seq=0&html=true) | **PDF** (/ao/viewmedia.cfm?uri=ao-51-36-8549&seq=0)

CME

Computational manufacturing as a tool for the selection of the most manufacturable design (/ao/abstract.cfm?uri=ao-51-36-8677)

Tatiana V. Amotchkina, Sebastian Schlichting, Henrik Ehlers, Michael K. Trubetskov, Alexander V. Tikhonravov, and Detlev Ristau

Appl. Opt. 51(36), 8677-8686 (2012) **View:** HTML (/ao/viewmedia.cfm?uri=ao-51-36-8677&seq=0&html=true) | **PDF** (/ao/viewmedia.cfm?uri=ao-51-36-8677&seq=0)

Vision, Color, and Visual Optics



Wavefront aberration reconstruction from tangential refractive powers measured with spatial dynamic skiascopy (/ao/abstract.cfm?uri=ao-51-36-8599)

Sergio Barbero

Appl. Opt. 51(36), 8599-8605 (2012) **View:** HTML (/ao/viewmedia.cfm?uri=ao-51-36-8599&seq=0&html=true) | **PDF** (/ao/viewmedia.cfm?uri=ao-51-36-8599&seq=0)

X-ray Optics



Structural properties of subnanometer thick Y layers in extreme ultraviolet multilayer mirrors (/ao/abstract.cfm?uri=ao-51-36-8541)

Jeroen Bosgra, Erwin Zoethout, Ad M. J. van der Eerden, Jan Verhoeven, Robbert W. E. van de Kruijs, Andrey E. Yakshin, and Fred Bijkerk

Appl. Opt. 51(36), 8541-8548 (2012) **View:** HTML (/ao/viewmedia.cfm?uri=ao-51-36-8541&seq=0&html=true) | **PDF** (/ao/viewmedia.cfm?uri=ao-51-36-8541&seq=0)

Information Processing

Holography

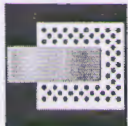


Fast algorithm for reliability-guided phase unwrapping in digital holographic microscopy
 (/ao/abstract.cfm?uri=ao-51-36-8800)

Lihong Ma, Yong Li, Hui Wang, and Hongzhen Jin

Appl. Opt. 51(36), 8800-8807 (2012) View: HTML (/ao/viewmedia.cfm?uri=ao-51-36-8800&seq=0&html=true) | PDF (/ao/viewmedia.cfm?uri=ao-51-36-8800&seq=0)

Image Processing



Modified two-dimensional digital image correlation method with capability of merging of data distributed in time (/ao/abstract.cfm?uri=ao-51-36-8641)

Marcin Malesa and Malgorzata Kujawska

Appl. Opt. 51(36), 8641-8655 (2012) View: HTML (/ao/viewmedia.cfm?uri=ao-51-36-8641&seq=0&html=true) | PDF (/ao/viewmedia.cfm?uri=ao-51-36-8641&seq=0)

Medical Optics and Biotechnology

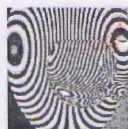


Fluorescence molecular tomography using a two-step three-dimensional shape-based reconstruction with graphics processing unit acceleration
 (/ao/abstract.cfm?uri=ao-51-36-8731)

Daifa Wang, Huiting Qiao, Xiaolei Song, Yubo Fan, and Deyu Li

Appl. Opt. 51(36), 8731-8744 (2012) View: HTML (/ao/viewmedia.cfm?uri=ao-51-36-8731&seq=0&html=true) | PDF (/ao/viewmedia.cfm?uri=ao-51-36-8731&seq=0)

Thin Films



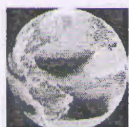
Spatial and temporal film thickness measurement of a soap bubble based on large lateral shearing displacement interferometry (/ao/abstract.cfm?uri=ao-51-36-8863)

Wei Lv, Huaichun Zhou, Chun Lou, and Jinrong Zhu

Appl. Opt. 51(36), 8863-8872 (2012) View: HTML (/ao/viewmedia.cfm?uri=ao-51-36-8863&seq=0&html=true) | PDF (/ao/viewmedia.cfm?uri=ao-51-36-8863&seq=0)

Lasers, Photonics, and Environmental Optics

Atmospheric and Oceanic Optics



On-orbit calibration of SeaWiFS (/ao/abstract.cfm?uri=ao-51-36-8702)

Robert E. Eplee, Gerhard Meister, Frederick S. Patt, Robert A. Barnes, Sean W. Bailey, Bryan A. Franz, and Charles R. McClain

Appl. Opt. 51(36), 8702-8730 (2012) View: HTML (/ao/viewmedia.cfm?uri=ao-51-36-8702&seq=0&html=true) | PDF (/ao/viewmedia.cfm?uri=ao-51-36-8702&seq=0)

Detectors



Ultrasensitive detection of amplified spontaneous emission at 710 nm by means of picosecond collinear optical parametric amplification near degeneracy (/ao/abstract.cfm?uri=ao-51-36-8877)

Jing Zhang, Qiu-lin Zhang, Kang-sheng Qiu, Man Jiang, Dong-xiang Zhang, Bao-hua Feng, and Jing-yuan Zhang

Appl. Opt. 51(36), 8877-8882 (2012) View: HTML (/ao/viewmedia.cfm?uri=ao-51-36-8877&seq=0&html=true) | PDF (/ao/viewmedia.cfm?uri=ao-51-36-8877&seq=0)

Diffraction and Gratings



Sharp plasmonic resonance on gold gratings in amplitude and phase domains (/ao/abstract.cfm?uri=ao-51-36-8563)

Shumei Chen, Guixin Li, Winghan Wong, Edwin Yue-Bun Pun, and Kok Wai Cheah

Appl. Opt. 51(36), 8563-8566 (2012) View: HTML (/ao/viewmedia.cfm?uri=ao-51-36-8563&seq=0&html=true) | PDF (/ao/viewmedia.cfm?uri=ao-51-36-8563&seq=0)

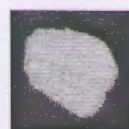
Image Processing



Motion compensated frequency modulated continuous wave 3D coherent imaging ladar with scannerless architecture (/ao/abstract.cfm?uri=ao-51-36-8745)

Brian W. Krause, Bruce G. Tiemann, and Philip Gatt

Appl. Opt. 51(36), 8745-8761 (2012) View: HTML (/ao/viewmedia.cfm?uri=ao-51-36-8745&seq=0&html=true) | PDF (/ao/viewmedia.cfm?uri=ao-51-36-8745&seq=0)



Optical evaluation of ink prints made with heat-treated alder and birch (/ao/abstract.cfm?uri=ao-51-36-8808)

Niko Penttinen, Kari Laitinen, Raimo Silvennoinen, Yrjö Tolonen, and Tuula Moilanen

Appl. Opt. 51(36), 8808-8816 (2012) View: HTML (/ao/viewmedia.cfm?uri=ao-51-36-8808&seq=0&html=true) | PDF (/ao/viewmedia.cfm?uri=ao-51-36-8808&seq=0)

Lasers and Laser Optics



Superficial and Shroud-like coloration of linen by short laser pulses in the vacuum ultraviolet (/ao/abstract.cfm?uri=ao-51-36-8567)

Paolo Di Lazzaro, Daniele Murra, Enrico Nichelatti, Antonino Santoni, and Giuseppe Baldacchini

Appl. Opt. 51(36), 8567-8578 (2012) View: HTML (/ao/viewmedia.cfm?uri=ao-51-36-8567&seq=0&html=true) | PDF (/ao/viewmedia.cfm?uri=ao-51-36-8567&seq=0)



Nanosecond soliton pulse generation by mode-locked erbium-doped fiber laser using single-walled carbon-nanotube-based saturable absorber (/ao/abstract.cfm?uri=ao-51-36-8621)

Mohd Afiq Ismail, Sulaiman Wadi Harun, Nurul Rozullyah Zulkepely, Roslan Md Nor, Fauzan Ahmad, and Harith Ahmad

Appl. Opt. 51(36), 8621-8624 (2012) View: HTML (/ao/viewmedia.cfm?uri=ao-51-36-8621&seq=0&html=true) | PDF (/ao/viewmedia.cfm?uri=ao-51-36-8621&seq=0)



Laser-induced damage behaviors of antireflective coatings at cryogenic condition (/ao/abstract.cfm?uri=ao-51-36-8687)

He Wang, Weili Zhang, and Hongbo He

Appl. Opt. 51(36), 8687-8692 (2012) View: HTML (/ao/viewmedia.cfm?uri=ao-51-36-8687&seq=0&html=true) | PDF (/ao/viewmedia.cfm?uri=ao-51-36-8687&seq=0)



Nitric-oxide planar laser-induced fluorescence at 10 kHz in a seeded flow, a plasma discharge, and a flame (/ao/abstract.cfm?uri=ao-51-36-8817)

Stephen D. Hammack, Campbell D. Carter, James R. Gord, and Tonghun Lee

Appl. Opt. 51(36), 8817-8824 (2012) View: HTML (/ao/viewmedia.cfm?uri=ao-51-36-8817&seq=0&html=true) | PDF (/ao/viewmedia.cfm?uri=ao-51-36-8817&seq=0)
[Suppl. Mat. (3)]



Pulse-front tilt for short-wavelength lasing by means of traveling-wave plasma-excitation (/ao/abstract.cfm?uri=ao-51-36-8848)

Davide Bleiner and Thomas Feurer

Appl. Opt. 51(36), 8848-8853 (2012) View: HTML (/ao/viewmedia.cfm?uri=ao-51-36-8848&seq=0&html=true) | PDF (/ao/viewmedia.cfm?uri=ao-51-36-8848&seq=0)

Optical Devices

Optical isolator based on the electro-optic effect in periodically poled lithium niobate with the addition of a half domain (/ao/abstract.cfm?uri=ao-51-36-8521)

Lei Shi, Linghao Tian, and Xianfeng Chen

Appl. Opt. 51(36), 8521-8525 (2012) View: HTML (/ao/viewmedia.cfm?uri=ao-51-36-8521&seq=0&html=true) | PDF (/ao/viewmedia.cfm?uri=ao-51-36-8521&seq=0)



Si₃N₄ waveguide-based parallel optical interconnect incorporating an interface comprising arrayed grating couplers combined with fiber arrays (/ao/abstract.cfm?uri=ao-51-36-8587)

Vivek Raj Shrestha, Hak-Soon Lee, and Sang-Shin Lee

Appl. Opt. 51(36), 8587-8593 (2012) View: HTML (/ao/viewmedia.cfm?uri=ao-51-36-8587&seq=0&html=true) | PDF (/ao/viewmedia.cfm?uri=ao-51-36-8587&seq=0)

Remote Sensing and Sensors



Signal-to-noise performance analysis of streak tube imaging lidar systems. I. Cascaded model (/ao/abstract.cfm?uri=ao-51-36-8825)

Hongru Yang, Lei Wu, Xiaopeng Wang, Chao Chen, Bing Yu, Bin Yang, Liang Yuan, Lipeng Wu, Zhanli Xue, Gaoping Li, and Baoning Wu

Appl. Opt. 51(36), 8825-8835 (2012) View: HTML (/ao/viewmedia.cfm?uri=ao-51-36-8825&seq=0&html=true) | PDF (/ao/viewmedia.cfm?uri=ao-51-36-8825&seq=0)

Spectroscopy



Qualitative assessment of laser-induced breakdown spectra generated with a femtosecond fiber laser (/ao/abstract.cfm?uri=ao-51-36-8669)

Huan Huang, Lih-Mei Yang, and Jian Liu

Appl. Opt. 51(36), 8669-8676 (2012) View: HTML (/ao/viewmedia.cfm?uri=ao-51-36-8669&seq=0&html=true) | PDF (/ao/viewmedia.cfm?uri=ao-51-36-8669&seq=0)



Atmospheric vertical profiles of O₃, N₂O, CH₄, CCl₂F₂, and H₂O retrieved from external-cavity quantum-cascade laser heterodyne radiometer measurements (/ao/abstract.cfm?uri=ao-51-36-8779)

Tracy R. Tsai, Rebecca A. Rose, Damien Weidmann, and Gerard Wysocki

Appl. Opt. 51(36), 8779-8792 (2012) View: HTML (/ao/viewmedia.cfm?uri=ao-51-36-8779&seq=0&html=true) | PDF (/ao/viewmedia.cfm?uri=ao-51-36-8779&seq=0)



Based on large lateral shearing displacement interferometry, the full field film thickness distribution of a hanging soap bubble could be continuously measured using the dynamic fringe patterns, after its birth and before its bursting. For details see Lv *et al.*, pp. 8863-8872 (<http://www.opticsinfobase.org/ao/abstract.cfm?uri=ao-51-36-8863>).

Topics

Sort by Name | Total Articles

★ My Topics (Change or Add (/user/toc_prefs.cfm))

Atmospheric and Oceanic Optics (3)

Detectors (1)

Diffraction and Gratings (2)

Fiber Optics and Optical Communications (2)

Holography (1)

Image Processing (3)

Imaging Systems (1)

Instrumentation, Measurement, and Metrology (3)

Lasers and Laser Optics (5)

Medical Optics and Biotechnology (3)

Optical Design and Fabrication (1)

Optical Devices (4)

Optics in Computing (1)

Physical Optics (1)

Remote Sensing and Sensors (2)

Scattering (1)

Spectroscopy (2)

Thin Films (3)

Vision, Color, and Visual Optics (1)

X-ray Optics (1)

Today's Top Downloads

1. Digital in-line holographic microscopy
(<https://www.osapublishing.org/ao/abstract.cfm?URI=ao-45-5-836>)
2. Phase retrieval algorithms: a comparison
(<https://www.osapublishing.org/ao/abstract.cfm?URI=ao-21-15-2758>)
3. Digital holographic microscope for measuring three-dimensional particle distributions and motions (<https://www.osapublishing.org/ao/abstract.cfm?URI=ao-45-16-3893>)
4. Measurement of the refractive index of distilled water from the near-infrared region to the ultraviolet region (<https://www.osapublishing.org/ao/abstract.cfm?URI=ao-46-18-3811>)
5. Review of passive imaging polarimetry for remote sensing applications
(<https://www.osapublishing.org/ao/abstract.cfm?URI=ao-45-22-5453>)

[Home \(/\)](#)[To Top ↑](#)[◀ Previous Issue \(/ao/issue.cfm?volume=51&issue=35\)](#)[Next Issue ▶ \(/ao/issue.cfm?volume=52&issue=1\)](#)[My Favorites ▼](#)[Recent Pages ▼](#)[Journals \(/about.cfm\)](#)[Proceedings \(/conferences.cfm\)](#)[Information for](#)[Authors \(/author/author.cfm\)](#)[Reviewers \(/submit/review/peer_review.cfm\)](#)[Librarians \(/library/\)](#)[Other Resources](#)

126

Fluorescence molecular tomography using a two-step three-dimensional shape-based reconstruction with graphics processing unit acceleration

Daifa Wang,^{1,2} Huiting Qiao,² Xiaolei Song,³ Yubo Fan,² and Deyu Li^{2,*}

¹State Key Laboratory of Software Development Environment, Beihang University, Beijing 100191, China

²Key Laboratory for Biomechanics and Mechanobiology of Ministry of Education, School of Biological Science and Medical Engineering, Beihang University, Beijing 100191, China

³The Russell H. Morgan Department of Radiology and Radiological Sciences, Division of MR Research, Johns Hopkins University School of Medicine, Baltimore, Maryland 21287, USA

*Corresponding author: deyuli@buaa.edu.cn

Received 27 August 2012; revised 10 November 2012; accepted 26 November 2012;
posted 27 November 2012 (Doc. ID 175036); published 19 December 2012

In fluorescence molecular tomography, the accurate and stable reconstruction of fluorescence-labeled targets remains a challenge for wide application of this imaging modality. Here we propose a two-step three-dimensional shape-based reconstruction method using graphics processing unit (GPU) acceleration. In this method, the fluorophore distribution is assumed as the sum of ellipsoids with piecewise-constant fluorescence intensities. The inverse problem is formulated as a constrained nonlinear least-squares problem with respect to shape parameters, leading to much less ill-posedness as the number of unknowns is greatly reduced. Considering that various shape parameters contribute differently to the boundary measurements, we use a two-step optimization algorithm to handle them in a distinctive way and also stabilize the reconstruction. Additionally, the GPU acceleration is employed for finite-element-method-based calculation of the objective function value and the Jacobian matrix, which reduces the total optimization time from around 10 min to less than 1 min. The numerical simulations show that our method can accurately reconstruct multiple targets of various shapes while the conventional voxel-based reconstruction cannot separate the nearby targets. Moreover, the two-step optimization can tolerate different initial values in the existence of noises, even when the number of targets is not known *a priori*. A physical phantom experiment further demonstrates the method's potential in practical applications. © 2012 Optical Society of America

OCIS codes: 170.6960, 170.3010, 170.6280, 170.3880.

1. Introduction

Using the advanced fluorescence-labeling and optical-imaging technique, fluorescence imaging makes it possible to better understand the mechanism of human disease at cell or molecular level in small animal models *in vivo*. However, conventional fluorescence imaging using reflected illumination can

only get two-dimensional projection images, which inherently results in poor localization and photon quantification due to the strong scattering of photons [1]. Recently, fluorescence molecular tomography (FMT), aiming at three-dimensional (3D) localization and quantification of fluorescence targets, has drawn great attention and become a research hot spot [2].

In FMT, one attempts to recover the 3D distribution of fluorescence targets embedded deeply (up to several centimeters) inside a small animal such as

OSA Publishing

(<https://www.osapublishing.org>)

Applied Optics

Ronald Driggers, Editor-in-Chief

([home.cfm](#))

Issues in Progress ([/ao/upcomingissue.cfm](#))

Current Issue ([/ao/issue.cfm](#))

All Issues ([/ao/browse.cfm](#))

Early Posting ([/ao/upcoming.cfm](#))

Feature Issues ([/ao/feature.cfm](#))

10 August 2015, Volume 54, Issue 23, pp. 6961-7141 28 articles

Sort:

EDITORIAL

Lesson in creativity: editorial ([/ao/abstract.cfm?uri=ao-54-23-ED9](#))

Ron Driggers and Harold Szu

📄 Appl. Opt. 54(23), ED9-ED9 (2015) View: HTML ([/ao/viewmedia.cfm?uri=ao-54-23-ED9&seq=0&html=true](#)) | PDF ([/ao/viewmedia.cfm?uri=ao-54-23-ED9&seq=0](#))

REGULAR PAPERS

Diffraction and Gratings

Analysis of stationary power/amplitude distributions for multiple channels of sampled FBGs (/ao/abstract.cfm?uri=ao-54-23-7054)

Ya Xing, Xihua Zou, Wei Pan, Lianshan Yan, Bin Luo, and Liyang Shao

Appl. Opt. 54(23), 7054-7061 (2015) View: HTML (/ao/viewmedia.cfm?uri=ao-54-23-7054&seq=0&html=true) | PDF (/ao/viewmedia.cfm?uri=ao-54-23-7054&seq=0)

Fiber Optics and Optical Communications



Investigation on the response of fused taper couplers to ultrasonic wave (/ao/abstract.cfm?uri=ao-54-23-6986)

Fengmei Li, Yiying Liu, Linjie Wang, and Zhenyu Zhao

Appl. Opt. 54(23), 6986-6993 (2015) View: HTML (/ao/viewmedia.cfm?uri=ao-54-23-6986&seq=0&html=true) | PDF (/ao/viewmedia.cfm?uri=ao-54-23-6986&seq=0)



Characterization of dual-polarization LTE radio over a free-space optical turbulence channel (/ao/abstract.cfm?uri=ao-54-23-7082)

J. Bohata, S. Zvanovec, T. Korinek, M. Mansour Abadi, and Z. Ghassemloooy

Appl. Opt. 54(23), 7082-7087 (2015) View: HTML (/ao/viewmedia.cfm?uri=ao-54-23-7082&seq=0&html=true) | PDF (/ao/viewmedia.cfm?uri=ao-54-23-7082&seq=0)

Holography



Speckle-suppressed phase-only holographic three-dimensional display based on double-constraint Gerchberg-Saxton algorithm (/ao/abstract.cfm?uri=ao-54-23-6994)

Chenliang Chang, Jun Xia, Lei Yang, Wei Lei, Zhiming Yang, and Jianhong Chen

Appl. Opt. 54(23), 6994-7001 (2015) View: HTML (/ao/viewmedia.cfm?uri=ao-54-23-6994&seq=0&html=true) | PDF (/ao/viewmedia.cfm?uri=ao-54-23-6994&seq=0)

Image Processing



Parametric distortion-adaptive neighborhood for omnidirectional camera

(/ao/abstract.cfm?uri=ao-54-23-6969)

Yazhe Tang, Youfu Li, and Jun Luo

Appl. Opt. 54(23), 6969-6978 (2015) View: HTML (/ao/viewmedia.cfm?uri=ao-54-23-6969&seq=0&html=true) | PDF (/ao/viewmedia.cfm?uri=ao-54-23-6969&seq=0) [Suppl. Mat. (1)]



Manipulative attack using the phase retrieval algorithm for double random phase encoding (/ao/abstract.cfm?uri=ao-54-23-7115)

Tieyu Zhao, Qiwen Ran, Lin Yuan, and Yingying Chi

Appl. Opt. 54(23), 7115-7119 (2015) View: HTML (/ao/viewmedia.cfm?uri=ao-54-23-7115&seq=0&html=true) | PDF (/ao/viewmedia.cfm?uri=ao-54-23-7115&seq=0)

Imaging Systems



Noncontact full-angle fluorescence molecular tomography system based on rotary mirrors (/ao/abstract.cfm?uri=ao-54-23-7062)

Daifa Wang, Jin He, Huiting Qiao, Ping Li, Yubo Fan, and Deyu Li

Appl. Opt. 54(23), 7062-7070 (2015) View: HTML (/ao/viewmedia.cfm?uri=ao-54-23-7062&seq=0&html=true) | PDF (/ao/viewmedia.cfm?uri=ao-54-23-7062&seq=0)

Instrumentation, Measurement, and Metrology



High data rate transient sensing using dielectric micro-resonator (/ao/abstract.cfm?uri=ao-54-23-7076)

Amir R. Ali, Volkan Ötügen, and Tindaro Ioppolo

Appl. Opt. 54(23), 7076-7081 (2015) View: HTML (/ao/viewmedia.cfm?uri=ao-54-23-7076&seq=0&html=true) | PDF (/ao/viewmedia.cfm?uri=ao-54-23-7076&seq=0)



Wavelength dependence for silicon-wafer temperature measurement by autocorrelation-type frequency-domain low-coherence interferometry (/ao/abstract.cfm?uri=ao-54-23-7088)

Takayoshi Tsutsumi, Takayuki Ohta, Keigo Takeda, Masafumi Ito, and Masaru Hori

Appl. Opt. 54(23), 7088-7093 (2015) View: HTML (/ao/viewmedia.cfm?uri=ao-54-23-7088&seq=0&html=true) | PDF (/ao/viewmedia.cfm?uri=ao-54-23-7088&seq=0)



Surface measurement of indium tin oxide thin film by wavelength-tuning Fizeau interferometry (/ao/abstract.cfm?uri=ao-54-23-7135)

Yangjin Kim, Kenichi Hibino, Naohiko Sugita, and Mamoru Mitsuishi

Appl. Opt. 54(23), 7135-7141 (2015) View: HTML (/ao/viewmedia.cfm?uri=ao-54-23-7135&seq=0&html=true) | PDF (/ao/viewmedia.cfm?uri=ao-54-23-7135&seq=0)

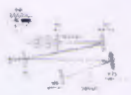
Lasers and Laser Optics



Q-switched 1329 nm Nd:CNGG laser (/ao/abstract.cfm?uri=ao-54-23-7071)

Kun Xiao, Bin Lin, Qiu-Lin Zhang, Dong-Xiang Zhang, Bao-hua Feng, Jing-Liang He, Huai-Jin Zhang, and Ji-Yang Wang

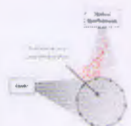
Appl. Opt. 54(23), 7071-7075 (2015) View: HTML (/ao/viewmedia.cfm?uri=ao-54-23-7071&seq=0&html=true) | PDF (/ao/viewmedia.cfm?uri=ao-54-23-7071&seq=0)



760 fs diode-pumped mode-locked laser with Yb:LuAG crystal at 1032 nm (/ao/abstract.cfm?uri=ao-54-23-7120)

Xian-Cui Su, Yi-Ran Wang, Jing-Liang He, Ru-Wei Zhao, Pei-Xiong Zhang, Yin Hang, Jia Hou, Bai-Tao Zhang, and Shuang Zhao

Appl. Opt. 54(23), 7120-7123 (2015) View: HTML (/ao/viewmedia.cfm?uri=ao-54-23-7120&seq=0&html=true) | PDF (/ao/viewmedia.cfm?uri=ao-54-23-7120&seq=0)

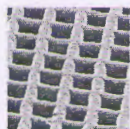


Effect of wall pressure and shear stress on embedded cylindrical microlasers (/ao/abstract.cfm?uri=ao-54-23-7124)

Amir Hosein Zamanian and Tindaro Ioppolo

Appl. Opt. 54(23), 7124-7130 (2015) View: HTML (/ao/viewmedia.cfm?uri=ao-54-23-7124&seq=0&html=true) | PDF (/ao/viewmedia.cfm?uri=ao-54-23-7124&seq=0)

Materials

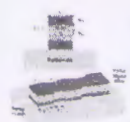


Study of the two-photon excitation of photoinitiator in various solvents, and the two-photon polymerization process (</ao/abstract.cfm?uri=ao-54-23-7020>)

Bibi Safia Haq, Hidayat Ullah Khan, Khan Alam, Shehnaz Attaullah, Islam Zari, and Mian Mateenullah

Appl. Opt. 54(23), 7020-7026 (2015) View: HTML (</ao/viewmedia.cfm?uri=ao-54-23-7020&seq=0&html=true>) | PDF (</ao/viewmedia.cfm?uri=ao-54-23-7020&seq=0>)

Nonlinear Optics



Quasi-phase-matched four-wave mixing generation between C-band and mid-infrared regions using a symmetric hybrid plasmonic waveguide grating (</ao/abstract.cfm?uri=ao-54-23-6961>)

Jing Dai, Minming Zhang, Feiya Zhou, Yuanwu Wang, Luluzi Lu, Lei Deng, and Deming Liu

Appl. Opt. 54(23), 6961-6968 (2015) View: HTML (</ao/viewmedia.cfm?uri=ao-54-23-6961&seq=0&html=true>) | PDF (</ao/viewmedia.cfm?uri=ao-54-23-6961&seq=0>)

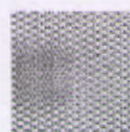
Optical Design and Fabrication



Modeling of surface topography in single-point diamond turning machine (</ao/abstract.cfm?uri=ao-54-23-6979>)

Chih-Yu Huang and Rongguang Liang

Appl. Opt. 54(23), 6979-6985 (2015) View: HTML (</ao/viewmedia.cfm?uri=ao-54-23-6979&seq=0&html=true>) | PDF (</ao/viewmedia.cfm?uri=ao-54-23-6979&seq=0>)



Registering functional defects into periodic holographic structures (</ao/abstract.cfm?uri=ao-54-23-7007>)

Jeff Lutkenhaus, David George, David Lowell, Bayaner Arigong, Hualiang Zhang, and Yuankun Lin

Appl. Opt. 54(23), 7007-7012 (2015) View: HTML (</ao/viewmedia.cfm?uri=ao-54-23-7007&seq=0&html=true>) | PDF (</ao/viewmedia.cfm?uri=ao-54-23-7007&seq=0>)

Optical Devices

132



Metallically coated dielectric rectangle resonator (/ao/abstract.cfm?uri=ao-54-23-7027)

Shuai Liu, Kai-jun Che, Chang-Lei Guo, Cheng-Xu Chu, Pan Zhang, Hui-Ying Xu, and Zhi-Ping Cai

Appl. Opt. 54(23), 7027-7031 (2015) View: HTML (/ao/viewmedia.cfm?uri=ao-54-23-7027&seq=0&html=true) | PDF (/ao/viewmedia.cfm?uri=ao-54-23-7027&seq=0)



Evaluation of low-cadmium ZnCdSeS alloyed quantum dots for remote phosphor solid-state lighting technology (/ao/abstract.cfm?uri=ao-54-23-7094)

Peter Siffalovic, Dominika Badanova, Andrej Vojtko, Matej Jergel, Martin Hodas, Marco Pelletta, Dusan Sabol, Marek Macha, and Eva Majkova

Appl. Opt. 54(23), 7094-7098 (2015) View: HTML (/ao/viewmedia.cfm?uri=ao-54-23-7094&seq=0&html=true) | PDF (/ao/viewmedia.cfm?uri=ao-54-23-7094&seq=0)

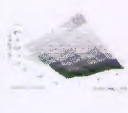
Optical Tweezers or Optical Manipulation



Exploring the physics of efficient optical trapping of dielectric nanoparticles with ultrafast pulsed excitation (/ao/abstract.cfm?uri=ao-54-23-7002)

Debjit Roy, Debabrata Goswami, and Arijit K. De

Appl. Opt. 54(23), 7002-7006 (2015) View: HTML (/ao/viewmedia.cfm?uri=ao-54-23-7002&seq=0&html=true) | PDF (/ao/viewmedia.cfm?uri=ao-54-23-7002&seq=0)



Time-series methods in analysis of the optical tweezers recordings (/ao/abstract.cfm?uri=ao-54-23-7106)

Sławomir Drobczynski and Jakub Ślęzak

Appl. Opt. 54(23), 7106-7114 (2015) View: HTML (/ao/viewmedia.cfm?uri=ao-54-23-7106&seq=0&html=true) | PDF (/ao/viewmedia.cfm?uri=ao-54-23-7106&seq=0)

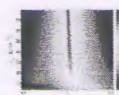
Scattering



Extending generalized Kubelka-Munk to three-dimensional radiative transfer (/ao/abstract.cfm?uri=ao-54-23-7045)

Christopher Sandoval and Arnold D. Kim

Appl. Opt. 54(23), 7045-7053 (2015) View: HTML (</ao/viewmedia.cfm?uri=ao-54-23-7045&seq=0&html=true>) | PDF (</ao/viewmedia.cfm?uri=ao-54-23-7045&seq=0>)



Sensitivity analysis for oblique incidence reflectometry using Monte Carlo simulations (</ao/abstract.cfm?uri=ao-54-23-7099>)

Faisal Kamran and Peter E. Andersen

Appl. Opt. 54(23), 7099-7105 (2015) View: HTML (</ao/viewmedia.cfm?uri=ao-54-23-7099&seq=0&html=true>) | PDF (</ao/viewmedia.cfm?uri=ao-54-23-7099&seq=0>)

Spectroscopy



High laser efficiency and photostability of pyrromethene dyes mediated by nonpolar solvent (</ao/abstract.cfm?uri=ao-54-23-7013>)

Monika Gupta, Priyadarshini Kamble, M. C. Rath, D. B. Naik, and Alok K. Ray

Appl. Opt. 54(23), 7013-7019 (2015) View: HTML (</ao/viewmedia.cfm?uri=ao-54-23-7013&seq=0&html=true>) | PDF (</ao/viewmedia.cfm?uri=ao-54-23-7013&seq=0>)



Fast two-dimensional fluorescence correlation spectroscopy technique for tea quality detection (</ao/abstract.cfm?uri=ao-54-23-7032>)

Yongjiang Dong, Hao Lu, Zhengdong Yong, Chunsheng Yan, and Sailing He

Appl. Opt. 54(23), 7032-7036 (2015) View: HTML (</ao/viewmedia.cfm?uri=ao-54-23-7032&seq=0&html=true>) | PDF (</ao/viewmedia.cfm?uri=ao-54-23-7032&seq=0>)

Surface Plasmons



Elliptic cylindrical silicon nanowire hybrid surface plasmon polariton waveguide (</ao/abstract.cfm?uri=ao-54-23-7037>)

Li Zhang, Qiulin Xiong, Xiaopeng Li, and Junxian Ma

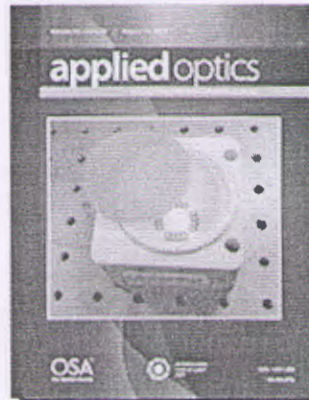
Appl. Opt. 54(23), 7037-7044 (2015) View: HTML (</ao/viewmedia.cfm?uri=ao-54-23-7037&seq=0&html=true>) | PDF (</ao/viewmedia.cfm?uri=ao-54-23-7037&seq=0>)



Silicon hybrid plasmonic microring resonator for sensing applications (</ao/abstract.cfm?uri=ao-54-23-7131>)

Meng Zhang, Genzhu Wu, and Daru Chen

Appl. Opt. 54(23), 7131-7134 (2015) View: HTML (/ao/viewmedia.cfm?uri=ao-54-23-7131&seq=0&html=true) | PDF (/ao/viewmedia.cfm?uri=ao-54-23-7131&seq=0) [Spotlight]



Thin layer of low-cadmium ZnCdSeS alloyed quantum dots deposited onto a commercial remote phosphor module Fortimo LED manufactured by Philips that offers a cost-effective LED solution with 90+ color-rendering index. For details, see Siffalovic *et al.*, pp. 7094–7098 (<https://www.osapublishing.org/ao/abstract.cfm?uri=ao-54-23-7094>).

Topics

Sort by Name | Total Articles

★ My Topics (Change or Add (/user/toc_prefs.cfm))

Diffraction and Gratings (1)

Fiber Optics and Optical Communications (2)

Holography (1)

Image Processing (2)

Imaging Systems (1)

Instrumentation, Measurement, and Metrology (3)

Lasers and Laser Optics (3)

Materials (1)

Nonlinear Optics (1)

Optical Design and Fabrication (2)

Optical Devices (2)

Optical Tweezers or Optical Manipulation (2)

Scattering (2)

Spectroscopy (2)

Surface Plasmons (2)

Today's Top Downloads

1. Digital in-line holographic microscopy
(<https://www.osapublishing.org/ao/abstract.cfm?URI=ao-45-5-836>)
2. Phase retrieval algorithms: a comparison
(<https://www.osapublishing.org/ao/abstract.cfm?URI=ao-21-15-2758>)
3. Digital holographic microscope for measuring three-dimensional particle distributions and motions (<https://www.osapublishing.org/ao/abstract.cfm?URI=ao-45-16-3893>)
4. Measurement of the refractive index of distilled water from the near-infrared region to the ultraviolet region (<https://www.osapublishing.org/ao/abstract.cfm?URI=ao-46-18-3811>)
5. Review of passive imaging polarimetry for remote sensing applications
(<https://www.osapublishing.org/ao/abstract.cfm?URI=ao-45-22-5453>)

[Home \(/\)](#)[To Top ↑](#)[◀ Previous Issue \(/ao/issue.cfm?volume=54&issue=22\)](#)[Next Issue ▶ \(/ao/issue.cfm?volume=54&issue=24\)](#)[My Favorites ▼](#)[Recent Pages ▼](#)[Journals \(/about.cfm\)](#)[Proceedings \(/conferences.cfm\)](#)[Information for](#)[Authors \(/author/author.cfm\)](#)[Reviewers \(/submit/review/peer_review.cfm\)](#)[Librarians \(/library/\)](#)[Other Resources](#)

Noncontact full-angle fluorescence molecular tomography system based on rotary mirrors

DAIFA WANG, JIN HE, HUITING QIAO, PING LI, YUBO FAN, AND DEYU LI*

Key Laboratory for Biomechanics and Mechanobiology of Ministry of Education, School of Biological Science and Medical Engineering, Beihang University, Beijing, China

*Corresponding author: deyuli@buaa.edu.cn

Received 5 May 2015; revised 19 July 2015; accepted 19 July 2015; posted 20 July 2015 (Doc. ID 240342); published 6 August 2015

We propose a novel noncontact fluorescence molecular tomography system that achieves full-angle capacity with the use of a new rotary-mirrors-based imaging head. In the imaging head, four plane mirrors are mounted on a rotating gantry to enable illumination and detection over 360° . In comparison with existing full-angle systems, our system does not require rotation of the specimen animal, a large and heavy light source (with scanning head), or a bulky camera (with filters and lens). The system design and implementation are described in detail. Both physical phantom and *in vivo* experiments are performed to verify the performance of the proposed system. © 2015 Optical Society of America

OCIS codes: (110.0113) Imaging through turbid media; (110.1758) Computational imaging; (110.3010) Image reconstruction techniques; (110.6960) Tomography.

<http://dx.doi.org/10.1364/AO.54.007062>

1. INTRODUCTION

Fluorescence molecular tomography (FMT) is an emerging technology that provides noninvasive, quantitative, three-dimensional imaging of fluorescence markers *in vivo*. Benefitting from mathematical modeling of light transport inside highly scattering tissue, this technique overcomes the limitations of depth information loss in the simple and widely used planar reflectance imaging [1]. At present, FMT has been successfully applied in observing fluorescence-tagged biological processes occurring deep inside tissues, such as enzyme activity [2], expressions of cancer markers [3,4], and targeted agent delivery [5].

The inherent scattering nature of biological tissue limits the spatial resolution of FMT in deep tissue. Many efforts have been made in the past decade to enhance the spatial and temporal performance of FMTs, including developing novel reconstruction algorithms and image acquisition designs [6,7]. In early FMT schemes, the imaging systems were generally fiber based [2], wherein optical fibers were used to transfer the input excitation light to the object surface and the output emission light to detectors. However, such systems are disadvantageous in several ways. The limited number of source–detector pairs in such systems restricts the achievable spatial resolution. Moreover, matching fluid is generally used to enhance the attachment of the fibers to irregular small-animal surfaces and photon transportation modeling; however, the presence of an additional scattering medium between fibers and the animal surface further degrades the spatial performance. The subsequently

developed camera-based noncontact imaging systems have overcome these limitations by allowing the implementation of over 1 million source–detector pairs [1,8].

As in the case of x-ray computed tomography (CT), it has been proven that multiple projection directions over full angles (360°) are crucial for accurate FMT reconstruction [9]. In this regard, several approaches have been proposed to increase the number of projection view directions for camera-based noncontact imaging systems. The most straightforward and easy way is to rotate the small animal [10–12]. However, the imaged small animal has to be carefully suspended by a holder, which unnaturally restricts the animal while also making the imaging preparation process rather complex. While the animal's rotation speed is generally set to very low values to reduce the risk of internal organ movement, this limits the system's temporal performance in observing fast dynamic processes. On the other hand, several groups have developed systems that involve the rotation of the camera/light source [13–15]. In these systems, the rotary gantry needs to be carefully designed to mount the bulky camera (with filters and lens) and light source (with a scanning head), and further, the problem of twisting of the large number of power and signal cables during rotation needs to be addressed. Currently, most systems of this type utilize the rotary gantry used in commercial small-animal CT systems, and the gantry rotation speed is generally low in consideration of the bulky mounted components.

In the context of the limitations of these approaches, researchers have noted that a conical mirror can be used to

ISSN 2095-2783
CN 10-1033/N
CODEN ZKJLHAF

中文核心期刊
原《中国科技论文在线》

中国科技论文

ZHONGGUO KEJI LUNWEN

中华人民共和国教育部 主管 教育部科技发展中心 主办

应用数学与物理

APPLIED MATHEMATICS AND PHYSICS



中国科技论文

CHINA SCIENCEPAPER

第十卷 第五期

二〇一五年三月

Vol. 10 No. 5 Mar. 2015

2015.5

2015年3月 第10卷 第5期
Vol. 10 No. 5 / Mar. 2015

CHINA
SCIENCEPAPER

美国《化学文摘》(CA)来源期刊
俄罗斯《文摘杂志》(AJ)来源期刊
美国《剑桥科学文摘》(CSA)来源期刊
美国《马科希期刊指南》(JCR)来源期刊
波兰《哥白尼索引》(IC)来源期刊
美国《史密森学会数据库》(EBSCOhost)来源期刊

本刊为:
中国期刊网来源期刊
万方数据—数字化期刊群来源期刊
中国科技论文在线数据库来源期刊
中文科技期刊数据库来源期刊
《中国化学化工文摘》收录期刊

总编辑委员会

主任: 韦钰

委员: (按姓氏笔画排序)

马建忠 王静波 王 敏 王永炎 王伙托 左铁捷 刘永坦 齐 康 张德茂 陈洪渊

吴中如 沈逸彤 沈志云 李 未 李郁仁 李榕璠 彭广田 岑可法 郝 永 钟 训

殷祥耀 钱 易 黄伯云 程书钧 潘和平 霍华涛

主 编: 李基民

副主编: 周 静

编辑部副主任: 李洁莹



中国科技论文

(半月刊, 2006年创刊)

第10卷/第5期 2015年3月

CHINA SCIENCEPAPER

(Semimonthly, Started in 2006)

Vol. 10/No. 5 Mar. 2015

主管单位 中华人民共和国教育部

主办单位 教育部科技发展中心

编辑单位 《中国科技论文》编辑部

电 话 010-62514378 62514339

地 址 北京市海淀区中关村大街35号教育部科技

发展中心 邮编: 100080

电子信箱 tongguo@caash.edu.cn

网 址 http://journal.paper.edu.cn

印 刷 北京信印印刷有限公司

发行范围 公开发行

广告经营许可证 京海工商广字第8067号

Corresponding Authority: Ministry of Education of P.R.C.

Sponsor: Ministry of Education, Science and Technology

Development Center

Editor: Editorial Department of China Sciencepaper

Tel: 010-62514378 62514339

Address: 35 Zhongguancun St. Haidian, Beijing Ministry

of Education, Science and Technology

Development Center, 100080

E-mail: tongguo@caash.edu.cn

http://journal.paper.edu.cn

Web Site: http://journal.paper.edu.cn

Printed by: Beijing Kexin Printing Co., Ltd.

ISSN 2095-2783



刊号: ISSN 2095-2783
CN 10-1033/N
邮发代号: 2-366
定价: 25.00元/期
25.00元/期
600.00元/年



中

国

科

技

论

文

第 10 卷
第 5 期
2015

目 次

直接泵浦中红外 Ho: BYF 激光器综述

..... 吉恩才, 汪 露, 柳 强, 巩马理 (503)

双开口谐振环超材料的偏振特性结构研究 孙 荣, 闵 力, 黄黎蓉 (508)

粒子在虚数周期磁场中的能带及其结构 吴玉梅, 缪炎刚 (510)

基于空间 Panel data 固定效应模型的人口增长影响分析 董春卫, 印凡成 (514)

GaAs/Ge 太阳电池电子辐射效应的移位损伤剂量分析

..... 王 荣, 刘运宏, 鲁 明, 冯 钊, 易天成 (520)

粒径分布对磁性粒子成像采样频率范围的影响 周 铭, 鲁建宇, 谢 迪 (523)

玻化微珠保温混凝土墙体温度场数值模拟与分析

..... 张 玉, 李 珠, 马 钢 (528)

修正的 Chaplygin 气体暗能量及其 Om 几何诊断法

..... 张 楠, 吴亚波, 张成国, 张 雪, 鲁军旺 (532)

有限积分法与有限差分法在弹性波数值模拟中的对比分析

..... 李明智, 熊章强, 张大洲 (538)

基于光电混合细分的激光自混合干涉测量技术

..... 陈俊雷, 刘 强, 郭冬梅, 祝宏彬, 王 鸣 (542)

微型冷库货物降温特性的 CFD 数值模拟 赵文锋, 杨 洲 (546)

一类具有自然治愈率的 SI 传染病模型的全局稳定性分析

..... 宋修朝, 任谨慎, 宋 昊, 郑明发 (552)

2014 美国大学生数学建模竞赛中的图论 郭瑛祎, 陈奕林, 金光球 (555)

时间测度链上一类二阶动力方程的振动结果 莫协强, 杨甲山 (564)

脆性裂纹在梯形板中的变速传播行为 麻鸳鸯, 张振亚, 周风华 (570)

基于信息权重自适应蚁群算法求解 TSP 问题 王 敏 (573)

高斯白噪声激励下约瑟夫森结的混沌分析 徐 明, 邓从政, 曾春花 (577)

AD5933 生物阻抗实时监测的便携式椎弓根内固定辅助系统

..... 孟 云, 米 宽, 郑诚功, 李德玉, 汪待发 (580)

基于 ARM 和 ZigBee 的智能家居系统研究与设计

..... 陈珍军, 赵秋霞, 李亚敏 (584)

一种短波固定监测站测向误差修正方法 赵延安, 俱 莹 (588)

基于经验模态分解空域相关滤波的脉冲星信号消噪

..... 赵 攀, 王文波, 龚邦明, 常毓祥, 张童硕 (592)

基于参数敏感性分析的弓形虫病传播动力学模型简化 杨 蕾, 江 雯 (597)

二次曲面的化简与分类方法探讨 谢伟献, 张奇业, 刘红英 (602)

基于线性方程组右端向量修改的拓扑图同构判别 罗贤海 (608)

广义逐次截尾数据下逆高斯分布参数的贝叶斯估计

..... 孟根其其格, 彭秀云, 闫在在 (613)

500 万像素手机摄像头优化设计

..... 陈 曦, 史江一, 杨 礼, 王斐斐, 刘艳阳 (617)

CHINA SCIENCEPAPER

Vol. 10 No. 5, 2015

CONTENTS

- Review of mid-infrared Ho: BYF laser with direct pumping method
..... *Ji Encai, Wang Lu, Liu Qiang, Gong Mali* (503)
- Theoretical study on polarization characteristics of metamaterial based on two-cut split ring resonator
..... *Sun Rong, Min Li, Huang Lirong* (508)
- Band spectrum and structure of a particle in an imaginary periodic magnetic field
..... *Wu Yumei, Miao Yangang* (510)
- Based on the fixed effect model-Panel data analysis on the effect of population growth
..... *Dong Chunwei, Yin Fancheng* (514)
- Using displacement damage dose to analyze electron irradiation effects on GaAs/Ge solar cells
..... *Wang Rong, Liu Yunhong, Lu Ming, Feng Zhao, Yi Tiancheng* (520)
- Particle size distribution on the influence of magnetic particle imaging acquisition frequency range
..... *Zhou Ming, Lu Jianyu, Xie Di* (523)
- Simulation and analysis for temperature field of glazed hollow bead insulation concrete
..... *Zhang Yu, Li Zhu, Ma Gang* (528)
- Modified Chaplygin gas as dark energy and the Om geometrical diagnostic
..... *Zhang Nan, Wu Yabo, Zhang Chengyuan, Zhang Xue, Lu Junwang* (532)
- Comparison of elastodynamic finite integration technique and finite difference method in numerical
simulation of elastic wave *Li Mingzhi, Xiong Zhangqiang, Zhang Dazhou* (538)
- Laser self-mixing interferometry measurement technology based on photoelectric hybrid subdivision
..... *Chen Junbao, Liu Qiang, Guo Dongmei, Zhu Hongbin, Wang Ming* (542)
- Study on the temperature-dropping characteristics of products in the mini cooling store using
CFD model *Zhao Wenfeng, Yang Zhou* (546)
- Global stability of an SI epidemic model with spontaneous cure rate
..... *Song Xiuchao, Ren Jinshen, Song Hao, Zheng Mingfa* (552)
- Graph theory in 2014 interdisciplinary contest (ICM) *Guo Zhenyi, Chen Yilin, Jin Guangqiu* (555)
- Oscillation results for certain second-order dynamic equations on time scales
..... *Mo Xieqiang, Yang Jiashan* (564)
- Variable speed propagating behavior of brittle crack in trapezoidal plate
..... *Ma Yuanyuan, Zhang Zhenya, Zhou Fenghua* (570)
- Solving travelling salesman problem by adaptive ant colony optimization method based on information
weight factor *Wang Min* (573)
- Chaos analysis of Josephson junction with Gaussian white noise excitation
..... *Xu Ming, Deng Congzheng, Zeng Chunhua* (577)
- Bioelectrical impedance aided surgery system for transpedicle screws fixation based on AD5933
..... *Meng Yun, Mi Kuan, Zheng Chenggong, Li Deyu, Wang Daifa* (580)
- Research and design of smart home system based on ARM and ZigBee
..... *Chen Zhenjun, Zhao Qiuxia, Li Yamin* (584)
- Error modification method for HF fixed monitoring station *Zhao Yanan, Ju Ying* (588)
- Pulsar signal denosing based on empirical mode decomposition spatial correlation filter
..... *Zhao Pan, Wang Wenbo, Gong Bangming, Chang Yuchan, Zhang Tongshuo* (592)
- Study on influence factors of toxoplasmosis transmission based on its transmission dynamic model
..... *Yang Lei, Jiang Wen* (597)
- Research on simplification and classification for quadratic surfaces
..... *Xie Weixian, Zhang Qiye, Liu Hongying* (602)
- Isomorphism identification of topological graphs based on dynamic modification to right-hand vector
term of linear equation systems *Luo Xianhai* (608)
- Bayesian estimation for the parameters of inverse Gaussian distribution under general progressive
censoring *Munguntsetseg Dashjav, Peng Xiuyun, Yan Zaizai* (613)
- Design of 5 mega-pixel mobile phone camera
..... *Chen Xi, Shi Jiangyi, Yang Li, Wang Feifei, Liu Yanyang* (617)

AD5933 生物阻抗实时监测的便携式 椎弓根内固定辅助系统

孟云¹, 米宽², 郑诚功¹, 李德玉¹, 汪待发¹

(1. 北京航空航天大学生物与医学工程学院, 北京 100191; 2. 纳通医学科技研究院, 北京 100082)

摘要: 为降低椎弓根内固定手术过程中的螺钉误置率, 基于 ADI 公司的生物阻抗测量芯片 AD5933, 设计了一种实时监测生物阻抗的便携式智能椎弓根开路装置——椎弓根开路器。开路器通过实时测量其头部电极处的组织电阻抗变化, 对电极处的组织进行分析后, 通过声音提示医生操作, 引导开通螺钉钉道, 并避免刺破神经组织。标定实验和离体猪椎骨实验表明, 系统在测量精度上满足实际应用要求, 能够有效区分软组织、松质骨和皮质骨, 将有望降低手术螺钉误置率。

关键词: 生物医学工程; 椎弓根内固定; 生物电阻抗; AD5933; 椎弓根开路器

中图分类号: R318

文献标志码: A

文章编号: 2095-2783(2015)05-0580-04

Bioelectrical impedance aided surgery system for transpedicle screws fixation based on AD5933

Meng Yun¹, Mi Kuan², Zheng Chenggong¹, Li Deyu¹, Wang Daifa¹

(1. School of Biological Science and Medical Engineering, Beihang University, Beijing 100191, China;

2. Naton Medical Institute of Science and Technology, Beijing 100082, China)

Abstract: To decrease the pedicle screw misplaced rate of trans-pedicle internal fixation surgery, this article presented an intelligent and hand-held pedicle drilling tool-pedicle awl, which monitored tissue bioelectrical impedance based on AD5933 of ADI company. It can prompt doctors via voice by analyzing the tissue bioelectrical impedance at the awl's tip. The voice prompt will help to drill pilot holes more accurately and avoid the risk of pricking nerves. Calibration and pigs' vertebrae experiments were performed. The results demonstrate that the impedance detection precision meets the practical application requirements, where the system can effectively produce obviously different sounds for soft tissue, spongy and cortical bones. The results indicate that the proposed system would have great potential in reducing the malposition rates in surgeries.

Key words: biomedical engineering; pedicle screw fixation; bioelectrical impedance; AD5933; pedicle drilling tool

椎弓根内固定手术是脊柱畸形、创伤等脊柱疾病常用的治疗手段, 其在生物力学稳定性、校正畸形的效果上有明显的临床优势^[1]。椎弓根内固定手术, 首先需用开路锥钻好钉道, 然后再置入椎弓根螺钉(pedicle screw, PS)。手术的难点在于 PS 必须在特定的空间内由椎板经椎弓根到达椎体^[2](图 1(b))。然而, 椎骨解剖结构复杂且毗邻很多血管及神经组织, 而椎弓根结构又常存在变异, 使得术中难以把握 PS 的进钉部位、方向和深度, 造成手术难度大、风险高, 图 1 所示为不同的置钉情况。

传统徒手椎弓根置钉手术中, 医生只能靠临床经验 and 手感定位螺钉轨迹^[3], 徒手椎弓根置钉的 PS 误置率一般在 3%~40%。为降低 PS 误置率, 一些椎弓根机械辅助装置得到了发展, 例如 Kashani 等^[4]发明了一种椎弓根钻孔导向器, 但其椎骨结构变异性大, 局限这类辅助装置的实际应用。PS 置入辅助导航技术, 如术中 X 线透视、CT 引导下的计算机辅助技术已得到临床应用, 一定程度上提高了 PS 置入

的准确性, 但使医生和患者均暴露于射线辐射伤害中, 且设备昂贵、学习周期长^[5-8]。

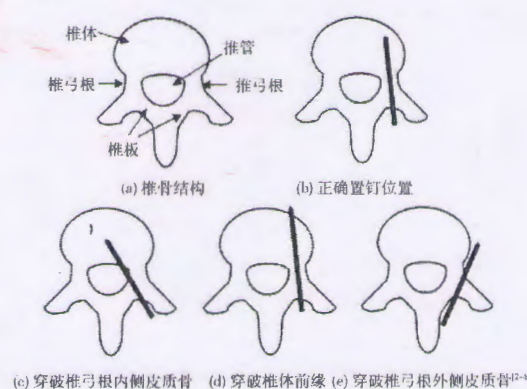


图 1 不同的置钉情况

由于骨组织和软组织电阻抗特性差异大^[9-10], 基于电阻抗测量技术的智能导航技术得到了关注。Myers 等^[11]、徐荣范等^[12]均采用普通椎弓根开路器

收稿日期: 2014-09-24

基金项目: 国家自然科学基金资助项目(61108084); 高等学校博士学科点专项科研基金资助项目(20111102120039)

作者简介: 孟云(1989—), 女, 硕士研究生, 主要研究方向为医学信息与仪器

通信联系人: 汪待发, 讲师, 主要研究方向为光学功能和分子成像、生理信号检测, daifa.wang@buaa.edu.cn

ISSN 2095-2783
CN 10-1033/N
CODEN ZKLHAF

中文核心期刊
原《中国科技论文在线》

中国科技论文

ZHONGGUO KEJI LUNWEN

中华人民共和国教育部 主管 教育部科技发展中心 主办

电子与信息

ELECTRONICS AND INFORMATION



中国科技论文

CHINA SCIENCEPAPER

第十卷 第二十期

二〇一五年十月

Vol. 10 No. 20 Oct. 2015

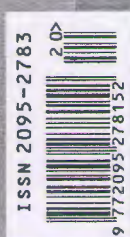
CHINA
SCIENCEPAPER
2015.20
2015年10月 第10卷 第20期
Vol. 10 No. 20 / Oct. 2015

美国《化学文摘》(CA)来源期刊
俄罗斯《文摘杂志》(AJ)来源期刊
美国《剑桥科学文摘》(CSA)来源期刊
美国《乌利希期刊指南》(UPD)收录期刊
波兰《爱白尼索引》(IC)来源期刊
美国《史蒂文斯数据库》(EBSCOhost)收录期刊

电子与信息(卷)
分卷编辑委员会
主任委员: 周海瑞
副主任委员: 吴宏鑫 滕国良
委员: (按姓氏笔画排列)
于戈 于剑 郭立芳 刘越 杨杰 杨华中
杨虎红 吕依 应星 朱秋环 关大晴 张进伟
周东华 赵耀 胡惠民 程卫华 殷建峰 徐恪
徐宝文 陶然 黄华
执行主编: 胡惠民

CHINA SCIENCEPAPER
(Semimonthly, Started in 2006)
Vol. 10 No. 20 Oct. 2015

Competent Authority: Ministry of Education of P.R.C.
Sponsor: Ministry of Education, Science and Technology
Development Center
Editor: Editorial Department of China Sciencepaper
Tel: 010-62514378, 62514379
Address: 35 Zhongguancun St. Haidian, Beijing, Ministry
of Education, Science and Technology
Development Center, 100080
E-mail: tcsp@csu.edu.cn
jwzdy@csu.edu.cn
Web Site: <http://journal.paper.edu.cn>
Printed by: Beijing Kewin Printing Co., Ltd.



本刊为:
中国期刊网来源期刊
万方数据—数字化期刊群来源期刊
中国科技论文在线数据库来源期刊
中文科技期刊数据库来源期刊

总编辑委员会
主任: 邢钰
委员: (按姓氏笔画排列)
马延章 王静 王旭 王永炎 王众托 左铁建
刘永超 齐康 张洪庆 陈伟刚 吴中如 沈德明
刘忠云 牟来 李德仁 李静 赵广田 李可法
钟西 殷雪福 魏 勇 黄伯云 魏书钧 谢和平
管华诗
主 编: 李志民
副主编: 周 静
编辑部部长: 李洁莹

中国科技论文
(半月刊, 2006年创刊)
第10卷/第20期 2015年10月



主管单位: 中华人民共和国教育部
主办单位: 教育部科技发展中心
编辑单位: 《中国科技论文》编辑部
电 话: 010-62514378 62514379
地 址: 北京市海淀区中关村大街35号教育部科技
发展中心, 邮编: 100080
电子信箱: tcsp@csu.edu.cn
jwzdy@csu.edu.cn
网 址: <http://journal.paper.edu.cn>
印 刷: 北京信印印刷有限公司
发行范围: 公开发行
广告经营许可证: 京聘工商广字第8067号

刊号: ISSN 2095-2783 邮发代号: 2-366 定价: 25.00元/期
CN 10-1033 N 800.00元/年



中

国

科

技

论

文

第 10 卷
第 20 期
2015

目次

低存储开销的二进制循环分布式存储编码设计	范永骏, 刘杜鹃, 代明军, 王 晖, 陈 彬, 林晓辉 (2339)
无线传感器网络基于树的路由安全模型研究	秦丹阳, 贾 爽, 王尔馥, 丁 群 (2343)
基于最小计数概要的无线传感器网络异常检测方案	李国瑞, 王 颖 (2351)
大数据环境下最小单调约束闭包 Hadoop 并行关联规则	李春青, 李海生, 梁婷婷, 赵 凯 (2356)
物联网环境下的情境感知服务开发方法	莫 同, 李伟平, 褚伟杰, 吴中海 (2362)
基于分辨矩阵和 Apriori 算法的关联规则挖掘研究与应用	杜晓明, 代逸生 (2369)
MOOC 平台学习行为数据的采集与分析	李 帅, 张岩峰, 于 戈, 焦明海 (2373)
一种贝叶斯优化 RSSI 和 ILS 的室内定位算法	刘 欢, 黄 丽, 杨 晓, 严春来 (2377)
高效并行递归高斯 SIFT 算法的实现	罗 勇, 叶正源, 陈远知 (2382)
一种基于类差分度的互信息特征选择方法	任 军, 葛卫丽, 陈家勇 (2386)
基于粒子群优化的 NLOS 环境的节点定位算法	文 恬, 余小平, 贾 勇 (2390)
多模情感数据库的设计与评价	王宝军, 薛雨丽, 于适宁, 毛 峡 (2395)
一种基于隐马尔可夫的软件可靠性监控方法	周宇鹏, 张鹏程, 滕剑锋, 李雯睿 (2399)
不同图像融合技术的融合性能分析比较	原惠峰, 杨风暴, 张 雷, 牛 涛 (2405)
基于 Kinect 骨骼信息的手势识别	赵飞飞, 刘喆颖, 吕玉祥 (2412)
基于傅里叶图像分析的机织物密度检测	潘如如, 高卫东, 李忠健, 张 杰 (2416)
基于广义预测控制的无刷直流电机控制研究	韩 蒙, 张 艳 (2422)
近红外多光谱荧光分子成像系统的软件设计与实现	祝永强, 乔惠婷, 贺 进, 李德玉, 汪待发 (2427)
DSP 控制的薄膜微阀组集成微流体驱动系统设计	王晓雨, 刘兴阳, 吴 剑, 钱 翔 (2433)
基于 Colpitts 振荡器的超宽带混沌雷达测距实验研究	杨 鹏, 徐 航, 刘 丽, 李静霞, 张建国, 王冰洁 (2437)
含集总元件的平面微波电路 Laguerre-FDTD 分析方法	文 星, 庄 伟, 刘 升, 唐万春, 聂守平 (2442)
新型双陷波超宽带印刷天线的研究	马 建, 庄 伟, 唐万春, 沈来伟, 周佳威 (2447)
基于操作模式的大型立式淬火炉温度控制方法研究	刘 琛, 贺建军, 喻寿益 (2452)
一种全变分二范数有限差分小波域超声成像测井修正算法	张 健, 王一举, 余华平 (2457)
基于信号传输模型的指纹井下目标定位算法	王永星, 华 钢, 徐永刚, 尹洪胜 (2463)

CHINA SCIENCE PAPER

Vol. 10 No. 20, 2015

CONTENTS

- Design of binary cyclic storage code with low storage overhead
..... FAN Yongjun, LIU Dujuan, DAI Mingjun, WANG Hui, CHEN Bin, LIN Xiaohui (2339)
- Research on tree-based routing security model for wireless sensor networks
..... QIN Danyang, JIA Shuang, WANG Erfu, DING Qun (2343)
- Count-min sketch based anomaly detection scheme in wireless sensor networks
..... LI Guorui, WANG Ying (2351)
- CMSC-HPAR: the closure minimal single constraint based Hadoop parallel association rules algorithm
for large data environment LI Chunqing, LI Haisheng, LIANG Tingting, ZHAO Kai (2356)
- A context-aware service development method in environment of internet of things
..... MO Tong, LI Weiping, CHU Weijie, WU Zhonghai (2362)
- Research and application of association rules mining algorithm based on discernibility matrix and apriori
..... DU Xiaoming, DAI Yisheng (2369)
- Learning behavior acquisition and analysis of MOOC
..... LI Shuai, ZHANG Yanfeng, YU Ge, JIAO Minghai (2373)
- Indoor localization algorithm via RSSI optimized Bayesian probability model and iterative least squares
positioning LIU Huan, HUANG Li, YANG Xiao, YAN Chunlai (2377)
- Efficient parallel recursive Gaussian SIFT algorithm
..... LUO Yong, YE Zhengyuan, CHEN Yuanzhi (2382)
- Improved mutual information based on difference factor among classes
..... REN Jun, GE Weili, CHEN Jiayong (2386)
- Particle swarm optimization-based node localization algorithm in non-line-of-sight environment
..... WEN Tian, YU Xiaoping, JIA Yong (2390)
- The design and evaluation of multimode affective database
..... WANG Baojun, XUE Yuli, YU Shining, MAO Xia (2395)
- Software reliability monitor method based on Hidden Markov Model
..... ZHOU Yupeng, ZHANG Pengcheng, TENG Jianfeng, LI Wenrui (2399)
- A comparative study of the performance of different image fusion technology
..... YUAN Hui Feng, YANG Fengbao, ZHANG Lei, NIU Tao (2405)
- Gesture recognition based on Kinect skeleton information
..... ZHAO Feifei, LIU Zhejie, LÜ Yuxiang (2412)
- Woven fabric density inspection using Fourier image analysis
..... PAN Ruru, GAO Weidong, LI Zhongjian, ZHANG Jie (2416)
- Study on brushless DC motor control based on generalized predictive control
..... HAN Meng, ZHANG Yan (2422)
- Design and realization of near-infrared multi-spectral fluorescence molecular imaging system software
..... ZHU Yongqiang, QIAO Huiting, HE Jin, LI Deyu, WANG Daifa (2427)
- Design and implementation of the integrated microfluidic driving system based on DSP
..... WANG Xiaoyu, LIU Xingyang, WU Jian, QIAN Xiang (2433)
- UWB chaotic radar for target detection and ranging using a Colpitts oscillator
..... YANG Peng, XU Hang, LIU Li, LI Jingxia, ZHANG Jianguo, WANG Bingjie (2437)
- Analysis of microstrip circuits with lumped components by Laguerre-FDTD method
..... WEN Xing, ZHUANG Wei, LIU Sheng, TANG Wanchun, NIE Shouping (2442)
- Research on a novel UWB printed antenna with double notches
..... MA Jian, ZHUANG Wei, TANG Wanchun, SHEN Laiwei, ZHOU Jiawei (2447)
- Study on the method of temperature control based on the operational pattern in large-scale vertical
quench furnace LIU Chen, HE Jianjun, YU Shouyi (2452)
- An total variational two norm finite difference wavelet domain inpainting algorithm in ultrasonic
imaging logging ZHANG Jian, WANG Yijun, YU Huaping (2457)
- Localization algorithm of coal mine miner based on the signal transmission model fingerprint
..... WANG Yongxing, HUA Gang, XU Yonggang, YIN Hongsheng (2463)

近红外多光谱荧光分子成像系统的软件设计与实现

祝永强, 乔惠婷, 贺 进, 李德玉, 汪待发

(北京航空航天大学生物与医学工程学院, 北京 100191)

摘要:针对自主研发的近红外多光谱荧光分子影像系统,采用模块化和分层设计方式设计了控制和分析软件,有效地实现了硬件模块访问和协调控制、反射和透射成像多光谱成像模式、自动化的数据采集、图像调整和滤波后处理、自发荧光扣除等功能,为用户提供了一体化的控制和分析平台。基于所设计的软件,采用反射和透射成像两种模式进行了小鼠活体荧光分子影像实验,有效地抑制了小鼠本体自发荧光对目标荧光信号的干扰,为荧光分子成像的研究提供了一种有效的工具。

关键词:荧光成像;分子成像;自发荧光扣除;数据采集;软件设计

中图分类号:TP311

文献标志码:A

文章编号:2095-2783(2015)20-2427-06

Design and realization of near-infrared multi-spectral fluorescence molecular imaging system software

ZHU Yongqiang, QIAO Huiting, HE Jin, LI Deyu, WANG Daifa

(School of Biological Science and Medical Engineering, Beihang University, Beijing 100191, China)

Abstract: The control and analysis software system is designed for our self-produced near-infrared multi-spectral fluorescence molecular imaging system. It provides a stand-alone control and analysis platform for fluorescence molecular imaging, which has the capacity of accessing and coordinately controlling the hardware modules, performing reflection and transmission multi-spectral imaging, automatic data acquisition, image adjustment and filter, and auto-fluorescence reduction. In *in vivo* mouse experiments, this software system is performed in both reflection and transmission imaging modes, where interference from the mouse auto-fluorescence was effectively reduced, and it facilitates the study of fluorescence molecular imaging.

Keywords: fluorescence imaging; molecular imaging; auto-fluorescence reduction; data acquisition; software design

分子影像是利用影像学的手段观察活体状态下细胞或分子水平的状态和变化,通过综合化学、物理、病理学等多个学科技术,在生物学活动的可视化方面取得了重要进展^[1]。荧光分子影像是一种新型的光学分子成像模式,通过投射特定波长的激发光,激发成像物体内的荧光团产生荧光,并通过高灵敏度的探测技术捕获出射的荧光,并传输到计算机进行分析和处理。荧光分子影像技术可以获取位于实验物体表面下方数个厘米处的荧光标记物的分布信息,从而实现对生物学活体特异性的在体可视化观察。随着荧光蛋白、探针技术及相关算法的不断发展,该技术及相关设备已被应用到非侵入式生物活体成像的多个领域^[2-3]中,如疾病诊断、药物研发、手术辅助治疗等,为从分子水平到系统水平的生物学研究提供了一个高度灵活的研究平台^[4-6]。

鉴于荧光分子影像技术的广泛应用前景,该领域受到国内外研究学者的广泛关注。国外PerkinElmer^[7]、Bruker^[8]、GE^[9]等公司分别推出了各自的荧光分子影像产品。国内的清华大学^[10]、中科院自动化所^[11]、苏州大学^[12]、天津大学^[13]以及本实验室^[14-15]等在荧光分子二维和三维成像方面开展

了多年的基础性研究工作,推进了该影像技术向快速三维成像和多模态方向的发展。但这些研究多集中于对基础性算法和搭建在光学平台上的实验系统的研究。鉴于基于光学平台的实验系统的易用性和通用性相对较差,为更方便地开展荧光分子影像生物学的应用研究,本文项目组在已有实验系统的基础上,自主研发了一套近红外多光谱荧光分子二维成像样机。本文主要介绍针对该样机开发的控制和分析软件。

1 系统硬件结构

光在动物组织中传播时,会因组织的吸收而逐渐减弱。而在波长为650~900 nm的近红外“光谱窗口”波段内,光在生物组织中的被吸收率较低,可以穿透数厘米厚的组织,因而该波段内的光适用于动物的在体成像^[16]。根据成像拓扑的不同,可将二维荧光分子成像(fluorescence molecular imaging, FMI)分为反射成像和透射成像两种。其中,反射成像向实验动物投射一个面光照,并在同侧用高灵敏度的相机采集出射的荧光信号,具有实现简单的优点,并已在荧光分子成像领域中得到了广泛的应

收稿日期:2015-02-06

基金项目:国家自然科学基金资助项目(61108084);高等学校博士学科点专项科研基金资助项目(20111102120039)

第一作者:祝永强(1992—),男,硕士研究生,主要研究方向为生物医学信息及仪器

通信作者:汪待发,讲师,主要研究方向为光学功能和分子成像、生理信号检测,daifa.wang@buaa.edu.cn

第一作者会议论文

Performance of fluorescence molecular tomography with hybrid diffuse optical tomography guidance and normalized born method

Daifa Wang^{1,2}, Ling Wang², Yubo Fan², Deyu Li^{2,*}

State Key Laboratory of Software Development Environment, Beihang University, Beijing, China, 100191¹

School of Biological Science and Medical Engineering, Beihang University, Beijing, China, 100191²

Email: daifa.wang@buaa.edu.cn, deyuli@buaa.edu.cn

Abstract—The image quality of fluorescence molecular tomography (FMT) can be significantly improved with diffuse optical tomography (DOT) guidance, by incorporating the prior optical properties information recovered from DOT into its forward photon propagation model. Although present studies all assume that the absolute transmitted excitation light intensity can be measured for DOT, the hypothesis doesn't hold for most cases, because some extent of deviation in the calibrated excitation light amplification factor is inevitable in a non-laboratory (i.e., *in vivo*) imaging environment. In this paper, we evaluate the impact on FMT reconstruction accuracy of the use of hybrid DOT guidance and normalized born method. Results demonstrate that the quantification ability of FMT with DOT guidance alone varies greatly as the absolute deviation in excitation light amplification factor increases. In contrast, the hybrid method investigated is robust to the deviations, suggesting that the hybrid of DOT guidance and normalized born method is essential for quantitative FMT in complex *in vivo* conditions.

Keywords—fluorescence molecular tomography; diffuse optical tomography; heterogeneous media; normalized born method

I. INTRODUCTION

As a noninvasive optical functional imaging technique, fluorescence molecular tomography (FMT) is capable of three dimensional quantification of the spatial distribution of molecular agents *in vivo*. Thus, it provides a depth-resolved quantitative characterization of specific biological processes occurring inside the small animal, such as protein-protein interaction, drug metabolism. At present, it has become an increasingly important tool in preclinical research and drug development [1].

In a typical FMT system, the imaged object is excited sequentially at different source positions on the boundary using a modulated or continuous wave (CW) light source in near-infrared wavelength (650-900nm). For each source position, the emitted light from the excited fluorophores is measured at multiple detector positions and used for reconstructing the spatial distribution of fluorophores. The reconstruction is highly ill-posed, due to the diffusive nature of light propagation in biological tissues.

Theoretically, propagation of both excitation and emission lights in tissue is described by the coupled diffusion equations, when the tissue optical properties including absorption

coefficient μ_a and reduced scattering coefficient μ_s' are given. However, the heterogeneous optical properties of small animal are unknown and often assumed to be homogenous throughout the tissue volume with values equal to their bulk averages. The homogeneity assumption greatly degrades the quantification and resolve abilities of FMT [2,3].

To handle the problem, two strategies are developed. The first strategy is normalized born method, which reduces the heterogeneous optical properties influences by dividing the measured fluorescence signals with its corresponding excitation light signals [3], while the optical properties are still assumed homogeneous. Using mouse atlas simulation experiments, D. Hyde *et al.* evaluated the extension of normalized born method in hybrid X-ray CT and FMT modalities [4], where different optical properties can be assigned to the different segmented organs. However, the need of X-ray CT modality and segmentation of structure images complicates small animal experiment. In addition, even for the same organ, the optical properties, especially the absorption coefficient, may vary greatly for different individuals with different physiological status. These factors all make near-accurate assumption of organ optical properties difficult, and will degrade the FMT image quality. The second strategy is reconstructing optical properties from the collected excitation light signals by using an optical tomography method called diffuse optical tomography (DOT). Based on this strategy, several investigations have been made. Y. Tan *et al.* demonstrated that the optical heterogeneous nature of the target itself, especially when its size was relatively large, should be considered for quantitative FMT [5]. Y. Lin *et al.* demonstrated that the true fluorophore concentration could be recovered only when both the prior structural information and the prior DOT information were utilized [6]. D. Wang *et al.* demonstrated that relatively consistent quantifications were obtained with the prior DOT information in a series of phantom experiments [7]. However, problems exist in DOT guided FMT, restricting its application *in vivo*. One major problem is that determining the exact excitation light amplification factor is very difficult in a non-laboratory (i.e., *in vivo*) environment. The difficulty is because of the small errors in the acquired small animal geometry, the physical errors in the calibration phantom including the optical properties and geometry, and the measurement noise, etc. Thus, some extent of deviation is generally inevitable in the determined excitation light amplification factor for a practical

146

Performance of fluorescence molecular tomography with hybrid diffuse optical tomography guidance and normalized born method

Daifa Wang^{1,2}, Ling Wang², Yubo Fan², Deyu Li^{2*}

State Key Laboratory of Software Development Environment, Beihang University, Beijing, China, 100191¹

School of Biological Science and Medical Engineering, Beihang University, Beijing, China, 100191²

Email: daifa.wang@buaa.edu.cn, deyuli@buaa.edu.cn

Abstract—The image quality of fluorescence molecular tomography (FMT) can be significantly improved with diffuse optical tomography (DOT) guidance, by incorporating the prior optical properties information recovered from DOT into its forward photon propagation model. Although present studies all assume that the absolute transmitted excitation light intensity can be measured for DOT, the hypothesis doesn't hold for most cases, because some extent of deviation in the calibrated excitation light amplification factor is inevitable in a non-laboratory (i.e., *in vivo*) imaging environment. In this paper, we evaluate the impact on FMT reconstruction accuracy of the use of hybrid DOT guidance and normalized born method. Results demonstrate that the quantification ability of FMT with DOT guidance alone varies greatly as the absolute deviation in excitation light amplification factor increases. In contrast, the hybrid method investigated is robust to the deviations, suggesting that the hybrid of DOT guidance and normalized born method is essential for quantitative FMT in complex *in vivo* conditions.

Keywords—fluorescence molecular tomography; diffuse optical tomography; heterogeneous media; normalized born method

I. INTRODUCTION

As a noninvasive optical functional imaging technique, fluorescence molecular tomography (FMT) is capable of three dimensional quantification of the spatial distribution of molecular agents *in vivo*. Thus, it provides a depth-resolved quantitative characterization of specific biological processes occurring inside the small animal, such as protein-protein interaction, drug metabolism. At present, it has become an increasingly important tool in preclinical research and drug development [1].

In a typical FMT system, the imaged object is excited sequentially at different source positions on the boundary using a modulated or continuous wave (CW) light source in near-infrared wavelength (650-900nm). For each source position, the emitted light from the excited fluorophores is measured at multiple detector positions and used for reconstructing the spatial distribution of fluorophores. The reconstruction is highly ill-posed, due to the diffusive nature of light propagation in biological tissues.

Theoretically, propagation of both excitation and emission lights in tissue is described by the coupled diffusion equations, when the tissue optical properties including absorption

coefficient μ_a and reduced scattering coefficient μ'_s are given. However, the heterogeneous optical properties of small animal are unknown and often assumed to be homogenous throughout the tissue volume with values equal to their bulk averages. The homogeneity assumption greatly degrades the quantification and resolve abilities of FMT [2,3].

To handle the problem, two strategies are developed. The first strategy is normalized born method, which reduces the heterogeneous optical properties influences by dividing the measured fluorescence signals with its corresponding excitation light signals [3], while the optical properties are still assumed homogeneous. Using mouse atlas simulation experiments, D. Hyde *et al.* evaluated the extension of normalized born method in hybrid X-ray CT and FMT modalities [4], where different optical properties can be assigned to the different segmented organs. However, the need of X-ray CT modality and segmentation of structure images complicates small animal experiment. In addition, even for the same organ, the optical properties, especially the absorption coefficient, may vary greatly for different individuals with different physiological status. These factors all make near-accurate assumption of organ optical properties difficult, and will degrade the FMT image quality. The second strategy is reconstructing optical properties from the collected excitation light signals by using an optical tomography method called diffuse optical tomography (DOT). Based on this strategy, several investigations have been made. Y. Tan *et al.* demonstrated that the optical heterogeneous nature of the target itself, especially when its size was relatively large, should be considered for quantitative FMT [5]. Y. Lin *et al.* demonstrated that the true fluorophore concentration could be recovered only when both the prior structural information and the prior DOT information were utilized [6]. D. Wang *et al.* demonstrated that relatively consistent quantifications were obtained with the prior DOT information in a series of phantom experiments [7]. However, problems exist in DOT guided FMT, restricting its application *in vivo*. One major problem is that determining the exact excitation light amplification factor is very difficult in a non-laboratory (i.e., *in vivo*) environment. The difficulty is because of the small errors in the acquired small animal geometry, the physical errors in the calibration phantom including the optical properties and geometry, and the measurement noise, etc. Thus, some extent of deviation is generally inevitable in the determined excitation light amplification factor for a practical

Optical tomography for dense scattering media using DLP based structured illumination

Daifa Wang, Jin He, Deyu Li*

Key Laboratory for Biomechanics and Mechanobiology of Ministry of Education, School of Biological Science and Medical Engineering, Beihang University
XueYuan Road No.37, HaiDian District, Beijing 100191, China
daifa.wang@buaa.edu.cn, deyuli@buaa.edu.cn*

Abstract: This article introduces an optical tomography system for dense scattering media, where DLP based structured illumination is adopted. Compared to conventional wide field approach, structured light processing obtained much better image resolution.

1. Introduction

Deep tissue imaging with near-infrared light has achieved significant development in recent years, and has found its applications in cancer diagnosis [1], brain function evaluation [1], as well as small animal fluorescence molecular tomography [2]. However, due to the inherent tissue scattering nature, it is still very challenging to achieve good image contrast and resolution. In recent years, by designing and optimizing different illumination patterns, a novel technique called structured illumination (SI) has demonstrated its capacity in improving image quality and/or speed. In most of the reports [3-5], diffuse light modeling using diffusion equation were performed, and an inverse problem was solved for 3D reconstruction. Another idea of structured light is to reduce out-of-focus light caused by scattering, which was firstly introduced by Neil [6] in the field of microscopy. Based on this idea, to observe turbid sprays tomographically, Kristensson used sinusoidal-intensity modulated patterns for illumination, and obtained greatly contrast enhanced projections at different viewing angles [7,8]. Then, using the well-know CT reconstruction algorithm called filtered back-projection method, 3D tomography result with good spatial resolution was achieved from these enhanced projections. However, a complex optical architecture was used to provide sinusoidally modulated illumination patterns, and the modulation frequency and depth can't be adjusted. Digital light processing (DLP) introduced by Texas Instruments is a modern technique to digitally manipulate structured light pattern, and has attracted great attention in biological optical imaging. In this article, we developed a full-angle imaging system with DLP technique, where the structured illumination light can be easily controlled. The preliminary results demonstrated that the system can get much better image resolution for turbid media via structured illumination than the conventional wide field approach.

2. Method

2.1 Structured Illumination

Structured illumination has the capabilities of filtering multiple-scattering light. The main concept of SI is to illuminate the sample using an incident beam with its intensity sinusoidally modulated in one direction [6],

$$I_{\phi} = I_C + I_S \cdot \sin(2\pi vx + \phi), \quad (1)$$

where I_{ϕ} is the detected image of one SI projection. I_C denotes the conventional image due to non-modulated light, which shows a poor quality due to photon scattering. I_S is the local amplitude of sinusoidal modulation, and bears the structure information unperturbed by scattering. ϕ is the spatial phase of sinusoidal modulation. Extraction of I_S can be achieved by recording three intensity modulated images with spatial phase shifts 0, $2\pi/3$ and $4\pi/3$. Then, an image free of scattering signals can be obtained by processing the recorded data as [6],

Review Article

The Transport and Deposition of Nanoparticles in Respiratory System by Inhalation

Huiting Qiao,^{1,2} Wenyong Liu,¹ Hongyu Gu,¹ Daifa Wang,¹ and Yu Wang¹

¹Key Laboratory for Biomechanics and Mechanobiology of Ministry of Education, School of Biological Science and Medical Engineering, Beihang University, Beijing 100191, China

²School of Biomedical Engineering, Science and Health Systems, Drexel University, Philadelphia, PA 19104, USA

Correspondence should be addressed to Yu Wang; wangyu@buaa.edu.cn

Received 18 September 2014; Accepted 25 December 2014

Academic Editor: Shuming Zhang

Copyright © 2015 Huiting Qiao et al. This is an open access article distributed under the Creative Commons Attribution License, which permits unrestricted use, distribution, and reproduction in any medium, provided the original work is properly cited.

The inhaled nanoparticles have attracted more and more attention, since they are more easily to enter the deep part of respiratory system. Some nanoparticles were reported to cause pulmonary inflammation. The toxicity of nanoparticles depends not only on its chemical component but also on the quantity and position of the deposition. The deposition of nanoparticles is not uniform and is influenced by airflow transport. The high deposition mainly occurs at the carinal ridges and the inside walls around the carinal ridges. Many factors could affect the transport and deposition of nanoparticles, such as particle size, flow rate, structure of airway, pulmonary function, and age. In this review, we discussed the methods and technique involved in particle transport and deposition studies. The features of particles deposition could be observed in clinic experiments and animal experiments. The mechanism of transport could be studied by numerical simulation. Numerical model and experiment study supplement each other. Some techniques such as medical imaging may support the study of nanoparticles transport and deposition. The knowledge of particles transport and deposition may be helpful both to defend the toxicity of inhaled particles and to direct inhaled drug delivery.

1. Introduction

More and more attention has been paid to air pollution. The high concentration of fine particle matter (PM 2.5) during the 2013 severe haze of north China has caused public worries [1, 2]. The most worries are due to the adverse effect of air pollution on health [3]. It is believed that the most airborne particles were derived from fossil, biomass, and solid fuels combustion [4–6]. The traffic exhausts have been verified as the source of particle matter [7, 8]. The particles emitted by engines have a high proportion of nanoparticles, though most of them are in accumulation mode [9]. Epidemiological studies have confirmed that air pollution makes adverse health effect, especially the pollutant in nanoscale [10, 11]. Thus, nowadays most attention paid to airborne pollutants lies in nanoparticles and ultrafine particles.

Though some studies did not differentiate ultrafine particles from nanoparticles [12], the different definitions have also been reported. The particles in nanoscales (<100 nm) in

one dimension could be generally called nanoparticles, while ultrafine particles are limited to 100 nm in all dimensions [13]. For the purposes of this review, we do not differentiate nanoparticles from ultrafine particles: they are both particles in nanoscales.

People have great expectation for nanotechnology and have been trying to apply nanomaterial in many fields [14, 15]. Thus airborne nanoparticles are unavoidable. For the reason of small size, nanoparticles may enter the deep part of human respiratory system with breathing. Pulmonary inflammation has been reported after inhalation exposure to nanoparticles [16, 17], so the toxicity of nanoparticles in air should be considered [18].

Respiratory system is an important pathway for substance to enter human body besides alimentary canal. Air enters the trachea through nasal and oral cavities, passing by the tracheobronchial tree, and arrives at the alveoli, so does some airborne nanoparticles. The transport and deposition of particles have great relations with the complicated airway.

The effect of tumor size on the imaging diagnosis: A study based on simulation

Huiting Qiao, Libin Wang, Deyu Li, Daifa Wang and Yu Wang*

School of Biological Science and Medical Engineering, Beihang University, Beijing 100191, China

Abstract. Positron emission tomography (PET) has been widely used in early diagnosis of tumors. Though standardized uptake value (SUV) is a common diagnosis index for PET, it will be affected by the size of the tumor. To explore how the tumor size affects imaging diagnosis index, dynamic PET images were simulated to study the relationship between tumor size and the imaging diagnosis index. It was found that the SUV of the region of the tumor varied with scan time, and the SUV was always lower than the true value of tumor. Even more deviations were found in SUV with a reduced tumor size. The diagnosis index SUV_{max} was more reliable than SUV, for it declined only when the volume of tumor was less than 3 mm^3 . Therefore, the effect of tumor size on the SUV and SUV_{max} that are used as diagnosis indices in the early diagnosis of tumors should not be neglected.

Keywords: Standardized uptake value, maximum standardized uptake value, positron emission tomography, tumor size, diagnosis

1. Introduction

As one of the most serious threats to life health, cancer is the second leading cause of death in developing countries. The number of people who are diagnosed with cancer and the mortality rates of people diagnosed with malignant tumor are still increasing in recent years [1,2]. It was reported that lung cancer was the leading cause of death in all the common cancer registries [3,4], and its mortality rate increased substantially in the past three years. Although there are some methods of oncologic treatment on clinical therapies, such as radiation, chemotherapy and surgery, it is still hard to improve the survival rate of lung cancer because of late diagnosis [5,6]. Therefore, early diagnosis is important to improve treatment and the survival rate of patients with lung cancer [7,8]. Imaging diagnosis [9] as well as identification of molecular biomarkers [10–12] have been used as two main methods in the studies of early diagnosis for lung cancer.

In terms of imaging diagnosis, positron emission tomography (PET) is the function imaging technology that can provide metabolism information of tissues by using a radioactive tracer [13]. Moreover, it is an important tool for staging, prognosis, evaluation of treatment, and, especially, for early diagnosis [14,15]. A tumor usually has a higher metabolic rate, so it can be recognized easily by using PET. Besides the visual cancer imaging, PET can also provide some detection indices for diagnosis,

*Corresponding author: Yu Wang, School of Biological Science and Medical Engineering, Beihang University, Beijing, China. Tel.: 82338755; Fax: 82315554; E-mail: wangyu@buaa.edu.cn.



A study of the metabolism of transplanted tumor in the lung by micro PET/CT in mice



Huiting Qiao^a, Jun Li^b, Yingmao Chen^c, Daifa Wang^a, Jintao Han^d, Mengqi Mei^a, Deyu Li^{a,*}

^a Key Laboratory for Biomechanics and Mechanobiology of Ministry of Education, School of Biological Science and Medical Engineering, Beihang University, Beijing 100191, China

^b Peking University Laboratory Animal Centre, Peking University, Beijing 100871, China

^c Department of Nuclear Medicine, General Hospital of PLA, Beijing 100853, China

^d Department of Interventional Radiology and Vascular Surgery, Peking University Third Hospital, Beijing 100191, China

ARTICLE INFO

Article history:

Received 5 January 2013

Received in revised form 12 August 2013

Accepted 12 November 2013

Keywords:

Micro PET/CT

Metabolic model

Tumor

Dynamic scan

ABSTRACT

The difference of tumor metabolism from that of normal tissue is an important factor for diagnosis through functional imaging such as positron emission tomography (PET). A quantitative description of the metabolic process will help to improve the diagnosis methods. In this study, the metabolism of tumor in lung was quantitatively described in mice. The melanoma was transplanted into the lung of mice, and the metabolism of the transplanted tumor was detected by micro PET/CT with [¹⁸F]fluoro-2-deoxy-D-glucose (FDG). Nine mice were transplanted with B16 melanoma cells through their tail vein. Lung tumor was detected by pathological method. The lesions smaller than 1 mm could hardly be directly detected directly by micro PET/CT, while the tumor with a 1–4 mm diameter could be detected by micro PET/CT. A metabolic model with three compartments was separately established for lung tumors and normal lung tissues. In this model, the lung cancer had a significantly higher metabolic rate constant as compared to that of the normal lung tissue ($p=0.01$). The outputs of the model fit well with the original curve from the dynamic images. It is also found that difference of tissue activity between tumors and normal lung tissues varied along scan time. Through this comparison, it was suggested that the difference in metabolism between the lung tissue and the tumor might contribute to the tumor diagnosis.

© 2013 IPEM. Published by Elsevier Ltd. All rights reserved.

1. Introduction

Malignant tumor is one of the great threats to human health. Early detection and early treatment is the key to reduce the mortality from malignant tumors. The distinction between cancer and normal tissue is the base of an early detection. For example, the difference of glucose metabolism between the cancer and normal tissue is the basic principle of cancer detection by Positron emission tomography (PET) with [¹⁸F]fluoro-2-deoxy-D-glucose (FDG) [1,2]. To develop a technique for tumor detection, it is important to understand the metabolic character of different tissues and cancers. Therefore quantitative metabolic models have been established for and cancer [3] as well as normal tissue [4,5].

In the process for the development of methods and techniques for tumor detection and therapy, small animals, such as mice, have been widely used [6,7]. These animals could also be used to assess

the treatment effects through imaging and semi-quantitative analysis [8,9]. Although many tumor models have been used in small animals for biomedical research and PET imaging [10,11], a quantitative metabolic study is lacking for small animal. In this study, we quantitatively investigated the tumor metabolism in mice. Unlike the existing kinetic analysis for subcutaneous tumors [12], we studied a transplanted tumor in lung by micro PET/CT imaging in mice.

The study of tumor metabolism in mice could be of great importance in order to develop tumor PET detection. There are two ways to increase the sensitivity and specificity of the PET detection, including: finding specific tracer [13], and proposing optimized scan scheme according to the metabolic distinction of focus [14]. Some previous studies have already shown the potential usefulness of dynamic PET in detection [15], due to an increased metabolic distinction that can be achieved in dynamic imaging as compared to the static imaging [16]. To optimize the scanning scheme of the dynamic imaging, the development of a metabolic model in small animals is necessary. In this effort, quantitative metabolic models were separately established for lung tumors as well as normal lung tissues, and their distinction was further discussed.

* Corresponding author. Tel.: +86 10 82339490.

E-mail address: deyuli@buaa.edu.cn (D. Li).

其他作者SCI论文

Multimed Tools Appl
DOI 10.1007/s11042-013-1589-3

Medical image retrieval based on unclean image bags

Yonggang Huang · Jun Zhang ·
Heyan Huang · Daifa Wang

© Springer Science+Business Media New York 2013

Abstract Traditional content-based image retrieval (CBIR) scheme with assumption of independent individual images in large-scale collections suffers from poor retrieval performance. In medical applications, images usually exist in the form of image bags and each bag includes multiple relevant images of the same perceptual meaning. In this paper, based on these natural image bags, we explore a new scheme to improve the performance of medical image retrieval. It is feasible and efficient to search the bag-based medical image collection by providing a query bag. However, there is a critical problem of noisy images which may present in image bags and severely affect the retrieval performance. A new three-stage solution is proposed to perform the retrieval and handle the noisy images. In stage 1, in order to alleviate the influence of noisy images, we associate each image in the image bags with a relevance degree. In stage 2, a novel similarity aggregation method is proposed to incorporate image relevance and feature importance into the similarity computation process. In stage 3,

Y. Huang (✉) · H. Huang
Beijing Engineering Research Center of High Volume Language Information
Processing & Cloud Computing Applications, Beijing Institute of Technology,
Beijing, 100081, China
e-mail: yonggang.h@gmail.com

Y. Huang · H. Huang
School of Computer Science and Technology, Beijing Institute of Technology,
Beijing, 100081, China

J. Zhang
School of Information Technology, Deakin University, VIC, 3217, Australia
e-mail: jun.zhang@deakin.edu.au

D. Wang
School of Biological Science and Medical Engineering, Beihang University,
Beijing, 100191, China
e-mail: daifa.wang@buaa.edu.cn

Published online: 14 July 2013

 Springer

Review Article

The Mutual Beneficial Effect between Medical Imaging and Nanomedicine

Huiting Qiao,¹ Libin Wang,¹ Jintao Han,² Yingmao Chen,³ Daifa Wang,¹ and Deyu Li¹

¹ Key Laboratory for Biomechanics and Mechanobiology of Ministry of Education, School of Biological Science and Medical Engineering, Beihang University, Beijing 100191, China

² Department of Interventional Radiology and Vascular Surgery, Peking University Third Hospital, Beijing, China

³ Department of Nuclear Medicine, General Hospital of PLA, Beijing 100853, China

Correspondence should be addressed to Deyu Li; deyuli@buaa.edu.cn

Received 13 June 2013; Accepted 15 July 2013

Academic Editor: Xiaoming Li

Copyright © 2013 Huiting Qiao et al. This is an open access article distributed under the Creative Commons Attribution License, which permits unrestricted use, distribution, and reproduction in any medium, provided the original work is properly cited.

The reports on medical imaging and nanomedicine are getting more and more prevalent. Many nanoparticles entering into the body act as contrast agents, or probes in medical imaging, which are parts of nanomedicines. The application extent and the quality of imaging have been improved by nanotechnology. On one hand, nanomedicines advance the sensitivity and specificity of molecular imaging. On the other hand, the biodistribution of nanomedicine can also be studied *in vivo* by medical imaging, which is necessary in the toxicological research. The toxicity of nanomedicine is a concern which may slow down the application of nanomedical. The quantitative description of the kinetic process is significant. Based on metabolic study on radioactivity tracer, a scheme of pharmacokinetic research of nanomedicine is proposed. In this review, we will discuss the potential advantage of medical imaging in toxicology of nanomedicine, as well as the advancement of medical imaging prompted by nanomedicine.

1. Introduction

Medical imaging is an important technology in clinical and medical research, which enables the observation of human and animals *in vivo*. The development of medical imaging contributes a lot to diagnosis and therapy. However, researchers are not satisfied with single anatomical image. To detect physiological function and biological process, functional imaging, molecular imaging, and multimodality imaging are invented and have developed prosperously [1–3]. Most molecular imaging today depends on synthesized probe with special property [4]. For nuclear medicine, for example, the probe is also expressed as radioactive tracer or tracer [5, 6] for positron emission tomography (PET). For fluorescence molecular tomography the probe is a fluorescence agent [7]. In terms of traditional imaging, some agents are used to increase the contrast of images [8, 9]. Contrast agent can enhance their applications and even upgrade them to cellular and molecular level.

Nanotechnology has a remarkable great contribution to the development of medical imaging. Nanomedicine is

a scientific specialty of nanotechnology, which has great potentials to develop the diagnostic and therapeutic approaches [10–12]. Nanomedicine has drawn broad interests in medical imaging, as well as the targeted therapy [13]. Modified by nanotechnology, some probes and contrast agents become more efficient [14], and then they can be called nanomedicine [15]. Some kinds of nanoparticle, just as metal nanoparticles, become nanomedicine used as contrast agent of medical imaging [16, 17]. With the application of nanomedicine, medical imaging will have a broader prospect in application.

Nevertheless, the nanomedicine, used in medical imaging, must eliminate the potential risks in safety issues. Most nanomaterials have been discovered to affect cell behavior [18, 19] and even to damage the physiological system [20, 21]. The discussion of the biocompatibility and toxicity of nanomaterial is of a great importance in biological and medical research. The toxicology of nanomaterials is usually studied on cellular scale or smaller size, while the pharmacokinetics is also necessary to understand its potential toxicity [22]. As pharmacokinetics of tracer is studied by

大型近红外光谱脑功能成像系统 NirScan

汪待发

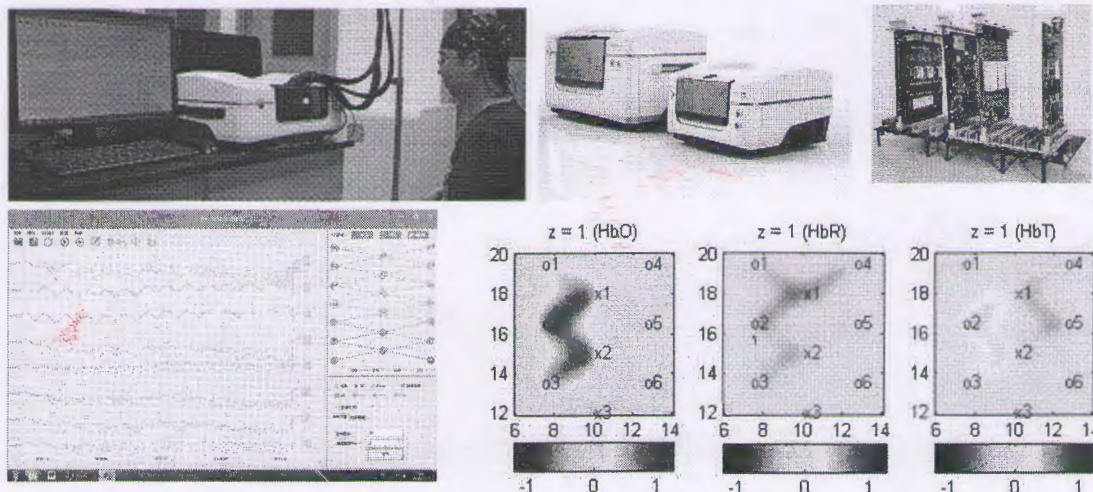
北京航空航天大学生物与医学工程学院, 100191

daifa.wang@buaa.edu.cn

18600201095

利用组织光谱特性的差异, 近红外光谱 (Functional near-infrared spectroscopy, fNIRS) 可以高时间分辨的探测和成像脑活动激活的脑皮层血流和血氧含量的变化, 进而有效的对脑活动进行可视化和定量评估。相对于脑电 (Electroencephalogram, EEG)、功能核磁共振 (Functional magnetic resonance imaging, fMRI) 等其他成像方法, fNIRS 具有成本适中、时间分辨率高、空间分辨率适中、对运动不敏感等特点或优势, 在近些年得到广泛关注, 已发展成为一种不可或缺的脑功能成像模态, 在基础科研和临床应用中发挥越来越重要的作用。近几年, 国内利用 fNIRS 开展基础和临床研究的课题组急剧增加。然而, 这一大型高端影像设备的庞大国内市场目前一直由国外公司包括日本的日立和岛津、美国的 Techon 和 NIRx 等控制。

国内市场, 除了北京航空航天大学本项目主持研发的大型近红外光谱脑功能成像设备 NeuroLight 外, 尚未见其它自主产品。该系统提供 24 通道 (每通道包含三波长激光: 785nm、808nm、850nm) 照明探头、42 通道基于雪崩二极管传感的探测探头, 以及从 20Hz 到 200Hz 的时间分辨率, 满足全脑功能成像的需求。结合激光功率数字可调与 24 位高精度数模转换, 该系统提供超过 110 dB 的动态范围和远低于 0.2 pW 的探测灵敏度, 确保了高质量的 fNIRS 信号探测和成像。通过典型的运动、听觉和视觉等实验范式, 我们验证了该系统的有效性。



下表比较了不同商业系统的核心参数, 包括光源、探测器、通道数、时间分辨率、空间分辨率、探测深度、探测灵敏度等。从这些产品的参数和指标对比来看, 本项目组研发的第一代产品 NeuroLight 的指标已经达到了国际同类先进产品水平, 并且部分指标还有超出。

表. 商用 fNIRS 产品参数对比

产品	厂家	光源	探测器	光源通道数	探测通道数	时间分辨率(Hz)	空间分辨率(cm)	探测灵敏度(pW)	探测深度(cm)
ETG-4000	日立	双波长激光 (695nm, 830nm)	APD (灵敏度高)	40x2	40	10	1.5 到 2	<0.2 pW	1.5 到 2
FOIRE-3000	岛津	三波长激光 (785nm, 805nm, 830nm)	PMT(灵敏度高)	4x3 到 16x3	4 到 16	7.5 到 40	1.5 到 2	<0.2 pW	1.5 到 2
CW6	Techon	双波长激光 (690nm, 830nm)	APD(灵敏度高)	4x2 到 48x	8 到 32	10 到 50	1.5 到 2	<0.2 pW	1.5 到 2
NIRScout X	NIRx	双波长 LED (760nm, 850nm)	PD(灵敏度低)	8x2 到 16x2	4 到 24	6.25 到 62.5	1.5 到 2	~1 pW	1.5 到 2
NirScan	北京航空航天大学	三波长激光 (780nm, 808nm, 835nm)	APD(灵敏度高)	4x3 到 24x3	6 到 42	20 到 200	1.5 到 2	<0.2 pW	1.5 到 2

专业技术职务
任职资格

汪待发 同志

证 书



经 北京航空航天大学 专业技术
职务评审委员会于二〇一〇年十月评审
通过具有 讲师 职务任职资格。

No 0131134

二〇一一年五月四日



991

清华大学
Tsinghua University
毕业证书



普通高等教育

注册号码: 100031200505003286

学生汪待发, 性别男,
生于1984年4月21日,
于2001年9月至2005年7月在本校
生物医学工程系
生物医学工程专业
四年制本科学习,
修完教学计划规定的全部课程,
成绩合格, 准予毕业。

校长

顾秉林



清华大学

二〇〇五年七月八日

151



学士学位证书

(普通高等教育本科毕业生)

汪待发，男，
1984年4月生。自2001
年9月至2005年7月



在清华大学生物医学工程系

生物医学工程

专业

完成了四年制本科学习计划，业已毕业。
经审核符合《中华人民共和国学位条例》
的规定，授予工学学士学位。

清华大学

学位评定委员会主席

顾秉林

二〇〇五年七月八日

证书编号：100031200505003286

851

清华大学

博士研究生

毕业证书



研究生 汪待发 性别 男

1984 年 4 月 21 日生，2005 年 9 月

入我校 医学院

生物医学工程 学科

学习，现已修完博士研究生培养计划规定的全部课程，成绩合格，于 2010 年 6 月通过毕业论文答辩，准予毕业。

校长

胡章珉



2010 年 7 月 15 日

证书编号: 100031201001000916

博士学位证书



汪待发，男，1984年4月21日生。在清华大学

生物医学工程

学科（专业）已通过博士学位的课程

考试和论文答辩，成绩合格。根据《中华人民共和国学位条例》的规定，授予工学博士学位。

校长

学位评定委员会主席

清华大学



证书编号：1000322010000499

二〇一〇年七月十五日